Structures and Dynamics of Optically Confined Matter

A thesis submitted for the degree of Doctor of Philosophy

Richard Daniel Dear



Balliol College, **University of Oxford**

Trinity Term 2013

Structures and Dynamics of Optically Confined Matter

A thesis submitted for the degree of Doctor of Philosophy
Richard Daniel Dear, Balliol College, University of Oxford
Trinity Term 2013

Abstract

This thesis explores the structures and dynamics of optically confined matter, ranging from single particle traps to complex optically bound colloidal arrays, investigating and quantifying the behaviour of each system. It begins with an introduction to optical manipulation techniques and a discussion of the development of the single beam gradient force trap, more commonly referred to as optical tweezers. Following this, the building of a single beam optical trap will be presented alongside a discussion of some of the key components in such a setup, before it is calibrated, allowing a demonstration of some of the techniques which are utilised later in the thesis.

The optical trapping of aerosol droplets is an area of key importance in atmospheric chemistry, as optical tweezers provide a valuable and versatile tool for droplet manipulation and characterisation. Trapping single aerosol droplets is facilitated by using annular rather than conventional Gaussian beams, as will be demonstrated, with significant advantages in increasing the size range of trappable droplets, and improving their axial localisation. These improvements will be demonstrated experimentally with an in-depth comparison of Gaussian and annular beam trapping. These enhancements are also verified theoretically using a model developed by Burnham and McGloin, showing excellent agreement with experimental results.

Ionic liquids, defined as organic salts with melting points below room temperature, are another area of great contemporary interest. They are highly tunable and so have been referred to as "designer solvents", and also have important applications as "green" solvents in organic chemistry. Trapping particles within these novel liquids allows a micro-rheological investigation of their properties to be conducted. This is demonstrated by determining the temperature dependent viscosity changes of these media, showing excellent agreement with previous macro-rheological studies. In addition, hydrodynamic effects such as Faxén's correction to viscous drag in proximity to a surface, and hydrodynamic coupling between pairs of colloids trapped in ionic liquids are demonstrated.

Following these single and dual particle studies, this thesis continues with an investigation of the structures and dynamics of optically bound matter formed of larger numbers of particles. The behaviour of these optically bound structures is particularly sensitive to the number

of particles involved, and so a counter-propagating evanescent field trap in conjunction with an inverted optical tweezers setup is utilised in order to controllably assemble these structures and study the factors affecting their behaviour. Initially one-dimensional chains of optically bound 3.5 µm diameter silica particles are studied, allowing an implementation of Generalized Lorentz-Mie Theory (GLMT) to be developed through collaboration with Dr. Jonathan Taylor of The University of Glasgow. Experimental and theoretical insights allow further understanding of the processes involved in the formation of these structures.

Having studied the behaviour of 3.5 µm diameter silica particles in a counter-propagating evanescent wave trap, the effects of changing particle size and refractive index are presented by using smaller silica and melamine particles. These results are explained in terms of the increased importance of interference fringes in determining the arrangement of the optically bound structures of smaller particles, and due to the increased interaction of the melamine particles with the evanescent field as a result of the larger refractive index contrast between them and the trapping medium.

The thesis then concludes with a study of the dynamics of the previously presented optically bound chains. Initially the diffusion of single particles in the evanescent field is compared to their freely-diffusing behaviour, quantifying the confining effect of the field. The addition of particles to the field then allows the diffusive behaviour to be studied as a function of particle number, and understood in terms of on-axis confinement by adjacent particles. The tilting of these optically bound chains relative to the inter-beam axis is also explored as a function of particle number, as is the rigidity of these chains. Finally a more complex, dynamic effect is presented, dubbed "Newton's Cradle", in which particles are ejected from the ends of the chains before returning and repeating this process. This behaviour is understood by utilising the previously developed GLMT simulations.

Acknowledgements

First of all I would like to say a huge thank you to Grant who, since my very first tutorial in Oxford, has been a fantastic tutor and inspiring supervisor. His endless enthusiasm and interest in my work has always been appreciated, as well as certain conference trips! Mike Summers is someone who I simply couldn't have completed this work without. He patiently taught me just about everything I know about optical trapping, stuck by me through those long nights of aerosol trapping and was always ready to help out even long after he'd left Oxford. I have also been lucky to work with Jonny Taylor and Daniel Burnham, both of whom have been incredibly helpful throughout our collaboration work. Arran Curran is also someone I must thank, having put up with me pestering him with all my questions, for being so generous with his time and for being a lot of fun at conferences!

There are many more people in the Ritchie and Hancock groups to thank, including Gus of course, who has always been supportive and full of good advice. Rich Walker and Martin Crow are two of my old office buddies and now close friends, through many Monday nights spent together! I hope this is a tradition we can continue in London soon. I have also worked with some fantastic Part II students; Lucy Fishwick who was so much fun to work with, Andrew Rickards - we will get to more festivals in the future!, Will Gault who helped me continually wind up Lee through some excellent and inspired schemes, and Emma Worrall who has kept me stocked up on sweets and goodies throughout the writing up period.

Lee deserves huge amounts of thanks for being so helpful, so much fun to spend time with and for being such a great friend over the last few years. I couldn't have asked for a better person to work with. I'm sorry about the air duster. Thanks as well to Ann and Julian, who have been in the group with me since my Part II year. I have really enjoyed getting to know you both. I also have to thank Alex of course, as well as Ian, Simon and Jamie for being some of my closest friends over the last eight years.

I would also like to thank all those in the MCR who I have got to know, and of course Heather who has been so supportive and who I have shared so many great times with. Thanks also to all of the members of the Hertford Wind Band, and everyone who has made my time in the triathlon club so much fun - I'm sure I will see plenty of you at races in the future. I have loved being part of both groups and will miss you all once I have left Oxford.

Finally I would like to thank my family who have supported me through the whole of my time at Oxford, I couldn't have done it without you.

List of Publications

R. D. Dear, E. K. Worrall, W. D. Gault and G. A. D. Ritchie. "Microrheological investigations in ionic liquids using optical trapping techniques." *The Journal of Physical Chemistry B*, **117**, 10567–71 (2013).
http://dx.doi.org/10.1021/jp405986q

R. D. Dear, D. R. Burnham, M. D. Summers, D. McGloin and G. A. D. Ritchie. "Single aerosol trapping with an annular beam: improved particle localisation." *Physical Chemistry Chemical Physics : PCCP*, **14**, 15826–31 (2012).
http://dx.doi.org/10.1039/c2cp42925j

M. D. Summers, R. D. Dear, J. M. Taylor and G. A. D. Ritchie. "Directed assembly of optically bound matter." *Optics Express*, **20**, 1001–12 (2012).
http://dx.doi.org/10.1364/OE.20.001001

L. J. Moore, R. D. Dear, M. D. Summers, R. P. A. Dullens and G. A. D. Ritchie. "Direct observation of grain rotation-induced grain coalescence in two-dimensional colloidal crystals." *Nano letters*, **10**, 4266–72 (2010).
http://dx.doi.org/10.1021/nl102786k

M. D. Summers, R. D. Dear, J. M. Taylor and G. A. D. Ritchie. "Controlled formation of optically bound matter in evanescent fields." *Proceedings of SPIE*, 776213–8 (2010).
http://dx.doi.org/10.1117/12.860685

Contents

Abstract i

Acknowledgements iii

List of Publications iv

1 Introduction 1
- 1.1 Thesis Outline . . . 2
- 1.2 The Development of Optical Tweezers . . . 4
- 1.3 The Physics of an Optical Tweezers Trap . . . 7
  - 1.3.1 The Geometric Optics Limit . . . 7
  - 1.3.2 The Rayleigh Limit . . . 9
  - 1.3.3 The Mie Regime . . . 10
- 1.4 The Dynamics of an Optically Trapped Particle . . . 10
- 1.5 Conclusions . . . 13

2 Construction of a Single-Beam Optical Trap 14
- 2.1 Experimental Considerations . . . 14
  - 2.1.1 Laser . . . 15
  - 2.1.2 Objective . . . 16
  - 2.1.3 Beam Steering . . . 17
  - 2.1.4 The Sample . . . 18
  - 2.1.5 Imaging . . . 19
- 2.2 Trapping Multiple Particles . . . 19
  - 2.2.1 Beam Splitting . . . 19
  - 2.2.2 Beam Scanning . . . 20
  - 2.2.3 Holographic Techniques . . . 20
- 2.3 Particle Tracking . . . 21
  - 2.3.1 Back Focal Plane Interferometry . . . 21
  - 2.3.2 High-Speed Camera Tracking . . . 23
  - 2.3.3 Allan Variance Considerations . . . 24
  - 2.3.4 Power Spectra Analysis . . . 26
- 2.4 Characterising an Optical Tweezers Trap . . . 27
  - 2.4.1 Particle Position and Trap Stiffness . . . 27

2.4.2 Faxén's Correction to Viscous Drag . . . 29
2.5 Conclusions . . . 30

3 Optical Trapping of Aerosol Droplets Using Annular Beams 32
3.1 Optical Trapping of Aerosol Droplets . . . 33
3.2 Modelling an Optical Trap . . . 35
3.3 Experimental Configuration . . . 40
3.4 Testing the Model . . . 42
3.4.1 Trapping Power . . . 42
3.4.2 Droplet Size . . . 45
3.4.3 Axial Localisation . . . 46
3.4.4 Trap Stiffness . . . 48
3.5 Conclusions . . . 52

4 Micro-Rheological Investigations of Ionic Liquids 54
4.1 Room Temperature Ionic Liquids . . . 55
4.2 Micro-Rheological Investigations using Back Focal Plane Interferometry . . . 56
4.2.1 Experimental Setup . . . 56
4.2.2 Trap Stiffness Measurements . . . 59
4.2.3 Temperature Dependant Viscosity Changes in ILs . . . 61
4.3 Micro-Rheological Investigations using a Fast Camera . . . 64
4.3.1 Experimental Setup . . . 64
4.3.2 Mean Square Displacement Measurements for a Particle Diffusing in EAN . . . 65
4.3.3 Trap Stiffness Measurements . . . 67
4.3.4 Temperature Dependant Viscosity Changes in EAN . . . 69
4.3.5 Measuring Faxén's Correction to Viscous Drag . . . 70
4.4 Hydrodynamic Coupling Studies . . . 72
4.4.1 Dual-Beam Optical Tweezers . . . 75
4.4.2 Hydrodynamic Coupling in Water . . . 76
4.4.3 Hydrodynamic Coupling in RTILs . . . 78
4.5 Conclusions . . . 82

5 Directed Assembly of Optically Bound Matter 84
5.1 Optical Binding . . . 84
5.2 Experimental Setup . . . 87
5.3 Directed Assembly of Silica Particles in an Evanescent Field . . . 89
5.3.1 Chain Building . . . 89
5.3.2 Factors Affecting Chain Length . . . 95
5.4 GLMT Modelling of Optically Bound Chains . . . 98
5.5 Conclusions . . . 102

6 Exploring the Effects of Particle Diameter and Refractive Index on Optically Bound Matter 104
6.1 Changing Particle Size . . . 105
6.1.1 Quantifying the Effect of Interference Fringes . . . 105
6.1.2 1.5 µm Silica Particles . . . 105
6.1.3 1.0 µm Silica Particles . . . 110

6.2 Changing Particle Refractive Index 111
6.3 Conclusions 118

7 Dynamics of Optically Bound Matter 120
7.1 Dynamics of Optically Bound Silica Chains 120
7.1.1 Chain Diffusion 120
7.1.2 Chain Angle 128
7.1.3 Chain Rigidity 131
7.2 Chain Dynamics for Smaller Silica Particles 135
7.2.1 More Concentrated Silica Samples 138
7.3 "Newton's Cradle" 141
7.4 Conclusions 144

8 General Conclusions and Further Work 146

References 150

Chapter 1

Introduction

Optical tweezers are a powerful and versatile tool with numerous applications in biology [1], physics [2], and colloidal science [3]. Their ability to manipulate matter, and to exert and measure pico-Newton sized forces, has facilitated a number of scientific investigations, ranging from the study of molecular motors at the single molecule level [4], to the investigation of single aerosol droplets [5], and their role in atmospherically important processes. They have been crucial in the study of colloids and mesoscopic systems, many of which provide readily observable analogues to atomic and nano-crystal phenomena [6]. More recent developments have increased the usefulness of this tool even further; beam sharing techniques have allowed the study of multiple colloidal particle interactions and coupling [7], while holographic advances have facilitated, for example, the trapping of particles and droplets using more complex beam types [8]. Trapping with novel beam types has included the optical guiding of droplets and particles over long distances using Bessel beams [9], the trapping of low refractive index particles using Laguerre-Gaussian beams [10], and the transfer of orbital angular momentum to trapped particles using optical vortices [11], with applications in pumping and mixing in microfluidic channels [12].

Optical manipulation is not confined to the interactions of these single particles with radiation forces however, and there is a rich and complex field of study surrounding the phenomena known as optical binding [13]. In these systems, the particles themselves influence the optical field experienced by the other particles in the system, leading to an intricate interplay of non-linear scattering effects. The result may be that these particles spontaneously assemble into low energy confirmations, forming optically bound arrays [14],

or experience more complicated collective driven motion [15], initiating studies of the non-linear optical response of condensed matter. Both of these areas of optical manipulation will be presented in this thesis, from the study of single colloids in optical fields, to the directed assembly of optically bound matter formed from multiple interacting particles.

1.1 Thesis Outline

In this thesis the interaction of both colloidal particles and aerosol droplets with light will be explored in a number of different systems. In this introductory chapter a brief historical overview of the development of optical tweezers will be presented and the underlying physics governing stable optical trapping will be discussed. Following this, the power spectrum method of trap stiffness determination will be introduced; a technique which will be used frequently in this thesis.

Chapter 2 will provide a description of how to build a simple optical tweezers setup, including a discussion of the important factors to be considered in order to produce a stable and efficient trap. This will be followed by a description of the techniques available for tracking optically confined particles, and an outline of the analytical procedures and software routines which will be used. This chapter will also include the characterisation of a simple optical tweezers trap, demonstrating the techniques which have been previously discussed. Finally the effects of Faxén's correction to viscous drag will be presented for an optically trapped microparticle in water, as a demonstration of a hydrodynamic effect which may be probed using optical tweezers.

Having demonstrated the stable trapping of colloidal particles, Chapter 3 will introduce the optical trapping of aerosol droplets using single beam optical tweezers. This has important applications in atmospheric studies as conventional Gaussian beam optical traps have limitations in the size range of particles which they can stably confine. In this chapter, the use of annular beams for the trapping of aerosol droplets is presented, providing a number of improvements over Gaussian beam traps. These improvements, including an increased size range of trappable particles and improved axial localisation, are explored experimentally and verified theoretically using a recent model proposed by Burnham and McGloin [16].

The use of optical tweezers as a technique for micro-rheology will then be presented in Chapter 4, where the Brownian behaviour of microparticles trapped within ionic liquids is

used to determine physically important properties. Ionic liquids are of great contemporary interest and optical tweezers provide a simple and convenient method of interrogation, due in part to the small sample volumes which are required and as a result of their ability to probe local properties on the micron length-scale. This chapter demonstrates this technique, and includes a comparison of back focal plane interferometry and camera based methods of particle tracking for determining temperature dependent viscosity changes. Finally the use of a dual beam setup is introduced in order to allow inter-particle interactions to be studied. Specifically the hydrodynamic coupling of pairs of melamine microparticles trapped in two different ionic liquids is successfully quantified, showing excellent agreement with theoretical expectations.

The exploration of multiple particle coupling effects which was introduced in Chapter 4 will then be continued into Chapter 5 as the optical binding of colloidal particles is studied. When illuminated with counter-propagating evanescent waves particles are seen to spontaneously assembly into chains and arrays, dictated by their interaction with the optical field and complex multiple particle scattering effects. By utilising an inverted optical tweezers setup this optically bound matter can be controllably assembled and studied, allowing the key effects responsible for this behaviour to be determined. While small numbers of particles will form stable chains, with inter-particle separations significantly larger than the particle diameter, the addition of further particles initiates a process of chain collapse, where the optically bound matter transitions to a chain of spheres which are almost in physical contact. Collaboration with Dr. Jonathan Taylor of The University of Glasgow has allowed modelling of this experimental system, showing good agreement with experimental results and shedding further light on the physical processes involved.

The effect of changing particle size and refractive index on these optically bound structures is then explored in Chapter 6 using a series of different particle types and further theoretical modelling. There are several competing factors which are responsible for the formation of this optically bound matter such as the underlying optical potential, the presence of interference fringes and multiple particle scattering processes, and the relative importance of each of these is seen to vary significantly with changing particle type. As a result, a range of different behaviours are observed including chain collapse, bi-stability and array formation, sensitively dependent on the particle type and size.

Having explored the configurations of this optically bound matter in the preceding two

chapters, the dynamic effects associated with these structures will be presented in Chapter 7. The optically bound chains are shown to exhibit diffusion and concerted motion which is strongly dependent on the number of particles in the chain. Initially the addition of particles to the optically bound chains acts to further confine these particles due to the effects of forward-scattered light. As more particles are added the compressive forces acting on the particles within the chain become more important, resulting in a destabilising effect and a limit in the length of stable chain which can be formed. These effects will be quantified before a dynamic effect dubbed "Newton's Cradle" is demonstrated, in which particles are seen to be repeatedly ejected from the ends of the optically bound chain in a manner similar to that seen in the children's toy.

Finally general conclusions and final comments will be given in Chapter 8, including suggestions for further study in these areas.

1.2 The Development of Optical Tweezers

The use of radiation pressure and optical tweezers for the manipulation and study of particles was pioneered by Arthur Ashkin and his colleagues throughout the 1970s and 80s. Following advances in laser development they were able to provide the first demonstration of particle acceleration using radiation pressure [17], though this concept was in fact experimentally confirmed nearly 70 years earlier by Lebedev, observing the displacement of a suspended radiometer when illuminated using a focused arc lamp [18]. In the work of Ashkin, micron sized latex spheres suspended in water were accelerated using a continuous wave laser focussed into a glass cell, by a radiation pressure force termed the *scattering force*. Perhaps more surprising was the observation that, as well as being accelerated in the direction of beam propagation, these particles were also simultaneously drawn on to the beam propagation axis. This latter effect can be understood due to the forces acting on the sphere as a result of refraction of the incident light, termed the *gradient force*. When placed off-axis the result is a force acting to pull the particle towards the region of highest light intensity, provided the refractive index of the particle is greater than that of the trapping medium. In contrast, when air bubbles were investigated, they were seen to be pushed out of the beam path due to the refractive index of the droplet being lower than that of the medium. Knowledge of these effects enabled stable optical confinement to be achieved

using counter-propagating beams, where the particles were drawn on to the inter-beam axis and confined due to balanced radiation pressure forces from the two opposing beams.

Single beam optical confinement was then demonstrated in 1971 where a vertically directed, focussed laser beam was used to trap a glass sphere [19]. In this levitation trap, the sphere was again drawn onto the beam axis while the upwards radiation pressure was balanced by the gravitational forces acting on the particle. Confirmation of this stable trapping being solely a result of radiation pressure effects was provided by the success of a similar experiment in high vacuum [20]. The use of feedback to damp particle oscillations was also demonstrated, whereby the droplet was trapped at a fixed height achieved by controlling the power of the beam in response to its position fluctuations, providing a method of directly monitoring the forces acting on the droplet [21].

One of the major breakthroughs in the use of optical techniques for particle trapping and manipulation came in 1986, when Ashkin *et al.* demonstrated the first true single beam optical trap, meaning that particles were confined using optical forces alone [22]. In this key paper, these workers presented a trap in which the scattering forces acting on the particle due to radiation pressure were balanced by gradient forces. This was achieved by tightly focussing the illuminating laser beam such that the gradient force acting to pull the particle back towards the laser focus was sufficient to balance the scattering force in the direction of beam propagation. This stable, three dimensional, single beam trap has revolutionised many areas of science. One of the first applications demonstrated by the Ashkin group was that of the trapping of viruses, bacteria and single cells [23, 24]. In these papers they were able to demonstrate the manipulation of individual viruses and live bacteria, proving the applicability of this technique in the area of biological particle manipulation. Damage free manipulation of cells and the organelles within them was also demonstrated, proving to be an important starting point for much recent biological research using optical trapping techniques [25].

As well as being used to confine and manipulate biological particles, optical tweezers have been employed to great effect in investigating force producing molecules in biology. This is generally achieved by attaching colloidal particles to the molecules of interest as handles, which has further advantages as it can also help prevent photo-damage to the system in question by displacing the laser focus. As the gradient restoring force acting on a particle at small displacements from the trap centre is simply proportional to this displacement,

the optical trap is described as acting like a Hookean spring. Therefore with knowledge of the optical trap stiffness, any displacement of the trapped particle can be quantified and used to determine the magnitude of the external force acting upon it.

One of the first examples of this technique was presented by Block *et al.*, where the movement of kinesin along a microtubule track was investigated [4]. In this work microscopic silica beads were attached to the kinesin molecules, providing a method for monitoring their movement along the microtubules as well as allowing forces to be applied to the kinesin molecules. Results demonstrating how the probability of pulling these beads from the microtubule varied with kinesin concentration provided new insights into potential mechanisms for kinesin movement. More recent work by this group has included the development of passive optical force clamps [26] and monitoring of the base-pair stepping of RNA polymerase as it moves along a DNA template [27]. In this case a dual-beam setup was utilised, where an RNA molecule was attached to one bead and the end of the DNA molecule fixed to another. This arrangement permitted the stepping process to be monitored at Angstrom level resolution, aided by using a second trap for tethering rather than fixing to the slide surface and resulting in reduced mechanical noise and drift. In work by Rohrbach, forces as small as 25 fN have been measured using an optical trap, thought to be the smallest measured using these techniques and demonstrating their remarkable sensitivity [28]. This sensitivity is part of the reason why optical tweezers and other optical techniques have had such a key impact in these areas, demonstrated by a number of comprehensive review articles and recent publications [29–35].

While the applications described so far have been centred in biophysics, optical trapping and manipulation techniques have also enabled huge advances to be made in fields as diverse as microfluidics [36], interfacial science [37], atmospheric chemistry [38], force measurements [39] and in the modelling of atomic processes [40] demonstrating the versatility of these techniques. In this thesis optical tweezers will be used to confine aerosol droplets, interrogate novel media, quantify colloidal particle interactions and controllably assemble optically bound matter, and pertinent previous studies will be introduced in subsequent chapters as appropriate. First a brief description of the physics of an optical tweezers trap will be presented.

1.3 The Physics of an Optical Tweezers Trap

As was described in Section 1.2 it is often convenient to separate the optical forces acting on a particle in a tweezers trap into two components; namely the gradient and scattering forces. The scattering force can be thought of as resulting from the radiation pressure of the incident photons impinging on the particle, leading to a net force in the direction of beam propagation. The gradient force acts in the direction of increasing light intensity for a particle with a higher refractive index than the trapping medium. While the scattering force will often dominate, the gradient force must be considered when there is a steep intensity gradient, explaining the use of high numerical aperture (NA) microscope objectives for optical trapping, where a higher NA relates to a steeper angle of the cone of light which can enter or exit the objective. In an optical tweezers trap it is the gradient force acting to pull the particle back towards the laser focus which balances the scattering force, leading to a stable trapping position being found slightly beyond the laser focus.

The basis of these forces will now be described for the two limiting cases of sphere size; when the particle is much larger than the wavelength of the trapping radiation, λ, these forces can simply be understood in terms of a ray optics approach, whereas particles much smaller than the trapping radiation can be treated as point dipoles in the Rayleigh limit. A more complex description is needed when these two dimensions are comparable, as is the case for most optical trapping experiments, and a full Mie scattering calculation is required.

1.3.1 The Geometric Optics Limit

The geometric optics limit describes the regime where $a \gg \lambda$, where a is the particle radius and λ the trapping wavelength. In this regime the optical forces can be discussed using a simple ray optics approach. The scattering force can be understood as arising from both reflection and absorption of photons by the particle, while it is refraction of the incident beam which is responsible for the gradient force. Figure 1.1 shows this process. As the incident light is refracted at the two interfaces there is a change in its momentum, necessarily giving an equal and opposite momentum change in the sphere and leading to a force in the direction shown. If multiple beams with differing intensities are considered it can be seen that the net force will act towards the region of highest light intensity, as the force due to each beam is directly proportional to its intensity.

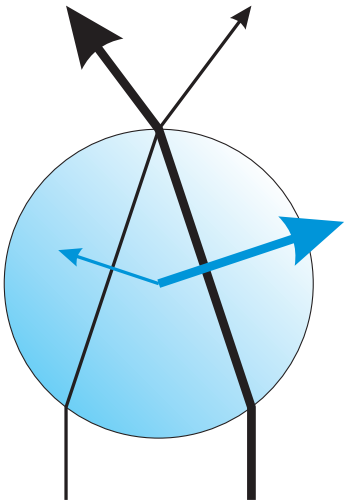


Figure 1.1: An illustration of the gradient force acting on a trapped microsphere. Each of the rays incident on the sphere (black lines) undergoes refraction leading to an equal and opposite momentum change in the sphere and resulting in the forces shown in blue. If there is an intensity gradient across the sphere as shown, there will be a net force in the direction of increasing light intensity.

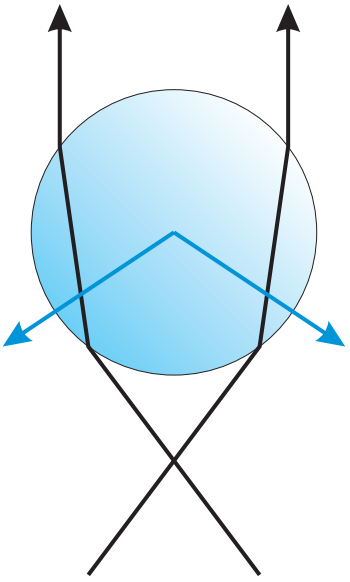


Figure 1.2: When the microsphere is positioned just beyond the laser focus, the refraction of the two beams shown now results in a net force in the opposite direction to beam propagation, allowing the scattering force to be balanced and a stable optical trap formed.

When the laser radiation is tightly focussed, typically using a microscope objective with an NA of at least 1.2, this gradient force can act in the opposite direction to beam propagation, balancing the scattering force and allowing the formation of a stable optical trap. This situation is illustrated in Figure 1.2 where the net force resulting from the two beams shown acts back towards the beam focus and opposes the scattering force. In this case a stable trap can be formed slightly beyond the beam focus.

1.3.2 The Rayleigh Limit

In the opposite limit, where the sphere is much smaller than the wavelength of the illuminating radiation ($a \ll \lambda$), the particle can be treated as a point dipole. In this case the scattering force is proportional to the incident light intensity and acts in the direction of beam propagation. This force results from the absorption and re-radiation of light by the particle, and can be written as:

$$F_{\text{scatt}} = \frac{I_0 \sigma n_m}{c} \tag{1.1}$$

where I_0 is the incident light intensity, σ is the scattering cross-section of the sphere, n_m is the refractive index of the trapping medium and c is the speed of light in a vacuum. The scattering cross-section of the sphere can be calculated *via*:

$$\sigma = \frac{128\pi^5 a^6}{3\lambda^4}\left(\frac{m^2-1}{m^2+2}\right)^2 \tag{1.2}$$

where $m = n_p/n_m$, and is the ratio of the refractive indices of the particle and the medium.

The gradient force can then be understood as a result of interactions of the induced dipole with the surrounding inhomogeneous field, described by:

$$F_{\text{grad}} = \frac{2\pi\alpha}{cn_m^2}\nabla I_0 \tag{1.3}$$

where F_{grad} is proportional to the gradient of the intensity, ∇I_0, and the polarisability of the particle, α, is given by:

$$\alpha = n_m^2 a^3 \left(\frac{m^2-1}{m^2+2}\right). \tag{1.4}$$

When the refractive index of the particle is greater than that of the medium, and $m > 1$, this gradient force will act in the direction of increasing light intensity as has already been discussed.

1.3.3 The Mie Regime

In the intermediate, and most commonly used regime, neither of these descriptions are valid and more involved calculations are required. Classical Mie theory cannot be used due to the inappropriateness of this plane wave scattering model when applied to the tightly focussed beams utilised in optical tweezers. Instead, one approach is to use the Mie-Debye basis derived by Mazolli *et al.* [41]. An extension to this work by Viana *et al.* incorporated the effects of spherical aberrations resulting from the glass slide and water interface present in a typical optical trap, leading to the development of Mie-Debye spherical aberration theory (MDSA) [42]. A further extension of this theory was then used by Burnham and McGloin to model an aerosol optical trap with great success [16] as will be explored further in Chapter 3. In Chapter 5 an implementation of Generalized Lorentz-Mie Theory (GLMT) will be discussed, and utilised in the modelling of optically bound matter.

1.4 The Dynamics of an Optically Trapped Particle

A discussion of the dynamics of an optically trapped particle begins with the Langevin equation for a microsphere of radius a trapped in a harmonic potential. In one dimension this expression is given by [43, 44]:

$$\ddot{x}(t) + \Gamma_0 \dot{x}(t) + \Omega_0^2 x(t) = \xi(t) \tag{1.5}$$

where $\Gamma_0 = \gamma_0/m$ is the viscous damping of the medium, m is the mass of the trapped particle and γ_0 the Stokes' drag coefficient. In the absence of any boundary effects γ_0 can be readily calculated for a spherical particle using Equation 1.6:

$$\gamma_0 = 6\pi\rho\upsilon a \tag{1.6}$$

where $\rho\upsilon$ is the dynamic viscosity of the trapping medium, ρ its density and υ its kinematic viscosity. The next term in the Langevin equation, $\Omega_0^2 = \kappa/m$, is the angular frequency of the oscillator where κ is the trap stiffness. Finally $\xi(t)$ represents a stochastic force, equal to $(2k_{\mathrm{B}}T\gamma_0)^{1/2}\eta(t)/m$, due to the thermal motion of the solvent molecules. Hence Equation 1.5 now describes the behaviour of an optically trapped particle, subject to Brownian stochastic forces and a Hookean restoring force due to the optical trap.

A system may be characterised as either over or underdamped by examining its "damping ratio", defined as Γ_0/Ω_0 [45]. While this value is always larger than one for an overdamped system, it may become less than one when air is the trapping medium and the system is underdamped. When studying overdamped colloidal systems Equation 1.5 can be simplified by noting that the time required for loss of energy through friction, given by $t_{\text{inert}} = m/\gamma_0$, will typically be on the order of a µs and far shorter than the experimental time resolution. This allows the inertial term in the equation to be dropped, and Equation 1.5 to be rewritten, giving:

$$\dot{x}(t) + 2\pi f_c x(t) = (2D)^{1/2}\eta(t) \tag{1.7}$$

where D, the diffusion constant, is given by the Stokes-Einstein relationship:

$$D = \frac{k_{\text{B}}T}{\gamma_0} \tag{1.8}$$

and a new parameter, f_c, has been introduced. This term is the *corner frequency*, and is given by:

$$f_c = \frac{\kappa}{2\pi\gamma_0}. \tag{1.9}$$

By Fourier transforming Equation 1.7 and finding its expectation value, the motion can be rewritten in terms of its frequency components. This gives a *power spectrum* of position fluctuations of the form [46]:

$$S_x(f) = \frac{D}{2\pi^2}\frac{1}{f_c^2 + f^2}. \tag{1.10}$$

This one-dimensional power spectrum has a tail tending to f^{-2} at high frequency values, and a low frequency plateau given by $2k_{\text{B}}T\gamma_0/\kappa^2$. The reason for introducing the corner frequency to Equation 1.7 is now apparent, as it defines the point at which the power spectrum drops to half of its low frequency plateau value. This is of importance as it means that f_c can readily be determined from experimental data and used to calculate κ, the crucial parameter required in order to make quantitative investigations using optical tweezers. It is also important to note that this interpretation is true even for an uncalibrated position detection system. If, for example, a quadrant photo-diode is being used for position detection, particle displacements will be monitored in terms of a voltage trace. If the voltage to micron calibration factor is unknown or subject to large errors, experimental trap stiffnesses can still be confidently assigned as the corner frequency is independent of the scale being used. An example particle power spectrum is given in Figure 1.3 (left) for a

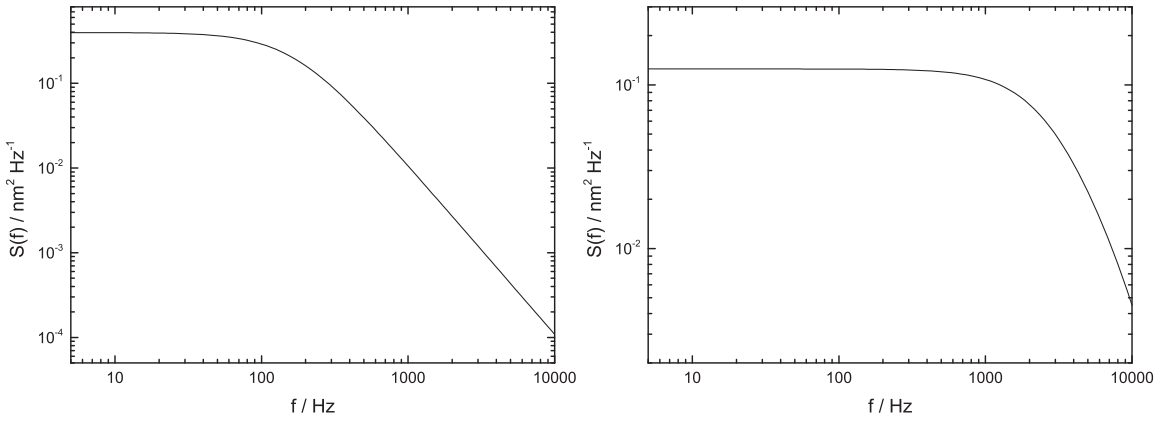


Figure 1.3: Simulated power spectra using parameters expected for a typical colloidal sample (left) and for a water droplet trapped in air (right), illustrating the Lorentzian form and the different tail gradients in each case. The parameters used are given in the text.

1 µm radius colloidal particle trapped in water with a trap stiffness of 20 pN/µm, calculated using Equation 1.10.

When trapping in air the timescale for energy loss through friction is now typically $\sim 50\times$ longer due to the lower viscosity of the trapping medium, and as a result it is no longer appropriate to drop the inertial term from Equation 1.5. In this case the full Langevin equation must be used for analysis.

Taking the Fourier transform of Equation 1.5 in the same way as before gives the following expression for the power spectrum of a system when inertia must be included:

$$S_x(f) = \frac{2k_\mathrm{B}T}{\kappa} \frac{\Omega_0^2 \Gamma_0}{((2\pi f)^2 - \Omega_0^2)^2 + (2\pi f)^2 \Gamma_0^2}. \tag{1.11}$$

In contrast to the power spectrum for a system neglecting inertia, this spectrum now has a high frequency tail tending to f^{-4}, characteristic of an underdamped system [47]. An example simulated power spectrum is shown in Figure 1.3 (right), calculated for a 1 µm radius water droplet trapped in air with a trap stiffness of 5 pN/µm using Equation 1.11. The different tail gradients can be clearly observed when compared to the overdamped power spectrum, indicating the importance of the inertial terms in the second example. The use of both of these forms will be demonstrated in this thesis; Chapter 3 will include analysis of the power spectra of salt water droplets trapped in air, while Chapter 4 will demonstrate the use this technique in the overdamped colloidal regime.

1.5 Conclusions

In this chapter an outline of the contents of this thesis has been presented, detailing the layout of the main body of this work. A brief history of the development of optical tweezers has been given, followed by a discussion of the physics behind such a trap in each of the different size regimes. Finally the dynamics of an optically trapped particle have been discussed and the power spectrum method of trap stiffness determination introduced, in preparation for an experimental demonstration in the following chapter.

Chapter 2

Construction of a Single-Beam Optical Trap

Having introduced optical tweezers and the physics governing the behaviour of optically trapped particles in Chapter 1, this chapter will now focus on some of the important experimental features of an optical tweezers setup. Following this, techniques for trapping multiple particles will be introduced. A discussion of the particle tracking and analytical techniques which will be used in this thesis will then be presented, followed by the characterisation of a typical colloidal tweezers trap.

2.1 Experimental Considerations

One of the main advantages of the optical tweezers technique is its simplicity, and the ease with which it can be incorporated into existing experimental setups. Often they are designed around optical microscopes as then many of the required optics and stage manipulation components are already in place. Whether modifying an existing microscope or building an entirely new setup, there are a number of important requirements to address. Neuman and Block provide an excellent discussion of the factors and components to be considered when building an optical trap [48] which, along with the protocol of Lee *et al.* [49], provides a thorough introduction into this area. This chapter will discuss the most important of these considerations, allowing the key components and design aspects to be understood.

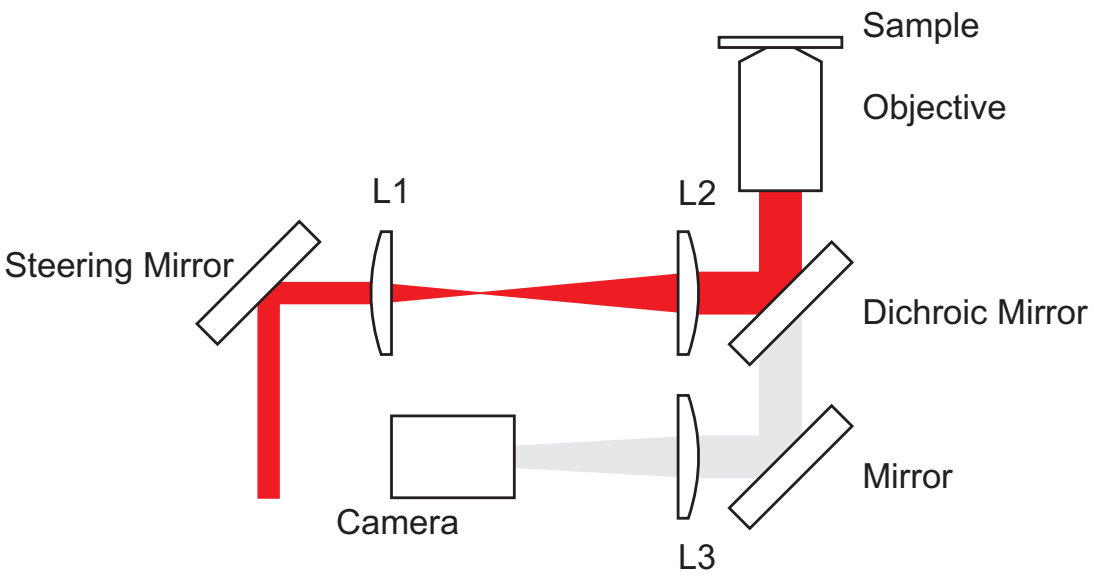


Figure 2.1: A simple optical tweezers setup including a laser beam, beam steering optics, an objective to focus the beam and a camera for sample imaging.

The experimental setup which will be characterised towards the end of this chapter is shown in Figure 2.1 in order to aid a discussion of the important components over the next few pages. The trap is formed using a Laser Quantum Forte continuous wave source (400 mW at 1064 nm), directed into the back aperture of a microscope objective using lenses L1 and L2 positioned in a $4f$ arrangement as will be described later. L1 and L2 have focal lengths of 50 mm and 150 mm, providing 3:1 beam expansion. The use of a dichroic mirror to direct the beam into the back aperture of the microscope objective, designed to reflect near-infrared radiation and transmit all others, means that the same objective can be used for imaging. The sample is illuminated from above using a white light source, and the transmitted radiation imaged onto the camera using L3.

2.1.1 Laser

There are many factors to consider when choosing a trapping laser, with the most crucial of these being its ability to output a single mode with high pointing stability in order to produce an efficient trap. A Gaussian mode is generally used, as it will focus to the smallest diameter beam waist. The quality of this Gaussian output may be quantified by a factor, M, relating it to that of a perfect Gaussian beam where $M = 1$. Typically a beam profile with $M^2 < 1.1$ is desired in order that an efficient and harmonic trap is produced.

Power stability is another important consideration, as any power fluctuation will result in a change in the optical trap stiffness, and variation in this parameter will greatly hinder any sensitive force measurements using the trap. Generally a laser will perform best in terms of its output and power stability when running at its maximum driver current. For this reason the laser will typically be run at full power, with additional optics used for fine power control. This often takes the form of a half-waveplate ($\lambda/2$) and polarising beam splitter (PBS). By directing the laser output through the half-waveplate, the polarisation of the output beam can be rotated. The PBS will then split this output into two orthogonally polarised beams, with the relative power in each determined by the initial polarisation of the input beam. While one of these outputs will be used in the optical trap, the second will typically go to a beam dump. Alternatively a power meter may be used to record the power of the rejected beam, allowing the actual trapping power to be determined.

A final important consideration is that of the laser wavelength. This is most crucial for biological samples as care must be taken to avoid optical damage. For this reason near infrared lasers are often used, as they are located in a region of relative transparency in the absorption spectrum of both water and proteins. While this becomes less crucial when not trapping biological samples, other considerations such as the optics being used, the sensitivity of any required detectors to that wavelength, and any potential sample heating effects must be considered.

2.1.2 Objective

The second important component to be considered is that of the microscope objective used to focus the laser radiation and form the optical trap. A key parameter is the *numerical aperture*, NA, of the objective, defined in terms of the half-angle of the maximum cone of light that can enter or exit the objective, θ, given by:

$$\mathrm{NA} = n_m \sin\theta \tag{2.1}$$

where n_m is the refractive index of the trapping medium. A high NA objective is needed to maximise the optical gradient force; typically an NA of 1.2–1.4 is required in order to form a stable optical trap.

In addition, the immersion medium of any objective being used must also be considered. Oil immersion objectives are common, requiring a drop of immersion oil to be used between the objective and the sample. They do however have relatively short working distances, largely due to the magnitude of the refractive index contrast between the immersion and trapping media, leading to significant spherical aberrations when trapping at longer working distances. Spherical aberrations result from a difference in the focus point from rays passing through the centre of a lens and those travelling through the peripheral region, leading to an axial elongation of the trap focus. This limitation can be overcome by using water immersion objectives [50], although they are typically more expensive.

Finally the transmission of the objective must be taken into account, as this is a key parameter dictating the resulting optical trap stiffness and this quantity may vary significantly with laser wavelength. The transmission of an objective may also be reduced by *overfilling* of the back aperture, a technique used to improve the efficiency of an optical trap. As a Gaussian beam is focused using an objective, it is the peripheral rays which will contribute most to the gradient force acting on the particle, while the central rays will generally contribute towards the scattering force. In a Gaussian beam, its profile dictates that the intensity of these central rays will be greater. It is therefore pertinent to increase the relative contribution of the peripheral rays in order to improve the optical trapping efficiency, thereby increasing the gradient relative to the scattering force. By overfilling the back aperture of the objective using a simple telescope arrangement, despite the reduced transmission due to power loss, the intensity of the peripheral rays is increased relative to those at the beam centre and the trapping efficiency is improved. In practise a balance between increased efficiency and decreased power transmission must be reached.

2.1.3 Beam Steering

In order to manipulate the optical trap a method of beam steering is required and a $4f$ system is typically used, as demonstrated in Figure 2.2. In this arrangement the steering mirror forms a *conjugate plane* with the back aperture of the microscope objective, achieved by arranging the two lenses such that the mirror sits a distance f_1 from the first lens, the two lenses are separated by $f_1 + f_2$, and the back aperture of the microscope objective is located a distance f_2 from the second lens, where f_1 and f_2 are the focal lengths of the two lenses. Imaging of the beam in this way means that an adjustment of the steering

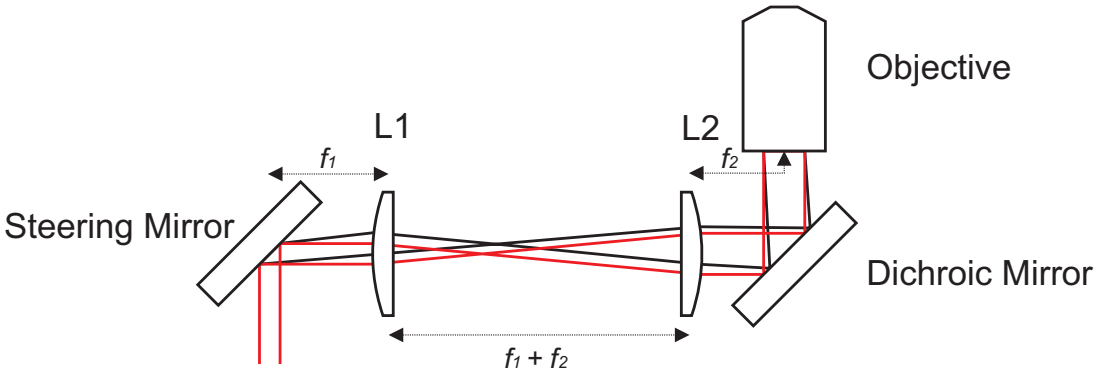


Figure 2.2: In this $4f$ imaging system the steering mirror and the back aperture of the microscope objective form conjugate planes. As the steering mirror is manipulated the angle at which the beam enters the back aperture of the microscope objective is altered while its position remains unchanged, allowing control of the trapping position without beam clipping.

mirror will alter the angle at which the beam enters the back aperture of the objective, but not the position, ensuring that no beam clipping occurs. This arrangement allows the position of the trap to be adjusted using the steering mirror with no power losses, as shown in Figure 2.2. This $4f$ system can also be used for beam expansion by choosing the lenses appropriately as demonstrated in the experimental setup shown in Figure 2.1.

2.1.4 The Sample

Once the beam has been directed into the back aperture of the microscope objective it will be focussed into the sample where trapping will take place. There are a few points to consider when preparing a sample, including the thickness of the cell or sample coverslip which is being used due to the limited working distance of the oil immersion objectives. In the work presented in this thesis No. 1 thickness borosilicate glass coverslips (Thermo Scientific Gerhard Menzel) will be used, with a thickness of $\sim 0.15\,\text{mm}$. A typical colloidal sample will be contained between two of these coverslips, with a custom vinyl spacer used to form a sealed volume of around $10\,\mu\text{L}$. Immersion oil will be placed between the objective and the sample. The colloidal sample itself may consist of silica or melamine microparticles suspended in Milli-Q water (Millipore). When trapping aerosol samples a different cell is required, consisting of two circular coverslips separated by a 3 mm thick rubber spacer. Aerosol droplets can then be introduced using a medical nebuliser, as will be described in Chapter 3.

2.1.5 Imaging

In the experimental setup shown in Figure 2.1 a dichroic mirror, chosen to reflect the trapping wavelength and transmit all others, has been used to reflect the trapping laser radiation into the back aperture of the microscope objective. This mirror greatly facilitates imaging of the sample, as the trapping objective can also be used for imaging purposes, achieved by illuminating from above the sample using a white light source. The light that is transmitted through the dichroic mirror is then focussed onto a camera for imaging. Commonly CCD (charge coupled device) cameras are used for imaging, although the affordability of CMOS (complementary metal-oxide semiconductor) cameras is making them an attractive option for particle imaging due to the high frame rates which are possible.

2.2 Trapping Multiple Particles

While the experimental setup presented so far enables the trapping of a single particle, it is clearly of interest to be able to trap multiple particles for a range of experiments. Previously this has included, for example, the work of Abbondanzieri *et al.* as described in Section 1.2 where a dual-beam setup was utilised in order to monitor the base-pair stepping of RNA polymerase [27]. In the work presented in this thesis a dual-beam trap will be utilised in order to investigate the hydrodynamic coupling between pairs of optically trapped particles, and so a brief outline of some of the methods available for constructing multiple optical traps will now be given.

2.2.1 Beam Splitting

Perhaps the most simple method of constructing a dual-beam setup is to split the beam using polarisation optics and then recombine along a common optical path, allowing independent manipulation of each beam in three-dimensions as demonstrated by Fällman and Axner [51]. The incoming beam is split by a polarising beam splitter, with each of the resulting orthogonal beams going through separate beam steering optics before being recombined using a second polarising beam splitter cube. By ensuring that the mirrors used to steer each of the traps are positioned at a conjugate plane to the back aperture of the microscope objective, positioning of each of the traps can take place independently with

no beam clipping occurring. Furthermore, the use of separate lens systems for each beam allows some control over the z position of each trap. This system forms a straight-forward method of constructing a dual-beam trap with limited additional components required and minimal power losses. For these reasons this is the technique which will be used in this thesis, and so will be described in more detail in Chapter 4.

2.2.2 Beam Scanning

An alternative to the beam splitting techniques of Fällman *et al.* [51] is to use beam scanning optics. In this system the trapping laser is "shared" over many trapping sites, at a rate (typically several kHz) such that each trapped particle cannot diffuse away from its position when its trap is off. One common technique is to use acousto-optic deflectors (AODs). In each AOD a diffraction grating is formed by applying a modulation to a piezoelectric transducer and propagating a sound wave through the crystal, allowing the laser beam to be deflected by an angle determined by this input frequency. The angle at which the first order diffracted beam will be deflected is given by:

$$\theta = \lambda f / v \tag{2.2}$$

where λ is the trapping wavelength, f the frequency of the acoustic wave and v its velocity [52]. Combining two AODs allows manipulation of the beam in both the x and y directions. An example of the use of AODs for the trapping of hundreds of colloidal particles can be found in Vossen *et al.*, where several different schemes were presented allowing the trapping and imaging of complex three-dimensional colloidal structures [53]. More recently work by Juniper *et al.* used AODs to generate optical potential energy landscapes which they then mapped using colloidal particles in a solvent flow [54].

2.2.3 Holographic Techniques

A final method of multiple trap generation is to use holographic techniques. By altering the phase of a light beam a hologram can be used to control how it will propagate, a technique first demonstrated by Fournier *et al.* [55]. In this work static glass holograms were used as a method of producing multiple trapping sites. More recently spatial light modulators (SLMs) have been used as a method of producing computer controlled holograms, allowing real-time

three-dimensional trapping of multiple particles [56, 57]. One of the first demonstrations of the real power of using SLMs in this way was by Curtis *et al.*, showing the use of iterative computer algorithms allowing simultaneous trapping and control of hundreds of particles [58].

There are drawbacks to using spatial light modulators, including much slower refresh speeds than can be obtained using AODs, and the relatively high losses resulting from a large proportion of the incident beam remaining unmodulated. These are offset however by significant advantages when compared to other techniques including the formation of more unusual traps, such as the optical vortices demonstrated by Ladavac and Grier [12], and the correction of optical aberrations using appropriate modifications to the hologram.

2.3 Particle Tracking

2.3.1 Back Focal Plane Interferometry

The tracking of optically confined particles can be achieved using a number of methods. One of the most common is back focal plane interferometry utilising a quadrant photodiode (QPD) due to its sensitivity, high temporal resolution and affordability. A QPD will allow particle tracking at rates of 10s of kHz, resolving pN forces. A section of a typical QPD setup is shown in Figure 2.3. The optical trap is formed using the lower objective, while the long working distance (LWD) objective above the trap is used to re-collimate the light scattered from the trapped particle. A $4f$ system is then used to image this interference pattern, resulting from the superposition of the directly transmitted and forward-scattered light, onto the QPD detector. The inset shown in Figure 2.3 illustrates the arrangement of diodes on the face of the QPD, each of which will output a voltage signal proportional to the light intensity incident upon it. When the interference pattern forms a symmetric image on the QPD, equal signals will be received from each of the four quadrants. If however there is a shift in this interference pattern resulting from movement of the trapped particle these voltages signals will be modified. By taking the difference in voltage signal across the QPD, *i.e.*:

$$\mathrm{V}_x = \frac{(\mathrm{V}_1 + \mathrm{V}_4) - (\mathrm{V}_2 + \mathrm{V}_3)}{\mathrm{V}_1 + \mathrm{V}_2 + \mathrm{V}_3 + \mathrm{V}_4} \tag{2.3}$$

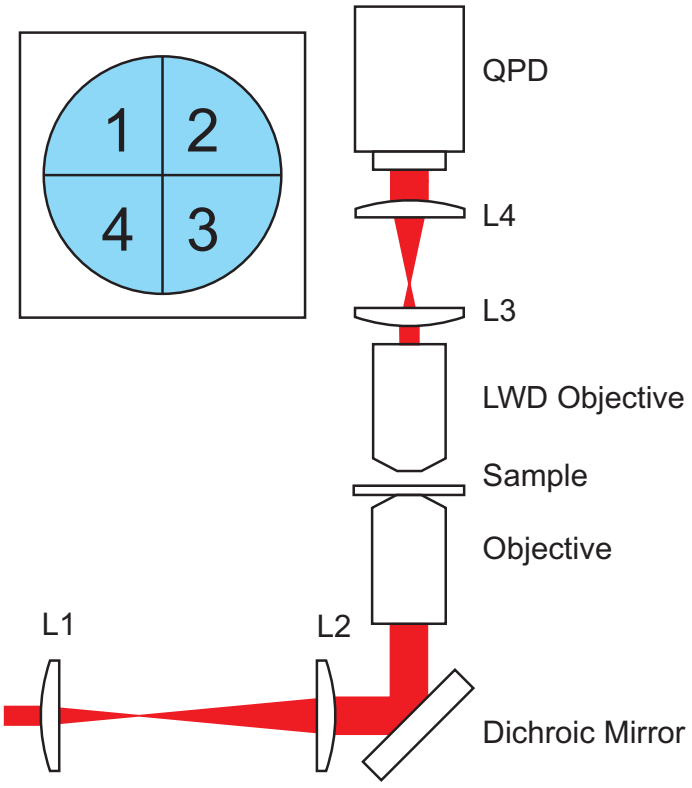


Figure 2.3: Modification of the setup to include a quadrant photodiode (QPD) allows rapid particle tracking. By re-collimating the trapping beam above the sample using a long-working distance objective the interference pattern, formed between the forward-scattered and transmitted light, can be imaged onto the QPD. Inset: The arrangement of photo-diodes on the QPD face.

where V_n represents the voltage signal output from quadrant n, the particle displacement in the x dimension may be determined. The y displacement of the particle can similarly be calculated using:

$$V_y = \frac{(V_1 + V_2) - (V_3 + V_4)}{V_1 + V_2 + V_3 + V_4}. \tag{2.4}$$

Calibration methods, such as movement of a fixed microsphere by a known displacement whilst monitoring the resulting voltage signals, allows these signals to be converted directly into particle displacements. Monitoring of the particle displacement in the z dimension is also possible using this technique; in this case it is the total signal from all four quadrants which is calculated. Processing of these signals is achieved using analogue electronics, before the output is digitised and recorded by a custom LabVIEW programme.

2.3.2 High-Speed Camera Tracking

An alternative method of particle tracking is to use a high-speed camera, arranged in the setup as shown in Figure 2.1. Recent technological advances have made this an affordable and straight-forward option due to the ease of alignment compared to a QPD system and its ability to track multiple particles. Calibration of the position data is facilitated by the use of a ruled objective micrometer, and sub-pixel accuracy may be achieved using centroid tracking algorithms [59–61].

For the experiments presented in this thesis a high-speed Dalsa Genie HM640 CMOS camera is used, capable of running at 300 fps at full resolution, with this frame rate significantly increasing as the number of vertical lines being imaged is reduced. Generally a reduced region of interest of around 50–75 pixels is chosen, allowing imaging at 1600–2000 fps. Using a custom LabVIEW programme it is possible to determine and record particle coordinates *on-the-fly* which is far more efficient than saving each frame for post-experimental analysis, meaning that a standard desktop computer can be used to run the experiment. This routine works by discarding those pixels below a pre-specified threshold limit, then finding the centre-of-mass of the resulting image. Having already determined the appropriate calibration factor, this can then be used to calculate particle positions in two-dimensions.

Modification of this programme has resulted in a number of improvements. This has included monitoring of the quantity of dropped frames over the course of a measurement, ensuring the reliability of the data, and more complete control over the camera functions such as image height, frame rate and exposure time. By manipulating these variables in concert it is possible to ensure that only appropriate values are chosen, *i.e.* given a required frame rate and imaging region the exposure time can be automatically adjusted to the largest permitted value. An additional modification allowed the tracking of multiple particles by specifying multiple regions of interest. The same analysis routine was then used for both particles with no noticeable degradation in the maximum obtained tracking speeds.

2.3.3 Allan Variance Considerations

While the colloidal and aerosol droplet experiments presented here and in Chapter 3 typically only require a few seconds of particle position data for analysis, due to the characteristic frequency of the optical trap being around several hundred Hz, this is not the case for the work on ionic liquids presented in Chapter 4. Due to the significant increase in optical trapping timescale resulting from the high viscosity of these media, the data collection timescale must also be increased, typically to several minutes. Over these timescales experimental drift may become important and can no longer be ignored. The impact of this drift and other noise in the system can be analysed by determining the Allan variance of position measurements, following Gibson *et al.* [62].

When recording particle positions using either the QPD or the camera, there are a number of sources of noise to be considered. Over short timescales this may include noise in the sensor or fluctuations in the system. Due to the Gaussian nature of these variations the accuracy of any measurements may then be improved by averaging over longer timescales. At some point however, this increased averaging will no longer result in an improvement in the determined mean value as the effects of experimental drift begin to dominate.

The standard error in the mean position of an optically trapped particle can be written as a function of the mean square particle position, $\langle x^2 \rangle$, and the number of independent measurements being taken, N, as follows [62]:

$$SE_{\langle x \rangle} = \sqrt{\frac{\langle x^2 \rangle}{N}} \tag{2.5}$$

with the error reducing with increasing values of N as expected. The number of independent measurements taken in time Δt is given by:

$$N \approx \frac{\Delta t}{\sqrt{2}\tau_0} \tag{2.6}$$

where $\tau_0 = \gamma/\kappa$ is the relaxation time of the optical trap. By utilising the fact that the trapped particle is a thermally excited, overdamped oscillator in a harmonic potential, $\langle x^2 \rangle$ can be determined by the equipartition of energy theorem as follows [46]:

$$\frac{1}{2} k_{\mathrm{B}} T = \frac{1}{2} \kappa \langle x^2 \rangle . \tag{2.7}$$

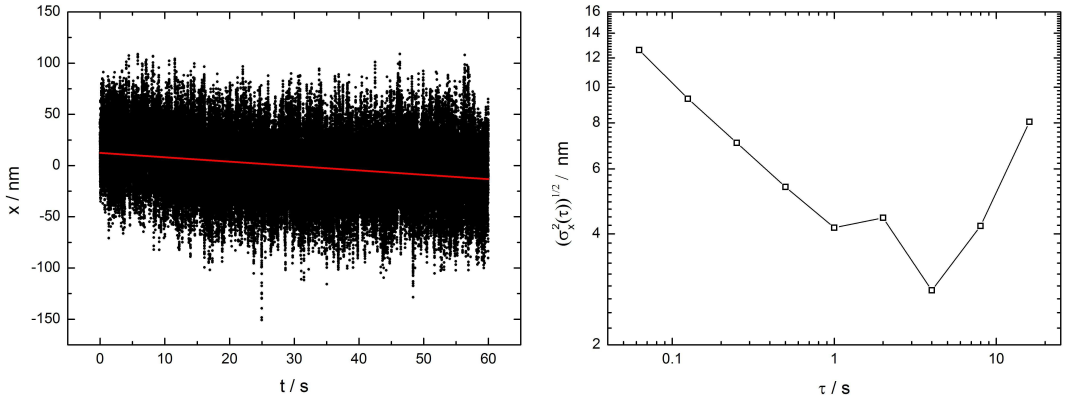


Figure 2.4: Left: Particle position as a function of time subject to experimental drift. Right: The Allan variance of particle position illustrates the optimum time-period for data averaging, corresponding to the minima in the above plot, is around 5 seconds.

Knowledge of these three expressions then allows the standard error of particle position to be rewritten as:

$$SE_{\langle x \rangle} \approx \sqrt{\frac{\sqrt{2} k_{\mathrm{B}} T \gamma}{\kappa^2 \Delta t}}. \tag{2.8}$$

This expression, which decreases with increasing measurement time, provides a limit in the standard error due to the Brownian motion of the particle being observed, but does not take into account the increase in error that occurs as a result of experimental drift, which dominates at longer timescales. By considering these two limits an optimum timescale for averaging can be chosen *via* the Allan variance [62], given by:

$$\sigma_x^2(\tau) = \frac{1}{2} \left\langle (x_{n+1} - x_n)^2 \right\rangle \tag{2.9}$$

where τ is the length of each sampling period and x_n gives the average particle position over the nth period [62]. In Figure 2.4 (left) the recorded particle position for a 2.31 µm diameter melamine particle trapped in water is shown for a period of one minute. Monitoring of this position in the x direction relative to its median value demonstrates the existence of experimental drift, verified by the non-zero gradient of the red line fitted through the data. By plotting the Allan variance of particle position as a function of time, as shown in Figure 2.4 (right), it is possible to select a time period for data averaging over which this drift is negligible. There are expected to be three different regimes observed in the Allan variance plot. Initially, at timescales shorter than the optical trapping timescale, the variance in position measurement increases with increasing measurement time, as the

particles will be diffusing with a constant velocity. Although it should be noted that this lies below the minimum timescale shown in Figure 2.4, this ballistic regime has been previously observed by Huang *et al.* [63]. As the timescale is increased further the effects of the optical trap must be considered and the result is an improvement in the reliability of the position measurement when averaging over longer times as would be expected (up to $\tau \sim 5\,\mathrm{s}$ in Figure 2.4). Finally the Allan variance increases again at the longest timescales, now as a result of experimental drift. By taking these considerations into account it can be seen that the optimum timescale for data averaging is around 5 seconds. As a result for the ionic liquid experiments presented later, where a high-speed camera was used to track particle positions over several minutes, this data will be binned into sequential 5 second segments for analysis with an aim to reduce the effects of long-term experimental drift.

2.3.4 Power Spectra Analysis

Following these considerations the experimental particle position data can then be analysed using the power spectrum method introduced in Chapter 1. By taking the Fourier transform of the position data, either the voltage signals output from the QPD or coordinates determined using the high-speed camera, a power spectrum of the form given by Equations 1.10 and 1.11 can be determined. The resulting QPD power spectrum will be in units of $\mathrm{V^2/Hz}$, with calibration into units of $\mathrm{nm^2/Hz}$ possible but not necessary for trap stiffness determination [46].

Trap stiffness determination takes place using a non-linear least squares fitting algorithm as follows. Firstly each power spectrum is binned into frequency windows, allowing average power values to be determined with a standard deviation calculated in each case. This allows a fit to be optimised, taking these standard deviations into account by minimising the following expression:

$$\chi^2 = \frac{(O_i - E_i)^2}{\sigma_i^2} \tag{2.10}$$

where the observed data point is labelled O_i, E_i is the value determined from the fit and σ_i is the standard deviation of that point [64]. Having determined a best fit power spectrum, the corner frequency allows κ, the trap stiffness, to be determined using Equation 1.9.

2.4 Characterising an Optical Tweezers Trap

In order to demonstrate a working optical tweezers trap and the power spectrum method of trap stiffness determination which will be used frequently throughout this thesis, results obtained using the experimental setup presented in Figure 2.1 to trap 2.31 µm diameter melamine particles in water will now be provided. In this work the high-speed camera was used for particle tracking, although once the time-dependent particle coordinates have been determined much of the analysis remains the same for the QPD technique.

2.4.1 Particle Position and Trap Stiffness

Using the experimental setup outlined in Section 2.1, a 2.31 µm diameter melamine particle was trapped with a power of 32 mW, where this value is the power at the trap, determined by recording the laser output power and accounting for the various losses along the optical path. The sample was prepared by dispersing the particles, obtained from microParticles GmbH with surface COOH functionalisation, in Milli-Q water (Millipore). Approximately 10 µL of this solution was then placed between two glass coverslips, separated by a custom vinyl spacer. A drop of immersion oil was placed on the slide surface before the sample was positioned above the microscope objective. Using the high-speed camera the position of this trapped particle was tracked for one minute, with centre-of-mass tracking used to determine x and y coordinates at a rate of 2 kHz as previously described. Analysis of these coordinates reveals a symmetric distribution as shown in Figure 2.5, indicating that the trap is well aligned and behaving as expected. By inverting a histogram of particle positions it is possible to determine the optical potential experienced by the particle, also shown in Figure 2.5. This is achieved by using the following Boltzmann distribution:

$$\rho(x, y) = Z^{-1} \exp[-U(x, y)/k_{\mathrm{B}}T] \tag{2.11}$$

where $\rho(x, y)$ is the normalised particle position histogram and Z^{-1} the normalisation constant, allowing $U(x, y)$ to be determined [65]. The symmetric nature of this optical potential shown in Figure 2.5 (right) confirms that the optical trap is well aligned.

Having obtained particle coordinates the experimental power spectrum will now be calculated, as described in Section 2.3.4. A pixel:micron calibration factor was determined using a ruled microscope slide, allowing the particle positions to be converted into microns. The

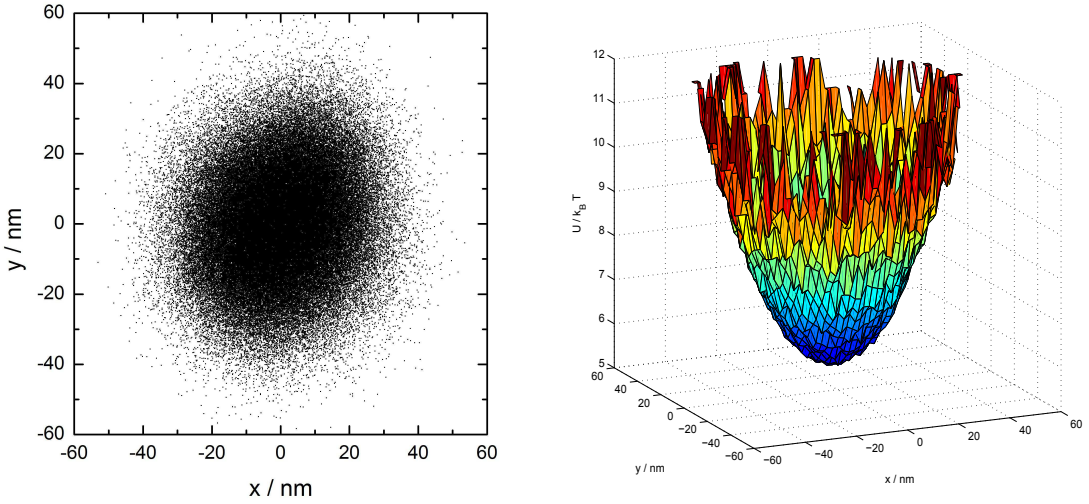


Figure 2.5: Left: A plot of particle position over a period of one minute demonstrates the symmetric optical trapping potential. Right: This potential can be determined in units of $k_{\mathrm{B}}T$ by inverting the histogram of particle positions, as given by Equation 2.11.

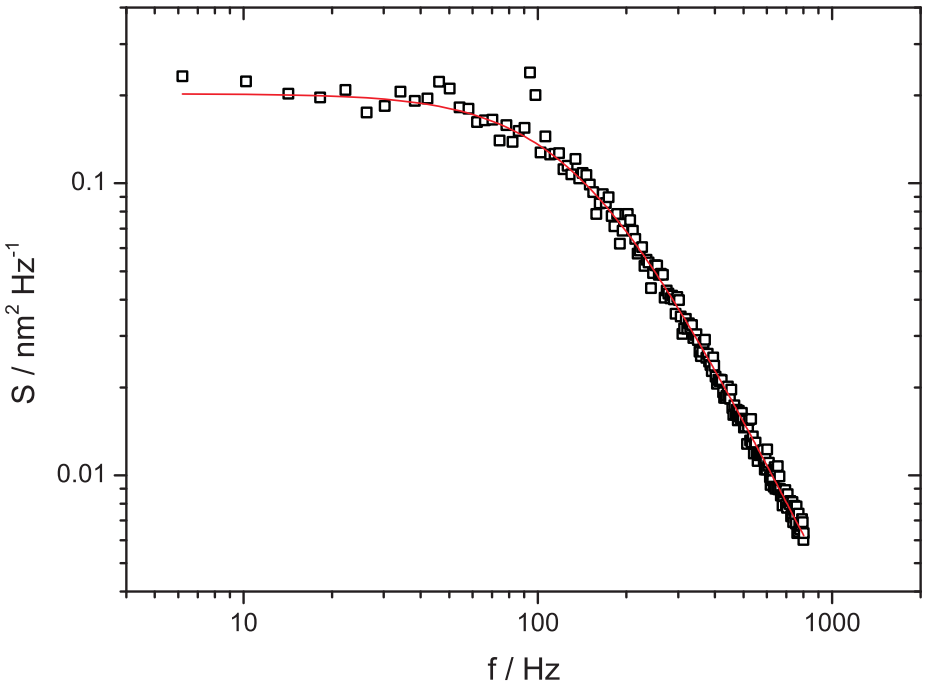


Figure 2.6: Experimentally determined power spectrum for a trapped 2.31 µm diameter melamine particle. A fit to Equation 1.10 is shown in red, allowing a trap stiffness of $17.19 \pm 0.31\,\mathrm{pN/\mu m}$ to be determined.

data was then separated into 5 second segments for power spectral analysis, before being averaged to produce the final power spectrum shown in Figure 2.6. A least-squares fit to Equation 1.10 is also shown in red, yielding a corner frequency, f_c, of 141.2 ± 2.6 Hz. Using Equation 1.9 a trap stiffness of 17.19 ± 0.31 pN/µm was calculated.

2.4.2 Faxén's Correction to Viscous Drag

Following the demonstration of a working optical trap, this chapter will conclude with an outline of Faxén's correction to the viscous drag experienced by a spherical particle, and the effect that this has when the particle is in close proximity to a wall such as the sample coverslip. This effect can be determined for particle motion both perpendicular and parallel to the surface, as given by Faxén's law [50, 66] and demonstrated by Leach *et al.* [67], and is highly dependent on the separation of the particle centre and the surface, h. For particle motion parallel to a plane surface, this correction is given by:

$$\gamma_{\text{Faxén}} \approx \frac{\gamma_0}{1 - \frac{9}{16}(\frac{a}{h}) + \frac{1}{8}(\frac{a}{h})^3 - \frac{45}{256}(\frac{a}{h})^4} \tag{2.12}$$

where $\gamma_{\text{Faxén}}$ is the corrected drag coefficient and γ_0 is the drag coefficient at large distances from the surface given by Stokes' law. This correction can be verified experimentally by first trapping a particle at a large distance from any surface and then gradually decreasing the particle-coverslip separation. With knowledge of the optical trap stiffness, verified to be constant within the height range chosen by monitoring the variance in particle position at each point, the power spectrum method can be used to determine γ from the fitted corner frequency at each height. In each case, the actual particle height above the coverslip, h_{particle}, can be related to the change in stage height, h_{stage}, by considering the ratio of the water and glass refractive indices [50, 68] as given in Equation 2.13:

$$h_{\text{particle}} = \frac{n_m}{n_g} h_{\text{stage}} \tag{2.13}$$

where n_m and n_g are the refractive indices of the trapping medium and glass respectively.

The ratio of these measured friction coefficient values, γ, to the values given by Stokes' Law, γ_0, for a melamine particle trapped in water at a series of trapping heights are given in Figure 2.7. The expected increase in viscous drag coefficient at reduced particle-coverslip separations is seen, with γ tending to γ_0 at larger separations. When analysing the data the

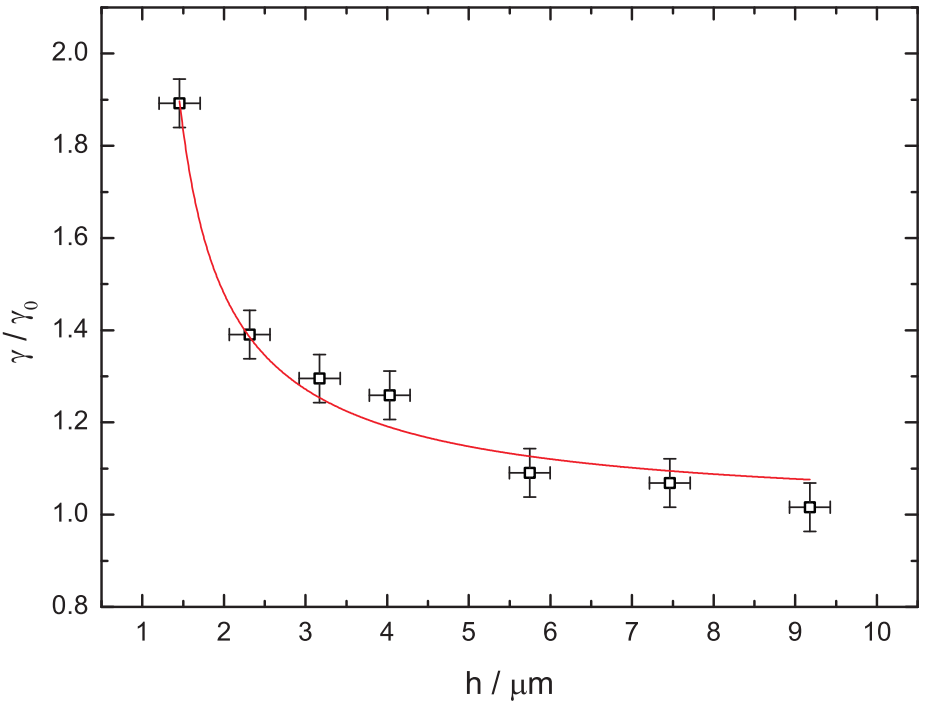


Figure 2.7: By recording the power spectrum of a trapped particle at a series of heights above the sample coverslip, Faxén's correction to viscous drag can be demonstrated. Knowledge of the trap stiffness at each point allows the corner frequencies determined from the power spectra to be used to calculate the effective viscous drag coefficient, showing excellent agreement with the expected form.

procedure of Vermeulen *et al.* is followed, defining $h = h_{\mathrm{m}} + \Delta h$, where h_{m} is the measured height, and Δh allows for the fact that the absolute particle-coverslip separation at the closest measurement point is unknown [50]. Fitting to this modified expression returns a Δh value of 1.46 µm as the minimum particle-coverslip separation, slightly larger than the particle radius as expected. This offset was then used to determine the absolute height values shown in Figure 2.7.

2.5 Conclusions

In this chapter the key features of an optical trapping setup have been discussed. Following an outline of some of the methods available for trapping multiple particles, including the beam splitting method which will be utilised later in this thesis, the particle tracking and analysis techniques which will be used were described. A simple optical trapping setup was then presented and characterised, as an exemplar of the preceding experimental and data analysis methods. These methods were further verified by demonstrating Faxén's correction

to viscous drag for particle motion parallel to a plane boundary, with results in excellent agreement with the theoretically expected values.

Chapter 3

Optical Trapping of Aerosol Droplets Using Annular Beams

In this chapter a study of the optical trapping of aerosol droplets is presented. Recent work on the modelling of optical traps for aerosol droplets by Burnham and McGloin demonstrated the potential improvements that may be achieved when trapping using an annular rather than a conventional Gaussian beam [16]. Specifically they showed that annular beams should allow an increased size range of droplets to be trapped, and an increase in axial trapping efficiency. In this chapter experimental results are presented to verify these effects and, alongside their model, utilised to make further comparisons between Gaussian and annular beams.

Initially the effects of trapping power on the system are studied both theoretically and experimentally. By calculating the minimum power requirements for stable optical trapping, a direct comparison between experiment and theory can be achieved, demonstrating excellent agreement. The increased size range of trappable droplets is then confirmed by trapping with an annular beam, and the significantly improved axial localisation which can be achieved is demonstrated. Finally axial:lateral trap stiffness ratios are presented, showing a significant increase in this value when trapping using an annular beam due to the reduction in axial scattering forces when using this type of beam.

3.1 Optical Trapping of Aerosol Droplets

The first demonstration of the stable levitation of particles in air using radiation forces was presented in 1971 by Ashkin and Dziedzic [19]. In this work $\sim 20\,\mu m$ diameter glass spheres were confined by vertically directing a focussed laser beam. The glass spheres were laterally trapped due to the gradient force, while the scattering force in the axial direction was balanced by gravitational forces. Trapping of this type was also demonstrated in high vacuum [20], confirming that radiation pressure forces were responsible for this trapping effect. Following the first demonstration of a single beam optical trap by Ashkin *et al.* in 1986 [22], where a tightly focussed laser beam allowed the scattering force in the axial direction to be balanced by gradient forces, Omori *et al.* presented the first observation of a single beam optical trap in air by stably trapping $3 - 5$ µm glass spheres [69]. In this work the spheres were placed on a glass plate, before rapid vibrations were used to dislodge the spheres allowing them to be trapped by a laser beam focussed just above the surface. This technique clearly has limitations in terms of the types of particle that can be delivered to the trapping region, and the experimental geometries which can be used. Improvements in solid particle delivery methods were presented in 2008 by Summers *et al.* [47], with important implications in addressing both of these limitations. Trapping of solid particles in air was achieved by suspending silica particles in ethanol and using a medical nebuliser to deliver them to the trapping region. Having successfully demonstrated this delivery method, a direct comparison of the trapping of solid particles in gaseous and liquid phases was shown. It was found that the experimentally determined trap stiffnesses, once normalised by trapping power, were significantly larger for trapping in air compared to water samples, believed to be a result of the higher refractive index contrast between the silica particles and the trapping medium in this case.

Further work has included the stable trapping of liquid aerosol droplets [70], with additional complications over solid particle trapping due to dynamic droplet growth and size determination. This technique does however have important applications, including the characterisation of the properties of aerosols and their role in atmospheric processes. The use of optical tweezers allows the study of single droplets, rather than ensembles of particles, which may contain a wide range of sizes and compositions [71]. Single droplet characterisation of this type has been performed by Hopkins *et al.*, where water and decane droplets were trapped and cavity enhanced Raman scattering (CERS) used to determine droplet

sizes and investigate dynamic size changes to nanometer precision [5]. This work also highlights the investigations that can be undertaken by combining spectroscopic techniques with optical tweezers, including monitoring the changing chemical composition of aerosol droplets. An extensive discussion of the characterisation of aerosol droplets using optical trapping techniques such as this is given by Wills *et al.*, demonstrating its use as a powerful analytical tool [72]. Further applications of these techniques include investigations of droplet coagulation, thermodynamic measurements, growth and evaporation studies and reactions within aerosol droplets [73]. One particular example can be found in the work of King *et al.*, where the reaction of aerosol droplets with ozone was studied using Raman spectroscopy, clearly demonstrating how by coupling optical trapping and spectroscopic techniques atmospherically important processes can be studied [38].

Despite the extensive applications of these techniques to the study of atmospheric chemistry at the single droplet level, there are significant limitations. Accumulation mode aerosol droplets, where $r < 1\,\mu\text{m}$, are of particular interest due to the significant proportion of atmospheric aerosols which fall within this size range [74]. Droplets in this size regime cannot be trapped with conventional Gaussian beam optical traps however, limiting the use of these techniques for their study. One solution to this is to use counter-propagating Bessel beam traps, as demonstrated by Carruthers *et al.*, allowing sub-micron aerosol droplets to be trapped [75]. Previous theoretical work has demonstrated that another method of increasing the range of trappable droplet sizes and optically confining single fine aerosol droplets ($r \geq 0.5\,\mu\text{m}$) is to use annular beams [16], as will now be discussed.

Although this chapter focusses on the improvements in aerosol droplet trapping which may be achieved when using annular beams, these effects have previously been modelled and demonstrated for a variety of systems in the over-damped trapping regime. The first detailed investigation of this was in 1992 by Gussgard *et al.* [76]. Using geometric optics approximations these researchers calculated the forces acting on a dielectric sphere near the focus of a laser beam, both for Gaussian illumination and for the case where a central field stop was used in order to form an annular beam and increase the relative contribution of the high NA illumination to the trapping force. This enhancement was demonstrated both theoretically and experimentally using polystyrene spheres. Further work on the modelling of optical trapping forces with annular beams has been performed by Ashkin [77] using a ray optics approach, and then Ganic *et al.*, detailing the failures of the ray optics models and instead presenting work based on vectorial diffraction theory [78].

For the work presented here, an annular beam will be formed by simply blocking the central portion of a Gaussian beam using an obstruction printed on an acetate sheet, as an example of a simple yet highly effective method of trap enhancement. Other methods of producing an annular beam for trapping applications include the use of a hollow-tipped fibre probe, as demonstrated by Taylor and Hnatovsky, with stable three-dimensional trapping achieved by balancing the scattering force with an electrostatic attraction towards the fibre tip [79]. As well as this, annular trapping has also been achieved using phase holograms [80], higher order TEM_{01}^{*} and TEM_{0n} modes [81], and Laguerre-Gaussian beams [82].

3.2 Modelling an Optical Trap

The modelling work of Burnham and McGloin [16] was performed using Mie-Debye spherical aberration theory [41, 42], with modifications included to account for the multiple mismatched refractive index interfaces often present within optical trapping systems. The interfaces present within the system used in this chapter are shown in Figure 3.1. An oil immersion objective is used and the objective lens, immersion oil and glass coverslip refractive indices are assumed to be matched. The first mismatched refractive index interface is therefore between the glass coverslip (with refractive index n_g) and a thin water layer of

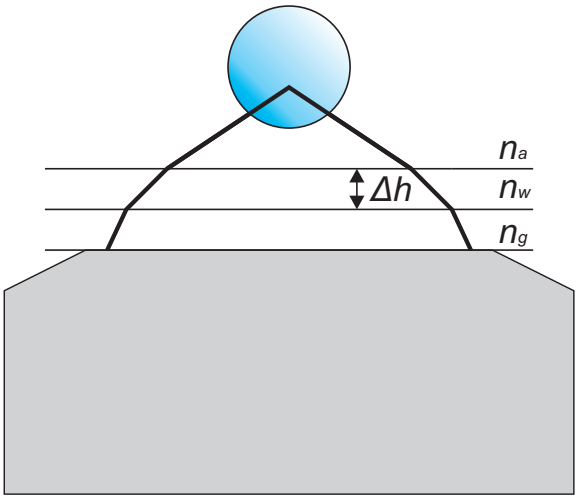


Figure 3.1: A diagram illustrating the refractive index interfaces to be considered when trapping an aerosol droplet in a glass sample cell. Radiation exiting a microscope objective is shown as it interacts with these interfaces. The simulation assumes two mismatched refractive index interfaces, one between the glass coverslip and a water layer of thickness Δh, and the other between the water layer and air. The refractive indices of glass, water and air are labelled n_g, n_w and n_a respectively.

thickness Δh on the slide surface (n_w). The second interface is between the water layer and air (n_a). Given these parameters, the model calculates the efficiency of momentum transfer to the object, Q, as a function of position in both the axial and lateral directions, although it is Q_{axial} which will be most important in determining whether or not a particle will be stably trapped.

Once Q has been calculated for a particle of given size and refractive index, the optical force acting on the particle, F, can be readily calculated using:

$$F = Qn_m P/c \tag{3.1}$$

where n_m is the refractive index of the trapping medium, P is the trapping power, and c is the speed of light. Total force curves can then be produced by taking in to account the force due to the mass of the trapped particle. An example force curve, including both optical and gravitational forces, is shown in Figure 3.2, calculated for a 3 µm radius salt water droplet trapped in air. Other modelling parameters, chosen to match those in the experimental work presented later, include a water layer thickness (Δh) of 10 µm and an objective converging angle, θ, of 41.23°, limited to this value due to total internal reflection at the coverslip interface. The trapping power in each case is taken to be 10 mW.

For the figures presented in this chapter the axial position has been calculated relative to the position of the paraxial focus in the absence of any aberrations. The total axial force is then calculated as a function of axial position, with a positive value indicating an 'upwards' resultant force. The stable trapping position occurs where this resultant force curve crosses the zero-force axis with a negative gradient; this is labelled z_{eq} in Figure 3.2 and can be seen to be around 6 µm below the paraxial focus in this case. Also shown in Figure 3.2 is $F^{-}_{\text{z,max}}$, defined as the maximum negative value of the force curve, providing a measure of the axial restoring force and an indicator of trapping performance [83].

In order to compare trapping using a Gaussian and an annular beam, the Gaussian beam profile in the simulation must be modified to include an annulus so the effects of an annular beam can be studied. This is achieved by introducing a cut-off angle to the beam profile and discarding the light exiting the objective below a certain threshold angle. Comparison between the two beam types is facilitated by maintaining the same total power for both beams once the annulus has been taken into account. A comparison between a Gaussian beam and annular beam is shown in Figure 3.3. The Gaussian force curve (black) is the

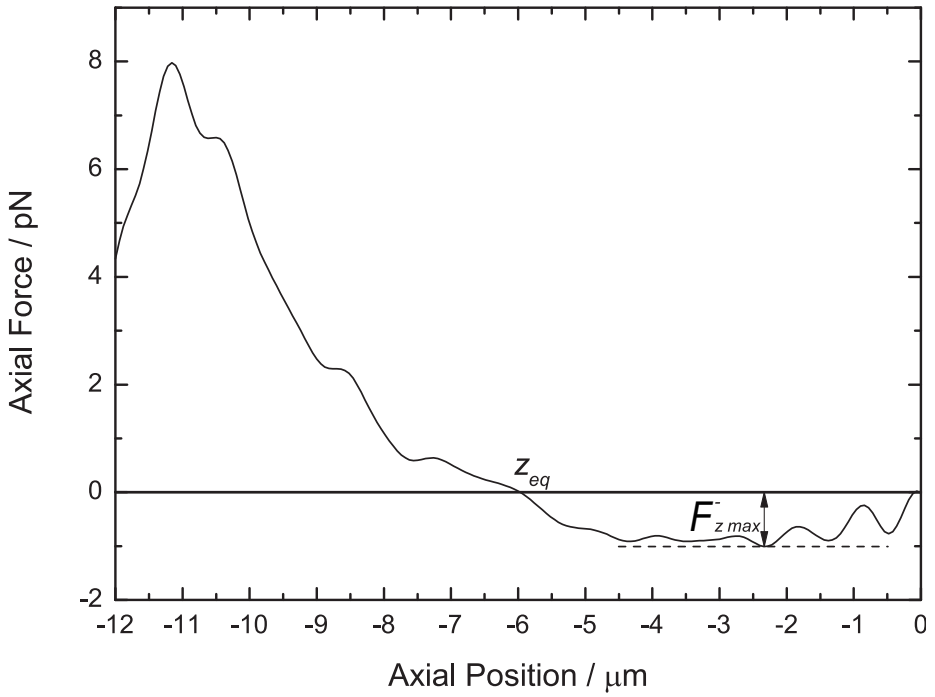


Figure 3.2: A modelled axial force curve for a 3 µm radius salt water droplet, including both gravitational and optical forces, for a trapping power of 10 mW. The stable equilibrium trapping position, z_{eq}, is given by the point that the curve crosses the x axis with a negative gradient, and is ~ 6 µm below the paraxial focus in this case. The magnitude of the axial restoring force, $F^{-}_{\mathrm{z,max}}$, is also shown, providing a good measure of trapping performance.

same as in Figure 3.2 while the annular beam force curve (red) has been calculated using the same experimental parameters and assuming a cut-off angle of 18.2°, chosen to match the obstruction used in the experimental work presented later.

While the annular beam force curve displays a similar trend to that of the Gaussian case, there are a few important differences to note. Firstly it can be seen that the position at which the curve crosses the zero-force axis, giving the stable droplet trapping position, has been significantly reduced for the annular beam case - the droplet is now trapped approximately 2 µm lower than for the Gaussian beam trap. This can be understood in terms of the scattering forces resulting from each beam type. The reason for the improved performance of the annular beam is a reduction in the scattering forces acting to push the droplet from the trap, as will be shown later. By removing the central portion of the Gaussian beam those photons with shallower incident angles, primarily responsible for the scattering force, are removed, necessarily resulting in a lower equilibrium trapping position.

Another comparison to be made is that of the maximum negative value of the force curve,

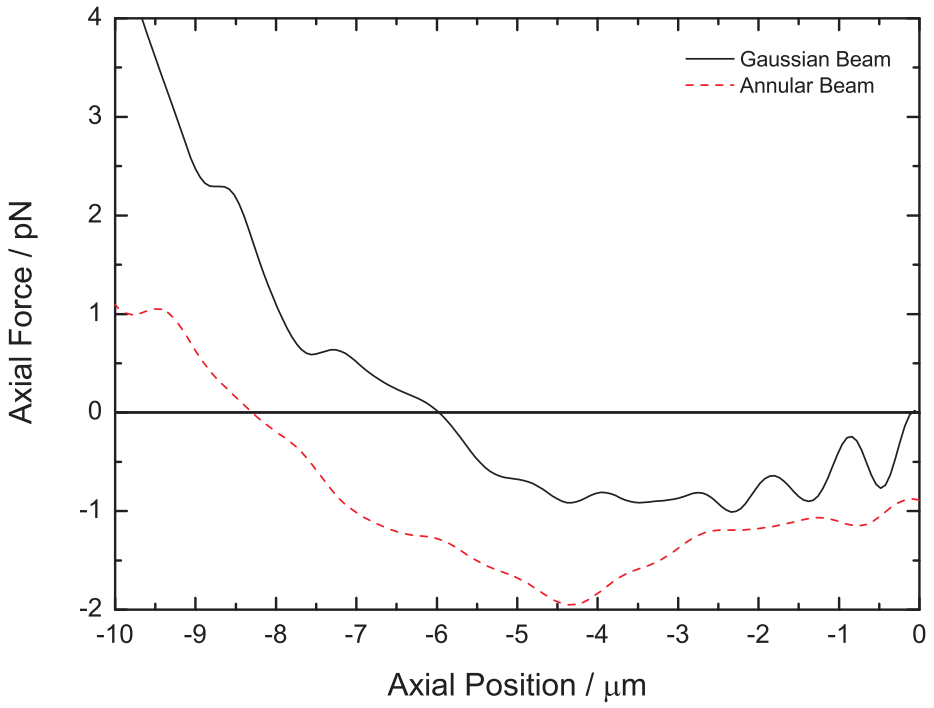


Figure 3.3: Modelled axial force curves for a 3 µm salt water droplet for both a Gaussian beam (black) and an annular beam (red). The parameters chosen are the same as for Figure 3.2, with an annular cut-off angle of 18.2°. z_{eq} has been reduced for the annular beam, indicating that the particle sits lower in the trap due to a reduction in the axial scattering force. The magnitude of $F^{-}_{\mathrm{z,max}}$ has increased for the annular beam, indicating an increased axial restoring force and therefore improved trapping performance in this case.

$F^{-}_{\mathrm{z,max}}$. The sign of this term indicates whether or not a stable trapping position exists, with a larger value relating to a larger axial restoring force. It can be seen that $F^{-}_{\mathrm{z,max}}$ is approximately twice as large for the annular beam, indicating improved axial trapping performance in this case. An alternative method of quantifying the trapping performance is to calculate the gradient of the force curve at the equilibrium position, as this value enables the axial trap stiffness to be calculated. This value is larger for the annular beam, but is extremely sensitive to the exact simulation parameters used due to the oscillatory nature of the force curves and, as a result, determination of $F^{-}_{\mathrm{z,max}}$ provides a more robust measure of trapping performance.

For the results presented so far a single particle size and refractive index have been chosen as an example study, however in order to fully compare Gaussian and annular beams a more thorough investigation is needed. In their modelling work Burnham and McGloin presented calculated $Q^{-}_{\mathrm{z,max}}$ values in the form of contour plots as a function of both particle radius and relative refractive index, where $n_{rel} = n_p/n_m$ with n_p and n_m being the refractive

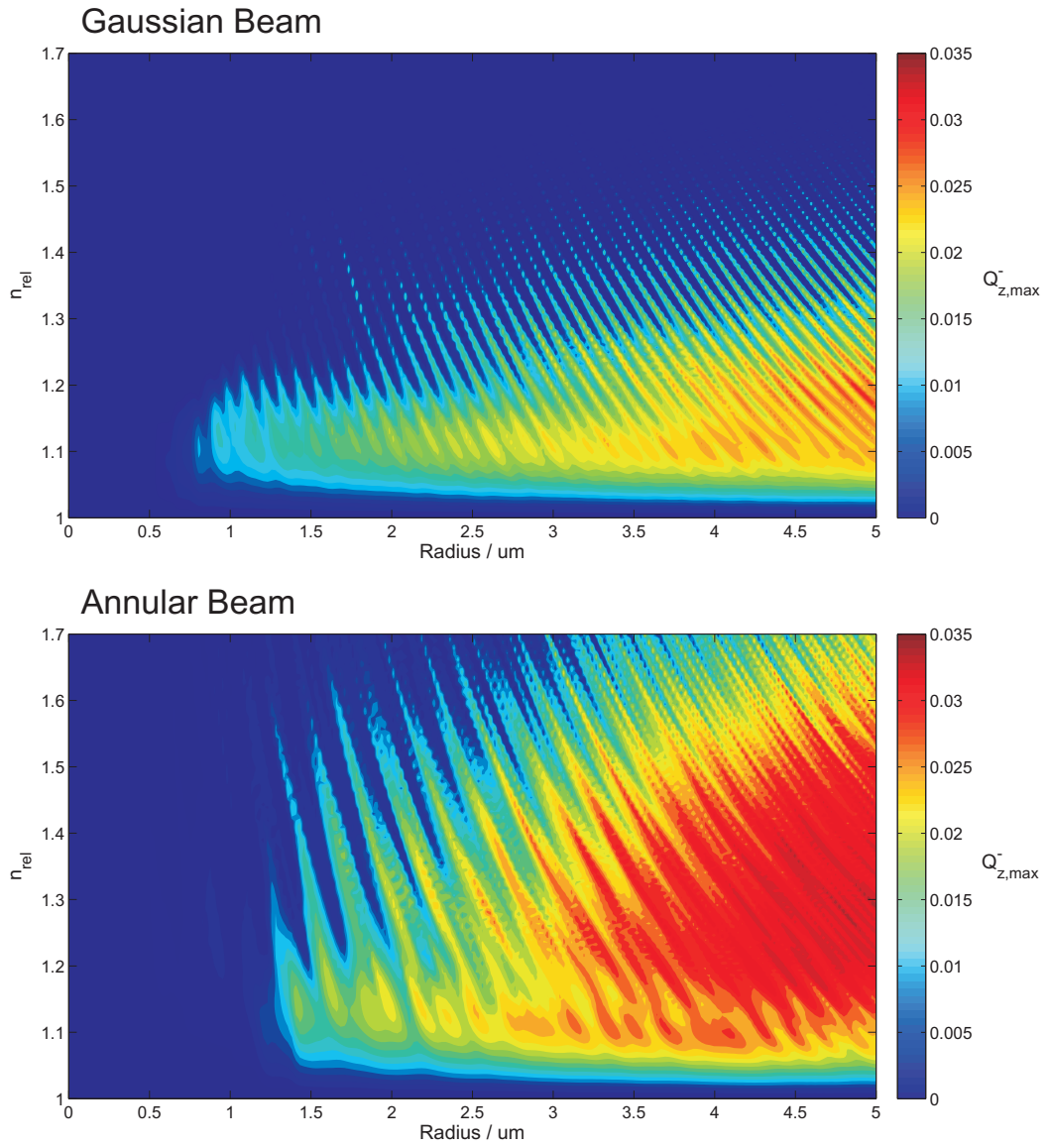


Figure 3.4: Simulated $Q^{-}_{\mathrm{z,max}}$ values as a function of particle radius and relative refractive index, where $n_{rel} = n_p/n_m$, and n_p and n_m are the refractive indices of the particle and trapping medium respectively. A large increase in the parameter space over which a particle can be trapped can clearly be seen for the annular beam.

indices of the trapped particle and the trapping medium respectively [16]. This is shown in Figure 3.4 for an annular cut-off angle of 30°, where the magnitude of $Q^{-}_{\mathrm{z,max}}$ is illustrated by the contours. It is clear that the parameter space over which a particle may be trapped has been significantly increased when the annular beam has been used, particularly in terms of trapping particles with higher n_{rel} values such as aerosols. Taking a horizontal line across each plot illustrates the trapping behaviour as a function of particle radius for a particular particle type. This is demonstrated in Figure 3.5, produced by taking a cross-section of Figure 3.4 at $n_{rel} = 1.34$; chosen as this is the value for water droplets in air. It can

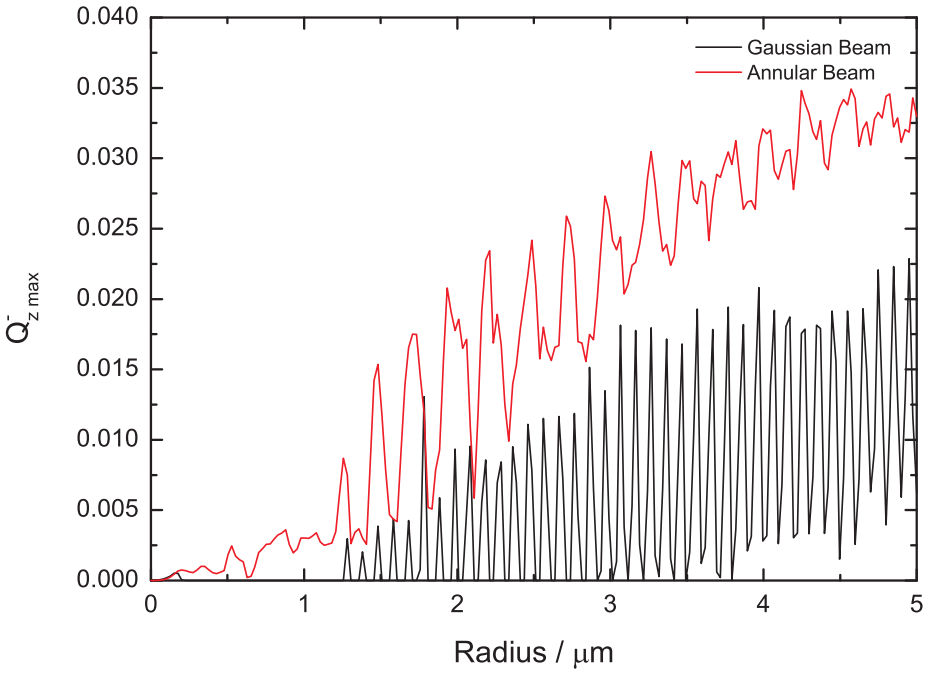


Figure 3.5: Taking a cross section through Figure 3.4 at $n_{rel} = 1.34$ allows the difference in $Q^-_{\mathrm{z,max}}$ values to be clearly seen for a salt water droplet trapped in air. The annular beam allows smaller droplets to be trapped, and larger droplets to be trapped with increased trapping efficiency.

be seen that the minimum trappable droplet size has been significantly reduced, and that the trapping performance for larger droplets has been enhanced when an annular trapping beam is used. This figure also highlights the rapid oscillations in $Q^-_{\mathrm{z,max}}$ which occur as a function of droplet radius. These result from variations in the sphere's reflectivity with radius [83].

3.3 Experimental Configuration

In order to validate the predictions of the theoretical modelling work already presented, an experimental setup was designed and built to trap a series of aerosol droplets using both Gaussian and annular beams, allowing them to be sized and their axial and lateral trap stiffnesses determined. This experimental set-up is detailed in Figure 3.6. The beam from a 532 nm cw laser (Laser Quantum Torus, with a maximum output power of 400 mW) is expanded using lenses L1 and L2, with focal lengths of 50 mm and 200 mm, in order to slightly overfill the back aperture of the microscope objective (OBJ) (Nikon E Plan, 100×/1.25 oil immersion). When annular trapping experiments are taking place a 0.60 mm

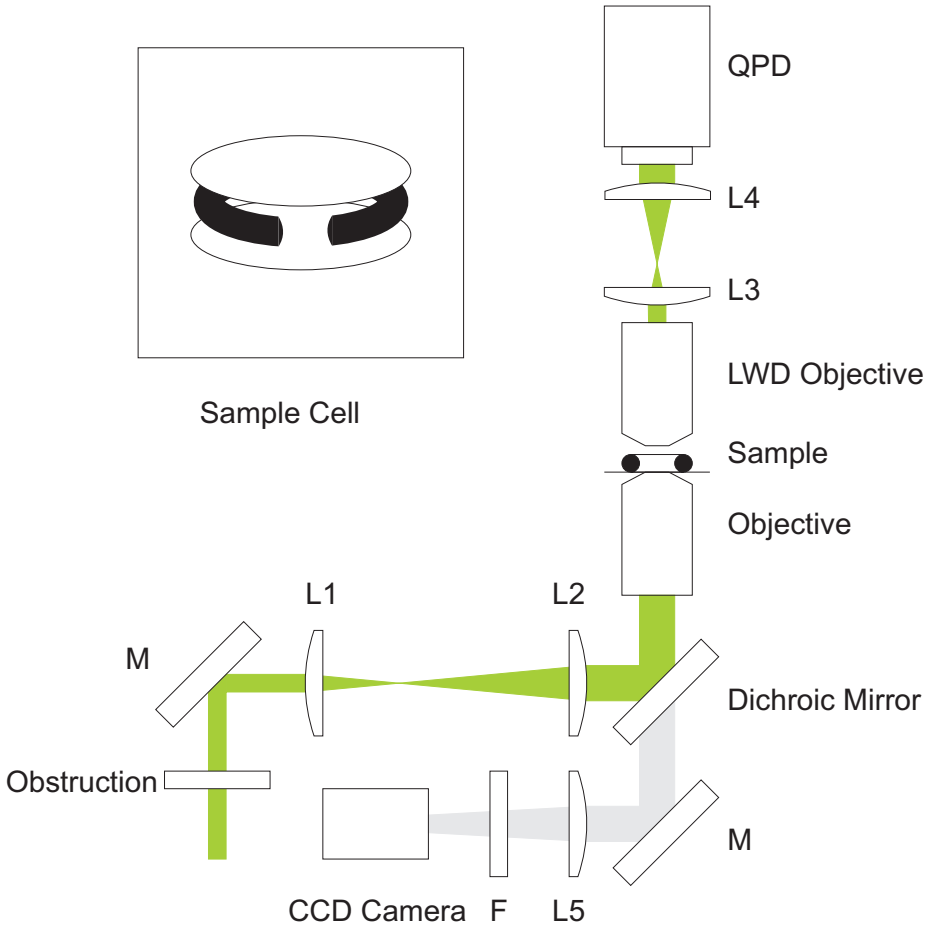


Figure 3.6: Experimental set-up as described in the body of the text. A 532 nm cw laser is used to form the optical trap, with an obstruction positioned at a conjugate plane to the back aperture of the microscope objective when annular trapping experiments are taking place. The long working distance objective collects the scattered radiation and images it onto the Quadrant-PhotoDiode (QPD) to allow fast position tracking.

diameter obstruction, consisting of a circle printed on an acetate sheet, is positioned at a conjugate plane to the back aperture of the microscope objective, blocking the central region of the Gaussian beam and reducing its power by 36%. Imaging of the sample onto a CCD camera (Watec, WAT DM3S), using lens L5 and a filter (F) to cut out the back-scattered 532 nm light, also takes place. Images are recorded for each droplet in order to size them at a later time [84]. Illumination of the sample is achieved using a white light source (Thorlabs, LIU004) reflected onto the back aperture of a condenser objective (Mitutoyo M Plan Apo, 100×/0.70) using a dichroic mirror situated between lenses L3 and L4 (not shown in Figure 3.6). A polydisperse sample of aerosol droplets is generated from a 40 g L^{-1} NaCl water solution using a Omron MicroAir NE-U22 nebuliser and introduced into a sample chamber consisting of two circular microscope slides separated by a 3 mm thick rubber spacer. The addition of NaCl to the water droplets allows them to reach

equilibrium size in a subsaturated environment such as the laboratory, by decreasing the equilibrium vapour pressure over the droplet surface. In addition a small piece of moist lens tissue is included in the sample cell in order to raise the relative humidity. Before forming the sample cell the slides are treated with Decon 90 in order to increase the hydrophilicity of their surfaces so that any water on the slide surface forms a thin layer rather than separate droplets, which can cause significant aberrations to the beam [64].

For the back focal plane interferometry experiments a Quadrant Photo-Diode (QPD) (RS Components Ltd, QD7-5T) is used to track the optically trapped aerosol droplets in 3 dimensions allowing the determination of axial and lateral trap stiffnesses for both the Gaussian and annular traps. In order to facilitate this, the condenser objective positioned above the sample is used to collect the scattered light before a $4f$ system, consisting of lenses L3 and L4 with focal lengths of 50 and 100 mm, images the sample onto the QPD. A DAQ card then acquires the QPD voltage signals at a frequency of 100 kHz for 5 seconds. Both the QPD and the condenser objective are mounted on independent translation stages in order to aid precise alignment. As the signals from each quadrant of the QPD are proportional to the incident scattered light intensity, the particle's position can be accurately and quickly mapped in 3-dimensions with the x and y positions determined by the signal differences across the QPD in each direction and the z position being a function of the total incident light intensity [46], as described in Section 2.3.1.

3.4 Testing the Model

3.4.1 Trapping Power

In order to test the previously presented optical trapping model, simulations were run to examine the effect of trapping power on the stable trapping of aerosol droplets. The results of these simulations are shown in Figure 3.7, for a 3 µm radius droplet in a Gaussian beam as the trapping power is increased from 10 to 200 mW. It can be seen that initially the equilibrium axial trapping position, z_{eq}, increases meaning that the droplet will be trapped at a higher position relative to the beam focus. This is readily observed experimentally as droplets can be seen to shift vertically as the laser power is increased. It can also be seen experimentally that once a threshold power has been reached, the droplet will no longer be stably trapped and will instead be 'pushed' from the trap. This can now be understood

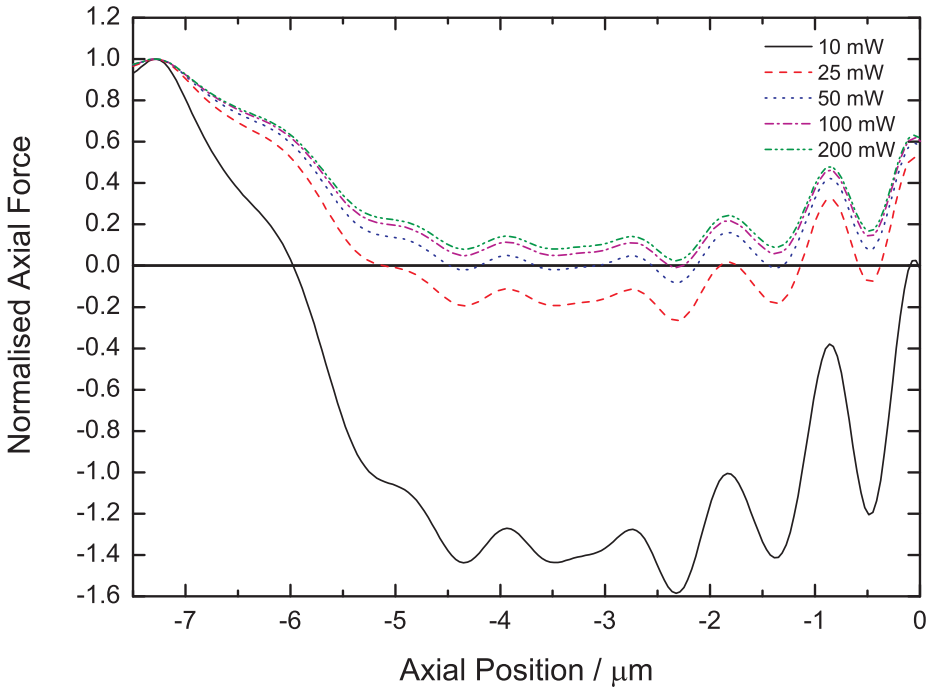


Figure 3.7: Simulated axial force curves for a 3 µm radius salt water droplet, calculated for trapping powers between 10 and 200 mW. The force curves have been normalised to unity in each case in order to facilitate comparison between them. The stable axial trapping position can be determined from the negative gradient intercept for each curve, and can be seen to shift 'upwards' back towards the laser focus with increasing power. At the highest powers the force curve becomes positive for all axial displacements, meaning no stable axial trapping position exists as can readily be observed experimentally for increasing trapping power.

in terms of the axial force curves presented in Figure 3.7. As the power is increased there reaches a point where a negative gradient intercept with the zero-force axis no longer exists, and so a droplet can no longer be trapped. Similarly at lower powers (< 10 mW, not shown in Figure 3.7) no such position exists within this range. By examining these force curves at suitable power ranges, upper and lower limits on the powers which will produce stable optical traps can be determined.

This behaviour was experimentally verified by trapping a range of salt water droplets of various sizes using the set-up given in Figure 3.6. By waiting for the droplet to equilibrate with its surroundings and then gradually decreasing the power until it is seen to fall out of the trap, a minimum trapping power (P_{min}) can be determined for each droplet. By evaluating the power required for a stable axial trapping position to exist for a given droplet size using the simulation, a direct comparison between experiment and theory can be made. Figure 3.8 illustrates this comparison, where a series of droplets have been trapped in both

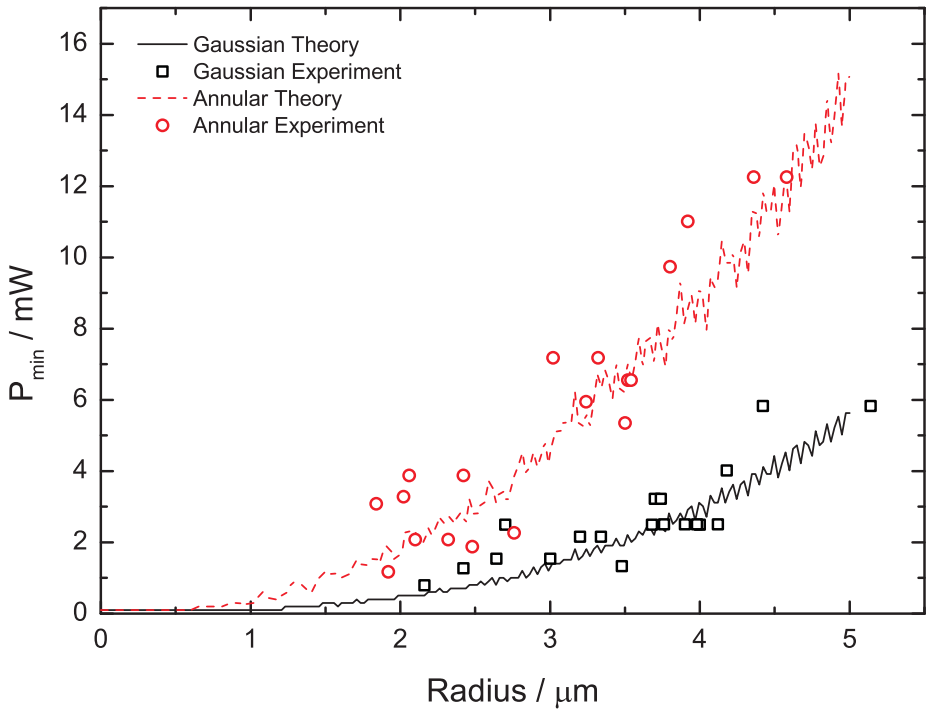


Figure 3.8: By running simulations at varying powers, as shown in Figure 3.7, minimum trapping powers (P_{min}) can be determined as a function of droplet size for both Gaussian (black) and annular (red) beams. These values are larger for the annular beam due to the reduction in scattering force and therefore the need for increased power to counteract the gravitational forces acting on the droplets. By trapping a series of droplets of varying sizes, and then gradually decreasing the trapping power until they are seen to fall from the trap, experimental P_{min} values have also been determined for each beam type, demonstrating excellent agreement with the theoretically predicted values.

Gaussian and annular beams, showing excellent quantitative agreement between experiment and the simulation results.

A comparison between the Gaussian and annular beam trapping powers shown in Figure 3.8 reveals that the minimum power required to trap a given aerosol droplet is larger when an annular beam is used. This can again be rationalised in terms of the reduction in scattering force achieved when using an annular beam, due to the removal of the low NA radiation from the trap. While this increases the axial trapping efficiency, as will be demonstrated later, it does mean that more power is required initially in order to balance the gravitational forces acting on the droplets.

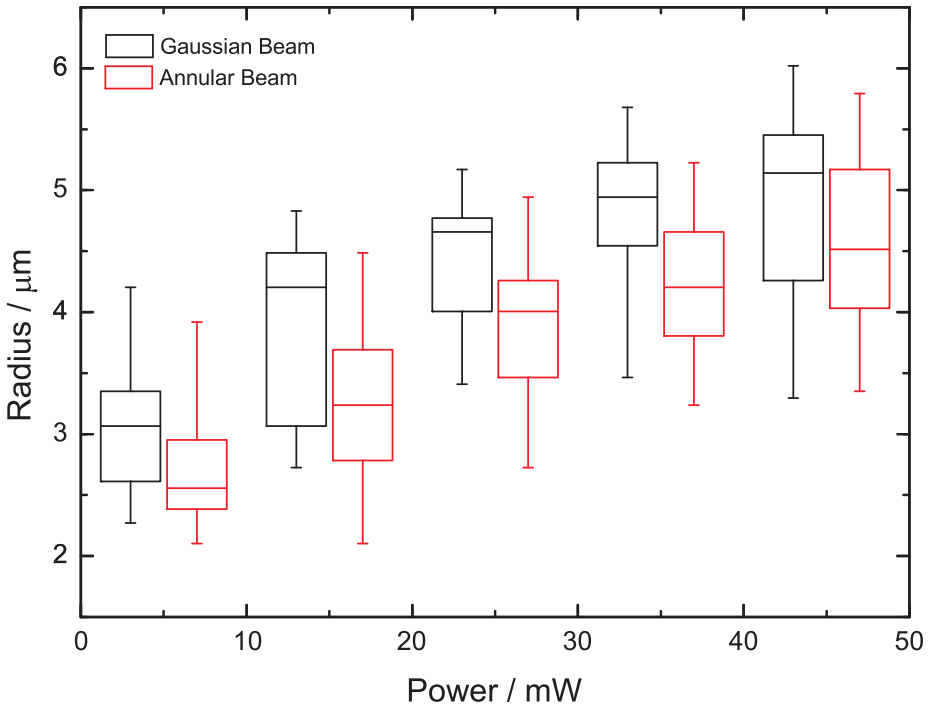


Figure 3.9: Experimental results comparing the sizes of droplet trapped when using a Gaussian and an annular beam. Data has been binned into equal 10 mW increments, and then horizontally displaced for clarity. The boxes represent the lower quartile, median and upper quartile for each data set, while the whiskers show the minimum and maximum trapped droplet radii for each power range.

3.4.2 Droplet Size

Having successfully verified the predictions of the theoretical trapping model, an investigation of trapped droplet size with each beam will now be presented. One of the initial predictions of the model, given in Section 3.2, is that by introducing an annulus into the beam the range of particles over which a true optical trap can be formed, defined as one in which the particle is confined by the optical forces alone, is greatly increased in terms of both refractive index range and particle size. In particular this means that for salt water droplets trapped in air, the minimum tweezable droplet size should be decreased by using an annular beam. In order to verify this behaviour a total of 340 droplets were trapped using Gaussian and annular beams at different trapping powers. This data is shown in the form of a box plot in Figure 3.9. Droplets were trapped at a range of powers between 3 and 50 mW and the results grouped into 10 mW bins, with the results in Figure 3.9 slightly horizontally displaced for clarity. The particle radii were determined using video microscopy and the annular droplet powers are quoted after taking into account the 36% power reduction caused by the obstruction. As expected, both data sets follow an approximately linear

trend with power [16]. A general decrease in the average trapped droplet size can also be seen when the annular beam is used compared to the Gaussian case. In addition smaller droplets trapped using the annular beam can be confined at higher powers without being 'pushed' out of the trap.

It is unclear whether the observed minimum trapped droplet size is due to the physical limit of the annular beam being used, or simply a result of the size of droplet formed by the nebuliser. It is clear however that the annular beam does allow smaller droplets to be trapped, and at higher powers, and it is believed that this improvement could be extended further by careful optimisation of the annular obstruction and nebulising technique.

3.4.3 Axial Localisation

In Figure 3.7 the effect of trapping power on z_{eq} for a droplet trapped in a Gaussian beam was demonstrated, showing that initially the axial equilibrium position moves up towards the laser focus as the power is increased, until a threshold power is reached at which point the droplet can no longer be trapped. This effect is shown in Figure 3.10 (top) for a 2.8 µm radius droplet trapped in a Gaussian beam (black line). As the trapping power is increased from 4 to 23 mW in the simulation, z_{eq} can be seen to vary from ~ 8 µm below the paraxial focus to around 7 µm above it at the highest power. It should be noted that at each power multiple stable axial trapping positions may exist due to the oscillatory nature of the force curve. In each case the most stable position has been plotted, determined by taking the crossing point with the largest negative gradient. This explains why the droplet is expected to shift upwards along a series of steps before, at 23 mW, the stable trapping position sharply drops. In contrast to this, the annular beam simulation data (red dashed line) for a 2.1 µm droplet shows very different behaviour; after a small initial rise in axial position, the droplet is seen to stabilise at around 7 µm below the paraxial focus, showing significantly improved axial localisation as a function of trapping power, again due to the reduction in scattering force in this case.

In the bottom half of Figure 3.10 this expected behaviour is experimentally verified for both beam types in a series of droplet screenshots. In each case a droplet of the same size as used for the simulation plot is trapped at 4 mW, before the power is gradually increased to 23 mW. For the Gaussian beam, the screenshots show a large change in axial position over this power range, evident as the droplet moves into focus as it rises in the

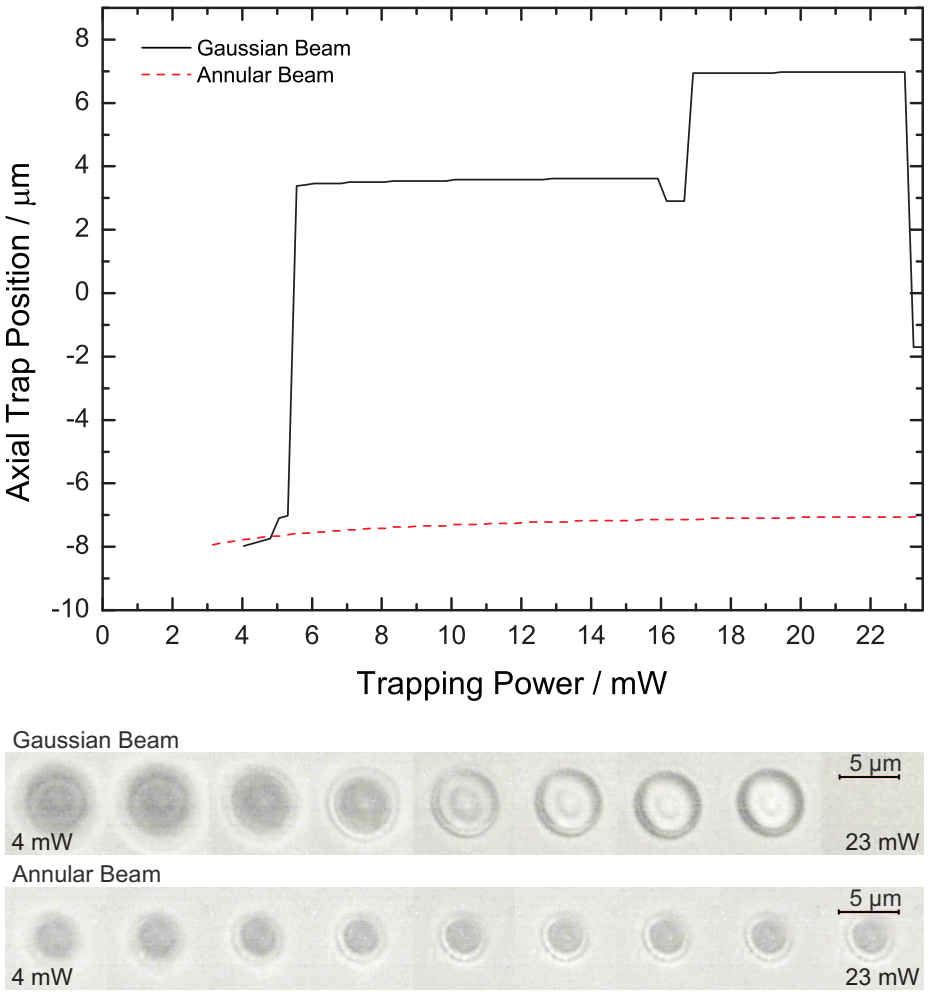


Figure 3.10: An illustration of the effect of power variation on the axial trapping position. Equilibrium trapping positions output from the simulation are shown above, with experimental screenshots below, taken over the same power range. The Gaussian graph (solid line) clearly shows a large vertical displacement in trapping height as the power is increased until a drop at around 23 mW. This is experimentally confirmed below for a 2.8 µm radius droplet trapped in a Gaussian beam, as the power is varied from 4 mW to 23 mW. The modelled annular beam (dashed line) shows far less vertical variation, as confirmed in the screenshots for a trapped 2.1 µm radius droplet over the same power range.

trap. This droplet is then lost at 23 mW. The magnitude of this axial displacement can be estimated by vertically displacing a fixed microsphere in the same experimental setup. By comparing the images this range is estimated to be between 10 and 20 µm, in agreement with the simulation results presented above. The 2.1 µm droplet trapped in the annular beam shows far less axial displacement as expected, and can still be stably trapped at powers beyond the 23 mW shown. This relative invariance in trap position with increasing laser power has potential applications in aerosol spectroscopy such as CERS [5] as it would allow measurements to be taken at higher intensity with far less axial position variation.

3.4.4 Trap Stiffness

The focus of the work presented in this chapter so far has been trapping in the axial direction, as it is this which generally governs whether or not a droplet will be stably confined. It is however of interest to compare axial with lateral trapping in each case in order to fully explore the effects of using an annular beam. Axial and lateral trap stiffnesses can be determined by using the Quadrant Photo-Diode shown in Figure 3.6. As the voltage signal from each quadrant of the QPD is proportional to the scattered light intensity incident upon it, the difference in signal across the detector in each direction can be calibrated in order to determine the droplet's lateral position. In addition, the axial position can be obtained from the total light intensity incident on all four quadrants. By taking the Fourier transform of these position *vs.* time signals, power spectra can be determined for both lateral and axial trapping, as described in Section 1.4. These take the form:

$$S(\omega) = \frac{2k_{\mathrm{B}}T}{\kappa} \frac{\Omega_0^2 \Gamma_0}{(\omega^2 - \Omega_0^2)^2 + \omega^2 \Gamma_0^2} \tag{3.2}$$

where ω is the angular frequency, equal to $2\pi f$, k_{B} is the Boltzmann constant, κ is the stiffness of the trap, Γ_0 is the viscous damping of the medium and Ω_0 is the natural angular frequency of the position fluctuations. By fitting experimental power spectra to this expression, information about the trap dynamics, including trap stiffness, can be extracted [46]. Two example lateral power spectra are shown in Figure 3.11, for a 4.7 µm radius droplet trapped in a Gaussian (top) and annular (bottom) beam. The data shows the expected form with the gradient of the high frequency tail tending to ω^{-4} at higher frequencies. In each case a fit to Equation 3.2 is also shown. It should be noted that although calibration of the power spectrum into units of $\mathrm{nm}^2\ \mathrm{Hz}^{-1}$ is possible, it is unnecessary for trap stiffness determination.

In Figure 3.12 the experimentally determined trap stiffnesses in both the lateral and axial dimensions have been presented as a function of power. Each point is the average of several droplets trapped at the same power, with the error bars representing the standard deviation of these values. An approximately linear trend of trap stiffness with power is observed in each case. While it must be noted that droplet radius also varies significantly with power, and so must be considered when drawing conclusions about the factors affecting trap stiffness, these figures do demonstrate that for a given series of droplets (*i.e.* at each power), the lateral trap stiffness is generally greater than the axial trap stiffness for the

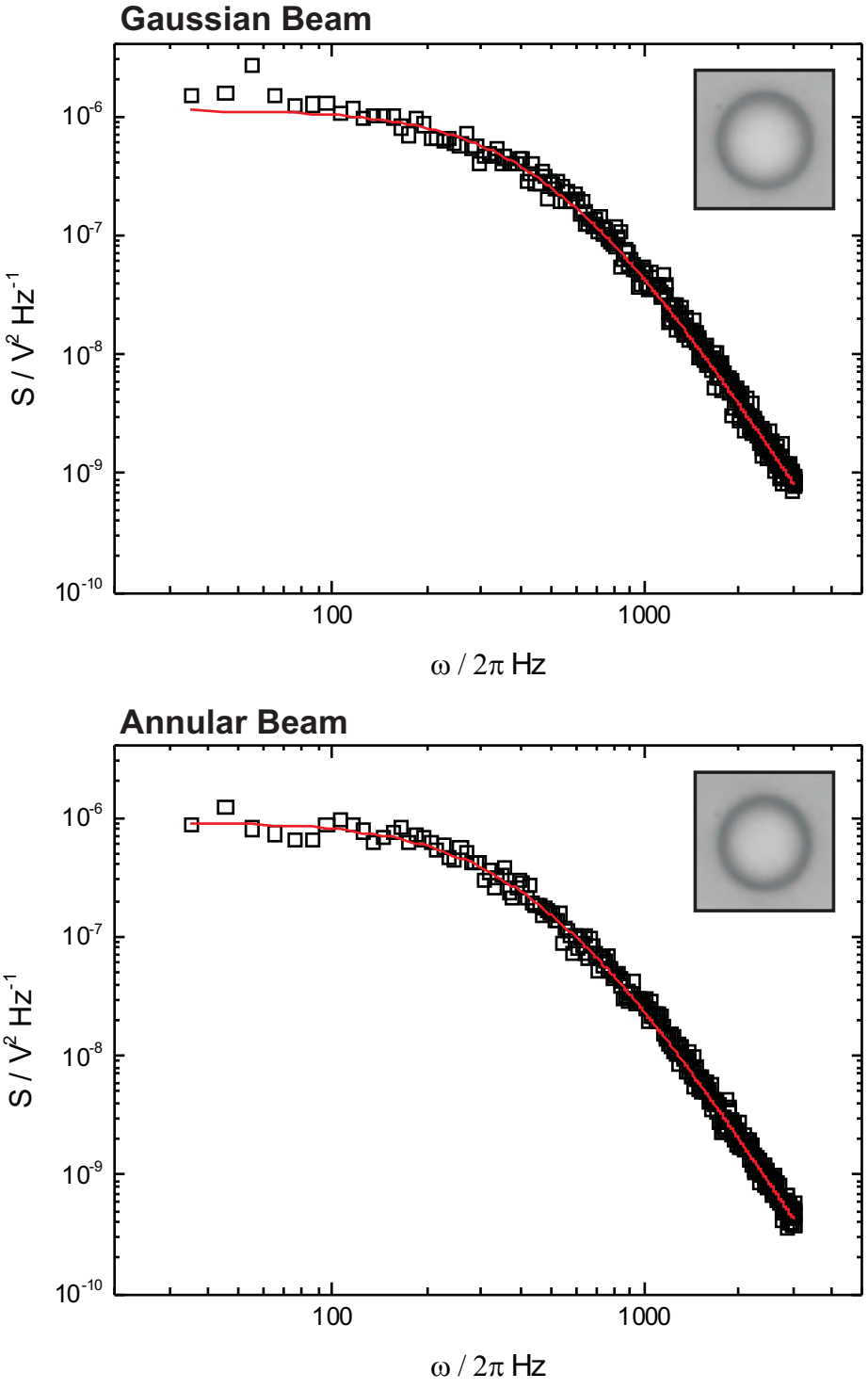


Figure 3.11: Example lateral power spectra for a trapped 4.7 µm radius droplet in a Gaussian beam (top) and an annular beam (bottom). The fit to Equation 3.2 is shown in red, allowing lateral trap stiffnesses to be extracted. A screenshot of each of the trapped droplets is also shown.

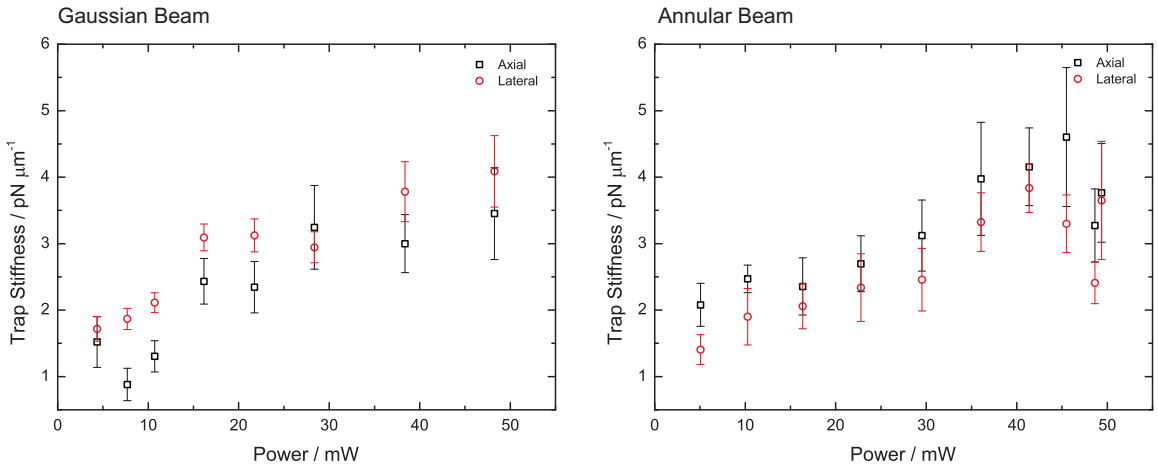


Figure 3.12: A plot of trap stiffness as a function of power is shown for both a Gaussian and an annular beam. In each case an approximately linear trend is seen, with the lateral trap stiffness being larger than the axial value for the Gaussian beam, and the reverse trend seen for the annular beam. This can be understood in terms of the reduction in scattering force achieved when the central core of the Gaussian beam is blocked.

Gaussian beam. This is expected due to the destabilising nature of the scattering force. In contrast, the annular beam plot demonstrates that the axial trap stiffness is now consistently higher than the corresponding lateral values, indicating the effect that the removal of the central core has had on stabilising the droplets in the axial direction.

To get a more quantitative understanding of this effect, axial *vs.* lateral trap stiffness plots are shown in Figure 3.13 for each beam type. By plotting lateral and axial trap stiffnesses for each individual droplet, any effects due to droplet radius or trapping power can be neglected, and a true measure of the axial compared to lateral stiffness can be obtained. For the Gaussian beam, shown in black, it can be seen that a linear fit through the origin yields a gradient and therefore axial:lateral trap stiffness ratio of 0.79 ± 0.04, in agreement with the observation that the lateral trap stiffness is generally larger when trapping with a Gaussian beam. In contrast to this, the annular beam plot gives an axial:lateral trap stiffness ratio of 1.15 ± 0.04, clearly indicating the significant improvement in axial trapping compared to lateral when the annular beam is used.

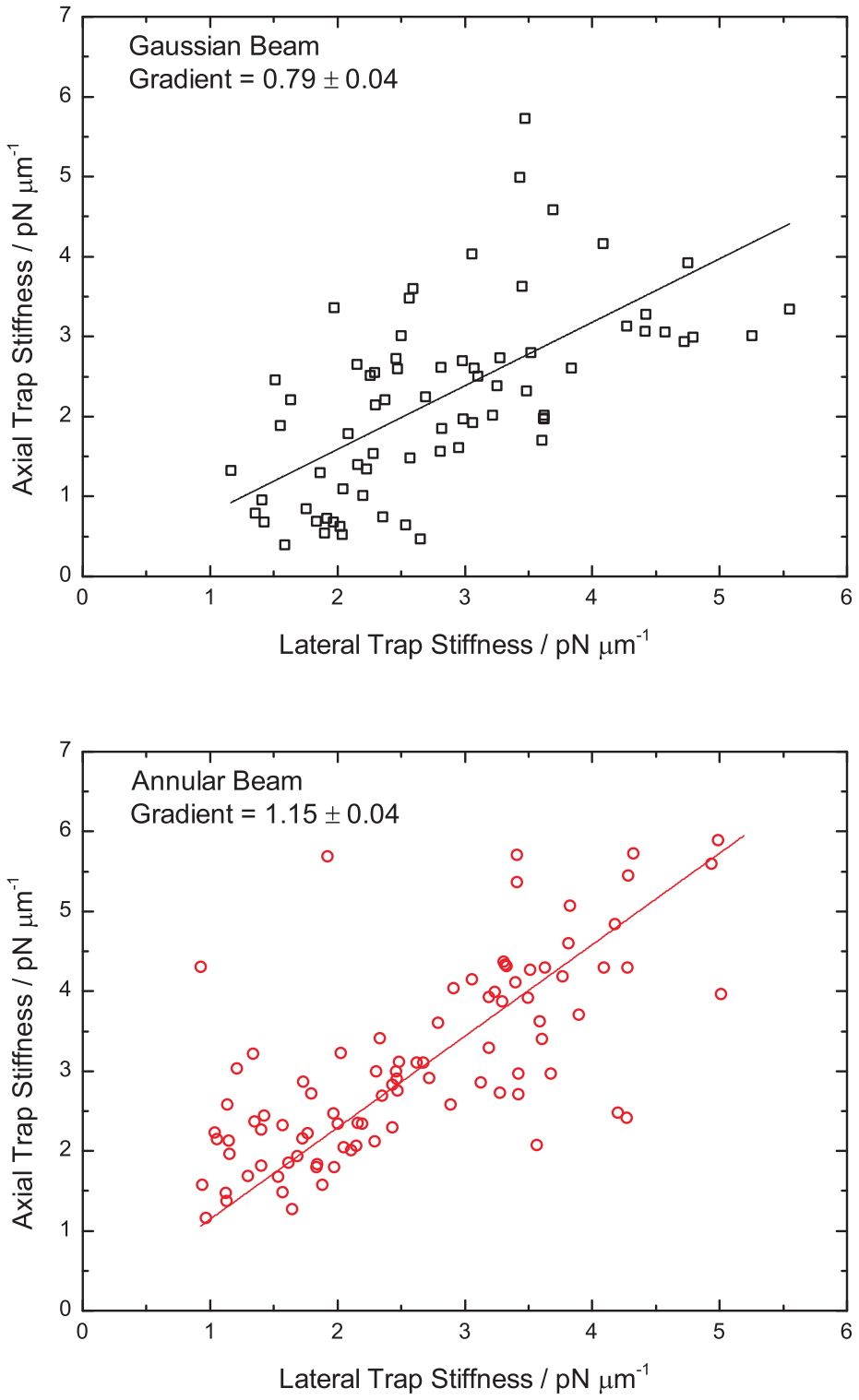


Figure 3.13: A plot of axial *vs.* lateral trap stiffness allows these values to be directly compared in the absence of droplet size or trapping power effects. A straight line fitted through the origin for the Gaussian beam data (top) gives an axial:lateral trap stiffness ratio of 0.70 ± 0.04, with this value increasing to 1.15 ± 0.04 when the annular beam (bottom) is used.

3.5 Conclusions

In this chapter the optical trapping of aerosol droplets using conventional Gaussian beams and annular beams has been studied. Modelling work on aerosol optical traps has indicated that significant improvements in trapping ability may be achieved using annular beams. By building a suitable experimental setup, these results were experimentally verified by simply blocking the central portion of a Gaussian beam.

By extending the model to determine the effects of trapping power on the stable trapping of droplets, minimum trapping powers were determined and directly compared to experimental results, demonstrating excellent agreement. A series of droplets were then trapped at a range of powers, confirming the increased size range of trappable droplets predicted by the simulation, and the ability to trap smaller droplets at higher powers using annular beams. Following this the greatly improved axial localisation that can be achieved when trapping with annular beams was demonstrated. The simulation was used to predict how the axial equilibrium position would vary with power, before this was also experimentally verified in both beam types.

Finally axial and lateral trap stiffness values were determined using back focal plane interferometry and the power spectrum method of trap stiffness determination. This revealed an average axial:lateral trap stiffness ratio of 0.79 ± 0.04 for the Gaussian beam, indicating stronger lateral trapping in this case. This value increased significantly to 1.15 ± 0.04 when the annular beam was used, indicating the effect that blocking the central core of the beam has had on improving the axial trapping, with the usually limiting axial trapping now being significantly stronger than trapping in the lateral direction.

There are several approaches that could now be taken in order to further optimise the annular beam trapping which has been presented here. It is unclear whether the droplet size limit presented in Figure 3.9 is due to true physical limitations of the beams being used or the size range of droplets formed by the medical nebuliser. As such, it would be interesting to explore new nebulising techniques to see if even smaller droplets could potentially be trapped using an annular beam. In addition to this, the effects of obstruction size have not yet been explored, and it is anticipated that this could have a significant impact in optimising this trapping behaviour. This could be achieved by using a different obstruction

size in the beam path, or by generating annular beams using another method such as a spatial light modulator, which would allow control over the annulus size.

Chapter 4

Micro-Rheological Investigations of Ionic Liquids

Ionic liquids (ILs), defined as organic salts which exist as liquids at room temperature, are a topic of great contemporary interest due in part to their use as "green" solvents in organic synthesis. There are in some cases difficulties associated with producing large volumes of high purity samples, particularly for more recently developed ILs, making the study of these compounds difficult. As a result optical tweezers are an ideal tool for investigating these samples due to the small sample volumes which they require. In the previous chapter aerosol droplets were studied using back focal plane interferometry, where it was the trapped aerosols themselves which were being investigated. In contrast, in this chapter ILs will be used as the trapping medium, and investigated by monitoring the motion of melamine tracer particles trapped within them.

Following a brief outline of the history of ILs and recent work within this field, several micro-rheological investigations of ILs will be presented, including a demonstration of Faxén's correction to viscous drag in close proximity to a surface and temperature dependant viscosity changes of ILs. As well as using the back focal plane interferometry techniques presented in the previous chapter, a high-speed camera will also be utilised for these studies, and a comparison of the two techniques will be presented. One of the advantages of using a high-speed camera over a QPD for particle tracking is the ability to track multiple particles. This will be utilised in the final part of this chapter, as hydrodynamic coupling between

pairs of optically trapped particles within ILs will be studied, showing excellent agreement with previously published theoretical models.

4.1 Room Temperature Ionic Liquids

In 1914 Walden reported the synthesis of Ethylammonium Nitrate (EAN) [85], credited as being the first deliberately developed room temperature ionic liquid. At first these liquids were mainly of interest for electrochemical applications [86], but since their proposal as organic solvents in the 1980s [87, 88], interest and research into these novel compounds has vastly increased. Often described as being "green" solvents [89], their appeal comes from their extremely low volatilities [90], large liquid range, high thermal and chemical stabilities [91] and their potential for decreasing the quantity of volatile organic compounds which are discharged into the atmosphere [89]. Ionic liquids show highly tunable properties through careful choice of the base cation and anion units, and modification of any alkyl groups on the cation, allowing solubility, viscosity, density and melting points to be altered [92, 93]. This tunability has led to them being referred to as "designer solvents" [94], where properties can be tailored to specific applications. In addition to their use in organic synthesis ILs have been used as industrial lubricants [95], in chemical processing [91] and in nanoparticle synthesis [96], as well as showing an ability to absorb gases such as CO_2 with important applications in post-combustion capture [97]. For example, Ahosseini *et al.* report CO_2 mole fractions of up to 76% in [EMIM][Tf_2N] at ambient temperature and a pressure of 93.5 bar [98].

Optical tweezers are a well established technique for micro-rheological investigations of properties such as viscosity and flow [99]. A particular advantage of using optical tweezers is the small sample volumes which are required ($\sim$10 µL) compared to conventional rheological methods. This makes them ideal for the study of ILs, particularly when it is difficult to prepare large volumes of high purity samples [100]. This micro-rheology also allows the investigation of local rather than bulk viscosities, which may be used to probe any sample micro-heterogeneity. Recently the use of optical tweezers as a tool for investigating IL solutions has been demonstrated in both aerosol and colloidal systems. Moore *et al.* have successfully trapped droplets of aqueous EAN solutions and spectroscopically characterised their change in composition in response to differing humidity conditions [101], while

Elmahdy *et al.* have trapped colloids in aqueous IL solutions (≤ 0.01 M) to investigate how their pair interaction forces are affected by salt concentrations [102].

In this chapter the first demonstration of the optical trapping of colloidal particles within *pure* IL samples is presented. This has the potential to open up a range of new studies and applications, as the behaviour of the optically trapped 2.31 µm melamine particles can be used to investigate local properties on a micron-scale within the ILs, as will now be demonstrated.

4.2 Micro-Rheological Investigations using Back Focal Plane Interferometry

4.2.1 Experimental Setup

The main features of the experimental setup used for the initial work presented in this chapter, shown in Figure 4.1, are the same as for the aerosol trapping setup outlined in Chapter 3. One of the main differences is that a Laser Quantum Forte system (maximum power of 400 mW at 1064 nm, although with typically only $\sim$ 20 mW used in the trap) is used as the trapping source in place of the Laser Quantum Torus used previously. Power control is again achieved using a half waveplate and polarising beam splitter before the steering mirror (not shown). Due to the lack of sensitivity of the silicon detector to near infra-red radiation, a second laser source (Novalus Protera at 488 nm) is used to image the sample onto the QPD, with a filter in place to remove any remaining forward-scattered 1064 nm radiation. Imaging of the sample is again achieved using a CCD camera (Watec, WAT DM3S) after illumination from above using a high intensity fibre source (Thorlabs OSL1-EC, not shown). A typical sample consists of $\sim$10 µL of IL containing dispersed 2.31 µm melamine particles purchased from microParticles GmbH with surface COOH functionalisation, sandwiched between two glass coverslips separated by a custom vinyl spacer. It is noted that ILs may cause swelling of certain polymers and therefore care must be taken in order to select appropriate probe particles such that they are unaffected by the IL environment. Over the timescale of these measurements the melamine particles used in this work are not swollen by being placed in EAN.

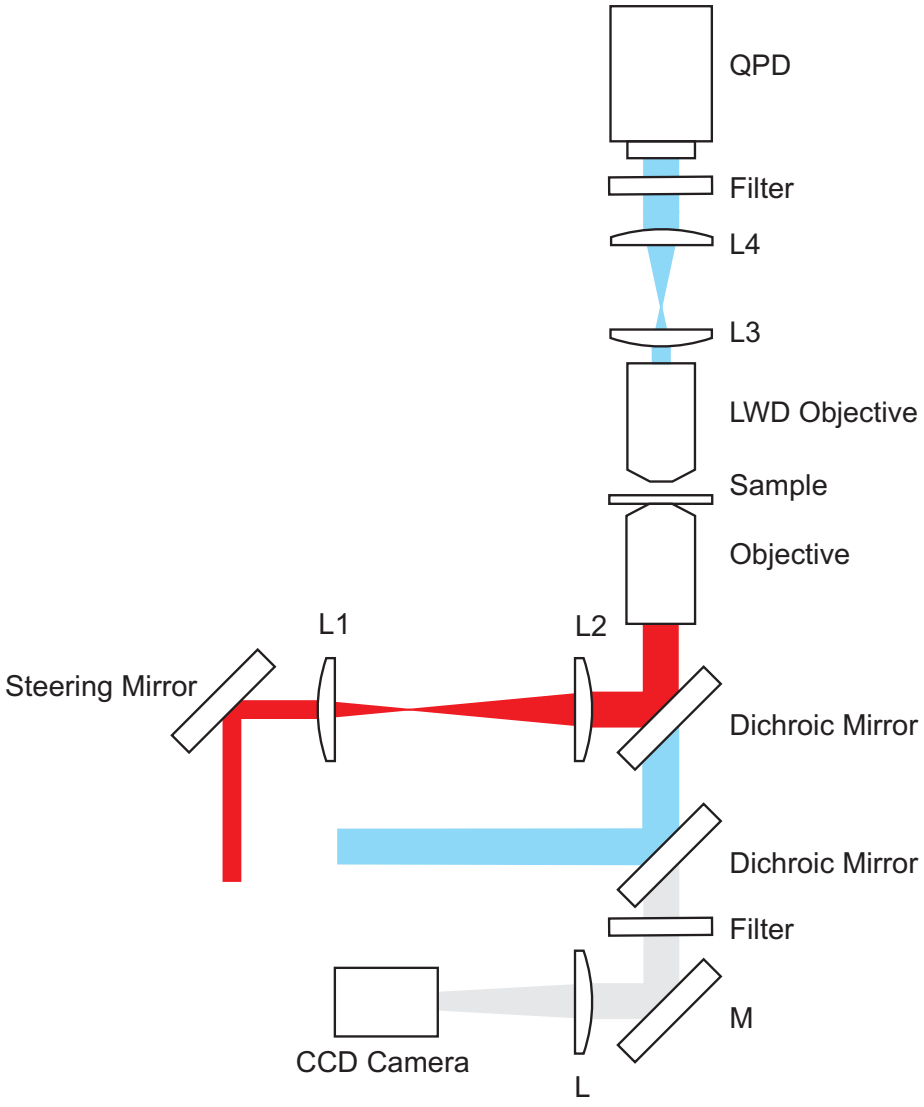


Figure 4.1: The setup used for the initial experiments presented in this chapter. Trapping is achieved using a Laser Quantum Forte source (400 mW at 1064 nm, red line), which is expanded using two lenses in a $4f$ arrangement before being focussed into the sample cell using an oil immersion objective (Nikon E Plan, 100 $\times$/1.25). A Novalus Protera source (488 nm, blue line) is used to image the sample onto the Quadrant Photo-Diode (QPD) due to the lack of sensitivity of the silicon detector to near infra-red radiation. This imaging is achieved using a second, long working distance (LWD) objective positioned above the trapping objective, and another $4f$ relay system consisting of L3 and L4. Imaging of the sample from below onto a CCD camera is achieved by illuminating using a high intensity fibre light source (Thorlabs OSL1-EC, not shown).

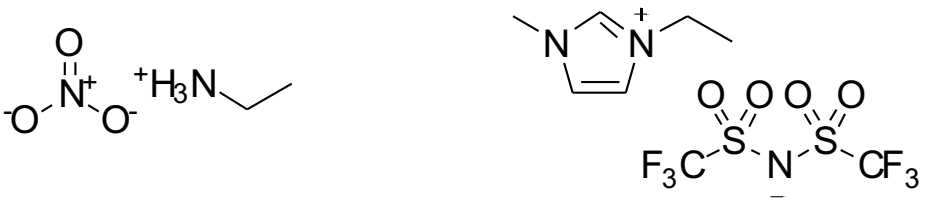


Figure 4.2: Left: Ethylammonium Nitrate (EAN)
Right: 1-ethyl-3-methylimidazolium bis(trifluoromethylsulfonyl)imide ([EMIM][Tf_2N])

The two ILs chosen for the work presented here are Ethylammonium Nitrate (EAN), due to it being one of the most widely used and best characterised ILs as well as being the first synthesised [85], and 1-ethyl-3-methylimidazolium bis(trifluoromethylsulfonyl)imide ([EMIM][Tf_2N]), chosen due to interest in its ability to absorb large volumes of CO_2 [103, 104]. Their chemical structures are given in Figure 4.2. EAN, obtained from io-li-tec and used without further purification, shows a number of similarities in its physical properties to water, as a result of its three-dimensional hydrogen bonded network [105, 106]. Its viscosity of 26.91 cP [107], around 30× that of water, gives a corresponding increase in the optical trapping timescale as will now be demonstrated. In contrast, the [EMIM][Tf_2N] ions form a relatively rigid network containing 'free volumes' which are able to accommodate CO_2 molecules with little perturbation of the ionic structure [103] as confirmed by molecular dynamics simulations [104]. Again the optical trapping timescale in [EMIM][Tf_2N] is significantly increased compared to water, due to its elevated viscosity of around 34 cP [108], although this value varies significantly with IL water content [109].

One problem which becomes immediately apparent when trapping in ILs is the increased effects of mechanical noise, as a direct result of the increased optical trapping timescale in these media. The experimental corner frequencies now lie in the tens of Hz range, in the region normally discarded when fitting to experimental power spectra. In addition, the longer timescales needed for data collection mean that the effects of long term mechanical drift become much more important. In this work these effects were minimised by using a vibrationally isolated table and reinforcing the cage assembly supporting the tweezers. In work presented later in this chapter a high-speed camera was used in place of the QPD for particle tracking and an electronic band pass filter was applied to the data, significantly reducing the magnitude and effects of mechanical noise.

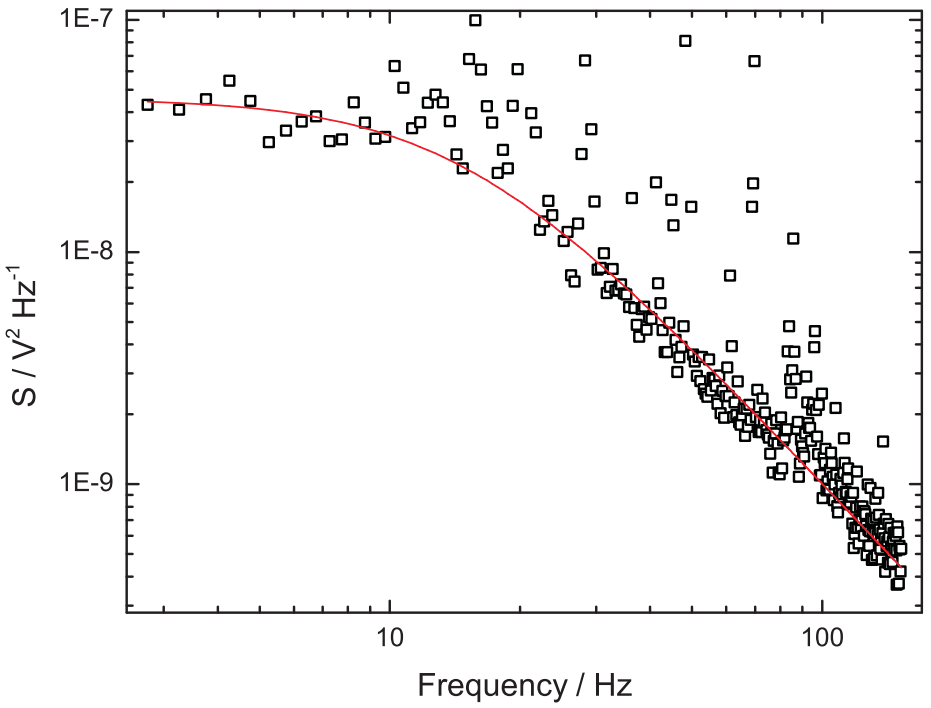


Figure 4.3: An example power spectrum for a 2.31 µm melamine particle trapped in EAN. Despite the increased mechanical noise evident in the power spectrum compared to those presented previously, a fit to Equation 4.1 does allow a trap stiffness of $55.0 \pm 4.0\,\mathrm{pN/\mu m}$ to be extracted.

4.2.2 Trap Stiffness Measurements

In order to determine physically useful properties from the Brownian dynamics of the optically trapped melamine particles, the power spectrum method of trap stiffness determination was used [46]. Particle positions were recorded at a rate of 100 kHz for 100 s using the QPD, with the increase in the data collection timescale a necessary result of the increased optical trapping timescale in EAN, and the need to study processes occurring at a lower characteristic frequency. The expected form of the power spectrum, $S(f)$, obtained by taking a Fourier transform of the position *vs.* time data, is given by Equation 4.1:

$$S(f) = \frac{D/(2\pi^2)}{f_c^2 + f^2} \tag{4.1}$$

where D is the diffusion constant, equal to $k_\mathrm{B}T/\gamma$, and f_c is the corner frequency, given by $f_c = \kappa/(2\pi\gamma)$. As before γ and κ are the viscous drag coefficient and trap stiffness respectively. Fitting the data to Equation 4.1 allows experimental corner frequencies to be determined, enabling accurate trap stiffnesses to be calculated. Figure 4.3 shows an example power spectrum for a trapped melamine particle in an EAN sample, with the

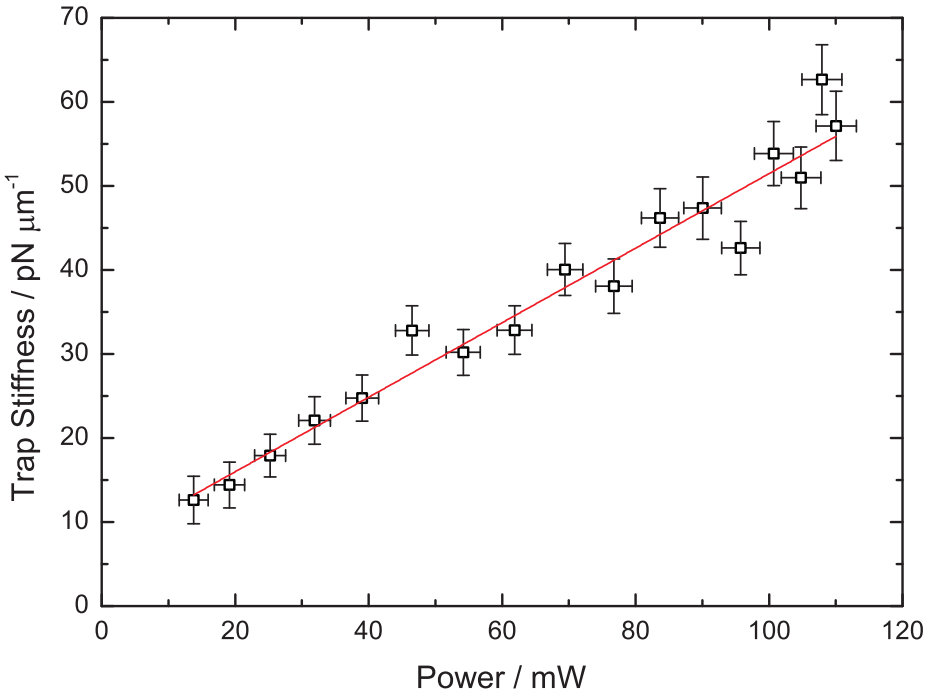


Figure 4.4: By recording the power spectrum of a single melamine particle trapped at a series of laser powers, the power dependence of the trapping behaviour can be studied. A linear fit is returned as expected, although the gradient has been reduced when compared to trapping in water due to the decreased refractive index contrast between the particle and the medium, and the additional aberrations present when using optics designed for use with water samples.

expected low frequency plateau and high frequency tail tending to f^{-2}, in contrast to the f^{-4} behaviour observed in the previous chapter when trapping aerosol droplets. Despite the clear increase in mechanical noise observed, a fit to Equation 4.1 is shown in red, returning a corner frequency of $14.95 \pm 1.08\,\mathrm{Hz}$ indicating a trap stiffness of $55.0 \pm 4.0\,\mathrm{pN/\mu m}$.

Having established the successful trapping of a colloidal particle in an IL, the optical trap can be characterised in terms of its behaviour as a function of trapping power. This can be seen in Figure 4.4 where a single melamine particle has been trapped, and its trap stiffness determined by fitting to its power spectrum at each power. The trapping power values have been calculated by taking into account the losses along the optical chain, giving a power at the trap in each case. An uncertainty in the fit to each power spectrum allows trap stiffness errors to be calculated, while the trapping power error bars are obtained by estimating the accuracy with which an angle on the half-waveplate power control can be set.

A linear fit to this data yields a gradient of $0.44 \pm 0.02\,\mathrm{pN\ \mu m^{-1}\ mW^{-1}}$ for trapping in EAN, significantly reduced from the value of $0.92 \pm 0.04\,\mathrm{pN\ \mu m^{-1}\ mW^{-1}}$ obtained when

trapping in water. This is expected to be due to a combination of two influencing factors. Firstly EAN has a relatively high refractive index of 1.452 [107], meaning that the refractive index contrast between the particle and trapping medium is reduced when compared to trapping in water. It is expected that this will decrease the trapping efficiency. Using Equations 1.3 and 1.4 the reduction in the magnitude of the gradient force can be estimated to be ~ 38 %. Secondly there may be additional aberrations present when trapping in EAN due to the microscope objective being designed for use with water samples. While these factors must be taken into consideration, they do not prevent the stable trapping of particles in EAN, or the use of this technique for micro-rheological investigation. It is also interesting to note that the intercept of the plot in this case is not zero, as might be expected, but is instead around 7 pN/µm. This is a result of the trapping effect of the additional imaging laser in the system despite low powers being used, and is another reason why a high-speed camera was used for the work presented later in the chapter as no additional imaging laser is required.

4.2.3 Temperature Dependant Viscosity Changes in ILs

Once the the trap stiffness has been calculated for a given particle and sample, this technique can be used to monitor properties of the system, such as viscosity, as any changes will be reflected in a shift in the power spectrum corner frequency. As an example of this, the effects of temperature on the viscosity of two ILs will now be presented.

The temperature dependence of the dynamic viscosity of EAN has been previously measured using macro-rheological techniques, with Poole *et al.* observing viscosity reductions of up to 50% just a few tens of degrees above room temperature [107], and reporting the following relationship:

$$\ln \eta = A_1 + A_2 T \tag{4.2}$$

where T is the temperature in degrees Celsius and A_1 and A_2, determined from a fit to their experimental data, are constants equal to 4.33 and -3.49×10^{-2} respectively. In addition, Jacquemin *et al.* have previously reported the effects of temperature on [EMIM][Tf_2N] solutions, instead quantifying this in terms of an Arrhenius type equation [109]:

$$\eta = \eta_\infty \exp(E_a/RT) \tag{4.3}$$

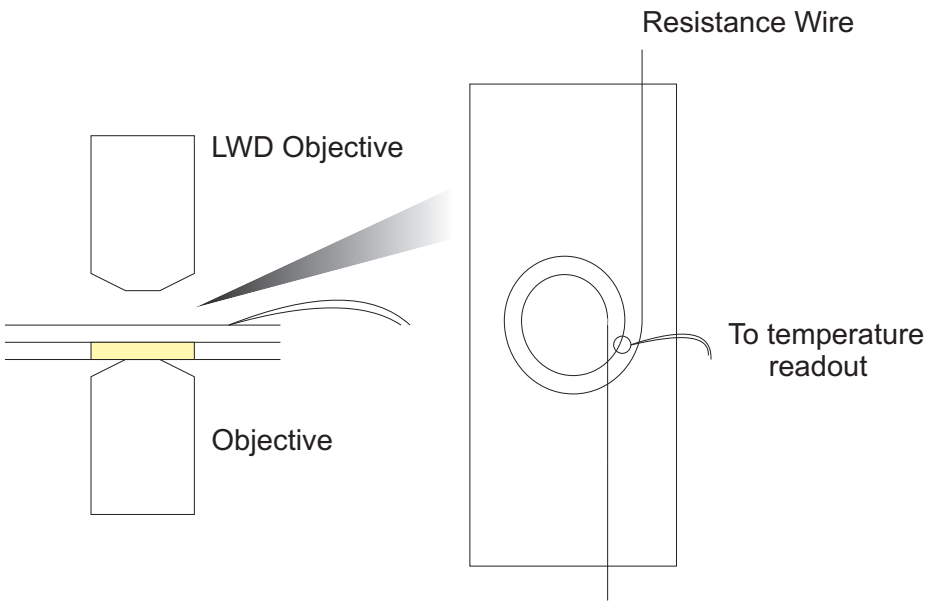


Figure 4.5: A custom built temperature controlled slide, consisting of a coil of resistance wire attached to a coverslip using Araldite glue. This slide allows control of the sample temperature by applying a voltage across the resistance wire. Monitoring of the slide temperature occurs using a K-type thermocouple on the slide surface, with the sample temperature calculated from this using conversion values obtained from prior calibration.

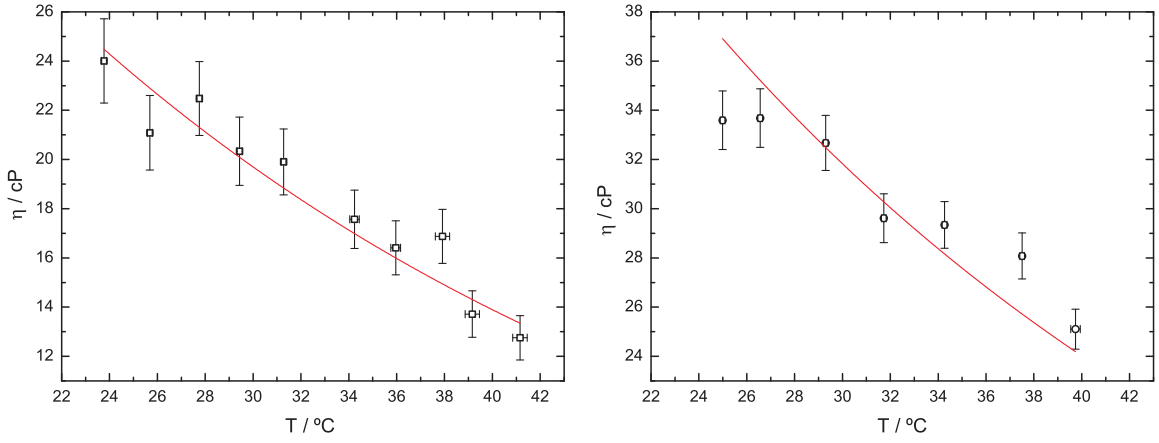


Figure 4.6: Temperature dependent viscosity changes of EAN (left) and [EMIM][Tf_2N] (right) determined by trapping a single melamine particle at a series of sample temperatures. The experimentally measured values show good agreement with the previously reported macro-rheological trends of Poole *et al.* [107] and Jacquemin *et al.* [109], shown in red.

where η_∞ is the high temperature viscosity limit, determined to be 4.339×10^{-4} cP, and E_a is the activation energy for viscous flow, with the value of 22.20 ± 0.33 kJ mol^{-1}.

In order to investigate these trends using optical tweezers a custom-built heater, consisting of a coil of resistance wire fixed to a coverslip using Araldite glue, is attached to the top of a sample slide. This slide is illustrated in Figure 4.5. The sample temperature is measured

using a K-type thermocouple (80 µm wire, Farnell Part No. 8598240) situated on the slide surface, read using a digital thermometer (Digitron 2000T). Monitoring of the temperature within the sample using the thermocouple was not possible due to its bulk, and so instead conversion between the slide surface and sample temperatures was achieved *via* a calibration factor. This factor was determined by recording the temperature of the slide surface as a function of electrical power, and then repeating this process when the thermocouple was located within a sample of the appropriate IL, allowing a conversion factor between the two temperature scales to be calculated.

By trapping a single melamine particle at a fixed height and constant power as the temperature of the sample is increased using the heater, power spectra can be recorded and EAN viscosities calculated utilising knowledge of the room temperature trap stiffness. In each case the temperature of the sample was allowed to stabilise over a period of 120 s before data was collected, and close attention was paid to ensure no convection effects were observed due to the heating process. The reduction of convection effects was aided by designing a slide with as tight a heating coil as possible in order to promote even heating of the sample, whilst still allowing clear imaging of the trapped particle.

The experimentally determined sample viscosities for both EAN and [EMIM][Tf_2N] are shown in Figure 4.6, with the error bars calculated from the uncertainty in the fit to the power spectra, and the stability of the sample temperature over the duration of each run. In each case the expected form of the temperature dependence is also shown in red, from Poole *et al.* [107] (Equation 4.2) for EAN, and Jacquemin *et al.* [109] (Equation 4.3) for [EMIM][Tf_2N] . While these viscosity changes can be confidently assigned using the methods presented here, they are reliant on knowledge of the room temperature values. As such the fits given in Figure 4.6 are fixed to the parameters responsible for dictating the rate of change in η (A_2 and E_a) while the absolute values are allowed to vary. It can be seen that despite the increased difficulties of trapping and recording power spectra for particles in IL media, the previously reported macro-rheological trends can be confidently reproduced using micro-rheological methods.

4.3 Micro-Rheological Investigations using a Fast Camera

Despite the good agreement observed between macro and micro-rheological measurements obtained using a QPD in conjunction with optical trapping techniques, there are a number of problems associated with using this method. One of these is the significant level of mechanical and electrical noise present across the frequency domain which is being studied, as demonstrated by the magnitude of the error bars on the experimentally determined trap stiffness values. In addition, the use of a second laser source for imaging the sample on to the QPD results in some residual trapping effects and so also adds to the errors associated with using the power spectrum method for monitoring properties of the ILs.

Recently the affordability of high speed CMOS cameras, capable of frame rates of several kHz, has made them an attractive alternative for particle tracking in optical trapping applications [110]. They are particularly suited to work in IL samples as the decrease in the typical resonance frequency of the trap, due to high IL viscosities, means that the higher temporal resolution offered by the QPD is unnecessary, and the high-speed camera frame rates are sufficient. For the work presented in the remainder of this chapter a high-speed CMOS camera will be used in place of the QPD system already described. The advantages of this new experimental setup include a reduction in the electrical noise present in the particle position data when compared to the QPD voltage traces, and the ease of alignment compared to the back focal plane interferometry measurements. As well as this only a single laser source is needed, removing the unwanted secondary trapping effects. In addition, the high-speed camera allows the tracking of multiple particles; a feature which will be utilised in the study of hydrodynamic coupling between pairs of particles in Section 4.4. The experimental setup has been further reinforced in order to reduce the effects of mechanical noise, facilitated by the more compact geometry of the camera arrangement. Finally the power spectra are calculated after splitting the data into suitable time periods for averaging determined by Allan variance measurements as demonstrated in Section 2.3.3.

4.3.1 Experimental Setup

The experimental setup used for the camera tracking micro-rheological experiments presented in the remainder of this chapter is shown in Figure 4.7. The optical trapping component remains the same as in Figure 4.1, while the second laser source has now been

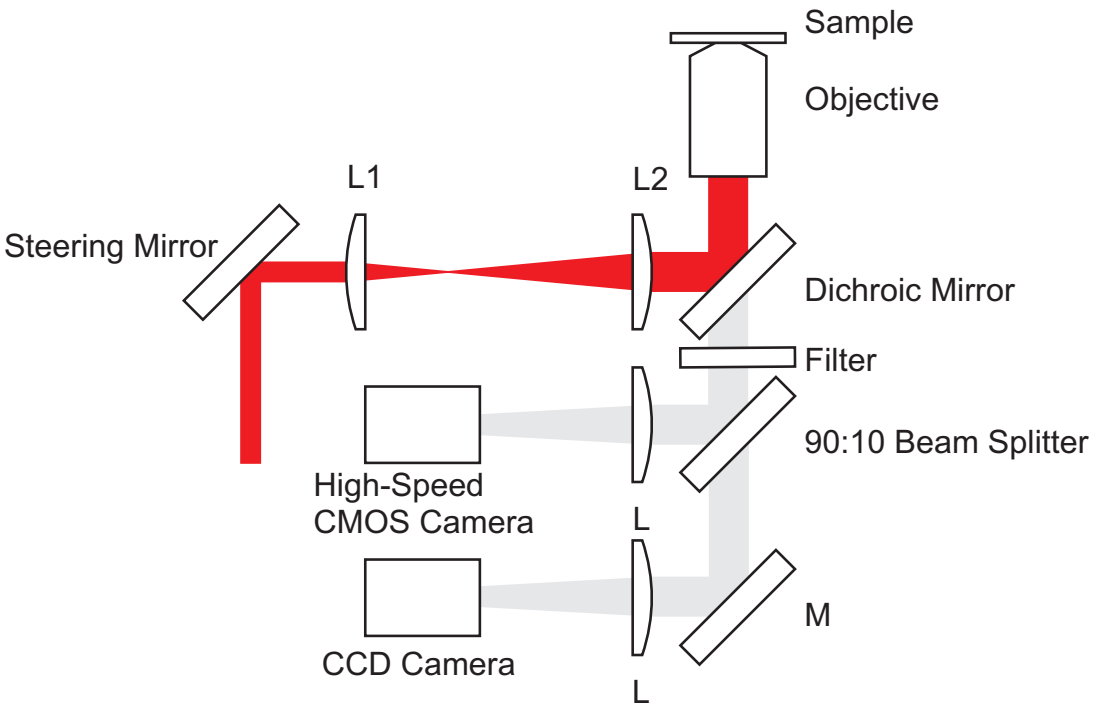


Figure 4.7: The experimental setup used for the camera tracking experiments presented in Sections 4.3 and 4.4. While the trapping laser remains the same as in Figure 4.1, the secondary imaging laser is no longer required, and has instead been replaced by a high-speed CMOS camera for particle tracking.

removed and replaced by a high-speed CMOS camera (Dalsa Genie HM640). When running the high-speed camera, particle tracking is performed *on-the-fly* using a centre-of-mass tracking algorithm. For the experiments presented here frame rates of 1600 Hz are used as a compromise between the speed of data capture and the particle tracking region required. Due to this limited imaging region, and the reduced performance when using the LabVIEW routines for both tracking and imaging using the high-speed camera, it is useful to have a secondary imaging camera in the system. As a result the CCD camera is still used for sample imaging, with a 90:10 beam splitter allowing both cameras to image simultaneously.

4.3.2 Mean Square Displacement Measurements for a Particle Diffusing in EAN

One of the advantages of using a camera rather than a QPD for particle tracking is the ability to work over a much larger region of interest. While this does necessarily mean a reduction in the maximum obtainable camera frame rate, the CMOS camera used here will still run at 300 fps when imaging over the full frame. This increased region of interest

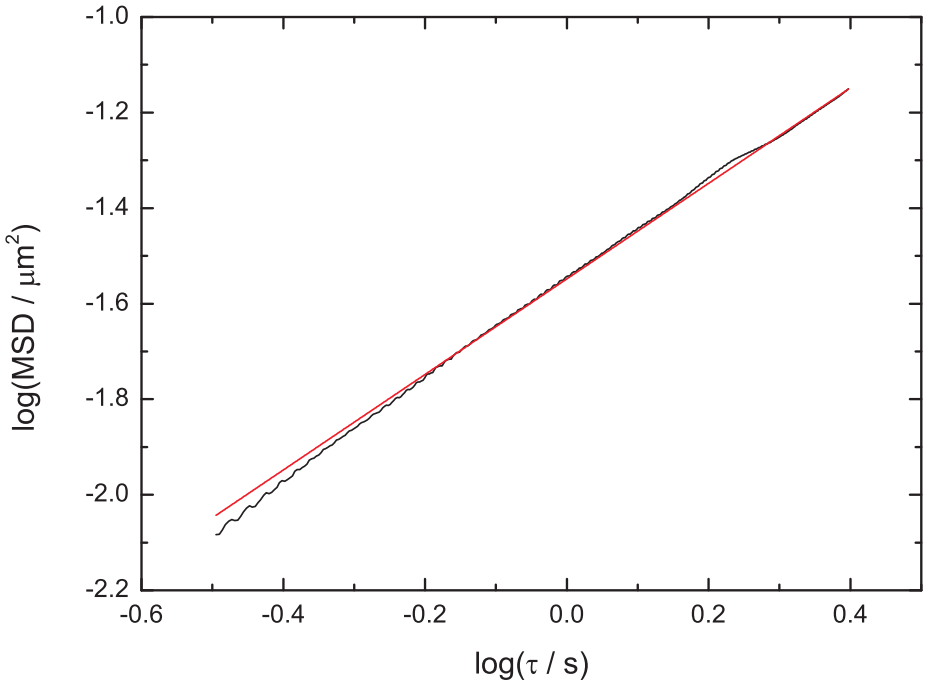


Figure 4.8: A plot of $\log(MSD)$ *vs.* $\log(t)$ for a freely diffusing melamine particle in EAN yields a straight line with a gradient of one, demonstrated by the linear fit shown in red. This indicates that EAN is behaving as a purely viscous fluid as expected.

compared to the QPD facilitates the tracking of free as well as trapped particles allowing, for example, measurement of the mean square displacement (MSD) of a particle's position when not trapped using optical tweezers. For a freely diffusing sphere in a purely viscous fluid, this function takes the form:

$$\left\langle \Delta\vec{r}^{\,2}(\tau) \right\rangle = \left\langle [\vec{r}(t+\tau) - \vec{r}(t)]^2 \right\rangle = 2dD\tau \tag{4.4}$$

where $\vec{r}$ is the particle position, τ is the lag time or time interval, t the absolute time, d the number of dimensions over which the MSD is being calculated, and D the diffusion coefficient [99]. At timescales longer than that which is required for the velocity autocorrelation function of the particle to decay to zero this function is expected to be a linear function of t. This leads to a plot of $\log(MSD)$ *vs.* $\log(t)$ yielding a straight line of gradient one. In contrast to this, if the sphere is in a purely elastic fluid the particles will not diffuse through the sample, and the slope of this plot will be zero. An intermediate value is an indication of the viscoelasticity of the trapping medium. It can be seen in Figure 4.8 that a fit to a $\log(MSD)$ - $\log(t)$ plot for a freely diffusing melamine particle in EAN does indeed yield a straight line of gradient one, shown in red, indicating that the assumption that EAN is behaving as a Newtonian fluid is correct. The oscillations observed in the MSD are due to

mechanical vibrations in the system.

4.3.3 Trap Stiffness Measurements

As noted in Section 4.3 there are a number of advantages in using a high-speed camera over a QPD for particle tracking in terms of both electrical and mechanical noise reduction. This can clearly be seen in Figure 4.9, where the power spectrum of a trapped melamine particle in EAN is shown, displaying considerably less noise when compared to Figure 4.3. This is attributed partly to the use of a camera for particle tracking, increased mechanical stability of the setup and improved data analysis techniques including splitting of the position data into shorter segments for averaging, as determined by Allan variance measurements. This significant noise reduction allows much more accurate trap stiffness determination than was possible previously. In this example a corner frequency of $15.1 \pm 0.2\,\mathrm{Hz}$ was obtained, indicating a trap stiffness of $55.7 \pm 0.9\,\mathrm{pN/\mu m}$ for a laser power of $84.0\,\mathrm{mW}$. This implies a reduction in the uncertainty of trap stiffness assignment from $\sim 7\%$ for the QPD tracking system, to $\sim 1.6\%$ in this case. In addition to this improvement, the power spectrum does not require further calibration provided that the particle coordinates are already converted from pixels to nanometres, unlike the QPD system which requires more complex calibration methods [48].

Following the procedure presented in Section 4.2.2 the camera setup can also be characterised in terms of its trapping behaviour with power as shown in Figure 4.10. Again a linear trend is observed, although now this passes through the origin due to the removal of the secondary imaging laser. The trap stiffness error bars, determined from the uncertainty in the Lorentzian fit to the power spectra, are significantly smaller than those presented earlier, and are smaller than the data symbols in some cases. The uncertainties in the trapping power are again determined from considering how accurately the power can be selected using the half-waveplate and PBS power control arrangement. A gradient of $0.66 \pm 0.01\,\mathrm{pN\ \mu m^{-1}\ mW^{-1}}$ is determined for trapping in EAN, still reduced from the value of $0.92 \pm 0.04\,\mathrm{pN\ \mu m^{-1}\ mW^{-1}}$ determined for water samples but significantly higher than the value of $0.44 \pm 0.02\,\mathrm{pN\ \mu m^{-1}\ mW^{-1}}$ obtained using the QPD setup for EAN trapping despite the same laser source being used. This is attributed to the improved alignment which is possible using the more simple camera setup, as some manipulation of the particle height was required when imaging on to the QPD detector.

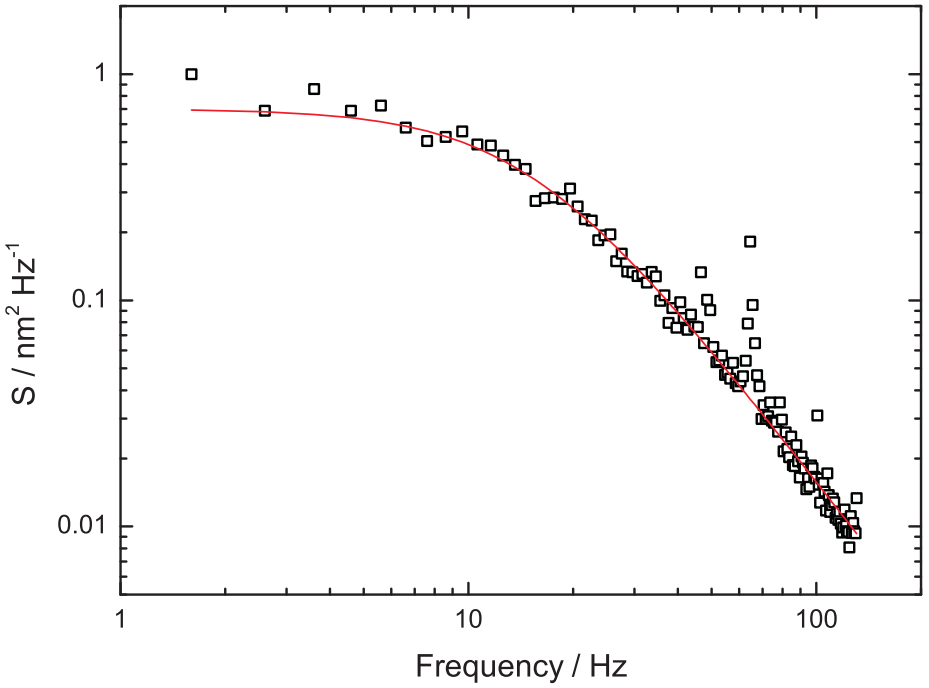


Figure 4.9: An example power spectrum for a 2.31 µm melamine particle in EAN for a trapping power of 84 mW, showing significantly reduced noise when compared to the previously presented QPD power spectra in Figure 4.3. A fit to Equation 4.1 is shown in red.

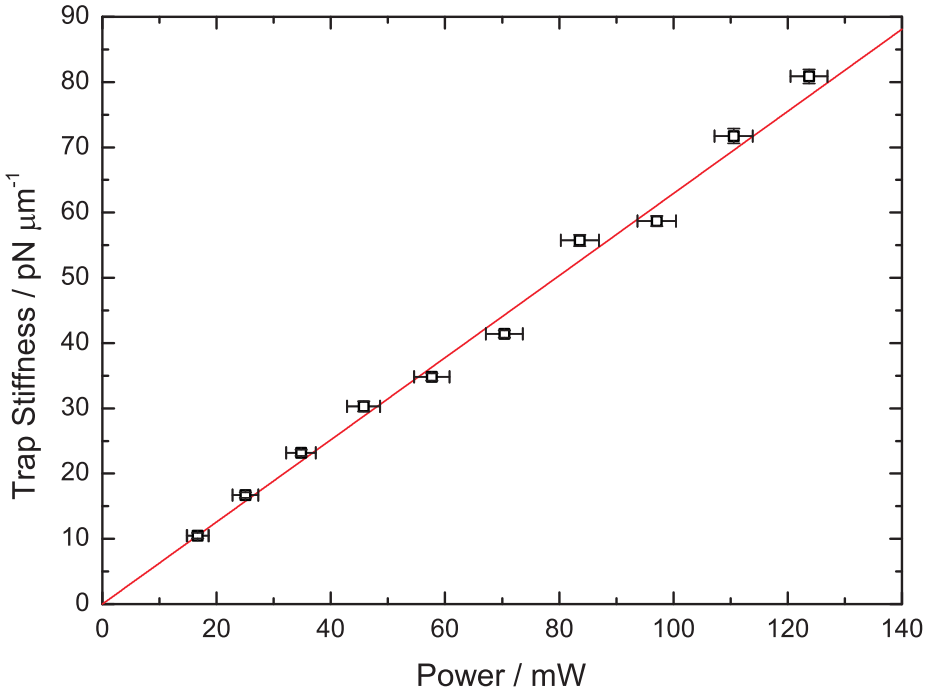


Figure 4.10: A plot of trap stiffness against laser power yields a straight line with gradient 0.66 ± 0.01 pN µm^{-1} mW^{-1} for trapping in EAN, reduced from the value determined for trapping in water due to refractive index and aberration effects.

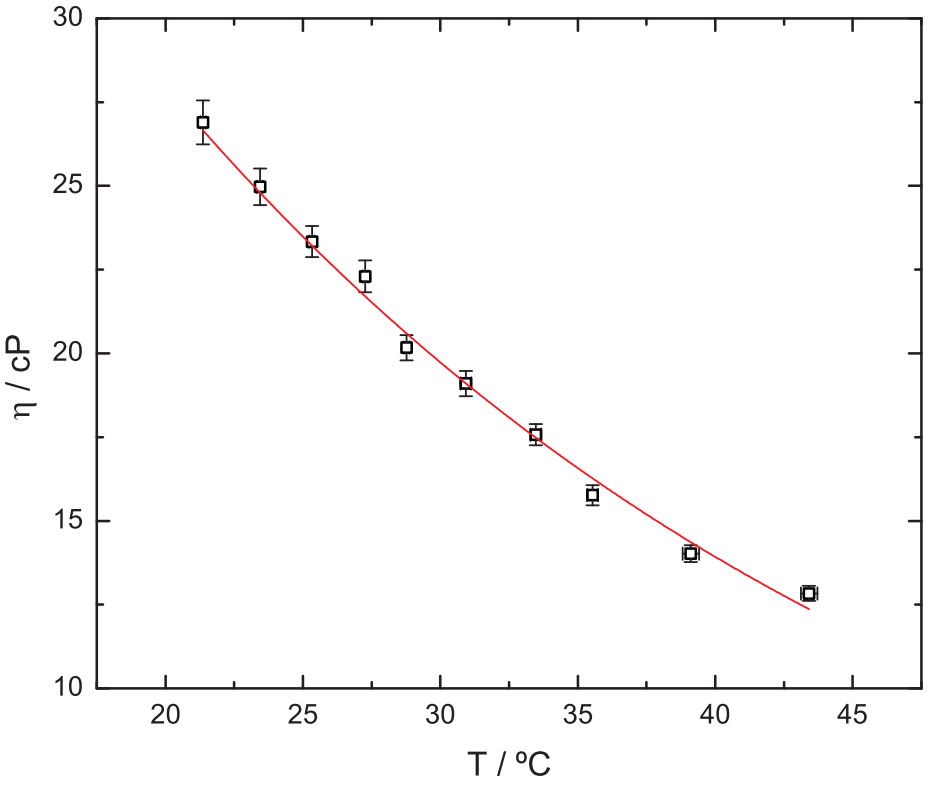


Figure 4.11: A plot of viscosity against sample temperature for EAN gives the same trend as previously observed but with much greater confidence in the assigned η values and closer agreement to the expected trend. A fit to Equation 4.2, shown in red, gives a value of $(-3.48 \pm 0.12) \times 10^{-2}$ for the decay constant, in excellent agreement with the values obtained by Poole *et al.* [107].

4.3.4 Temperature Dependant Viscosity Changes in EAN

Having demonstrated the improved performance of the high-speed camera system, the experimental determination of the temperature dependent viscosity changes in EAN will now be repeated following the method of Section 4.2.3. While the same trend is still observed there is a vast improvement in the accuracy with which the experimental viscosities can be assigned, as demonstrated in Figure 4.11. Fitting to Equation 4.2 given by Poole *et al.* [107], shown in red, gives a value of A_2 of $(-3.48 \pm 0.12) \times 10^{-2}$ in excellent agreement with the value of -3.49×10^{-2} obtained by macro-rheological techniques.

An Arrhenius-like law can also be used to interpret these temperature dependent viscosities as previously demonstrated for the studies of [EMIM][Tf_2N] [109]. This allows the activation energy for viscous flow, E_a, to be determined *via* a plot of $\ln(\eta)$ against T^{-1}, as shown in Figure 4.12. Okoturo and VanderNoot describe three different possibilities relating to the curvature of such a plot, finding that those ILs with less symmetric cations and no functional

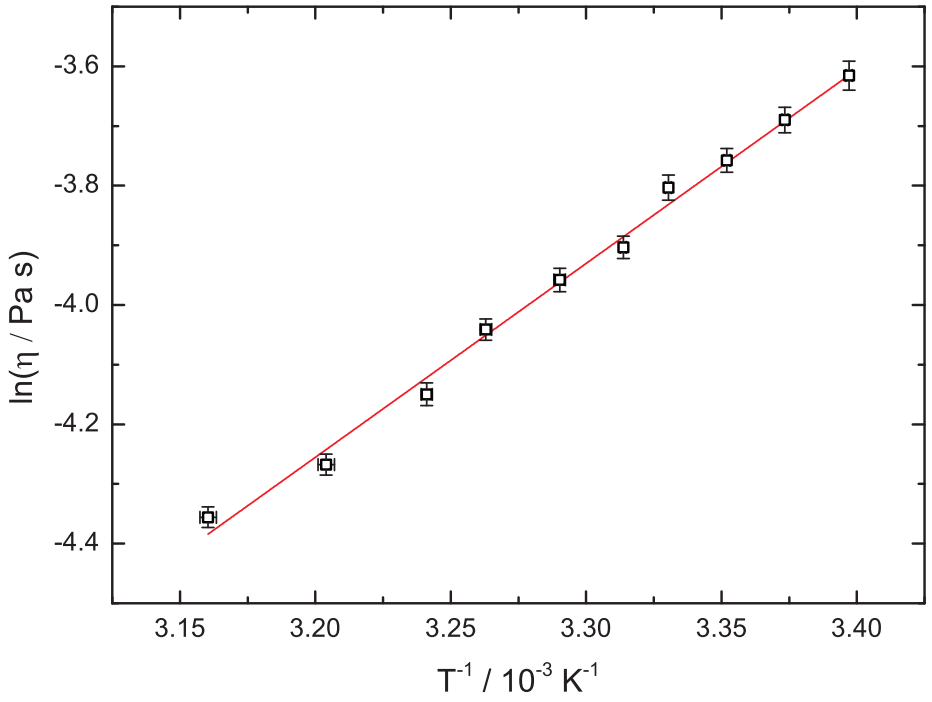


Figure 4.12: By plotting $\ln(\eta)$ against T^{-1} the activation energy for viscous flow in EAN can be determined *via* a linear fit as shown in red.

groups on the alkyl chain generally display a linear trend and are well fit by the Arrhenius model [111]. This is the case for EAN, as demonstrated by the quality of the linear fit shown in Figure 4.12. This fit returns an activation energy of $27.0 \pm 0.8\,\mathrm{kJ\ mol^{-1}}$, in good agreement with the previously reported value of $24.26 \pm 1.91\,\mathrm{kJ\ mol^{-1}}$ [112] and a clear demonstration of the applicability of optical trapping techniques for the micro-rheological study of ILs.

4.3.5 Measuring Faxén's Correction to Viscous Drag

Another well studied perturbation to an optically trapped particle is that of the increase in viscous drag experienced by a sphere in close proximity to a plane surface, as demonstrated for melamine particles trapped in water in Chapter 2. Here, the same procedure will be used in order to quantify this effect for these particles trapped in EAN. As presented earlier, the correction for particle motion parallel to a plane surface is given by:

$$\gamma_{\text{Faxén}} \approx \frac{\gamma_0}{1 - \frac{9}{16}(\frac{a}{h}) + \frac{1}{8}(\frac{a}{h})^3 - \frac{45}{256}(\frac{a}{h})^4} \tag{4.5}$$

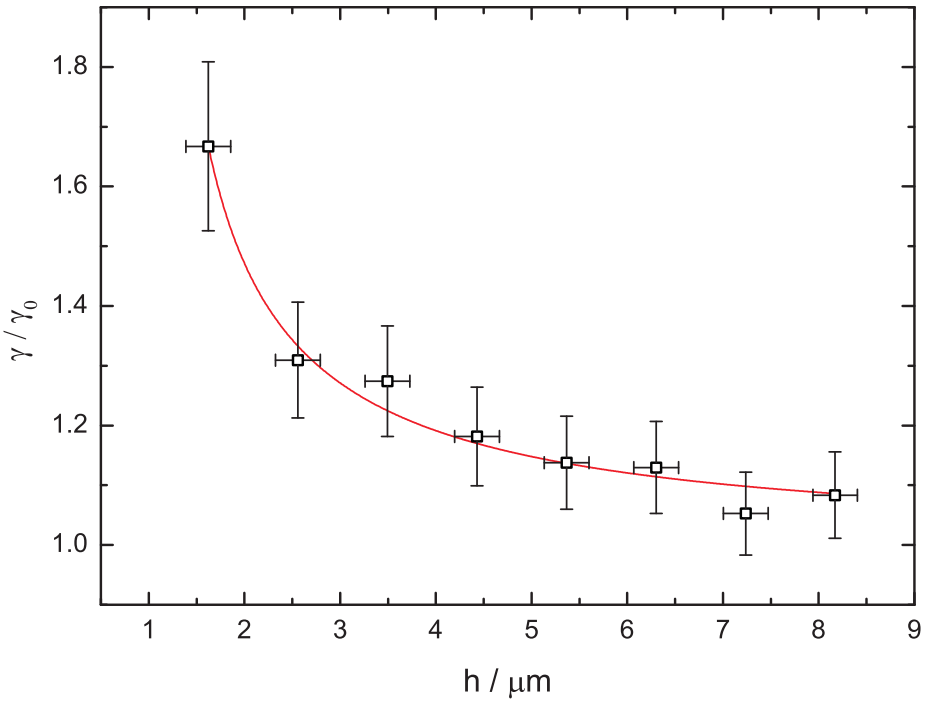


Figure 4.13: Variation of the friction coefficient, γ, for a trapped melamine particle in EAN relative to its bulk value, γ_0, as a function of particle height above the sample coverslip. A best fit to the expected form, given by Faxén's law, is shown in red.

where h is the separation between the particle and the surface, $\gamma_{\text{Faxén}}$ is the corrected drag coefficient and γ_0 is the drag coefficient at large distances from the surface given by Stokes' law. As before, a particle is trapped a large distance from the coverslip, before the particle-coverslip separation is reduced and γ inferred from analysis of the particle power spectrum. The trap stiffness is assumed to be constant over this height range, confirmed by recording the variance in particle position observed at each trapping position.

The ratio of γ/γ_0 for a melamine particle trapped in EAN at a series of trapping heights is given in Figure 4.13. In this case the height offset, determined from the fit and defined as the absolute trapping height at the minimum particle-coverslip separation, was 1.6 µm, again slightly larger than a, allowing absolute height values to be presented in Figure 4.13. The excellent agreement with the expected form, shown in red, further confirms the behaviour of EAN as a viscous, Newtonian fluid.

4.4 Hydrodynamic Coupling Studies

Aside from the noise reduction apparent in the data obtained using the high-speed camera, one of the most important advantages that it brings is the ability to track multiple particles simultaneously. This allows the study of multi-particle interaction phenomena such as hydrodynamic coupling, as will be presented here. This interaction will be verified in water, as previously demonstrated by Meiners and Quake [7], before being quantified in both EAN and [EMIM][Tf_2N]. Again, the viscosity of the ILs results in an increased optical trapping timescale, evident in the longer timescale of the hydrodynamic interactions. In addition, hydrodynamic coupling will also be demonstrated within ethylene glycol (EG) as its intermediate viscosity of 16.1 cP provides a reference between the limiting timescales observed in water and ILs.

There are a number of reasons for studying hydrodynamic coupling within colloidal systems due to the role that these interactions play in many important systems. For example, hydrodynamic effects play a key role in the theory of polymer dynamics [113], and in the dynamics and excitations of protein molecules [114, 115]. While these interactions can be challenging to study using bulk methods, optical tweezers provide an ideal tool for this due to their ability to isolate and measure the interactions between individual particles. This can be achieved by optically trapping two particles a fixed distance apart in separate tweezer traps. By monitoring their position fluctuations, correlation functions can be calculated. When the cross-correlation function between the particles is evaluated, a time delayed anti-correlation is observed which varies in magnitude with inter-particle separation. This time delayed component is observed despite the lack of "memory" of low Reynolds number fluid systems [116], and the assumed instantaneous propagation of forces through the fluid. Instead this delay is a result of the relaxation time of the optical tweezer trap and can be understood using Langevin dynamics [7].

By using the Langevin equation for particle motion in a fluid in the presence of an external potential [113], Meiners and Quake derive expressions for the correlation functions for particle motion in three dimensions. These correlation functions take the form:

$$\langle R_{1,i}(t)R_{1,j}(0)\rangle = \langle R_{2,i}(t)R_{2,j}(0)\rangle = \delta_{ij}\frac{k_{\mathrm{B}}T}{2\kappa_i}\left(e^{-(1+\epsilon_i)t/\tau_i} + e^{-(1-\epsilon_i)t/\tau_i}\right) \tag{4.6}$$

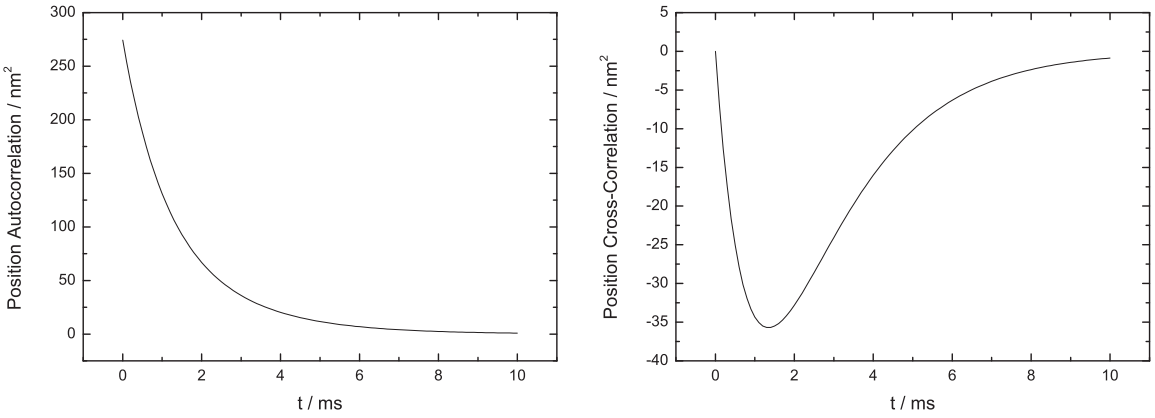


Figure 4.14: Calculated autocorrelation (left) and cross-correlation (right) functions for a pair of 2.31 µm melamine particles trapped in water at a separation of 5 µm. These have been determined using Equations 4.6 and 4.7, clearly illustrating the expected exponential decay in the autocorrelation function, and the pronounced time delayed anti-correlation in the cross-correlation function.

and

$$\langle R_{1,i}(t)R_{2,j}(0)\rangle = \langle R_{2,i}(t)R_{1,j}(0)\rangle = \delta_{ij}\frac{k_{\mathrm{B}}T}{2\kappa_i}\left(e^{-(1+\epsilon_i)t/\tau_i} - e^{-(1-\epsilon_i)t/\tau_i}\right) \tag{4.7}$$

where Equation 4.6 is an autocorrelation function, and Equation 4.7 a cross-correlation function, describing the coupling between the motion of the two trapped particles [7]. In each of these expressions R_1 and R_2 are vectors describing the positions of particles one and two, where i and j take the values x, y and z to describe motion in each dimension. κ_i and τ_i are the trap stiffness and relaxation time for dimension i, while ϵ_i is a measure of the hydrodynamic coupling between the particles. This coupling takes the value:

$$\epsilon_x = 3r/2E \tag{4.8a}$$

$$\epsilon_y = \epsilon_z = 3r/4E \tag{4.8b}$$

where x is defined as the longitudinal axis between the two trapped particles, while y and z describe the two transverse axes. In these expressions r is the particle radius, and E the mean inter-particle separation. Analysis assumes a no-slip boundary condition between the particle and the IL, though it would be interesting to investigate potential violations of no-slip boundary conditions in other IL media [117].

The expected forms of the autocorrelation (Equation 4.6) and cross-correlation functions (Equation 4.7) for a pair of particles trapped in water are given in Figure 4.14. These have been calculated for 2.31 µm diameter particles, separated by 5 µm with a trap stiffness of

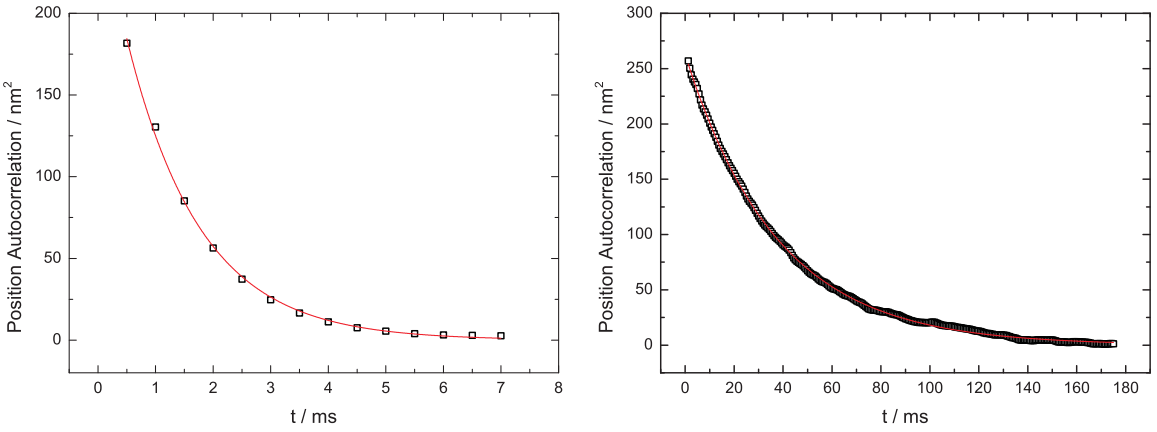


Figure 4.15: Experimentally determined autocorrelation functions for a melamine particle trapped in water (left) and EAN (right). Both systems have comparable trap stiffnesses, but a large difference in relaxation time is observed due to the increased viscosity of EAN. The reduced number of points on the water autocorrelation function results from the time resolution of the high-speed camera.

15 pN/µm, giving a trap relaxation time of $\tau = 1.29\,\text{ms}$ from $\tau = \gamma/\kappa$. The cross-correlation function has been calculated for hydrodynamic coupling along the longitudinal inter-particle axis (x). It can be seen that t_{min}, the minimum in the cross-correlation function, occurs close to τ, due to the anti-correlation delay being caused by the optical trap preventing the second particle from responding to the perturbation caused by the first for a finite amount of time, equal to the trap relaxation time, τ.

It can be seen that the autocorrelation expression, given by Equation 4.7, consists of two exponential decays with very similar time constants given by $\tau_i/(1 \pm \epsilon_i)$, and so readily approximates to the autocorrelation function expression for a single trapped particle neglecting any hydrodynamic interactions:

$$\langle R_{1,i}(t) R_{1,j}(0) \rangle \approx \delta_{ij} \frac{k_\text{B}T}{\kappa_i} e^{-t/\tau_i}. \tag{4.9}$$

When considering the components of the cross-correlation function however, the difference in time constant between the two exponential terms leads to the experimentally observed time-delayed anti-correlation. This minimum occurs at $t_{\text{min}} \approx \tau_i$ with a depth given by:

$$\langle R_{1,i}(\tau_i) R_{2,i}(0) \rangle = -\frac{1}{e} \frac{k_\text{B}T}{\kappa_i} \sinh(\epsilon_i) \approx -\frac{1}{e} \frac{k_\text{B}T}{\kappa_i} \epsilon_i. \tag{4.10}$$

The depth of this correlation function is proportional to the magnitude of the hydrodynamic

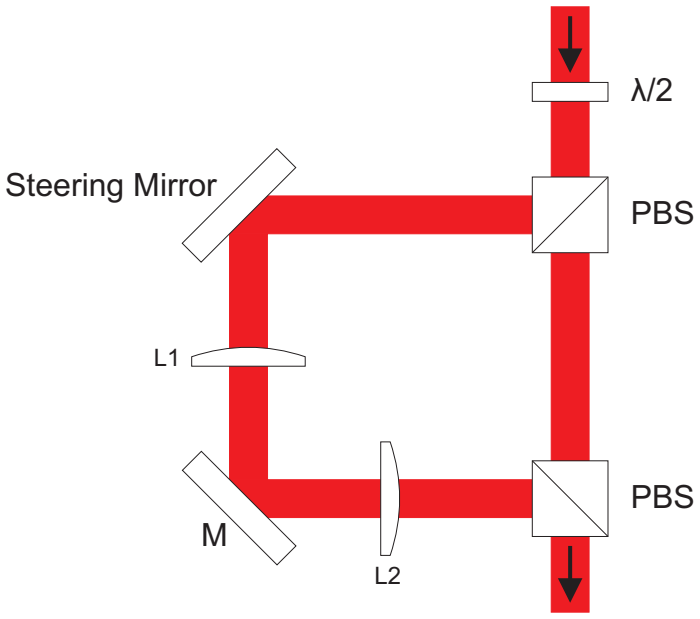


Figure 4.16: A small modification to the setup presented in Figure 4.7 allows dual-beam experiments to take place. The incoming laser beam (from top of image) is split using polarisation optics, before being recombined along a common optical path. The position of the new trap can now be adjusted independently of the first using the steering mirror shown.

coupling, ϵ, given by Equations 4.8a and 4.8b, and so is inversely proportional to the inter-particle separation [7].

When comparing the auto and cross-correlation functions for melamine particles trapped in water and EAN, the key difference between them will be due to the change in relaxation time, τ_i, between the two systems. If the trap stiffness remains constant, the timescale of the interactions will scale with the viscosity of the medium. This is demonstrated in Figure 4.15, where experimental autocorrelation functions have been determined for a trapped melamine particle in water (left) and EAN (right). Both samples shown the exponential decay expected for an over-damped system, with the water sample exhibiting a relaxation time, τ_x, of $1.283 \pm 0.001\,\text{ms}$ corresponding to a trap stiffness of $15.10 \pm 0.07\,\text{pN/µm}$. In contrast, a fit to the EAN data with a comparable trap stiffness of $15.66 \pm 0.05\,\text{pN/µm}$ gives $\tau_x = 37.4 \pm 0.1\,\text{ms}$.

4.4.1 Dual-Beam Optical Tweezers

In order to perform these cross-correlation experiments, the high-speed camera setup presented in Figure 4.7 is modified to allow dual-beam trapping to take place. This is achieved

by splitting the incoming trapping beam using polarisation optics, then recombining following the protocol of Lee *et al.* [49]. This procedure is shown in Figure 4.16. Here the laser beam is incoming from the top of the image, and is split into two orthogonally polarised beams using a polarising beam splitter (PBS). The relative power in each of the two beams can be controlled using the half-waveplate shown ($\lambda/2$). One of the components of the beam is transmitted through both beam splitters and continues along the optical path shown in Figure 4.7. The remainder of the beam passes through an additional $4f$ system consisting of a 1:1 telescope formed using two lenses, before being recombined with the first beam. The position of one of the trapping beams can now be altered independently using the steering mirror shown in Figure 4.16, while both beams can be manipulated together using the steering mirror of the original setup.

4.4.2 Hydrodynamic Coupling in Water

Having modified the LabVIEW centre-of-mass tracking routine in order to allow the tracking of multiple particles, experimental cross-correlation functions can be determined as shown in Figure 4.17. Here a pair of melamine particles are trapped in water using the dual-beam optical tweezers setup, and their positions recorded for a period of 120 s at 1600 fps. The cross-correlation between the position data along the inter-particle axis was then calculated, as the magnitude of the coupling will be strongest in this direction. Single particle autocorrelation functions were also determined in order to calculate a calibration constant, allowing the cross-correlation functions to be calibrated into units of nm^2. The expected time-delayed anti-correlation is observed at around 1 ms, as expected for a trap stiffness of $20.48 \pm 1.57\,\mathrm{pN/\mu m}$, though it can be seen that the curves are not smooth due to the limited time resolution of the camera. Cross-correlation functions are shown as a function of inter-particle separation, and the magnitude of the interaction can be seen to increase, as expected, as the particles are trapped closer together.

The expected depth of the minimum seen in the water cross-correlation functions can be determined by combining Equations 4.10 and 4.8a giving:

$$\langle R_{1,x}(\tau_i) R_{2,x}(0) \rangle \approx -\frac{1}{e} \frac{k_\mathrm{B} T}{\kappa_x} \frac{3r}{2E}. \tag{4.11}$$

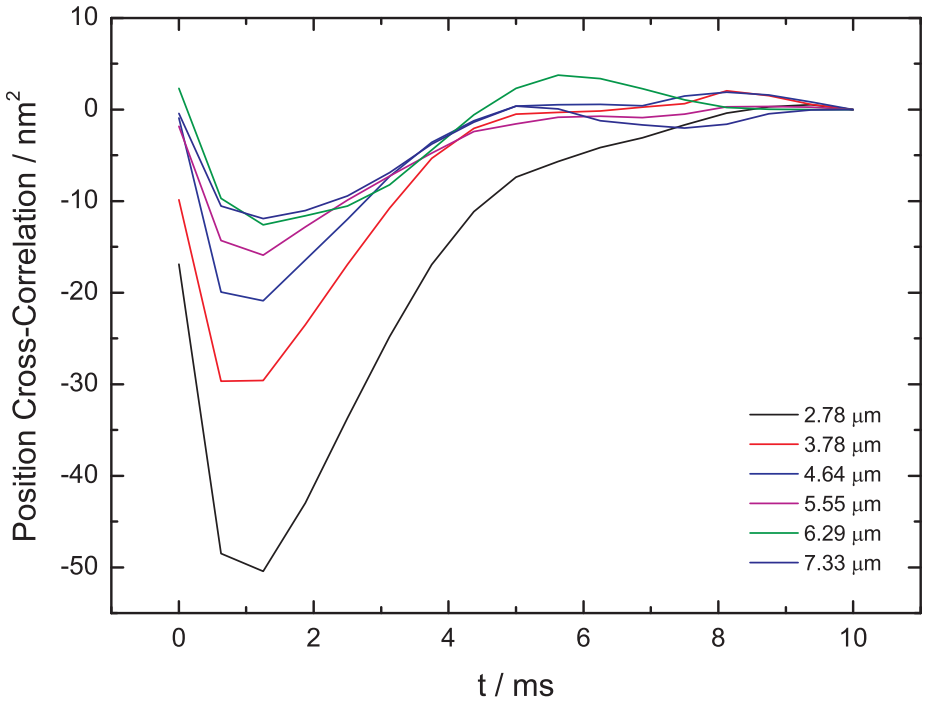


Figure 4.17: Cross-correlation functions for a pair of melamine particles trapped in water at a series of inter-particle separations. The expected anti-correlated dip is observed, which increases in depth with decreasing inter-particle separation.

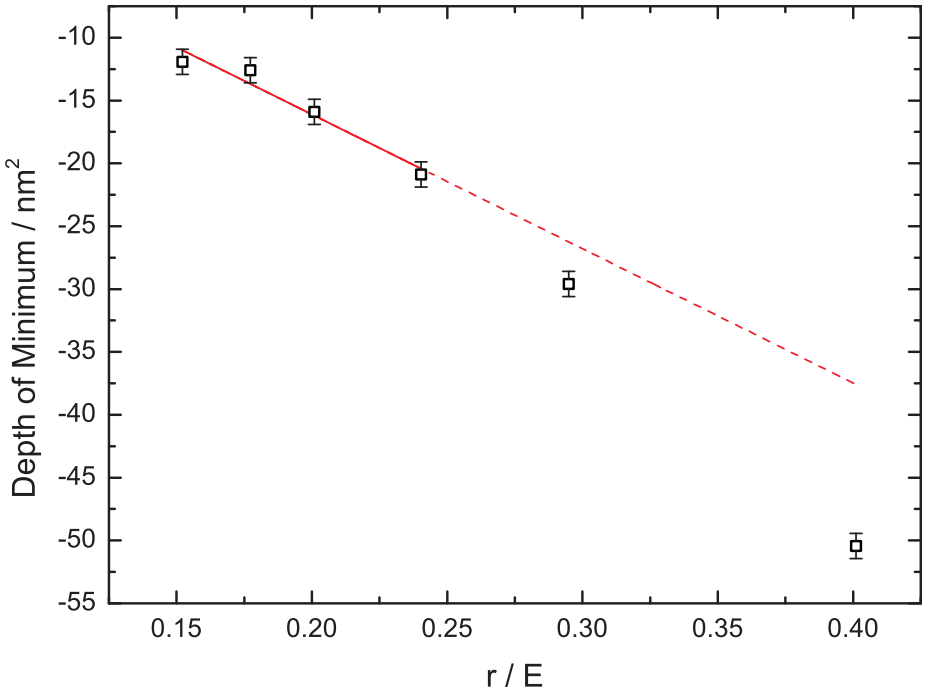


Figure 4.18: A plot of the cross-correlation depths observed in Figure 4.17 shows the expected straight line as a function of r/E until the assumption of independent optical traps breaks down at larger values, corresponding to small inter-particle separations.

It can be seen that a plot of the cross-correlation minimum as a function of r/E, where r is the particle radius and E the average separation between the trapped particles, should give a straight line with gradient $-(3k_{\mathrm{B}}T)/(2e\kappa_x)$. This is verified in Figure 4.18 where the minimum depth of each of the cross-correlation curves shown in Figure 4.17 has been plotted. A linear fit through the first four data points yields a slope of gradient $-106.8\,\mathrm{nm}^2$, which gives a trap stiffness of $21.40 \pm 3.95\,\mathrm{pN/\mu m}$, in good agreement with the value of $20.48 \pm 1.57\,\mathrm{pN/\mu m}$ obtained from the autocorrelation functions, especially when the limited time resolution in this domain is considered. The final two points in Figure 4.18 are not included in this fitting due to the small inter-particle separations and the break down in the assumption of independent harmonic trapping potentials. This results in the linear trend no longer being followed with much larger cross-correlations observed.

4.4.3 Hydrodynamic Coupling in RTILs

Having verified the results and theoretical model of Meiners and Quake for the hydrodynamic coupling between two optically trapped particles, this procedure will now be repeated with ethylene glycol (EG) as the trapping medium in order to verify its validity for particles trapped within more viscous media, before extending to the study of ILs. One advantage of moving towards media with longer relaxation times is the increased resolution of the high-speed camera at these timescales. There are however, new sources of mechanical noise and drift which need to be addressed. The complete process for determining experimental cross-correlation functions is as follows: After recording particle coordinates at 1600 fps for 120 s, this data is filtered to remove specific mechanical vibrational frequencies. It is then split into shorter segments for auto and cross-correlation analysis allowing averaging over multiple segments. From the single particle autocorrelation function a calibration factor and trap stiffness can be determined. This allows the calibration of the experimentally determined cross-correlation function into units of nm^2, before a constant offset is removed to account for long term experimental drift, following Meiners and Quake [7]. The resulting cross-correlation functions are then smoothed before being plotted along with the expected form of the functions given by Equation 4.7. Having determined κ and therefore τ from the autocorrelation decays this function can be plotted exactly with no free parameters. It should be emphasised that the figures plotted in the remainder of this chapter are direct comparisons to the predicted theoretical form and not experimental fits.

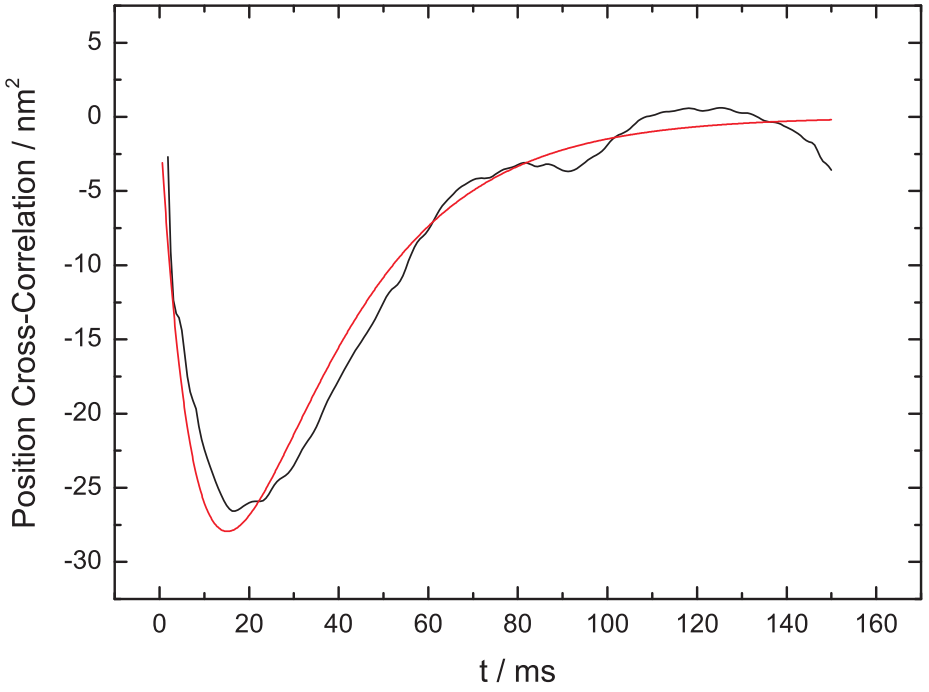


Figure 4.19: The experimentally determined cross-correlation function for a pair of melamine particles trapped 4.11 µm apart in ethylene glycol (black line), showing an anti-correlation at the longer time of around 20 ms due to the increased viscosity compared to water. The theoretically predicted curve is shown in red, demonstrating excellent agreement.

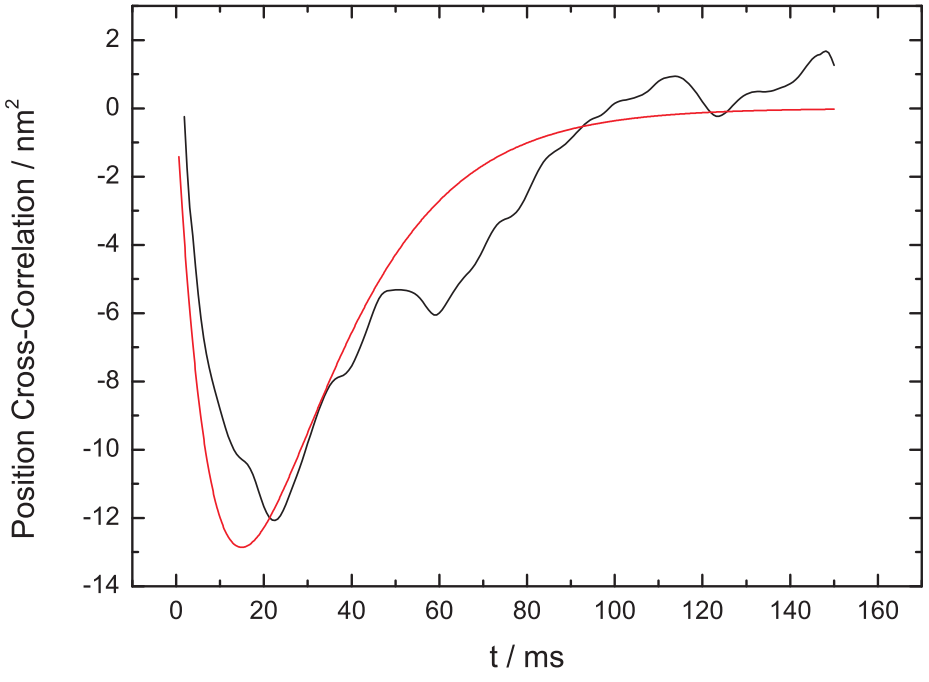


Figure 4.20: Transverse cross-correlation function for the same particles as shown in Figure 4.19. Despite the increased noise and reduced size of the effect in this direction, the anti-correlated dip can still be observed, with the depth of the cross-correlation function now half of that measured for longitudinal coupling as expected from Equations 4.8a and 4.8b.

The cross-correlation function for two melamine particles trapped at a separation of 4.11 µm in ethylene glycol is shown in Figure 4.19. The minimum of the anti-correlation now occurs at around 20 ms due the increased viscosity of EG. κ was determined to be 25 pN/µm from fitting to the autocorrelation decay, allowing Equation 4.7 to be plotted exactly (red line). Excellent agreement can be seen between the experimentally determined and theoretically predicted cross-correlation functions despite there being no variable fitting parameters.

While the cross-correlation functions presented so far have all been calculated along the longitudinal axis between the trapped particles, it can also be demonstrated along the transverse axis (in the image plane, perpendicular to the inter-particle axis), although the magnitude of the hydrodynamic coupling constant, ϵ, is halved in this case. Despite this Figure 4.20 illustrates the transverse cross-correlation function for the same two particles as shown in Figure 4.19. Despite the increased noise in this data, due to the reduced magnitude of the effect in this direction and the reduction in mechanical stability of the setup along this axis, the depth of the minimum still agrees well with that expected from Equation 4.7, with this value being close to half of that determined for longitudinal coupling.

Finally, the hydrodynamic coupling between pairs of particles in an IL will now be demonstrated, concluding the micro-rheological investigations presented in this chapter and again verifying the behaviour of the ILs as viscous Newtonian fluids. The cross-correlation function for two melamine particles trapped 5.53 µm apart in EAN is shown in Figure 4.21. The same analysis procedure is used as for the ethylene glycol results presented earlier, yielding a trap stiffness of 22.6 pN/µm and allowing the expected form to again be plotted in red with no variable fitting parameters. Excellent agreement is observed despite the increased mechanical noise issues which become apparent when working at these longer timescales.

The strength of the hydrodynamic coupling within the ILs again follows the expected trend with decreasing inter-particle separation, as can be observed in Figure 4.22 for two melamine particles trapped in [EMIM][Tf_2N]. In each case the expected theoretical form has also been plotted, showing excellent agreement in all cases except at the closest separation. This behaviour is expected to be due to the lack of independence of the optical traps at this distance.

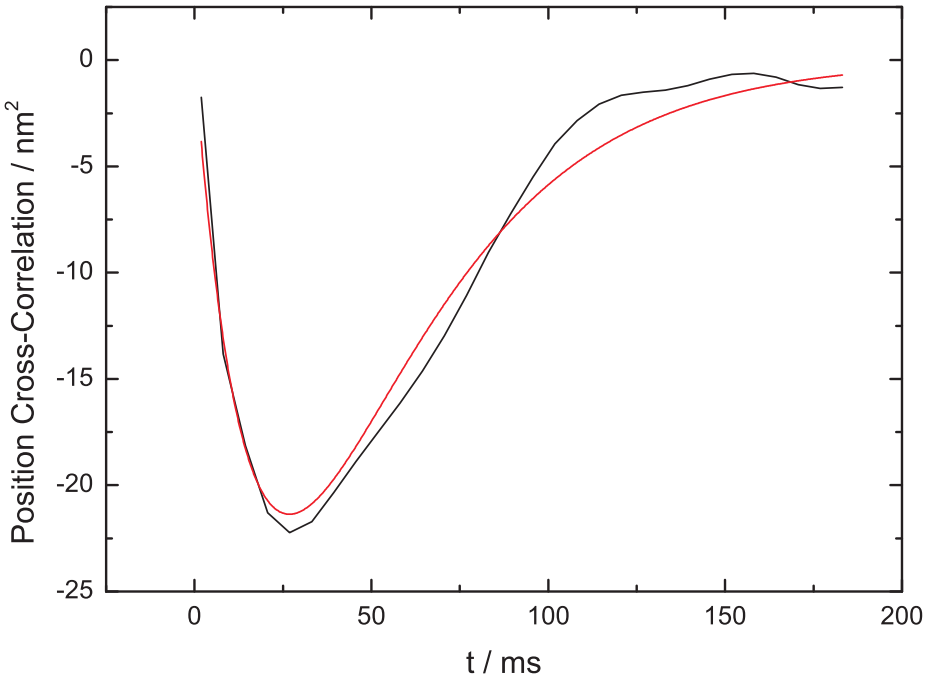


Figure 4.21: Experimental and theoretical cross-correlation functions for a pair of melamine particles trapped at a separation of 5.52 µm in EAN, showing excellent agreement.

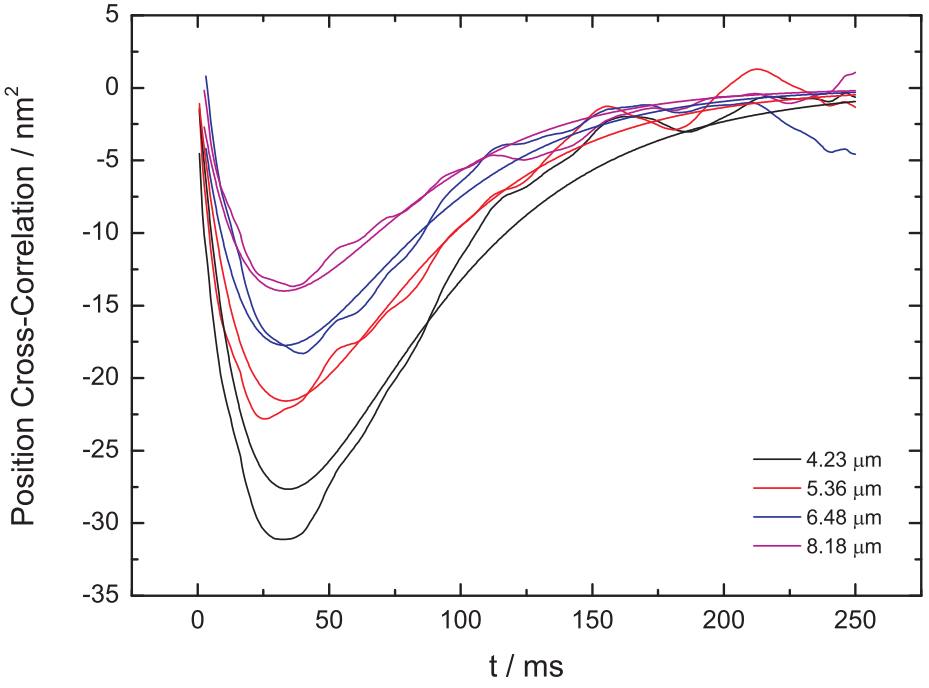


Figure 4.22: Cross-correlation functions determined as a function of inter-particle separation in [EMIM][Tf_2N]. Again, good agreement is observed between the experimental and theoretical curves in each case, with the only discrepancies seen at the closest inter-particle separation as the assumption of independent optical traps begins to break down.

4.5 Conclusions

In this chapter the applicability of optical tweezers as a tool for micro-rheological investigations of ILs has been clearly demonstrated. Initial experiments were performed using back focal plane interferometry particle tracking techniques and, after characterisation of the system, this method was used to explore the temperature dependent viscosity changes of two ILs, showing good agreement with the trends observed using macro-rheological techniques in each case.

Further work was then performed using a high-speed camera in place of the QPD, allowing trap stiffness determination with much greater accuracy as a result of reduced electrical noise, enhanced mechanical stability and improved data processing routines. Initially the temperature dependent viscosity experiment was repeated, showing the same trend as observed previously but with much reduced error and increased confidence in the viscosity values assigned in each case. This allowed the determination of the activation energy for viscous flow in EAN, in good agreement with literature values. Single particle studies on the increase in viscous drag experienced by a particle in close proximity to a plane surface were also conducted, showing excellent agreement with the values predicted using Faxén's Law.

Finally the high-speed camera was utilised for multiple particle trapping, and specifically a study of hydrodynamic coupling in media of differing viscosities. The hydrodynamic coupling measured between pairs of particles in water agreed well with previously published results and derived theoretical predictions. Trapping in ethylene glycol, EAN and [EMIM][Tf_2N] revealed hydrodynamic coupling over much longer timescales as a result of the increasing viscosities of these liquids. This was again in excellent agreement with theoretical predictions for coupling in both longitudinal and lateral directions, and at varying inter-particle separations.

Following these initial demonstrations of the use of optical trapping techniques for the micro-rheological investigation of ILs, there are many new potential studies and applications to be explored. The simplicity of the high speed camera setup allows investigations using a wide range of cell designs as long as they are sufficiently well illuminated for high frame rate capture. As well as including temperature controlled slides as demonstrated here, experiments investigating CO_2 capture and its effect on IL viscosity could easily be

performed with a suitable cell design, potentially also incorporating real-time optical spectroscopy. The technique also lends itself to further examination of the effect of impurities such as water on the physical properties of IL samples [118].

Chapter 5

Directed Assembly of Optically Bound Matter

In this chapter the optical binding of 3.5 µm diameter silica particles is studied. When placed within an evanescent field, formed by counter-propagating lasers, these particles spontaneously assemble into one-dimensional chains due to coherent scattering of the field. Using optical tweezers, particles can be controllably added and removed from the field allowing a detailed study of the structure and dynamics of this optically bound matter. In this chapter equilibrium configurations of these chains are determined and then compared with a model using an implementation of Generalized Lorentz-Mie Theory (GLMT).

5.1 Optical Binding

Optical binding is the name given to the generation of stable micro-particle configurations formed due to interaction of the micro-particles with a light field, first described in 1989 by Burns *et al.* [13]. In this work a pair of 1.43 µm diameter polystyrene particles in water were observed to be preferentially found at discrete inter-particle separations when exposed to laser illumination. These spacings, equal to multiples of the illuminating wavelength, were due to interference between light scattered by each of the particles and the incident wave, forming a series of potential wells. This early work was then extended to include the study of colloidal crystals formed by illuminating with multiple optical standing waves [119]. A key feature of optical binding is the modification of the light field by the presence

of each particle, where this inter-particle light scattering can result in the formation of ordered structures as well as complex dynamic behaviour.

Since the work of Burns *et al.* optical binding has been observed in a range of other experimental geometries. This has included counter-propagating Gaussian beams [120] and dual-beam fibre traps [121, 122], with stable one-dimensional optically bound matter observed in each case. Similar effects have also been observed in the optical trapping of micron-sized oil droplets in air, where optically bound droplets were seen to preferentially sit on the interference fringes arising as a result of the counter-propagating beam geometry [123]. Much longer one-dimensional chains of optically bound particles were also observed by Garcés-Chávez *et al.* when using a vertical Bessel beam, due to an interplay between optical scattering forces and the non-diffracting nature of the Bessel beam core [124].

A common geometry for these optical binding experiments is to use counter-propagating evanescent waves, formed by the total internal reflection of two laser beams incident on the surface of a prism. This arrangement builds on work by Kawata and Sugiura in 1992 who demonstrated the interaction of colloidal particles with an evanescent field formed by total internal reflection at a prism surface [125]. This evanescent field decays exponentially away from the surface but, if there is a particle close to the surface, may be converted to a propagating wave within the particle. Due to momentum transfer from the incident beam, colloidal particles were driven along the prism surface at velocities of up to 20 µm/s. Stable trapping has been demonstrated using focussed evanescent wave illumination [126], but can also be achieved by using two counter-propagating laser beams in order to balance this tangential radiation pressure [127]. The first observations of optical binding in these evanescent wave systems were reported by Mellor and Bain [14, 128], and Siler *et al.* [129, 130] in 2005. Further work has shown that these optical forces can be enhanced in several ways. For example by using resonant dielectric waveguides [131], surface plasmon resonance techniques [132], and by utilising an actively locked cavity [133].

In the experiments of Mellor and Bain, and Siler *et al.* sub-micron sized particles self assembled into ordered two-dimensional arrays. The formation of these arrays can be explained in terms of five forces acting upon the colloidal particles [134]:

- As it penetrates into the sample, the evanescent wave gives rise to a gradient force acting to attract particles towards the interface and constrain them in a plane parallel to the surface.

- Negative surface charges present on the particles result in electrostatic repulsion between themselves and between the particles and the silica prism surface.
- The weak focus of the Gaussian beam used to form the evanescent field results in a gradient force, acting to accumulate particles in the region of highest light intensity.
- The scattering of the field by each particle influences the field experienced by, and therefore the behaviour of, any other particles in the array, leading to complex multiple-particle scattering effects.
- The interaction of particles with interference fringes, formed due to the counter-propagating trap geometry, can be either attractive or repulsive and is a sensitive function of the particle size parameter. The nature of this interaction can be determined following the approach of Lekner [135] as will be described here.

The influence of interference fringes on the arrangement of optically bound matter will be most pronounced for smaller particles as the spacing between the interference fringes becomes significant compared to the particle diameter. The spacing between adjacent fringe maxima, D, is given by:

$$D = \frac{\lambda_0}{2n} \tag{5.1}$$

where λ_0 is the vacuum wavelength of the illuminating radiation and n is the refractive index of the medium. This expression is valid for counter-propagating beams or counter-propagating evanescent waves where $\theta_i = \theta_c$, where θ_i and θ_c are the angle of incidence and critical angle respectively. The value of D given in Equation 5.1 will be reduced by a factor of $\sin\theta_c / \sin\theta_i$ when the angle of incidence is not equal to the critical angle. For the experimental setup used in this work this fringe spacing is calculated to be $\sim 400\,\text{nm}$. As a result of this, the 3.5 µm diameter silica particles chosen for this initial work experience only a very weak interaction with the underlying interference fringes within the optical potential, meaning that the resulting structures are primarily determined by the interplay between the particles interacting with the evanescent field and the optical binding forces due to multi-particle scattering processes. These conditions facilitate a study of the optical binding interactions and allows direct comparison to the GLMT simulations presented later as the optically bound structures presented here can be discussed in terms of the evanescent field and scattering processes alone.

Various models have been used to try and explain the multiple particle scattering effects which are crucial in the formation of optically bound matter, including the coupled dipole method [136] and Generalized Lorentz-Mie Theory (GLMT) [137], typically dealing with only small numbers of particles due to the increasing complexity of the scattering processes involving larger numbers. These scattering effects become more important for longer chains and two-dimensional arrays with increasingly large numbers of particles [138], and the aim of this work is to try and bridge the gap between these simple model systems and the more complex structures which are observed. As a result, this chapter explores the optical binding of colloidal silica particles in a counter-propagating evanescent wave arrangement, with the addition of an inverted optical tweezers setup in order to facilitate controlled assembly of the optically bound chains. This has allowed the development of a GLMT simulation of the system through collaboration with Dr. Jonathan Taylor of The University of Glasgow, resulting in improved understanding of the factors responsible for the static and dynamic properties of this optically bound matter.

5.2 Experimental Setup

Figure 5.1 shows the experimental setup used for the optical binding experiments presented here and in the following chapters. The evanescent wave component of the setup is built around a silica glass isosceles prism with a critical angle, θ_c, of 66.7°. The prism is cut to an angle of 68° allowing focussing onto the top prism surface at an angle just above the critical angle, important due to the decrease in penetration depth of the evanescent field with increasing incident angle [139] and also to ensure that the finite beam size and focussing effects do not result in the formation of propagating waves. For the results presented in this chapter the output from a Laser Quantum Forte system (400 mW at 1064 nm) is coupled into a polarisation maintaining fibre splitter, ensuring an even power balance of 100 mW in each output beam. These beams are then counter-propagated and focussed onto the prism surface by 50 mm focal length lenses situated in x-y-z adjustable mounts. Two half-waveplates ($\lambda/2$) allow control of the polarisation of each beam, with p-polarised light used for the results presented here unless otherwise stated, as the force on the particles due to the evanescent field is expected to be greatest in this case [131]. The resulting light distribution at the surface consists of two spots which each have a major

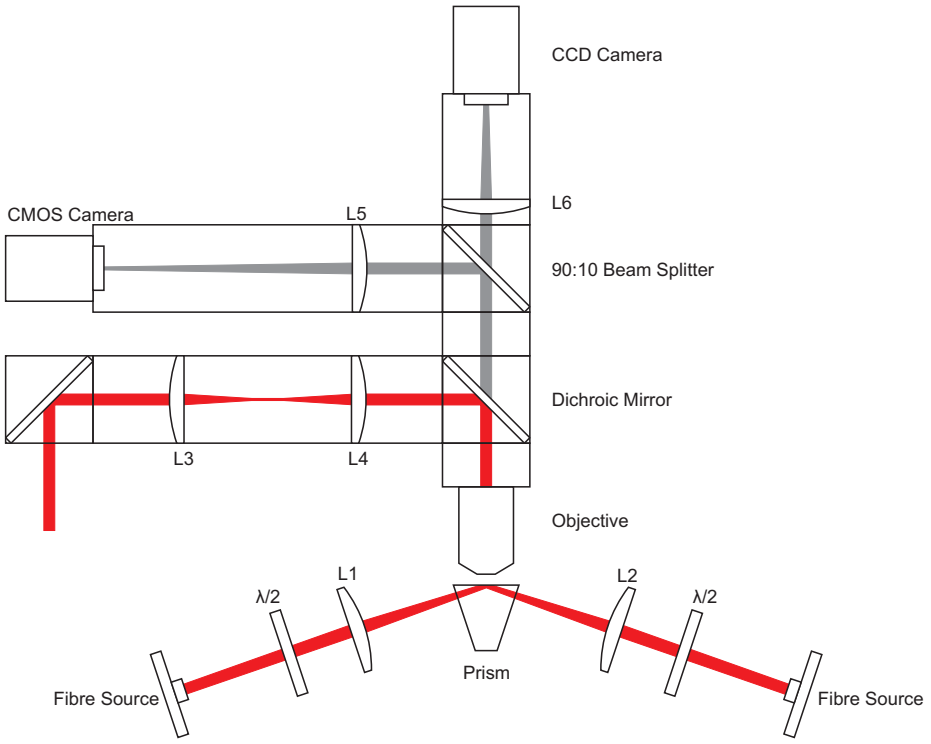


Figure 5.1: The experimental setup used for the optical binding work presented in Chapters 5, 6 and 7. Two 1064 nm laser beams are focussed onto the surface of a silica glass prism at an angle greater than the critical angle, forming two counter-propagating evanescent waves. An inverted optical tweezers arrangement allows directed assembly within the evanescent field. Imaging of the sample using a CCD camera is performed through the same objective by illuminating from below the prism, and the addition of a high-speed CMOS camera allows high frame rate particle tracking.

radius of 20 µm and are separated by 50 µm, giving a peak intensity contribution on the surface of 0.48 mW µm^{-2} from each.

A typical sample consists of either melamine or silica micro-spheres suspended in Milli-Q water (Millipore), with ∼10 µL pipetted directly onto the prism surface. A coverslip with a polyvinyl spacer is then placed on top, forming a sample with a lifetime of around 1 hour. The experiments in this chapter were performed using 3.5 µm diameter silica particles obtained from Bangs Laboratories (SS05N).

Direct manipulation of the particles can be achieved using the inverted optical tweezers arrangement shown in Figure 5.1. The tweezing source is a CrystaLaser (350 mW at 1064 nm), aligned into the back aperture of the imaging objective (Leica Hi-Plan, 100× NA = 1.2) using a $4f$ imaging system. Lenses 3 and 4, with focal lengths of 100 mm and 200 mm respectively, ensure overfilling of the back aperture of the microscope objective. A steering mirror allows movement of the optical trap within the focal plane of the objective, whilst

small changes to the trapping position along the z-axis can be achieved by altering the positions of L3 and L4.

Imaging of the sample onto a CCD camera (Watec, 902-H3) occurs through the same objective, and is achieved by illuminating from below the prism with a high intensity fibre light source (Thorlabs OSL1-EC). Particles can be tracked using either the CCD or high speed CMOS (Dalsa Genie HM640) camera.

5.3 Directed Assembly of Silica Particles in an Evanescent Field

5.3.1 Chain Building

Figure 5.2 shows two 3.5 µm diameter silica particles forming an optically bound dimer in the evanescent field. The two evanescent waves, converted into propagating waves within the silica particles, act to drive the particles towards the centre of the screen, while the

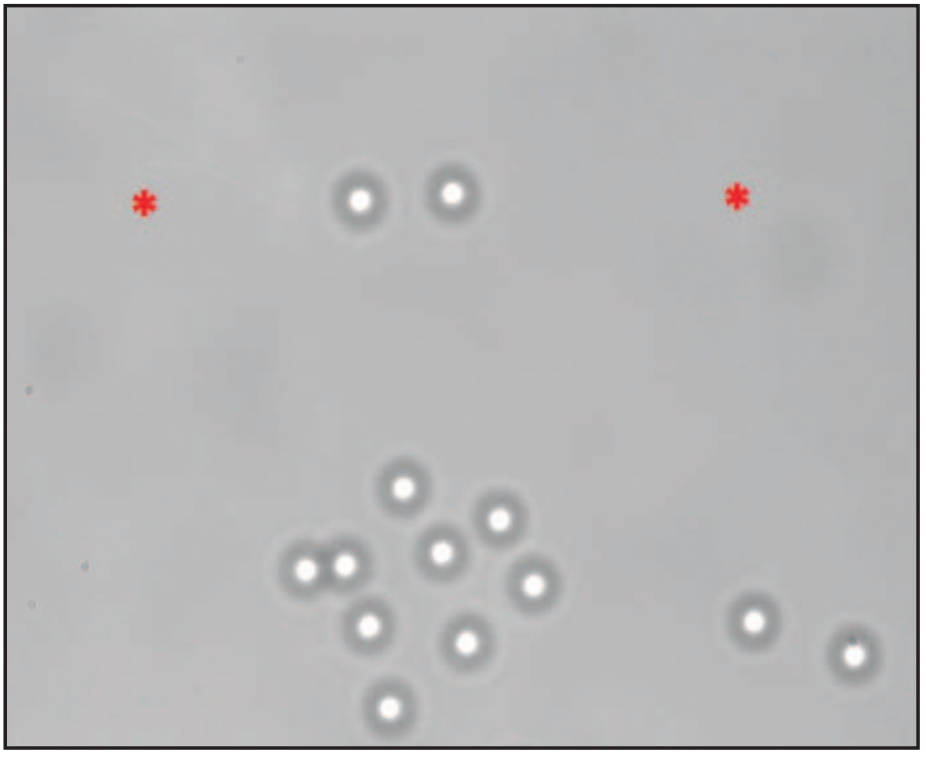


Figure 5.2: Two 3.5 µm diameter silica particles forming an optically bound dimer in an evanescent field (top of image). The red stars indicate the approximate positions of the centres of the two evanescent spots.

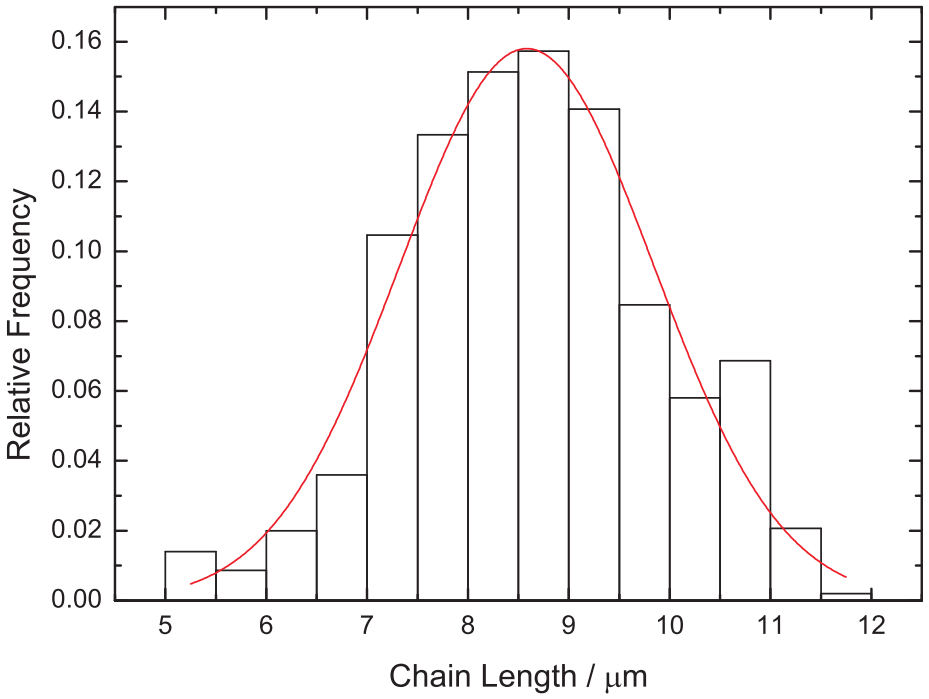


Figure 5.3: The experimentally determined variation in inter-particle separation for an optically bound dimer, showing a mean value of 8.6 µm and a standard deviation of 1.3 µm.

forward scattered light from each particle leads to a repulsion between them. The result is an optically bound dimer with an inter-particle spacing of around 9 µm, formed due to a balance of these forces. The approximate positions of the two evanescent wave spots are shown in red, with the optically bound particles sitting between these. The slight asymmetry observed in this particular frame is a result of the dimer diffusing within the optical potential, as will be explored further in Chapter 7. The freely diffusing particles in the lower half of the image are not affected by the evanescent field, and can be added sequentially to the chain as needed using the optical tweezers. By recording the positions of these particles over a period of one minute, after allowing time for the equilibrium separation to be reached, the average inter-particle spacing within the dimer is found to be 8.6 µm, with the actual chain length varying between 5 and 12 microns. The variation in separation is shown in Figure 5.3. A best-fit Gaussian distribution with a standard deviation of 1.3 µm is also shown.

The histogram presented in Figure 5.3 can be used to directly determine the optical potential, and therefore determine an effective "force constant" for the bond between the

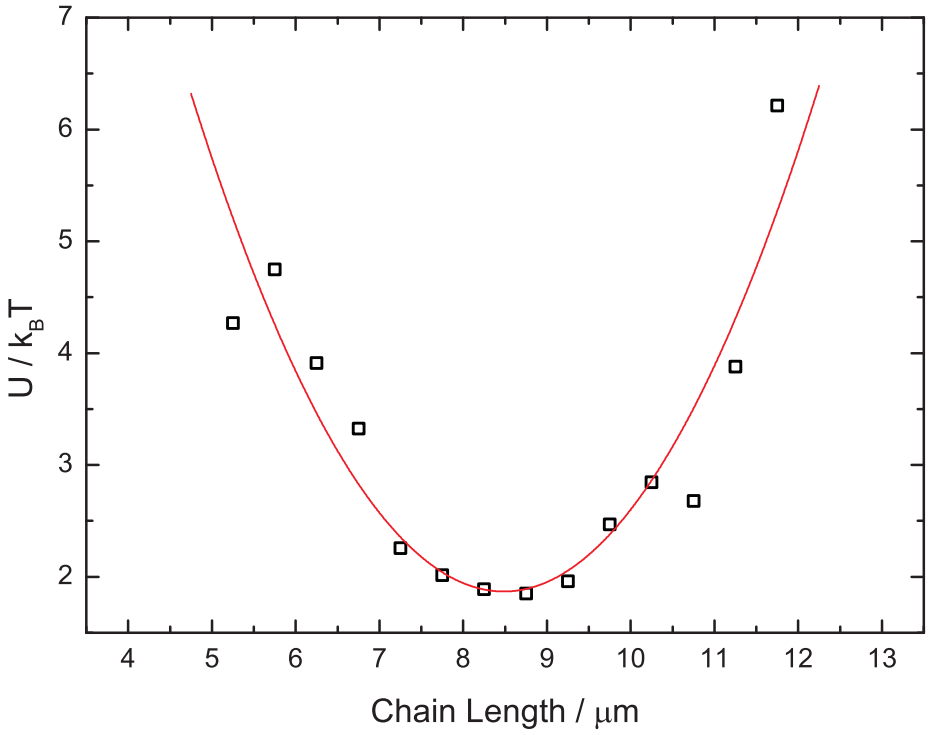


Figure 5.4: By inverting the dimer separation histogram shown in Figure 5.3 it is possible to determine the underlying optical potential in units of $k_{\mathrm{B}}T$ as shown here. A quadratic fit to the data, shown in red, returns an effective force constant of 2.6 fN/μm for the optically bound dimer.

constituent particles of this optically bound dimer. This can be achieved using the following expression:

$$\rho(r) = Z^{-1}\exp(-U(r)/k_{\mathrm{B}}T) \tag{5.2}$$

where $\rho(r)$ is a normalised histogram of dimer separations, r is the dimer bond length, Z is a normalisation constant and $U(r)$ is the optical potential as a function of inter-particle separation. This experimentally determined potential is shown in Figure 5.4, showing the expected quadratic form. A fit to this data, shown in red, yields an effective force constant of 2.6 fN/μm, approximately one-hundred times smaller than the value obtained in a typical optical tweezer trap.

The controlled addition of further particles into the evanescent field allows longer optically bound chains to be studied. In Figure 5.5 it can clearly be seen that the average inter-particle separation decreases significantly as more particles are added to the chain. This behaviour can be understood using similar arguments to those presented by Taylor and Love in their discussion of the optical binding forces acting on a one-dimensional chain within a counter-propagating Gaussian beam trap [137]. As the size of the particles being

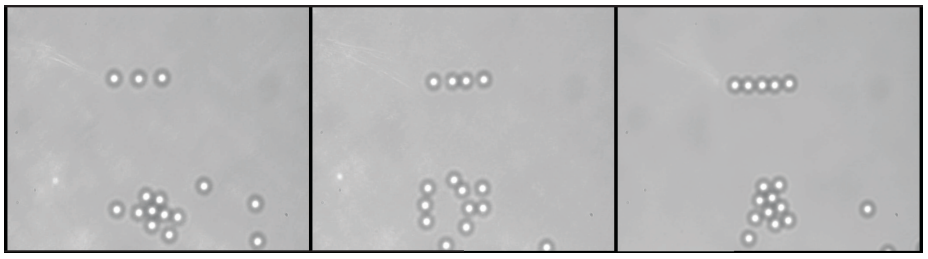


Figure 5.5: Controlled assembly of a one-dimensional chain of optically bound particles. Each screenshot is taken at least 1 minute after particle addition, allowing equilibrium separations to be reached. It can be seen that the inter-particle spacing decreases significantly with the addition of further particles, until complete chain collapse is seen when the fifth particle is added.

considered is large relative to the wavelength of the laser light, the binding forces in this case are dominated largely by forward-scattered light from each of the particles. The counter-propagating evanescent waves provide a balanced trapping potential which, when combined with the repulsive forces between the two particles as a result of forward-scattered radiation, explains the formation of a stable, spaced chain. Using symmetry considerations it is easy to visualise why the addition of further particles to the chain will result in a decrease in equilibrium separation. As an additional particle is added, the inwards force acting upon the adjacent particle is now increased, due to the additional scattered light incident upon it due to the newly added particle. Optical losses along the chain require the outwards force acting upon the second-to-last particle to be increased but by a smaller amount than that for the particle closest to the newly added particle, and so when both beams are considered the result is a necessary reduction in inter-particle spacing [137].

In addition, spontaneous *chain collapse* is observed when a fifth or occasionally sixth particle is added (Figure 5.5). This effect can be explained by considering the increasing compressive forces with additional particles in combination with the near-field attractive gradient force effects which act at small sphere separations. When the increasing compressive forces become large enough to overcome the repulsive forces from the forward-scattered radiation of adjacent particles, it is possible for the particle to overcome this potential barrier and enter the attractive regime associated with these smaller particle separations, and so form a stable, collapsed chain. This process is reversible, and removal of the fifth particle using the optical tweezers results in the chain separating to reform a spaced chain of four particles.

Average particle positions measured relative to the centre of the optically bound chain are

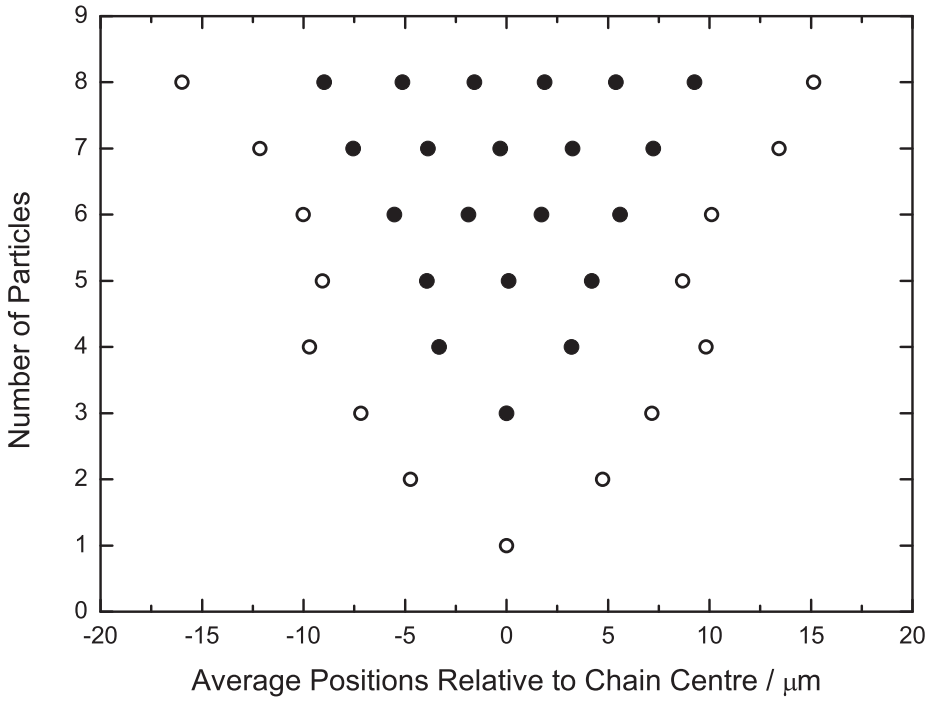


Figure 5.6: Average particle positions within an optically bound chain as a function of chain length, measured by sequentially adding additional particles to the chain and averaging positions over 30 seconds once equilibrium separations have been reached. Both the decrease in inter-particle separation towards the centre of any given chain, and the "chain collapse" as the fifth particle is added can clearly be seen. The standard deviation in each particle position is typically less than 1 µm, with the smallest values seen for the collapsed chains.

presented in Figure 5.6. The chain collapse as the fifth particle is added can be clearly seen, as well as a general reduction in inter-particle spacing with increasing numbers of particles. Furthermore it can also be seen that inter-particle spacing is not constant within a given chain but decreases towards the centre of the chain. This is seen for all chain lengths, and is demonstrated for a chain of six particles in Figure 5.7. Here the separation between adjacent particles is shown as a function of the position within the chain. The separation between particles 1–2, and 5–6 show an average value of around 4.5 µm, whereas this is reduced to around 3.6 µm, just slightly larger than the particle diameter, for the virtually collapsed central particles. This behaviour can also be understood using the previously described arguments of Taylor and Love [137]. By again modelling and balancing the forces acting on particles within a counter-propagating Gaussian beam trap they show that in order to achieve a symmetric force profile, required for a symmetric balanced chain, the inter-particle separations must vary along the chain with the central particles being more closely spaced; if the inter-particle separation is constant and the effects of a single beam are considered, the force acting inwards on the first particle is less than the force acting outwards on the

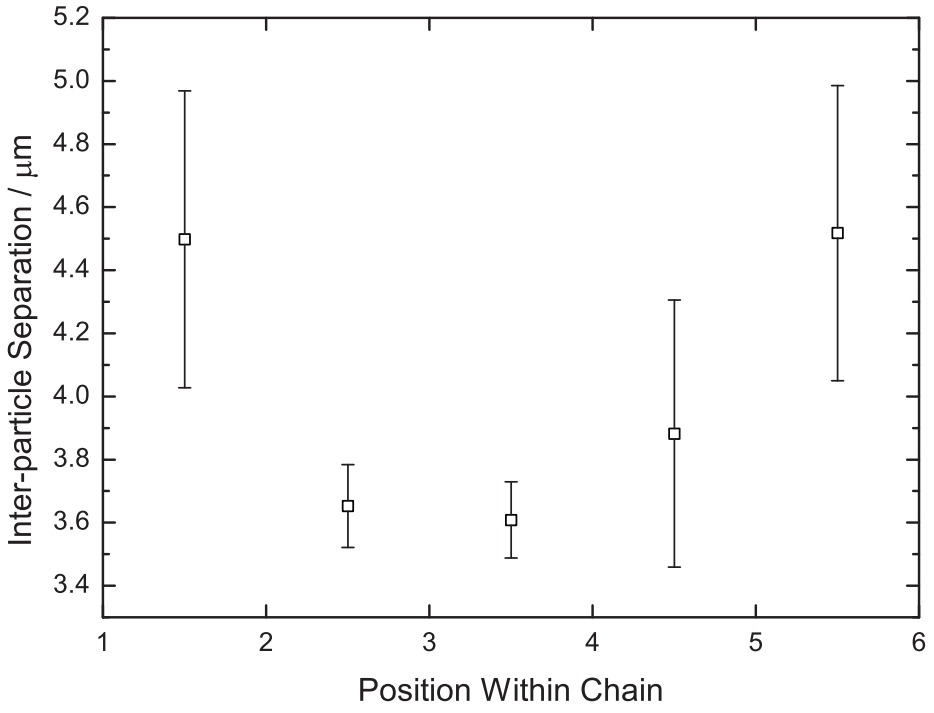


Figure 5.7: Average inter-particle separation as a function of position for an optically bound chain of six particles, where the first data point represents the separation between particles one and two and so on, while error bars give the standard deviation of inter-particle separation. The inter-particle separation can be seen to decrease towards the centre of the chain, with the standard deviation of these values also significantly decreasing, indicating tighter binding towards the chain centre.

final particle due to focussing and waveguiding effects along the chain. When both beams are considered this results in a separation of the outermost particles. Figure 5.7 also shows the standard deviation in inter-particle separation for this chain, represented by error bars, clearly showing the tighter binding and reduction in position variation seen at the chain centre.

Continued addition is possible up to eight particles, with these longer chains showing the same collapsed central portion and increased spacing towards the chain ends. Screenshots of these longer chains are shown in Figure 5.8. Stable, collapsed chains of six and seven particles are shown in (a) and (b), while very different behaviour is observed for the eight particle chain shown in (c). Instead of forming a chain aligned horizontally along the axis between the two evanescent wave spots, the chain immediately rotates on addition of an eighth particle while also exhibiting much increased chain drift. This chain tilt can be qualitatively explained by the expected increase in compressive forces acting on the end particles as the additional particle is added, and the increasing chain length compared to the range of the underlying optical potential, defined by the spot separation. As this chain

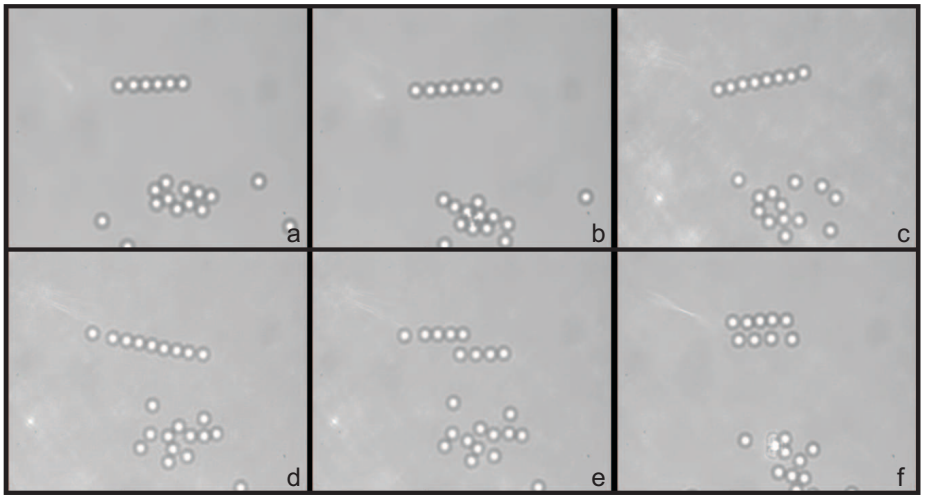


Figure 5.8: Screenshots showing the building of longer optically bound chains.
a-b: A stable chain of six and seven optically bound particles.
c: As the eighth particle is added, the chain exhibits immediate rotation and increased drift within the field.
d-f: Formation of a stable nine particle chain is not possible, as the chain spontaneously splits into shorter chains of four and five particles, which relax to their equilibrium positions towards the middle of the evanescent field.

length increases a chain aligned parallel to the axis between the two evanescent wave spots is no longer stable, resulting in a tilting of the chain axis. A further result of this is an increase in chain displacement, as will be presented in Chapter 7. Finally the addition of a ninth particle causes further rotation and almost immediate chain splitting (d–f). The nine particle chain splits to form chains of four and five particles, which then settle back into their equilibrium positions in the centre of the evanescent field (f) with an initial lateral separation between them of 5.1 µm, however these chains are short lived due to the limited perpendicular repulsive forces between them.

5.3.2 Factors Affecting Chain Length

Before comparison of these experimental results with a GLMT model, additional factors which may play a part in determining the behaviour of these optically bound chains must also be considered. Firstly, due to the much weaker optical forces being considered here when compared to those in typical optical tweezer traps (tens of fN's compared to pN's in optical tweezers), electrostatic repulsion between the colloidal particles must be included in any discussion of these structures. These effects were investigated by studying the formation of these optically bound chains in both Milli-Q water and a range of samples of varying

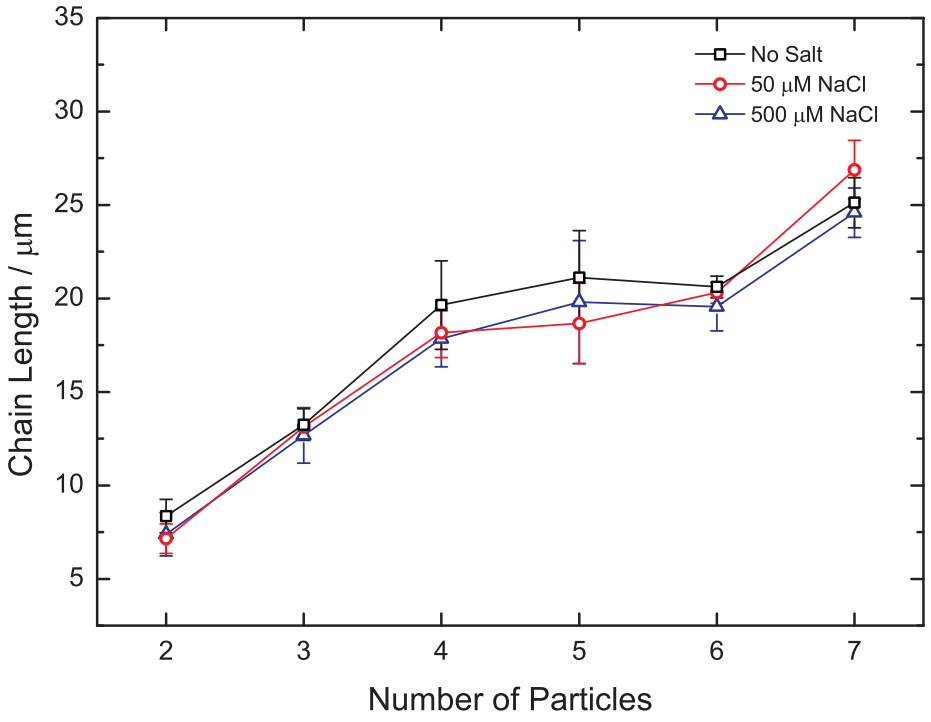


Figure 5.9: End-to-end chain length as a function of sample salt concentration. A small decrease in chain length can be seen for the salt samples, but as this reduction is smaller than typical variations observed for a given chain length, illustrated by error bars and due to the Brownian motion of the optically bound particles, electrostatic effects are deemed to not play an important role in the formation of this optically bound matter.

salt concentrations. Samples were prepared using $NaNO_3$ concentrations of up to 0.5 mM, giving Debye lengths ranging from $\sim 1\,\mu m$ for the Milli-Q sample, to 14 nm for the most concentrated salt solution. The results from three of these experimental runs are given in Figure 5.9, with the error bars representing the standard deviation in chain length in each case. A modest decrease in the chain lengths can be seen when using salt solutions, however this decrease is smaller than the variation in chain length seen within a given run due to Brownian motion of the bound particles, and also smaller than the typical variation seen between different runs with the same experimental parameters. As a result it is concluded that electrostatics do not play an important role in dictating the structure of this optically bound matter.

Further experiments were performed in order to investigate the effects of power on these equilibrium configurations. By using a higher powered laser as the evanescent wave source (Laser Quantum Ventus, 1064 nm) 200 mW was produced in each fibre output arm compared to the 100 mW previously used. By keeping all other experimental parameters the same the effects of this power increase were investigated, as shown in Figure 5.10. Results

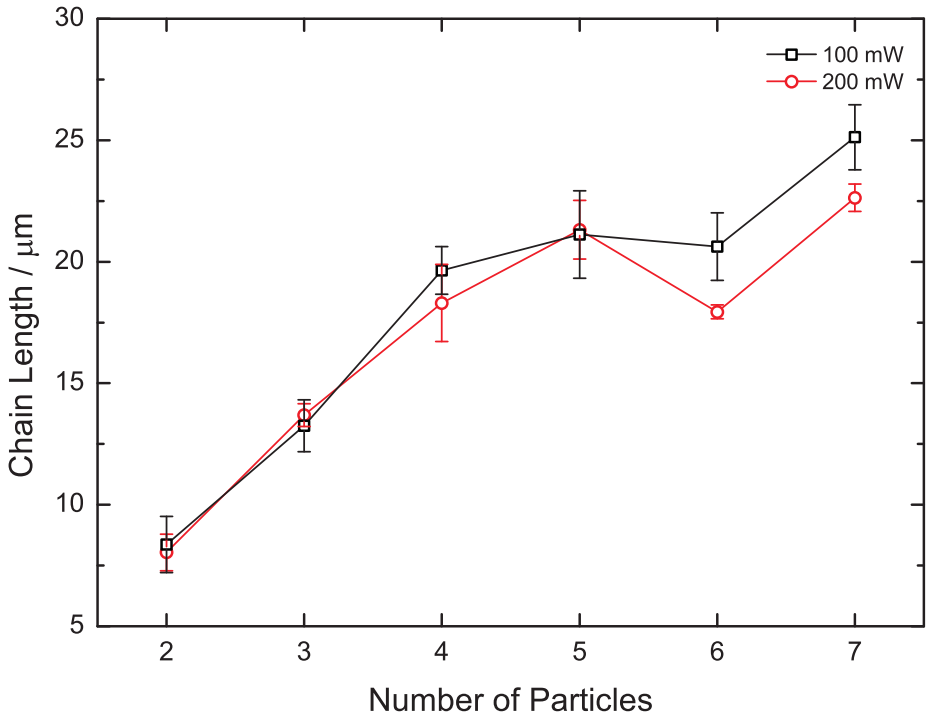


Figure 5.10: The effect of field strength on equilibrium chain length is determined by using a higher power laser source. The same trend is observed in each case, with a small decrease in chain length observed with the higher power source. In addition the stronger field results in much reduced chain length variations, illustrated by error bars.

show the same trend of decreasing inter-particle separation followed by chain collapse with the introduction of further particles. The data presented in the 100 mW case is the average chain length measured over several experimental runs, with the error bars showing representative standard deviation values taken from a typical run. The chain collapse is seen to occur at either five or six particles, and so the averaged plot shows a general transition at this point rather than the sharp collapse seen in a single run. The data for the lower and higher powers show very good agreement for the shorter chains, with the standard deviation in chain length decreasing markedly for the higher power case as would be expected due to the increased optical forces and tighter optical binding. In the stronger evanescent field chains made of the largest number of particles are more compressed, and a marked collapse at the addition of a sixth particle is seen. In addition, the longer chains show a much smaller separation between the outermost particles, with the six and seven particle chains being almost completely collapsed with very small chain length deviations.

Finally the Laser Quantum Ventus system was used to examine the effects of polarisation on these optically bound chains. This was done by rotating the polarisation of both input beams using the half-waveplates shown in Figure 5.1 in order to repeat the experiment

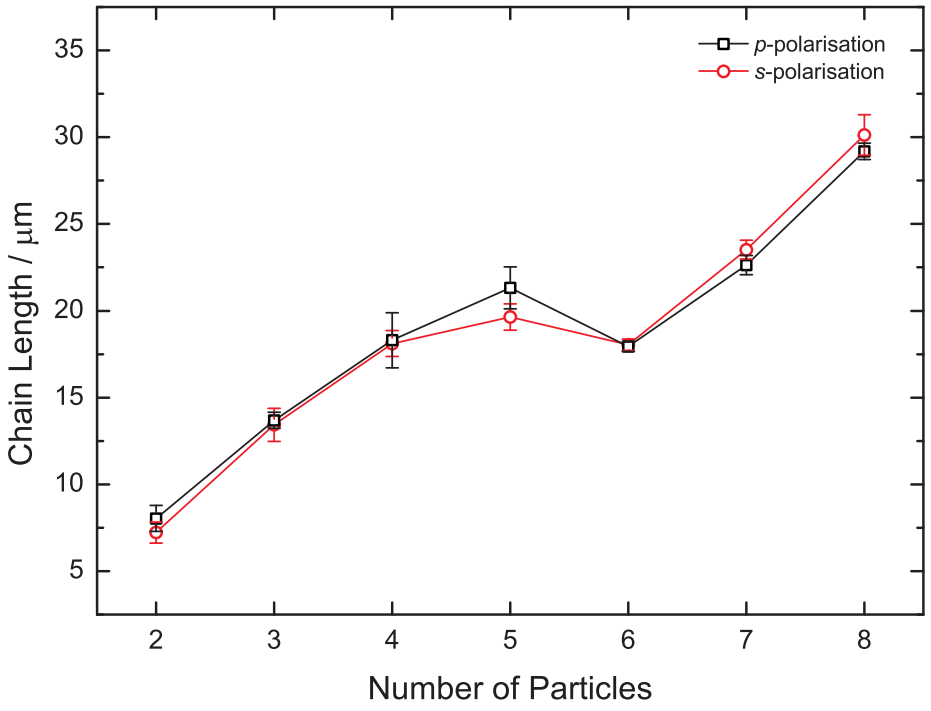


Figure 5.11: By rotating the polarisation of the two beams forming the counter-propagating evanescent waves, the effects of polarisation on the optically bound structures can be determined. The results are in good agreement, with any differences between them on the order of the standard deviation in chain lengths observed within a typical 30 second run, shown above by error bars.

with *s*-polarised light. A small increase in chain length was observed for the seven and eight particle chains when *s*-polarised light was used, as shown in Figure 5.11, suggesting a small decrease in the compressive optical forces, but it is noted that this chain length reduction is generally within the standard deviation of chain lengths seen within a typical run. In contrast to this, in the work of Kawata and Sugiura [125], particles were observed to move more rapidly when *s*-polarised light was used due to a stronger evanescent field being produced. More recently however Reece *et al.* [131] have presented results exhibiting a similar trend but with the stronger effect observed with *p*-polarisation. This result is in agreement with theoretical predictions showing that the force due to the evanescent field is greater for *p*-polarised light [140, 141] and is consistent with our findings.

5.4 GLMT Modelling of Optically Bound Chains

Collaboration with Dr. Jonathan Taylor at The University of Glasgow has allowed this experimental system to be modelled using an implementation of Generalized Lorentz-Mie

Theory (GLMT). While the approach is similar to that used in previous work [138], two additional factors have also been considered in this case. Firstly, there exists very little published work which takes full account of the Gaussian nature of the laser beam used to form the evanescent field by total internal reflection. This will clearly have important implications in the behaviour of our system and so must be included. For a broad laser spot it is possible to simply approximate the beam as an ideal evanescent wave, while if the spot is more tightly focussed the position dependant evanescent field experienced by the particle must be considered. This can be achieved by simply modifying the evanescent wave intensity experienced by a particle to be dependant on its position in the field, although this cannot account for behaviour such as the gradient force effects which will act to draw particles towards the centre of the laser beam spot. Alternatively a more rigorous approach, and the one used in this work, considers the Gaussian beam in terms of its plane wave spectrum and treats each plane wave separately as it interacts with the interface. Combining the resulting components yields the correct representation of the field on the far side of the interface.

For the work presented here the plane wave decomposition method of Khaled *et al.* has been used [142], allowing the interaction of each wave vector with the interface to be calculated [143] and its components represented by standard evanescent or plane wave expansions. While similar to the approach of Chang *et al.* [144], here the non-evanescent components of the incident beams are retained, as they can have significant effects when the angle of incidence approaches the critical angle. This approach works well except when very high numerical apertures are used, but for the spot sizes used in this work the approximations remain valid.

The second additional effect to be considered when modelling this system is that of surface reflections. As light scattered by a particle hits the prism surface it may be reflected, and this reflected light may interact with either the original or additional particles. As a result, the effects of these reflections must also be considered in a full theoretical model of our system. This is an extremely challenging problem, due to the planar interface and the spherical symmetry of the basis functions used in GLMT. A simple solution to this problem however is to approximate the planar surface as that of a large sphere. This enabled the effect of surface reflections to be established and, having verified their importance, the full reflection model was then used.

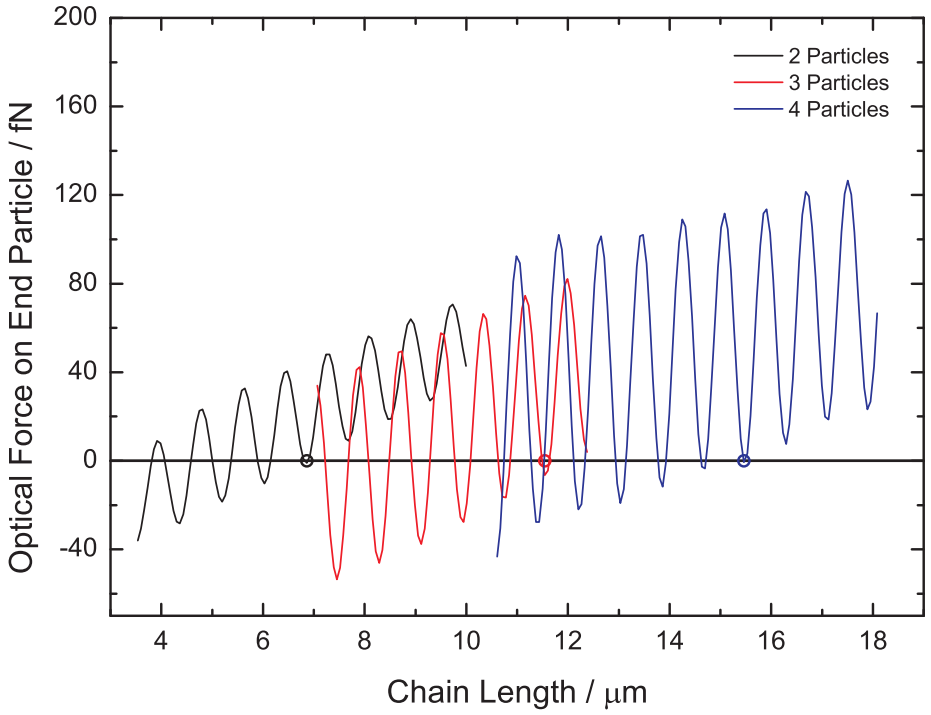


Figure 5.12: Calculated optical forces acting on the end particle within an optically bound chain. The stable chain length is given by the largest positive gradient intercept of the force curve with the x-axis, and is shown by an open circle in each case.

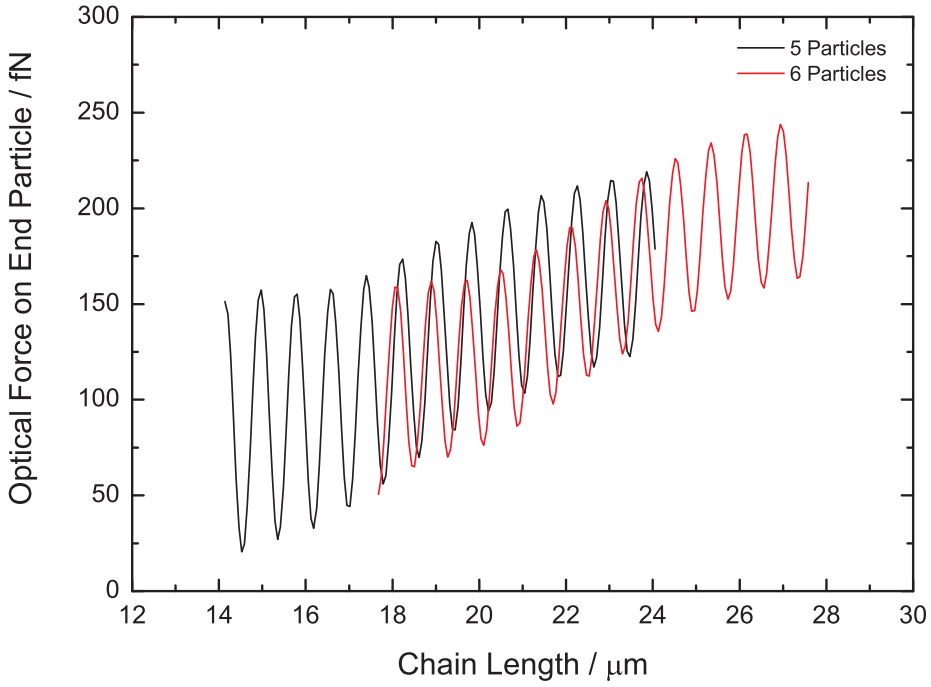


Figure 5.13: Calculated optical forces acting on the end particles in a collapsed chain of 5 and 6 particles, assuming the central particles are in contact as observed in experiment. The resulting positive forces, indicating compressive forces acting on each of the end particles, confirm that a completely collapsed chain is indeed stable.

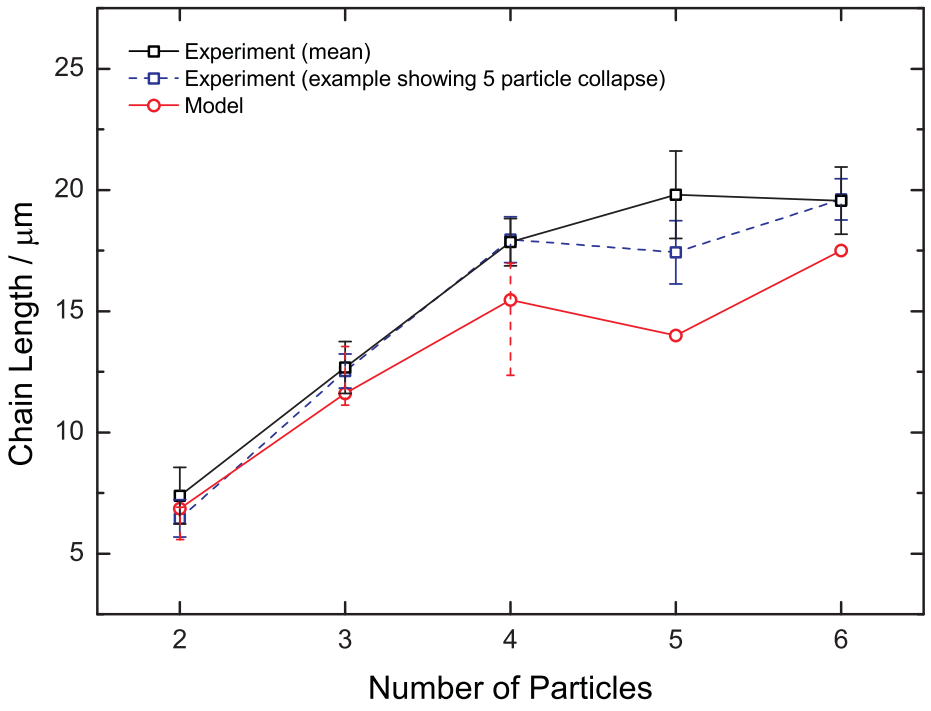


Figure 5.14: A comparison of experimentally determined equilibrium chain lengths and simulated values showing good qualitative agreement. The experimental values shown are the average of several runs and so do not show the sharp collapse at five particles as seen in the simulated data, as often a sixth particle is needed to initiate collapse. Data taken from a run where chain collapse was observed at five particles shows closer agreement with the predicted values. Error bars on the experimental data illustrate the standard deviation of chain length within an experimental run, while the error bars for the simulation results are calculated based on the potential uncertainties outlined in the text.

The results from these simulations are shown in Figures 5.12 and 5.13, where in each case the optical force acting on the end particle in an optically bound chain is shown as a function of the total chain length. For the two, three and four particle chains, shown in Figure 5.12, the stable equilibrium chain lengths are shown by an open circle. Although the simulation predicts multiple stable chain lengths, indicated by the positions where the force curves cross the x-axis with positive gradient, it is the largest of these which is used when comparing to the experimental work presented here. During the process of building these chains, particles are added at initially large distances from the trap centre and allowed to diffuse to their equilibrium positions. Because of the low laser intensities used, it is anticipated that the particles will have a low probability of crossing the potential barriers required to access the smaller equilibrium spacings, and so the kinetic product will be the largest chain length in each case. For the two, three and four particle simulations all of the inter-particle spacings were allowed to reach their equilibrium values. For the five and six particle simulations however, the increased number of degrees of freedom complicates

this challenging and time-consuming calculation. As a result the central particles in the five and six particle chains are assumed to be in contact with each other, as observed in experiment, and only the outermost particle separations allowed to vary. The resulting force curves, shown in Figure 5.13, are positive at all chain lengths, indicating that relatively large compressive forces act on the end particles in each case. This analysis confirms that a completely collapsed chain is stable for both five and six particle chains, though it is noted that other stable configurations may also exist.

In Figure 5.14 the GLMT simulation results are compared to the experimental results shown in Section 5.3. Good qualitative agreement is seen, with the simulation predicting stable, spaced chains of two, three and four particles, with complete chain collapse for chains of five or more particles. The experimental and theoretical results diverge at five particles, as the simulation predicts collapse at this point whilst in practise a sixth particle is often required to initiate this collapse experimentally. Data from a single example run, where collapse was seen on the addition of a fifth particle, is also shown, showing closer agreement with the simulation. The experimental results in Figure 5.14 are the average of several runs, with representative error bars indicating the typically observed standard deviation of chain length in each case. Error bars on the simulation results are estimated assuming a 5% potential uncertainty in sphere and illuminating spot radii, 1% uncertainty in the refractive index of the spheres and 0.2% uncertainty in the angle of incidence of the incoming beam.

5.5 Conclusions

In this chapter the optical binding of 3.5 µm diameter silica particles has been studied within a counter-propagating evanescent field. These particles are observed to spontaneously arrange into one-dimensional chains, largely as a result of an interplay between the underlying evanescent optical potential and forward-scattered radiation from adjacent particles. An inverted optical tweezers setup allowed directed assembly of this optically bound matter and an in depth investigation of their optically bound behaviour with changing particle number. A number of effects were observed including a reduction in inter-particle separation with the addition of further particles to the chain, and *chain collapse* which occurred as a fifth or sixth particle was added. These effects are similar to those observed in other experimental work including that of Taylor and Love [137], allowing them to be qualitatively understood

in terms of the forward-scattering of the incident field by adjacent particles in each case. In addition, sample salt concentration, optical power and polarisation were varied in order to investigate their influence on the resulting optically bound chains.

A collaboration with Dr. Jonathan Taylor allowed further investigation of the processes responsible for these effects using a theoretical model of the system, developed using an implementation of Generalized Lorentz-Mie Theory (GLMT). This model successfully predicted the occurrence of stably spaced chains of silica particles, up to a critical number of five particles where chain collapse was observed, in excellent agreement with experimental results. In addition, good numerical agreement was observed between experiment and theory, validating the discussion of the factors responsible for the optically bound structures observed. Having successfully investigated and explained the equilibrium behaviour of optically bound silica particles, the next chapter will present a discussion of the effects of particle size and of refractive index on the resulting structures of this optically bound matter.

Chapter 6

Exploring the Effects of Particle Diameter and Refractive Index on Optically Bound Matter

In the previous chapter the optical binding of 3.5 µm diameter silica particles was studied, and then described using an implementation of Generalized Lorentz-Mie Theory. For these particles the optically bound chains are formed largely due to an interplay between two effects; the underlying optical potential formed due to the counter-propagating evanescent waves, and the forward-scattered light from neighbouring particles. There are, however, other effects to consider including particle interaction with interference fringes, formed due to the counter-propagating geometry and initially described in Section 5.1. For the 3.5 µm diameter particles previously studied, their large diameter relative to the spacing of these fringes (~ 400 nm in this case), means that the interference has minimal influence on the resulting optically bound structures. The effect of these fringes and their influence is expected to change significantly with particle size, and will be most important for those particles up to around half a wavelength in diameter. These effects will be investigated in the first half of this chapter, comparing optically bound chains of smaller diameter silica particles ($n_p = 1.405$, $d = 1.5$ and 1.0 µm) to the results presented in Chapter 5. Although the diameter of these particles is still larger than the spacing between interference fringes, the increasing importance of these fringes in dictating the optical bound structures can be readily seen. Another factor which is expected to play a large role in determining these

structures is that of the refractive index of the particle. In the second half of this chapter the effect of changing refractive index is explored by investigating the optical binding of melamine particles ($n_p = 1.68$, $d = 2.31\,\mu\text{m}$), again comparing to the results presented in Chapter 5.

6.1 Changing Particle Size

6.1.1 Quantifying the Effect of Interference Fringes

The interaction of a spherical scatterer with counter-propagating electromagnetic beams can be understood in terms of a *force factor*, A, which quantifies the effective area for momentum transfer to the sphere, and is given by:

$$A = \frac{16\pi}{k^2}\sum_{l=1}^{\infty}(-)^l \text{Im}\left\{\frac{l(l+2)}{l+1}(a_l^* a_{l+1} + b_l^* b_{l+1} + \frac{2l+1}{l(l+1)}a_l^* b_l\right\} \tag{6.1}$$

where $k = 2\pi/\lambda$, and a_l and b_l are Mie-Debye coefficients [135]. Three examples of this oscillatory function are shown in Figure 6.1, for silica, polystyrene and melamine particles. In each case a positive value of A relates to a preferred position on an intensity maxima, while a negative value shows a preference for an intensity minima. It can also be seen that for some particle sizes the resulting force on the sphere due to the presence of the fringes is zero.

Using Figure 6.1, the force factor quantifying the interaction of these spherical particles with the counter-propagating beams can calculated. For both sizes of silica particles used in this chapter $A \sim -0.013$, where $A_{\text{max}} \sim 0.07$, meaning that both particle types should show a similar preference for sitting between the interference fringes, although this effect is likely to become more important for the smaller silica particles as the particle diameter and fringe spacings become comparable.

6.1.2 1.5 µm Silica Particles

In order to explore the effect of changing particle diameter on optically bound matter formation, experiments were conducted using both 1.5 µm and 1.0 µm diameter silica particles. The same experimental setup detailed in Figure 5.1 was used, in conjunction with the Laser

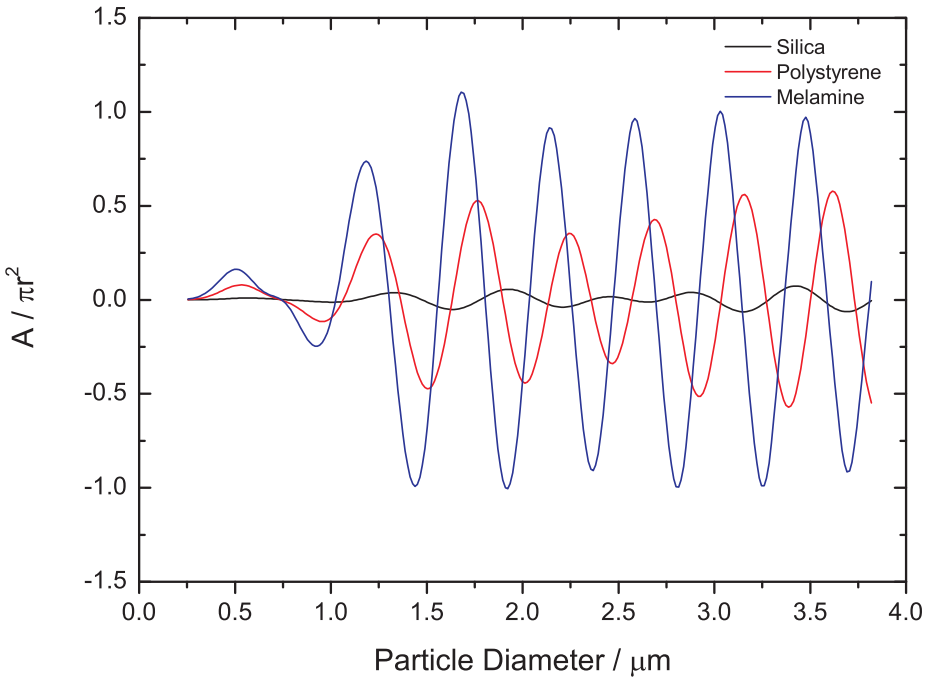


Figure 6.1: The effective area for momentum transfer to a scatterer in the presence of counter-propagating electromagnetic beams, evaluated using Equation 6.1. This factor has been calculated for three particle types, and is a sensitive function of particle diameter. In each case a positive value indicates a preference for a particle to be located on the interference fringes, whereas a negative value indicates the particle prefers to sit at the intensity minima.

Quantum Ventus source, giving 200 mW in each fibre output arm. Chains were built up in the same way as before using an inverted optical tweezers assembly.

Figure 6.2 shows an optically bound chain of eight 1.5 µm diameter silica particles being assembled. There are several differences to note when comparing these chains to those of the 3.5 µm diameter silica particles previously studied. These include:

- Chain collapse is not observed for chains of two – eight particles,
- Inter-particle separations do not vary smoothly as a function of position within a given chain,
- Increased off-axis particle displacement is observed.

These effects can all be qualitatively understood in terms of the increased relative importance of fringe effects in determining the positions of these optically bound particles. Despite still being significantly larger than the expected fringe spacing, the reduced size of



Figure 6.2: An optically bound chain of 1.5 µm diameter silica particles is assembled using an optical tweezers setup. Stable chains are observed but, unlike the 3.5 µm diameter particles shown in Chapter 5, chain collapse is no longer seen. These effects, as well as the increased off-axis displacement which is observed, can all be understood in terms of the increasing importance of interference fringes in determining the optically bound structures of these smaller particles.

the 1.5 µm diameter particles means that these fringes will start to play more of a role in dictating the arrangement of these optically bound structures.

The key factor responsible for chain collapse occurring in an optically bound chain is the growing compressive forces acting on the particles, resulting from the increased forward-scattered radiation as additional particles are added. For the chains presented in Figure 6.2 the relative effect of this forward-scattered radiation is reduced and the particle positions are more a result of the underlying interference fringes, explaining why chain collapse is no longer seen in this case. The increased contribution from the interference fringes also explains why the inter-particle separations no longer vary smoothly throughout the chain, as would be expected if these were determined solely by the forward-scattered radiation. In addition to this it can be seen that the particles are less well confined to the chain axis, as will be quantified in Chapter 7 where the dynamics of these optically bound arrays will be studied. Again, this chain axis confinement is largely due to the forward-scattered radiation from adjacent particles, and so will again be reduced for this smaller particle size.

By plotting the chain length as a function of particle number, an approximately linear trend can be observed. This is shown in Figure 6.3 for optically bound chains formed using p-polarised counter-propagating beams. In addition to this, end-to-end chain lengths are

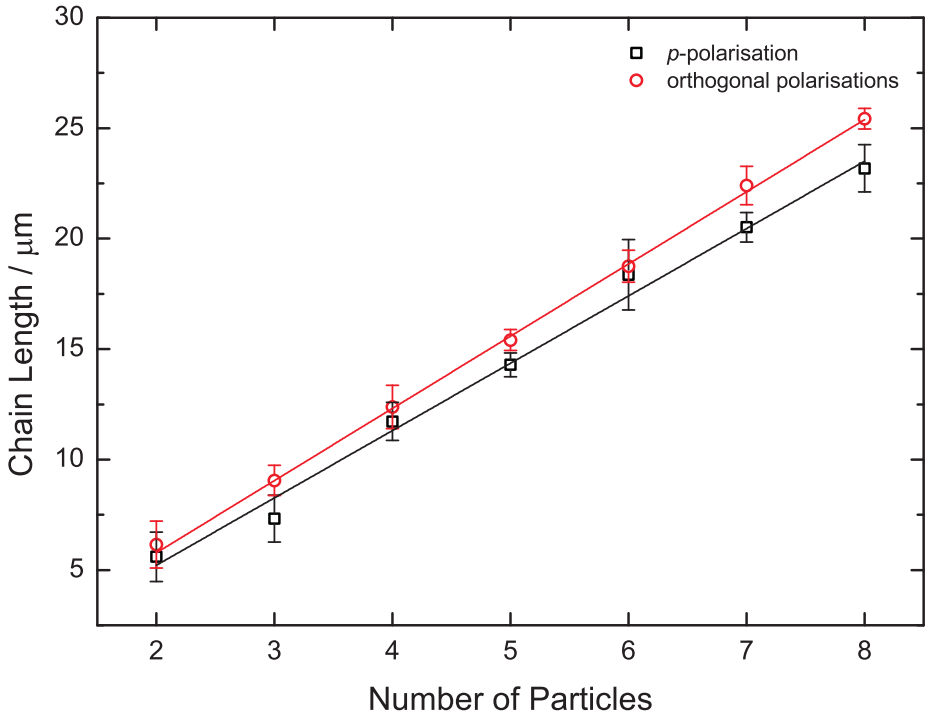


Figure 6.3: An investigation of chain length with particle number reveals an approximately linear trend in this case as would be expected when particle spacings are dominated by equally spaced interference fringes. Chain length is also shown when orthogonal polarisations are used in order to remove these fringes, showing a consistent increase in chain length.

also shown when the polarisation of one of the input beams has been rotated such that the two counter-propagating beams are orthogonal. A small, consistent increase in chain length can be observed in this case, indicating the larger compressive forces operating with p-polarised radiation.

This interpretation is corroborated in Figure 6.4 which shows a histogram of inter-particle spacings for the eight particle chain, for both p and orthogonally polarised light. The p-polarisation data clearly shows the effect that the interference fringes are having on the inter-particle spacings. Several maxima are clearly seen, spaced approximately 400 nm apart as expected, as each particle prefers to sit between the interference fringes. In contrast, for the orthogonally polarised light, a much smoother probability distribution is seen, illustrated with a best-fit Gaussian function (red dashed line). Some residual effects due to the interference fringes can still be seen, at spacings consistent with those seen for the p-polarised case, due to imperfect polarisation of the beams. This may result from the sensitive alignment of the two half-waveplates in the beam arms or the fibre outputs not being perfectly polarised. The dominant effect in determining inter-particle separations

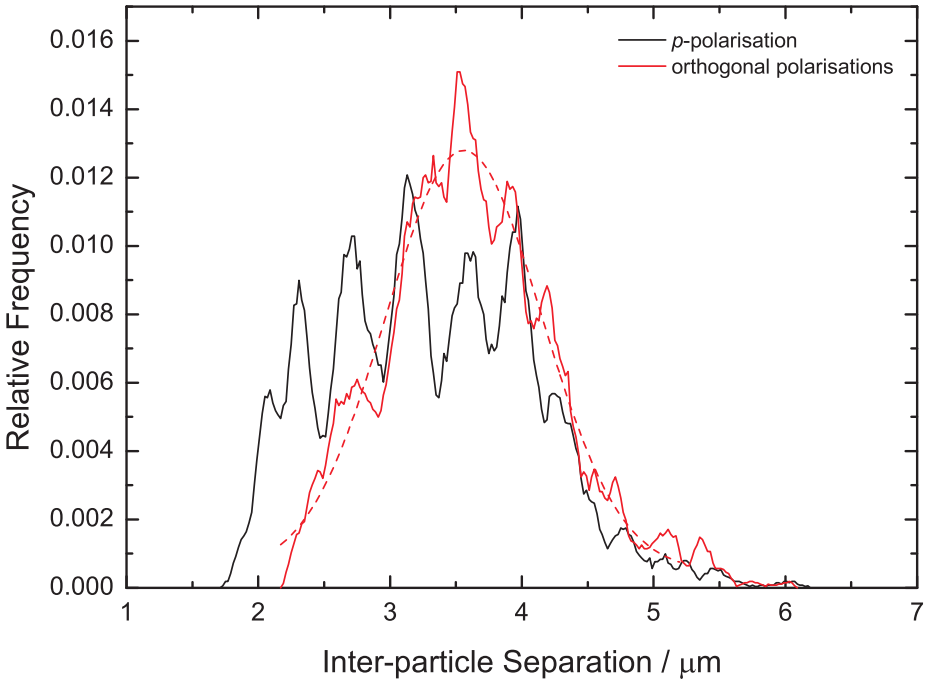


Figure 6.4: Inter-particle separation histograms are shown for both p-polarised and orthogonally polarised trapping beams. The orthogonal data shows a distribution formed largely due to an interplay between forward-scattered radiation and the underlying evanescent field, giving a preferred spacing of around 3.5 µm. When the effects of interference fringes are considered with the p-polarised beams, clear peaks can be seen in the distribution, with spacings consistent with the fringe spacing. In addition the presence of these fringes enables particles to access closer separations than would otherwise be observed, explaining the decrease in chain length seen in Figure 6.3.

when using orthogonally polarised light is now the forward-scattered radiation, leading to a preferred spacing of around 3.5 µm, similar to that obtained for the collapsed eight particle 3.5 µm diameter silica particles. The distributions for the 1.5 µm diameter particles follow a similar form at higher inter-particle separations for both polarisation geometries and only differ at smaller distances, as the particles in the p-polarised field experience forces due to the interference fringes which allow them to access smaller inter-particle separations than would otherwise be observed, as well as the larger compressive forces experienced when both beams are p-polarised. This shift in the distribution at smaller separations explains the general decrease in average chain length which is observed when trapping with p-polarised beams.



Figure 6.5: An optically bound array of 1.0 µm diameter silica particles.

6.1.3 1.0 µm Silica Particles

When the particle size is reduced still further, and the formation of optically bound matter of 1.0 µm diameter silica particles is studied, the increased importance of the interference fringes becomes even more apparent. Stable one-dimensional chains can still be formed, with particle positions again dominated by the presence of these fringes. When more concentrated samples are used, the silica particles can be seen to form optically bound *arrays*, in preference to multiple or longer chains. These arrays are similar to those observed by Mellor *et al.* using sub-micron polystyrene spheres [14]. An example of one such array is given in Figure 6.5. The array is elongated in one-dimension, but now also shows particles arranging perpendicular to the beam-axis.

Using a MATLAB centroid-tracking script, the positions of each of these particles can be determined to sub-pixel accuracy, allowing the arrangement of this array to be closely studied. This tracking is performed for the central, two-dimensional portion of the array shown in Figure 6.5. By taking the particle coordinates along the beam-axis, these positions can be compared to the expected fringe pattern. This analysis is shown in Figure 6.6, where the white lines represent particle positions along the beam-axis, while the sinusoidal function shown in red represents the expected fringe pattern, with a fringe spacing of 395 nm determined *via* Equation 5.1 with a small correction to account for the fact that $\theta_i \neq \theta_c$. It is expected that these particles will prefer to sit between the fringes, due to their negative force factor, and it can be seen that their positions show excellent agreement with this fringe spacing. Each fringe spacing accommodates a single particle, explaining the array structure shown in Figure 6.5.

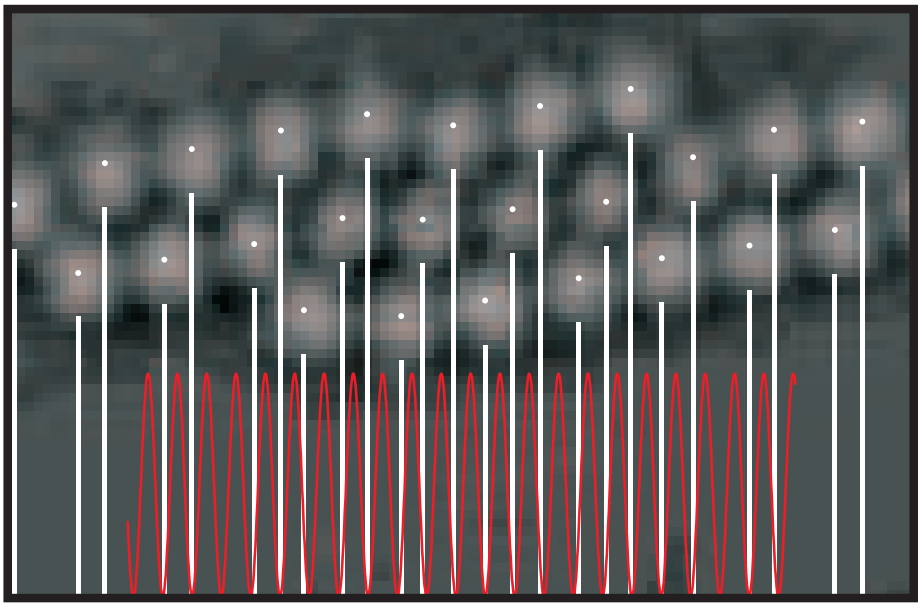


Figure 6.6: A close up of the array shown in Figure 6.5 with white data points indicating the particle coordinates determined using a centroid tracking routine. The sinusoidal function in red shows the expected fringe pattern, while the white lines relating to the position of each particle along the beam axis demonstrate that the structure of this array can be explained by the particles preference to sit between these fringes.

6.2 Changing Particle Refractive Index

In the second half of this chapter the effect that changing particle type has on the optically bound structures that are observed will be explored, by comparing structures formed using 2.31 µm diameter melamine particles to the results already presented. These particles have a refractive index, n_p, of 1.68, significantly larger than the value of 1.405 for the silica particles. This is expected to have an appreciable effect on the interaction of these particles with the optical field, due to the increased refractive index contrast between the particles and the medium, as can be seen from the much larger $A_{\max}$ values in Figure 6.1. In addition, these melamine particles are less dense than the silica particles, ($\rho_{\text{melamine}} = 1.51\,\text{g/cm}^3$, $\rho_{\text{silica}} = 2\,\text{g/cm}^3$), which will result in a difference in gravitational height of the two particles, defined as $h_g = k_\text{B}T/m_b g$ where m_b is the buoyant mass of the particle and g the gravitational field strength. The gravitational height for the 2.31 µm diameter melamine particles is still significantly smaller than the particle diameter however ($h_g \sim 0.05d$), indicating that this reduced density will not have a large impact on the equilibrium height of these particles and therefore the strength of the evanescent field which they experience. Finally the melamine particles will have negatively charged surfaces in solution, due to their

surface COOH functionalisation, introducing additional repulsive interactions between the particles and the prism surface, and between the particles themselves.

Experiments were conducted using the same experimental setup as presented and described in Figure 5.2, except that two separate fibres and laser sources were used in this work (Laser Quantum Forte and CrystaLaser, both at 1064 nm) giving a maximum power output of 130 mW in each arm. The Laser Quantum Torus (532 nm) was utilised as the tweezers source. Optically bound chains of particles were assembled using the optical tweezers as before, and screenshots of these stable structures are shown in Figure 6.7. Stable chains of up to five optically bound particles were assembled, while chains of six particles split and separated into shorter chains in a manner reminiscent of the behaviour of the nine particle 3.5 µm diameter silica chains in Chapter 5. For some particle numbers there exist multiple stable conformations which are interchangeable using the optical tweezers. These forms were observed for three and four particle chains, as shown in Figure 6.7, and represent two equilibrium conformations which are not seen to inter-convert without intervention. The main observations relating to these structures are as follows:

- Stable structures can be formed for chains of up to five particles, beyond this the chains are unstable,
- Multiple stable forms exist for some particle numbers, including collapsed and separated three particle chains,
- Four optically bound particles can also exist in at least two conformations, with a stable collapsed chain, and a chain consisting of a collapsed trimer and one satellite particle,
- If the most compressed optically bound conformation is considered in each case the different regimes observed with changing particle number mirror that observed with the 3.5 µm diameter silica particles, as will now be explained.

When the directed assembly of 3.5 µm diameter silica particles was presented in Chapter 5, the optically bound chains initially consisted of separated forms for two – five particles, collapsed chains for five – eight particles with increased separation of the outermost particles in the longest of these chains, and finally rotation and splitting of the optically bound chain on the addition of a ninth particle. This behaviour can be seen to be followed for the 2.31 µm



Figure 6.7: Screenshots showing one-dimensional chains of optically bound 2.31 µm diameter melamine particles in the evanescent field. Multiple stable conformations are seen to exist for chains of three and four particles.

diameter melamine particles shown in Figure 6.7. Initially a two particle dimer is formed, which cannot be converted into a collapsed form using the optical tweezers. On addition of a third particle either a stable separated trimer is observed, or a completely collapsed chain of three particles, depending on the insertion location of the third particle. If inserted several particle diameters away from the chain end the result is the separated form, while insertion from either above the chain or from a position adjacent to one of the end particles results in the collapsed trimer. This collapsed form is maintained for the four particle chain, with an additional longer form also observed dependent on the position of the newly added particle as before. Finally, for the five particle chain, the two outermost particles are seen to be separated from the chain ends, in a manner similar to that observed for the longer 3.5 µm diameter silica chains.

In order to discuss the factors responsible for the behaviour of these melamine particles in the evanescent field, first the effects of the underlying optical fringes will be examined. This can again be understood in terms of the force factor, A, quantifying the effective area for momentum transfer to the particle as shown in Figure 6.1. While a similar, oscillatory form as a function of particle diameter is observed for the three particle types shown, the magnitude of these oscillations is significantly increased for particles with a larger refractive

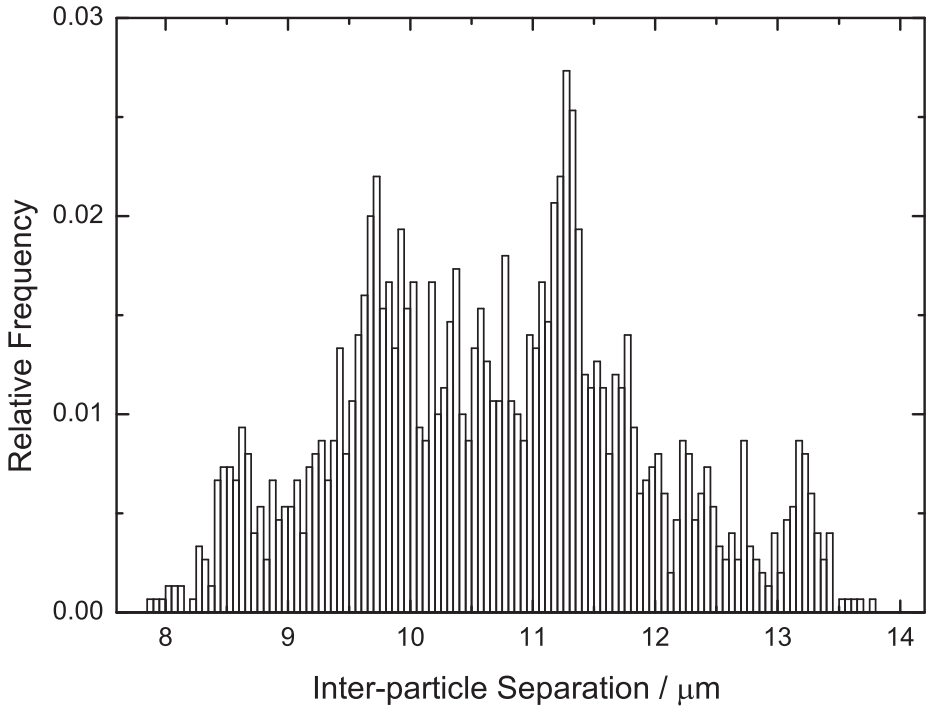


Figure 6.8: Inter-particle separation histogram for the two particle dimer shown in Figure 6.7, showing limited evidence of effects due to interference fringes as expected.

index. This results in the 2.31 µm diameter melamine particles having a large, negative A factor of around -0.7, indicating a preference for sitting between the interference fringes. This is not, however, expected to have a large effect on the observed optically bound matter due to the small size of the fringe spacing ($\sim$ 400 nm) when compared to the particle diameter.

Insight into the impact that these fringes are having on dictating the optically bound structures can be gleaned by looking at particle positions in the field, and inter-particle separations, and seeing if any evidence of preferential positions or spacings are observed. In both cases minimal structure due to the fringes is observed, as shown in Figure 6.8 for the inter-particle separation in the optically bound dimer, indicating that the presence of these interference fringes is not a key effect in the discussion of this optically bound matter as anticipated.

For each of the optically bound structures observed, end-to-end chain lengths were recorded for a period of 2 minutes after allowing the particles to reach their equilibrium conformations. These chain lengths are given in Figure 6.9, with error bars calculated from the standard deviation of these values. The values for the most compressed forms are shown in black, clearly showing the chain collapse observed at three particles and then increasing

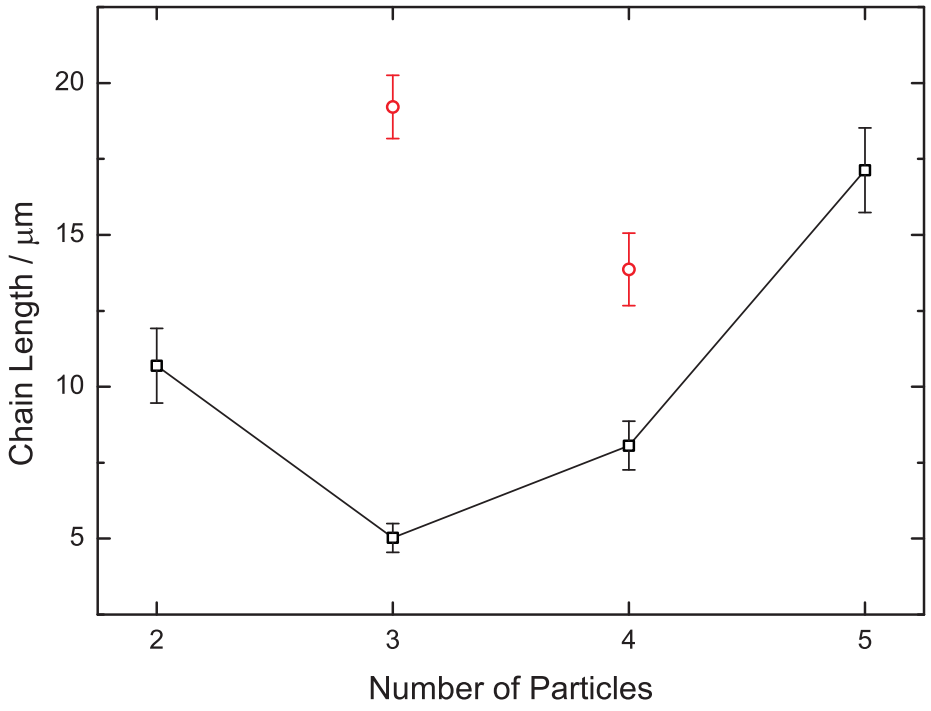


Figure 6.9: Mean end-to-end lengths for optically bound chains of 2.31 µm diameter melamine particles. The results in black show the chain collapse at three particles in a manner similar to that observed with the 3.5 µm diameter silica spheres, while the additional stable forms which were observed are shown in red.

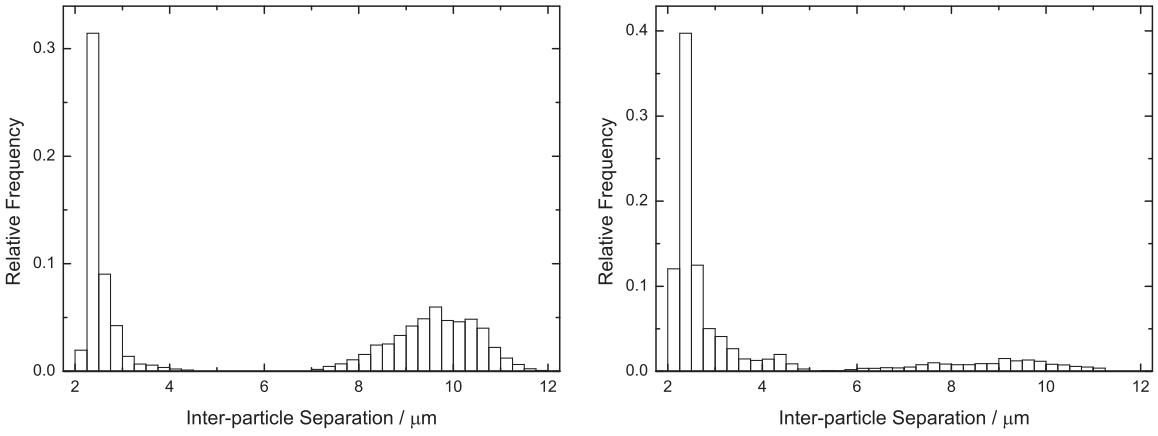


Figure 6.10: Histograms illustrating the inter-particle separations observed between adjacent particles in the three particle (left) and four particle (right) chains, including all of the observed conformations.

chain length with the addition of further particles. Mean chain lengths are also given for the extended three and four particle forms.

Further analysis of the accessible conformations for three and four particle chains are shown in Figure 6.10. The two histograms represent inter-particle separations for both three (left) and four (right) particle chains, with the values including both the collapsed and extended

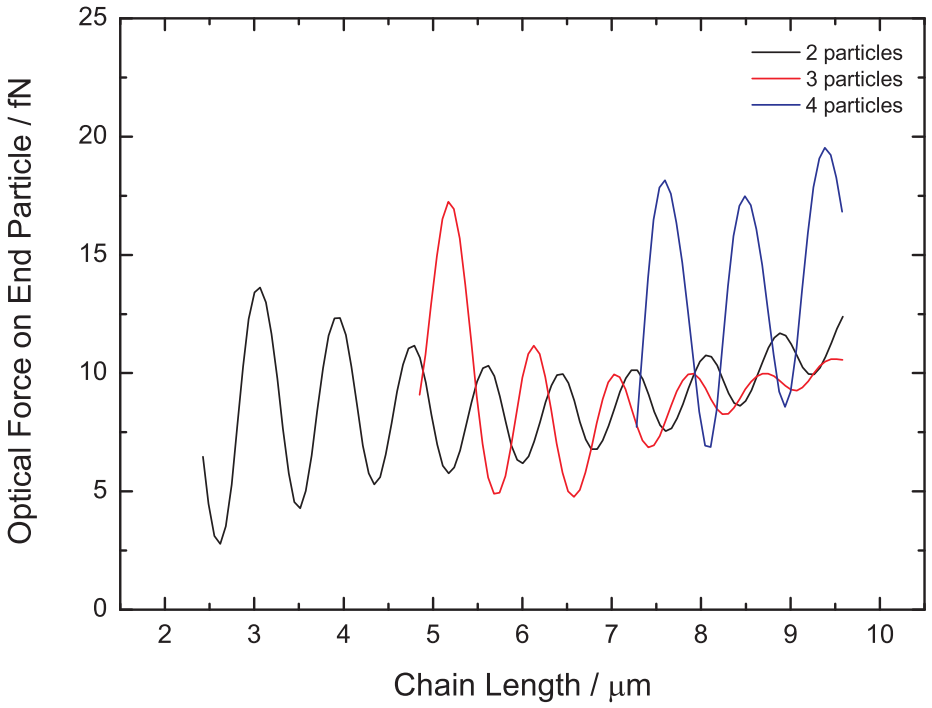


Figure 6.11: GLMT results showing the optical forces acting on the outermost particles for chains of two, three and four melamine spheres. Positive values indicate compressive forces, showing that collapsed chains are expected in each case.

conformations. In each case a distinct maximum can be seen at distances slightly larger than the particle diameter ($d = 2.31\,\mu m$) as expected for the collapsed particles, with a secondary maximum observed corresponding to the separated forms. This additional maximum occurs at around 10 µm for the three particle chain, and 9 µm for four particles, clearly indicating the presence of at least two stable inter-particle separations.

In order to understand the underlying physical processes governing the formation of these optically bound chains, the GLMT simulations of Dr. Jonathan Taylor presented in Section 5.4 will be used. Optical force curves were calculated using the same parameters as previously, with the optical power, particle diameter and particle refractive index values changed to represent the new system. These simulations are shown in Figure 6.11 for chains of two, three and four 2.31 µm diameter melamine particles, and again show the optical force acting on the end particle of the chain in each case.

In contrast to the simulation results presented for the 3.5 µm diameter silica spheres, these simulated curves do not cross the zero-force axis at any point, and show compressive optical forces for all chain lengths, indicating that collapsed chains should be observed in each case. While this is true for the three and four particle chains, the two particle dimer is never

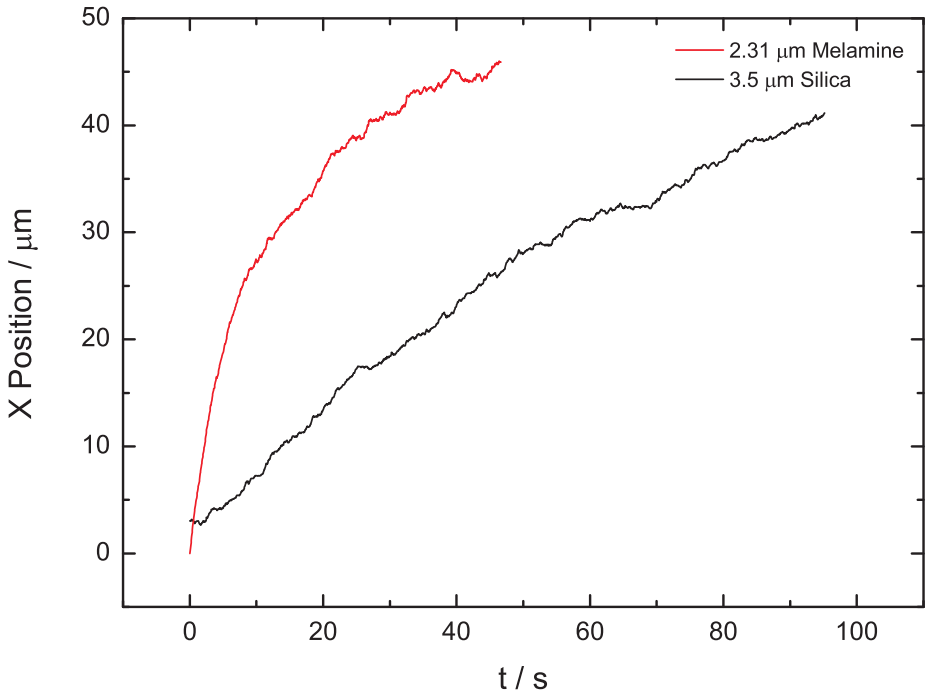


Figure 6.12: Particle trajectories for 2.31 µm diameter melamine and 3.5 µm diameter silica particle, exposed to a single evanescent wave. The stronger interaction of the melamine particles with the field is manifest by the higher particle velocities.

observed to collapse experimentally. It should be noted, however, that the magnitude of the compressive forces returned in this case are far smaller than those calculated for the silica chains (tens of fN compared to hundreds), meaning that the compressive forces acting on the particles in this case are far weaker. It is therefore likely that other effects such as the surface charges on the melamine particles must be considered, and may be the reason for the observation of the separated dimer in the two particle case.

Further understanding of the reasons for these much reduced compressive forces can be obtained by monitoring the behaviour of single 3.5 µm diameter silica and 2.31 µm diameter melamine particles. By blocking one of the fibre outputs and positioning a single particle close to the centre of the remaining evanescent wave spot, the optical forces due to the evanescent field can be estimated. In both cases, once released by the optical tweezer, the particles were propelled in the direction of beam propagation as expected, with maximum velocities observed close to the centre of the evanescent wave spot. The resulting trajectories are shown in Figure 6.12 for both particle types. Both particles are seen to move in the x direction due to the single evanescent wave, though the melamine particle exhibits far more rapid motion. It should be noted however that the setup utilised for the melamine particle work had an input power of 130 mW from each beam, compared to 100 mW for the

silica particle experiment. By differentiating these curves and filtering to remove the high-frequency oscillations present in the velocity plots, maximum velocities were determined equal to 1.49 µm/s for the 3.5 µm diameter silica particle, and 6.1 µm/s for the 2.31 µm diameter melamine particle. Using Stokes' Law, the viscous drag acting on each of these spheres can be calculated, allowing the drag force, F_d, to be determined at these maximum velocities *via*:

$$F_d = 6\pi\eta a v \tag{6.2}$$

where η is the viscosity of the medium, a the particle radius and v its velocity. Assuming that the optical force resulting from the evanescent field is balanced by this drag force, the maximum optical force is calculated to be 0.438 fN/mW for the silica bead, and 0.913 fN/mW for the melamine particle. This factor of two difference in the optical force acting on the melamine particles, once the power difference has been accounted for, can be used to explain the results obtained in this chapter. While the single beam forces are greater for the melamine particles, the underlying optical potential within the trap means that the forces acting on the particle are defined by the difference between the two evanescent waves, and will therefore be much smaller in magnitude. Indeed, at the centre of the evanescent wave trap the total force is zero. The forward-scattered radiation from each of the melamine particles will be enhanced due to the stronger interaction of the particles with each beam and their increased A factor. When the small optical forces resulting from the underlying potential and the larger forces due to forward-scattered radiation are considered together, the net result is a large *decrease* in the overall compressive forces acting on the particles in each optically bound chain. This is consistent with the small magnitude of the compressive optical forces output from the GLMT simulation, and with the experimental results indicating the stability of the non-compressed two, three and four particle forms.

6.3 Conclusions

In this chapter the effects of changing particle size and composition on the optically bound matter formed by colloidal micro-particles has been explored. Following on from the work presented in Chapter 5, in which 3.5 µm diameter silica particles were studied, smaller silica particles and melamine micro-particles have been investigated, allowing a deeper understanding of the multiple effects underpinning the formation of this optically bound matter.

Initially 1.5 µm diameter silica particles were studied, showing an increased influence of the underlying interference fringes due to the reduced particle diameter. These effects resulted in preferential inter-particle separations being observed, with these spacings consistent with the calculated fringe separations. This was verified by using orthogonally polarised beams, partially removing the fringes and showing a much smoother probability distribution.

Following this, 1.0 µm diameter silica particles were investigated, showing an even greater response to the interference fringes. In contrast to the results presented for the larger silica spheres, these particles spontaneously assembled into arrays at higher particle concentrations. Closer analysis of these arrays revealed a structure consistent with each melamine particle occupying the space between two interference fringes, as expected due to the negative force factor calculated for this particle type.

Finally, 2.31 µm diameter melamine particles were used to examine the effects of changing particle refractive index. Due to their larger diameter these particles were not expected to be influenced by the interference fringes to a large extent, as experimentally verified by examining the separations observed in the optically bound dimer. Through single particle studies it was shown that these particles experience a stronger interaction with the evanescent field, as a result of the higher refractive index contrast between the particles and the trapping medium. A consequence of this is the increased optical forces resulting from the forward-scattered light from each particle, meaning that the overall compressive forces, due to the balance of these forces with the underlying optical potential, are much reduced. This is consistent with further GLMT simulation work, showing compressive forces an order of magnitude smaller than those calculated for the 3.5 µm diameter silica spheres. Clearly this data provides a stringent test of these scattering calculations, particularly with regards to the bistability of the three and four particle configurations.

Chapter 7

Dynamics of Optically Bound Matter

In Chapter 5 the equilibrium behaviour of optically bound one-dimensional chains was discussed and successfully modelled using Generalized Lorentz-Mie Theory (GLMT), before the effects of changing particle size and refractive index were presented in Chapter 6. In this chapter the dynamics of these optically bound chains will be explored and quantified. It will be seen that optically bound chains exhibit a rich range of dynamic behaviour, heavily dependant on the particle type and number present within the chain. Firstly, the diffusion of these chains will be quantified and compared to that of individual particles by monitoring their mean square displacement. Following this is an investigation of the angular distribution of these chains, and of the chain rigidity as a function of chain length. Finally more complex, waveguide driven dynamic behaviour of these chains will be studied, and explained using GLMT simulations.

7.1 Dynamics of Optically Bound Silica Chains

7.1.1 Chain Diffusion

When studying the diffusion of individual colloidal particles, an essential quantity to calculate is their mean square displacement (MSD). For the thermally excited motion of a sphere in a purely viscous fluid, the MSD is expected to be a linear function of time for

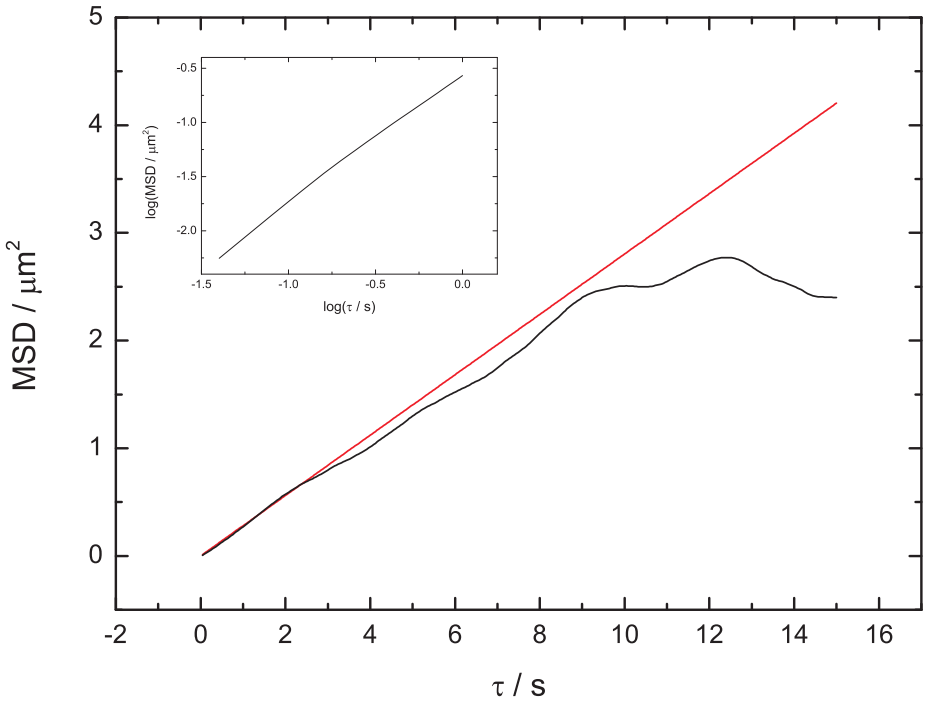


Figure 7.1: The experimentally determined mean square displacement (MSD) for a single 3.5 µm diameter silica particle in an evanescent field, shown for two-dimensional diffusion. The expected form for a freely diffusing 3.5 µm diameter silica particle is shown in red. While the lines are initially in good agreement, at longer times the diffusion of the particle in the evanescent field is suppressed, resulting in the MSD reaching a plateau value.
Inset: A plot of $\log(MSD)$ *vs.* $\log(t)$ allows the calculation of diffusion coefficients.

timescales greater than that over which the velocity autocorrelation function decays, given by m/γ. For the particles considered in this chapter, this value is of the order of 1 ms. At timescales longer than this, the MSD for a freely diffusing particle is given by:

$$\left\langle \Delta\vec{r}^{\,2}(\tau) \right\rangle = \left\langle [\vec{r}(t+\tau) - \vec{r}(t)]^2 \right\rangle = 2dD\tau \tag{7.1}$$

where $\vec{r}$ is the particle position, τ is the lag time or time interval, t the absolute time, d the number of dimensions over which the MSD is being calculated, and D the diffusion coefficient. The diffusion coefficient can be calculated *via* the Stokes-Einstein relationship:

$$D = \frac{k_{\mathrm{B}}T}{6\pi a\eta} \tag{7.2}$$

where a is the particle radius, and η the viscosity of the surrounding medium.

In order to explore the diffusive behaviour of optically bound chains within an evanescent field, first the diffusion of a single particle within the field will be studied. Using the experimental setup presented in Section 5.2, a single 3.5 µm diameter silica particle was placed

into the evanescent field. After allowing time for the particle to reach its equilibrium position, the particles position was tracked over a period of 30 s using the LabVIEW routines previously described. The resulting two-dimensional single particle MSD is given in Figure 7.1. Also shown in this figure (red line) is the expected form of the MSD for a freely diffusing 3.5 µm diameter silica particle in the absence of the evanescent field, calculated using Equations 7.1 and 7.2. While at short timescales ($\tau < 2\,\mathrm{s}$) the two lines are in good agreement, at longer timescales the experimental MSD plot is seen to plateau to a value of $2.5\,\mu\mathrm{m}^2$ as a result of confinement by the evanescent field.

In general, the MSD of a particle in an evanescent field will not follow the form given in Equation 7.1, but will exhibit a more complex time dependant behaviour. This behaviour is often described by a power law in the form of a modified MSD expression, given by:

$$\left\langle \Delta\vec{r}^{\,2}(\tau) \right\rangle = 2dD_{\mathrm{eff}}\tau^{\alpha} \tag{7.3}$$

where a new factor, α, has been incorporated in order to quantify the new, unknown, time dependence [145]. If $\alpha > 1$, the behaviour is described as *super-diffusive*, where $\alpha < 1$ indicates *sub-diffusive* behaviour. Taking the single particle MSD and producing a plot of $\log(MSD)$ *vs.* $\log(t)$ allows both α and an effective diffusion constant, D_{eff}, to be calculated for each particle. For a single particle diffusing in the evanescent field an α value of 1.21 ± 0.01 is determined by fitting to the data shown in Figure 7.1 for $\tau \leq 1\,\mathrm{s}$; this time period was chosen so that the diffusive behaviour can be studied in the linear regime of the MSD plots. This procedure is shown in the inset to Figure 7.1. From the intercept of the $\log(MSD)$ *vs.* $\log(t)$ plot an effective diffusion coefficient of $D_{\mathrm{eff}} = (6.86 \pm 0.06) \times 10^{-2}\,\mu\mathrm{m}^2/\mathrm{s}$ is returned, slightly reduced from the value of $7.01 \times 10^{-2}\,\mu\mathrm{m}^2/\mathrm{s}$ calculated for a freely diffusing particle, indicating the weak confining effect of the evanescent field.

By sequentially adding particles and calculating the MSD of the centre of mass of the chain after allowing equilibrium conformations to be reached, the influence of additional particles on the diffusive behaviour of the chains can be explored. For chains of up to five particles the same behaviour as for the single particle is followed, with the plateau value of the MSD plot reducing with increasing particle number. The MSD plateau reaches a minimum for the five particle chain, shown in Figure 7.2 (left), with a value of $0.3\,\mu\mathrm{m}^2$, quantifying the effect that the additional particles have had on reducing their collective diffusion. The

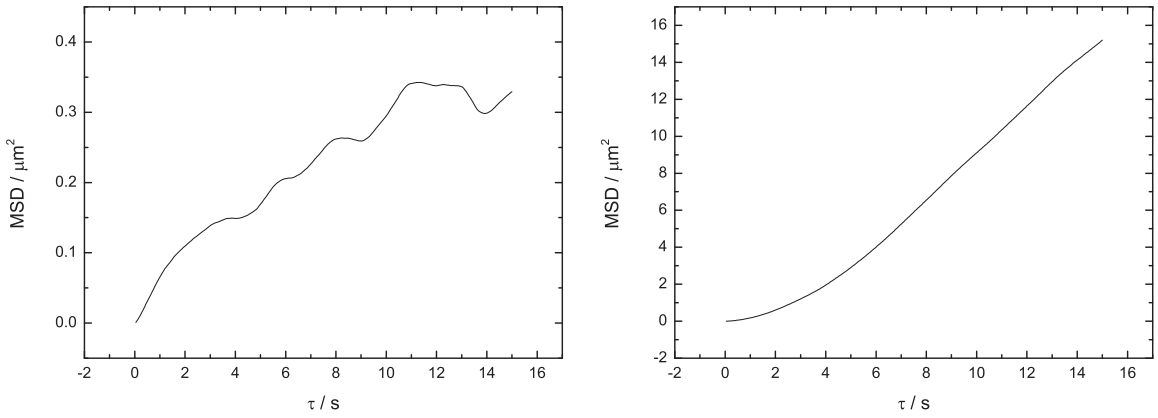


Figure 7.2: MSD plots for a five (left) and eight (right) particle chain, showing markedly different behaviour to each other, and to the single particle MSD shown in Figure 7.1. In comparison to the single particle MSD, the five particle chain shows a reduction in the MSD values, reaching a plateau at 0.3 μm^2 compared to 2.5 μm^2 due to the confining presence of additional particles within the chain. Transitioning to an 8 particle chain greatly changes this behaviour as the MSD values increase markedly, quantifying the increased chain drift which is observed.

reducing plateau values suggest that the presence of additional particles within the optically bound chain reduces the MSD of the chain as a whole, as the increase in forward-scattered light stabilises particle positions relative to each other. This behaviour appears to reverse for the longer, collapsed chains (six–seven particles), with the MSD values now increasing with particle addition in line with the observed reduced stability of these longer chains. The MSD for an eight particle chain is shown in Figure 7.2 (right), with significantly larger MSD values being observed and no evidence of the MSD tending to a plateau value over the timescale of this experiment. This sharp transition in chain dynamics was first introduced in Section 5.3, where it was seen that addition of an eighth particle caused rapid rotation of the chain away from the parallel axis, defined as the axis connecting the two evanescent wave spots. A large increase in chain drift was observed, which is also quantified *via* the MSD plot shown.

In order to compare the diffusive behaviour of this range of optically bound chains, the analysis introduced for the single particle MSD plot will be repeated, allowing α and D_{eff} values to be determined for each chain. It is emphasised that the following phenomenological analysis focusses on the short-timescale, linear regime of the log-log plots (where $\tau \leq 1\,\text{s}$), providing comparison for short-timescale behaviour only. Figure 7.3 shows these calculated α values for chains of up to eight particles, indicating that pseudo super-diffusive behaviour is observed in all cases. The error bars shown quantify the standard error in the linear fit

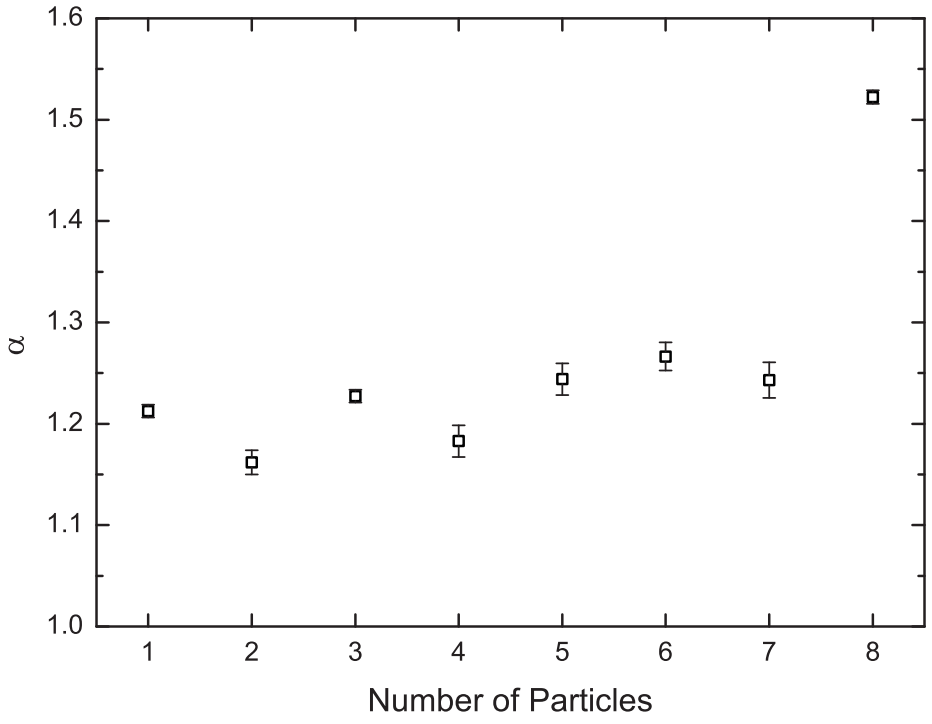


Figure 7.3: By plotting $\log(MSD)$ *vs.* $\log(t)$, α can be obtained for each optically bound chain. In each case α is larger than 1, indicating pseudo super-diffusive behaviour over short timescales. The error bars shown are determined from the standard error in the linear fit.

used to obtain these values. It is seen that α does not seem to vary significantly as a function of particle number, though a particularly marked increase is seen for the case of the eight particle chain, which is consistent with the observations already presented. While this super-diffusive behaviour is seen for all chain lengths on timescales of less than one-second, it does not necessarily persist. Over longer timescales a transition towards sub-diffusive behaviour, away from the free-diffusion limit, is observed for all chains, apart from the seven and eight particle cases. This is indicative of constrained motion due to the field, as shown in Figure 7.2 (left) for the five particle chain [146].

In addition to determining α from a $\log(MSD)$ - $\log(t)$ plot, D_{eff} values have also been calculated, and are presented in Figure 7.4. Error bars show the standard error returned from the fitting routine, and are often smaller than the data symbols. A dashed horizontal line indicates the diffusion coefficient for a 3.5 µm diameter silica particle in the absence of the evanescent field and is included for comparison. It can be seen that in all cases the returned D_{eff} values are less than this limit. The small reduction in the single particle case when compared to a freely diffusing particle confirms the weakly confining nature of the evanescent field. For longer chains, the presence of additional particles increases their

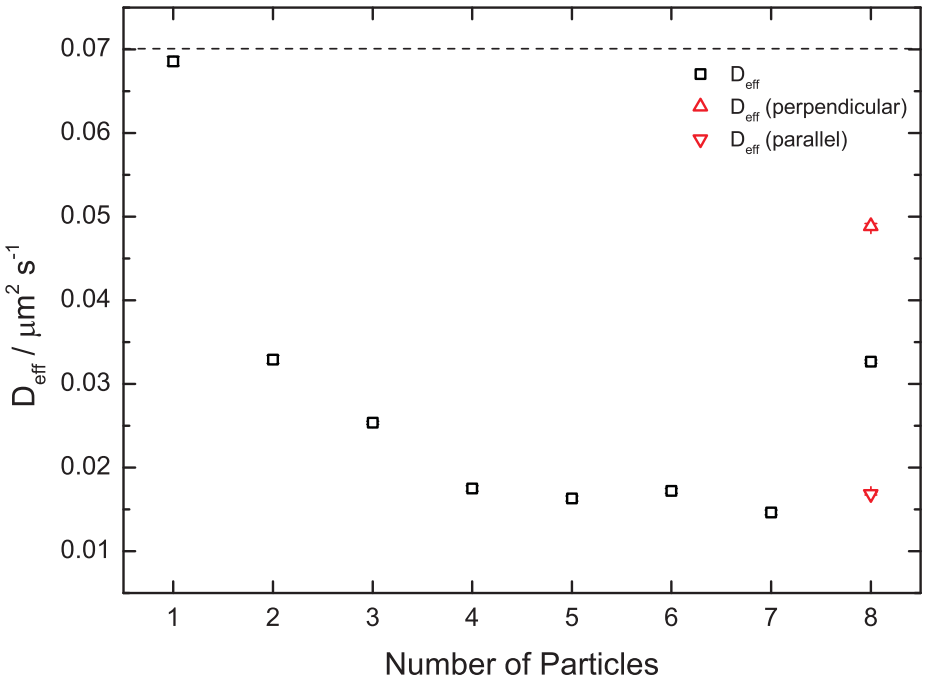


Figure 7.4: Effective diffusion coefficients, calculated for diffusion of the optically bound chains as a function of particle number. As might be expected, the addition of further particles into the chain reduces this concerted diffusion when compared to the free particle case (illustrated by a horizontal line, for a particle in the absence of the evanescent field). Again a transition in behaviour is seen for addition of an eighth particle, as a large increase in D_{eff} is observed. This is largely due to an increase in perpendicular diffusion, as shown by the separate parallel and perpendicular D_{eff} values.

confinement in the evanescent field and the diffusion coefficient reduces monotonically with the number of particles in the chain to a limit of $\sim 0.015\,\mu\text{m}^2\ \text{s}^{-1}$. Again a transition in behaviour is seen for addition of an eighth particle, with relatively large diffusion coefficients being returned. This effect is dominated by a significant increase in the perpendicular diffusion coefficient in this case, illustrated in Figure 7.4 by splitting the eighth data point into its constituent parallel and perpendicular components. For the shorter chains these two components are generally similar, and so two-dimensional diffusion coefficients have been presented for clarity.

For a collapsed optically bound chain the diffusion coefficient values may be compared to those calculated for a rigid rod of length L and diameter d. This is performed using Broersma's relations, giving the diffusion coefficient, D, to be: [147–149]:

$$D = \frac{k_{\text{B}}T}{3\pi\eta L}(\delta - (1/2)(\gamma_{\parallel} + \gamma_{\perp})) \tag{7.4}$$

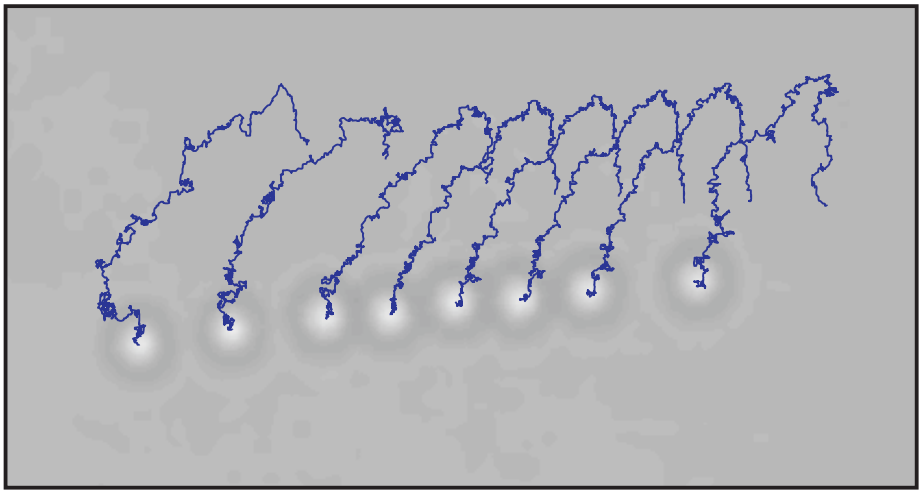


Figure 7.5: The circulatory motion of this eight particle chain is similar to that observed and modelled by Taylor *et al.* in a counter-propagating Gaussian beam trap [15], where increasing lateral repulsive forces in longer chains can cause the chain to circulate around the beam axis in a dynamic trapping state.

where:

$$\delta = \ln(2L/d) \tag{7.5a}$$

$$\gamma_{\parallel} = 1.27 - 7.4(\delta^{-1} - 0.34)^2 \tag{7.5b}$$

$$\gamma_{\perp} = 0.19 - 4.3(\delta^{-1} - 0.39)^2. \tag{7.5c}$$

By approximating the collapsed, seven particle chain to be a rigid rod with a diameter of 3.5 µm and a length of 24.5 µm (equal to $7d$), D is calculated to be $3.83 \times 10^{-2}\,\mu\text{m}^2/\text{s}$. The experimentally determined value of $(1.46 \pm 0.03) \times 10^{-2}\,\mu\text{m}^2/\text{s}$ is less than half of this, and further quantifies the significant confining effects of the other particles in the field resulting from the forward-scattered radiation.

Finally in this section, the trajectory of an eight particle optically bound chain is mapped in Figure 7.5. The eight particle chain shows the form previously described in Chapter 5, with a collapsed chain centre and increased inter-particle spacings towards the chain ends. The blue lines illustrate the individual particle trajectories obtained using LabVIEW tracking routines over a period of 1 minute. It can be seen that the chain exhibits concerted motion across several particle diameters over this timescale. The onset of this dynamic motion is strongly reminiscent of work presented by Taylor and Love on the circulation of micro-particle chains within a counter-propagating Gaussian beam trap [15]. Those experimental results showed off-axis circulation of a chain of optically bound 3 µm silica beads, with

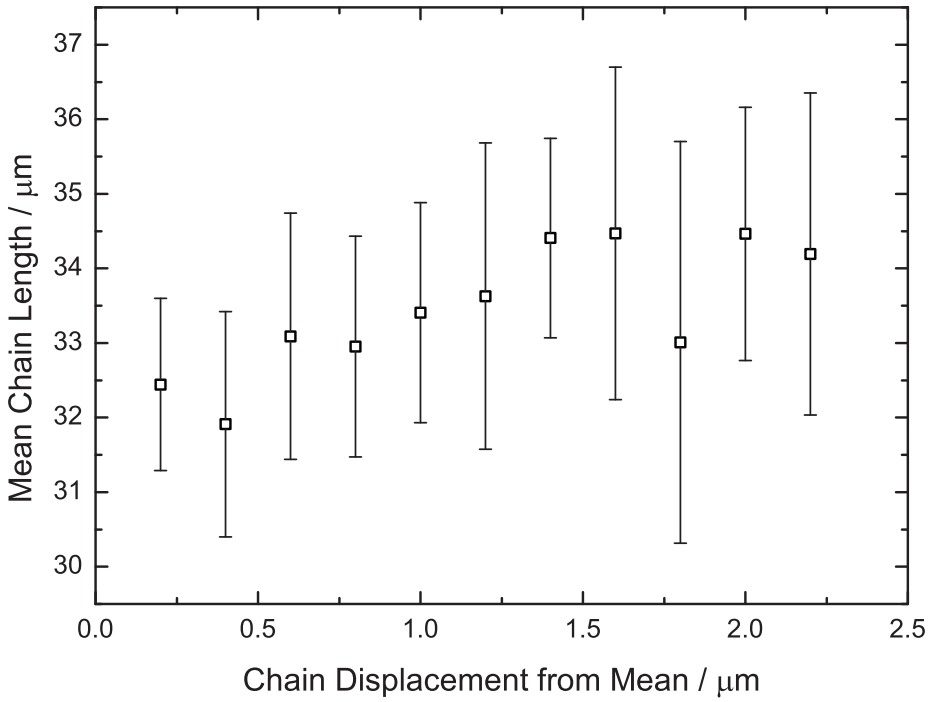


Figure 7.6: A plot of mean chain length against chain displacement for the eight particle chain shown in Figure 7.5 shows generally larger end-to-end chain lengths are observed at greater displacements from the inter-beam axis.

the results explained using a Mie scattering model. While a single particle offset from the beam axis will be drawn back into line due to the gradient force, a second particle adjacent to this in the chain may be drawn further from the beam axis as a result of the slightly offset focussing effects of the first particle in the field. Considering the scattering effects of both particles, this leads to a range of inter-particle spacings for which a chain of particles will actually be repelled from the beam axis. It should be noted however that this inter-particle separation range does not typically overlap with the stable equilibrium particle separation, and so stable on-axis trapping is still observed. Taylor and Love's discussion of these circulatory modes continues to state that, as more particles are introduced and the particles move closer together, this repulsion may be seen at the stable inter-particle separation, and off-axis trapping may be observed. In their experimental work this occurred for chains of between seven and ten particles. In this case, a chain will similarly be repelled off-axis due to this lateral force, at which point the stable inter-particle separations may change. The resulting reduction in the off-axis repulsive force allows the chain to move back towards the beam axis before the inter-particle spacings are again reduced and the process continues, producing complex, circulatory modes. While the two experimental arrangements are clearly very different, their discussion provides a useful framework with

which to understand the processes occurring in this work. A plot of the mean chain lengths observed for this eight particle chain as a function of displacement from the inter-beam axis is given in Figure 7.6, where the inter-beam axis is defined as the vector connecting the two evanescent wave spots, determined from the mean chain positions. The observed positive correlation further supports the above reasoning following Taylor and Love, with the optically bound chain being most compressed when aligned on the inter-beam axis, and around 2 µm longer at its maximum displacement.

7.1.2 Chain Angle

Another feature of the dynamics of this optically bound matter, initially demonstrated in Figure 5.8, is the increased off-axis tilt seen when an eighth particle is added to the chain. In order to quantify this, the optically bound silica particles were tracked and an angle, θ, defined as the angle the chain makes with the inter-beam axis, was determined. This was achieved by performing a linear fit through the individual particle coordinates, and defining this as the chain axis. It is expected that, for a well aligned system, θ will show a symmetric distribution centred around 0°.

Figure 7.7 illustrates the distribution of chain angle for the two particle optically bound dimer. A symmetric distribution is seen, and fitting to a Gaussian form yields a full width at half maximum (FWHM) spread of 4.3° as shown. It can also be seen that the distribution shown in Figure 7.7 is not quite centred around zero, and is instead centred at 1.7°, potentially due to imperfect alignment of the system. Similar distributions are seen for chain lengths of up to seven particles, displaced from zero by values between 1.7°–2.3°, suggesting alignment is the principle factor in this distribution shift. The underlying dimer rotational potential can be determined from the histogram shown in Figure 7.7 by following the inversion procedures introduced to determine the dimer stretching potential in Figure 5.4. The resulting potential energy curve is shown in Figure 7.8, displaying strong similarities to that of the dimer stretching potential. This good agreement is expected, as the previously determined stretching potential was an average over all chain angles, whereas the rotational potential is averaged over bond length, meaning that these curves are not truly decoupled.

Addition of an eighth particle to the chain results in a large increase in the angular distribution, and the loss of this symmetric Gaussian-like profile, as shown in Figure 7.9. The

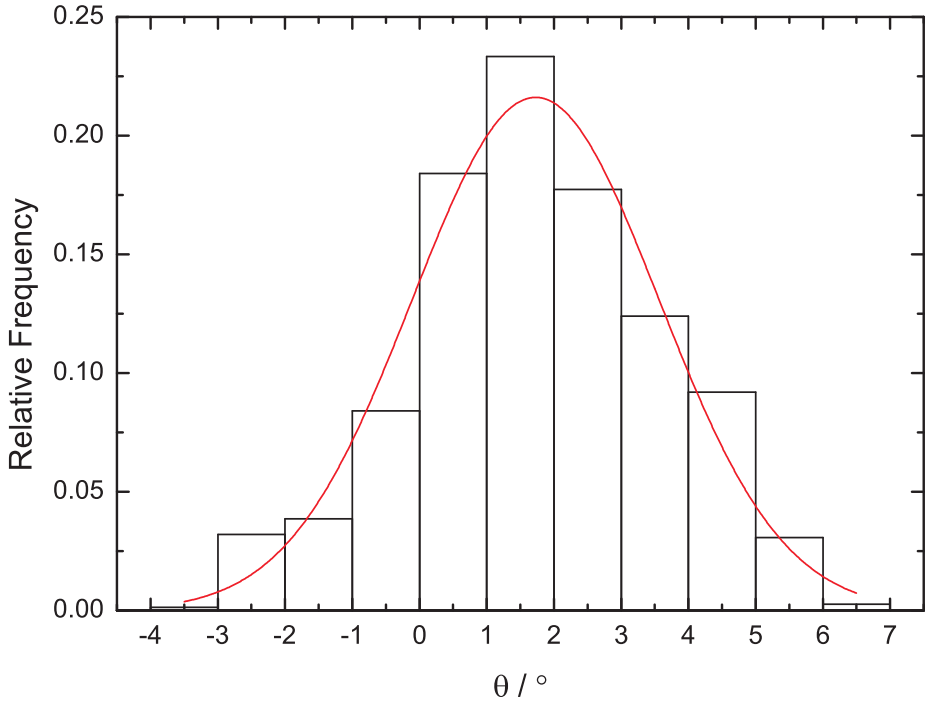


Figure 7.7: Histogram illustrating the distribution of θ, defined as the angle formed between the chain and beam axis, for a two particle dimer. A symmetric distribution is seen as expected, although it is not centred around zero, potentially due to imperfect alignment of the system. A Gaussian fit (red) returns a FWHM value of 4.3°.

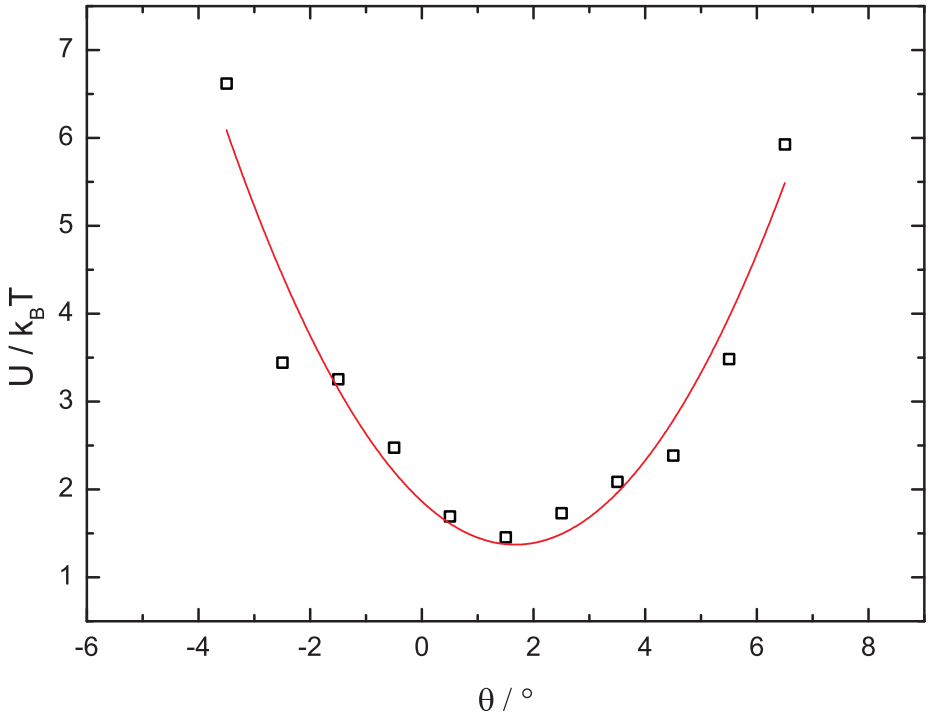


Figure 7.8: Inversion of the histogram shown in Figure 7.7 allows the underlying rotational potential to be determined, following the procedure introduced to determine the dimer stretching potential shown in Figure 5.4.

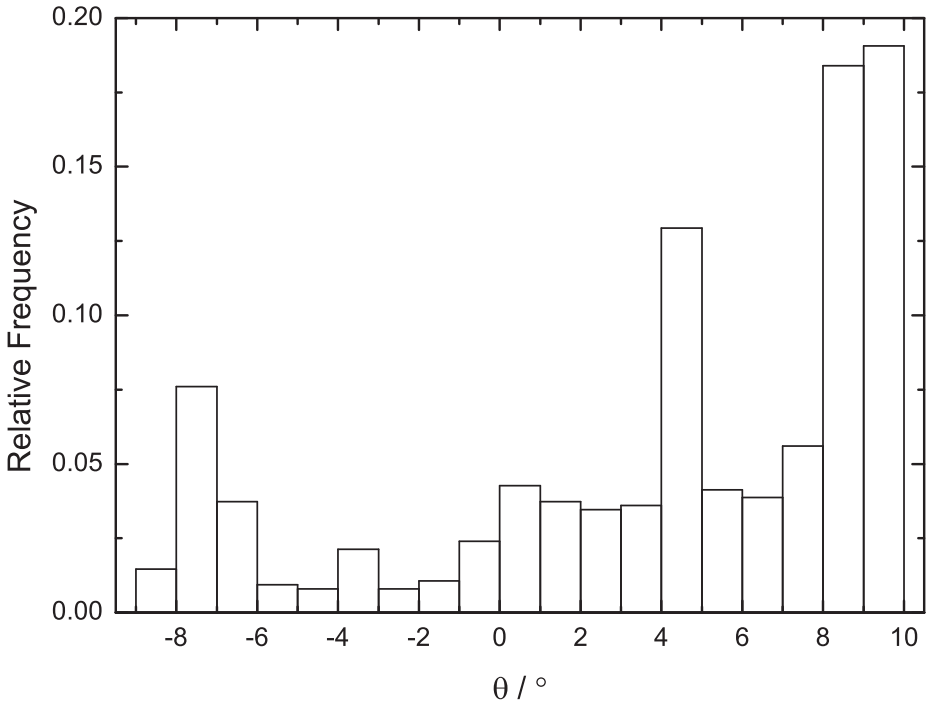


Figure 7.9: Histogram illustrating the distribution of θ, for an eight particle chain. A symmetric distribution is no longer seen and the angular distribution has increased significantly, consistent with the reduced stability and increased dynamic motion of this chain length within the evanescent field.

chain preferentially sits at large (8–10°) angles relative to the beam axis due to the increased compressive forces acting upon the longer chain forcing it to twist within the optical potential. This reasoning is further supported by the behaviour of the chain as the ninth particle is added - as the compressive forces on the outermost particles are increased still further, the chain accesses even greater angles relative to the beam-axis, at which point the forward-scattered radiation is no longer sufficient to keep the particles in line. The result is the splitting of the chain into shorter four and five particle chains which are more stable in the optical potential.

By calculating root mean square θ values for each chain, defined as $\theta_{\mathrm{RMS}} = \left\langle \theta^2(t) \right\rangle^{1/2}$, comparisons can be made regarding the angular behaviour of these optically bound chains. This comparison is shown in Figure 7.10 for chains of two–eight particles. The error bars in each case are the standard deviation in observed chain angle. As might be expected, θ_{RMS} is reasonably consistent within chains of two–seven particles, although the standard deviation in angle markedly reduces to a minimum for chains of five particles, due to the increased stability of the collapsed optically bound chain. The addition of further particles then causes this angular variation to increase. As previously discussed, the increasing

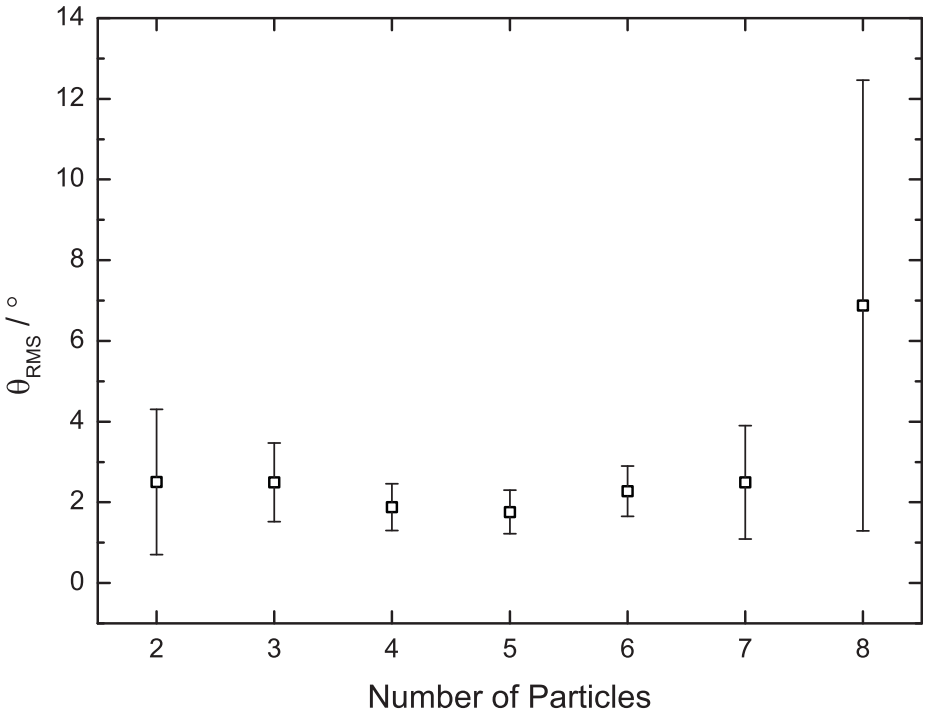


Figure 7.10: θ_{RMS} for chains of two to eight particles. The increased stability of the collapsed five particle chain can be clearly seen, illustrated by error bars representing the standard deviation of the observed values. Decreasing chain stability can be seen for seven and then eight particles, as θ_{RMS} and the angular distribution dramatically increases.

chain length relative to the separation between the two evanescent wave spots means that a chain aligned parallel to the inter-beam axis becomes less stable as a result of the large compressive forces along the beam axis, and the minimum energy configuration requires the chain to rotate off-axis. Finally, as the eighth particle is added, a very large θ_{RMS} value is observed, along with a correspondingly large angular variation, demonstrating and quantifying the reduced stability of this longer chain.

7.1.3 Chain Rigidity

Having established the dynamic behaviour of optically bound chains in terms of their mean square diffusion and angular variation, the flexibility within a given chain will now be examined. This will be discussed in terms of the RMS transverse displacement within a chain, $\left\langle \delta^2(s) \right\rangle^{1/2}$, where δ is the transverse separation between two points on the chain, separated by a number of particles s. This approach was used by Furst and Gast in their study of dipolar chains in magnetorheological suspensions [150], exhibiting an approximately quadratic increase of this quantity with inter-particle separation. In the case of optical binding it

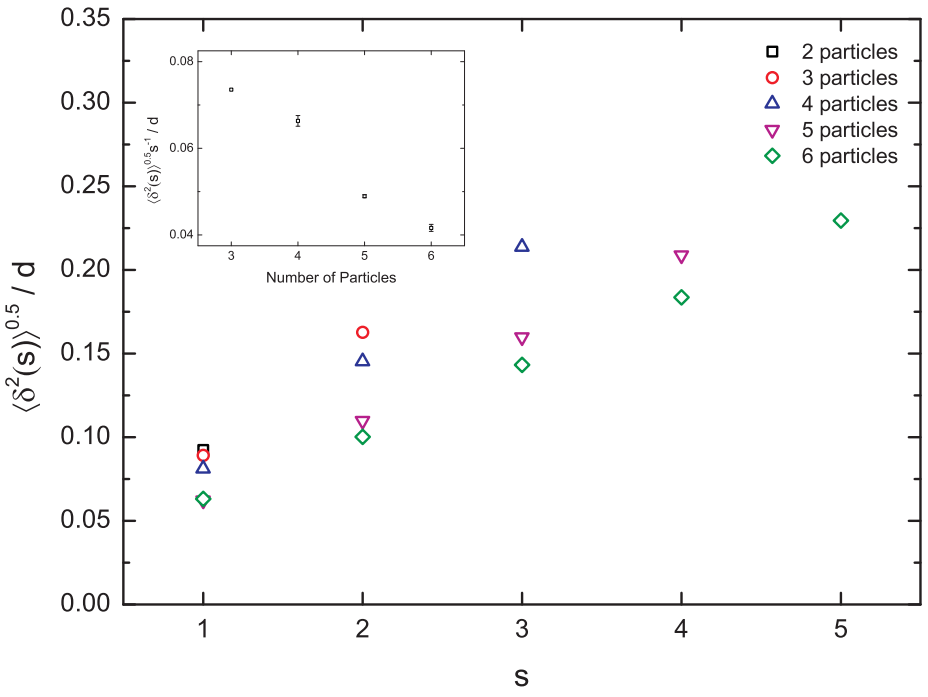


Figure 7.11: RMS transverse displacement within an optically bound chain of 3.5 µm diameter silica particles, as a function of the number of particles separating the two points, s, and normalised by particle diameter, d. This value increases smoothly with increased separation along the chain as expected. The inset illustrates the gradient obtained for each chain length from a linear fit to this data, showing an approximately linear trend with number of particles and demonstrating the reduced flexibility and stronger binding within the five and six particle chains.

is expected that $\langle\delta^2(s)\rangle^{1/2}$ will initially decrease with increasing particle number, as the particles move closer together until chain collapse occurs at five particles, this being the configuration with the strongest on-axis optical binding forces, which will act to keep the particles in a linear conformation. As has already been demonstrated, increasing the number of particles beyond this point will decrease the chain stability, before the increasing compressive forces acting in the eight particle chain causes it to tilt relative to the beam axis.

By averaging over all pairs of particles within a chain, the RMS transverse displacement can be determined as a function of separation along the chain, and is presented in Figure 7.11, where the RMS transverse displacement has been scaled by the particle diameter, d. The s value in each case is simply the number of particles separating the two points being measured. It can be seen in Figure 7.11 that the RMS transverse displacement within an optically bound dimer is around 0.10 particle diameters. This quantity decreases with increasing particle number as the increased forward-scatter enhances binding along the

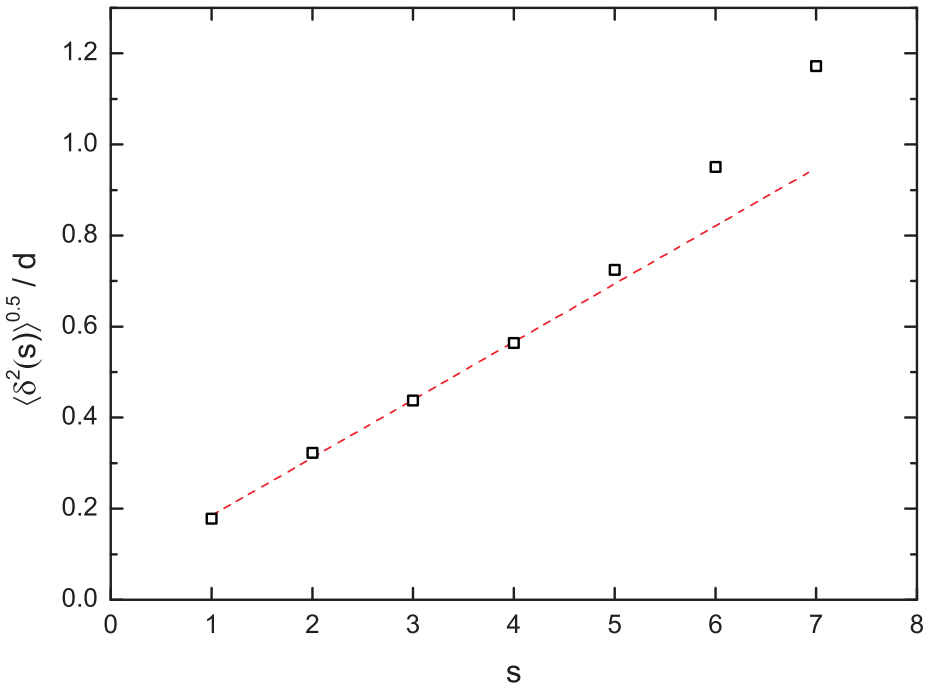


Figure 7.12: RMS transverse displacement for a chain of eight 3.5 µm diameter silica particles, showing a large increase from the values shown for two to six particles. This is consistent with the decrease in stability and linearity of this longer chain as previously shown in this chapter. Deviation of the plot from the straight line shown at larger separations is a result of the increasing on-axis inter-particle separations observed towards the ends of these longer chains.

chain axis, and acts to constrain the particles, so that this quantity is just 0.06 for a five and six particle chain. As would be expected, this quantity smoothly increases with increasing separation between points on the chain, and is smallest for the most tightly bound six particle chain, exhibiting an average end-to-end RMS transverse displacement of only 0.23 particle diameters. This trend can be confirmed by analysis of a linear fit to the data for each chain length, as shown in the inset to Figure 7.11. The decreasing slope with increased particle number confirms that the strongest on-axis confinement is observed for the chain of six particles.

Consistent with the behaviour already presented for the longer chains, this trend of decreasing RMS transverse displacement with increasing particle number is not continued for the longer seven and eight particle chains. This is illustrated in Figure 7.12 for the eight particle chain. The increasing trend with separation along the chain is still observed, with the deviation from linearity a result of the inconsistent on-axis inter-particle separations along the chain. In particular, the end-to-end RMS transverse displacement has increased to greater than one particle diameter, indicating the reduced stability and rigidity of the

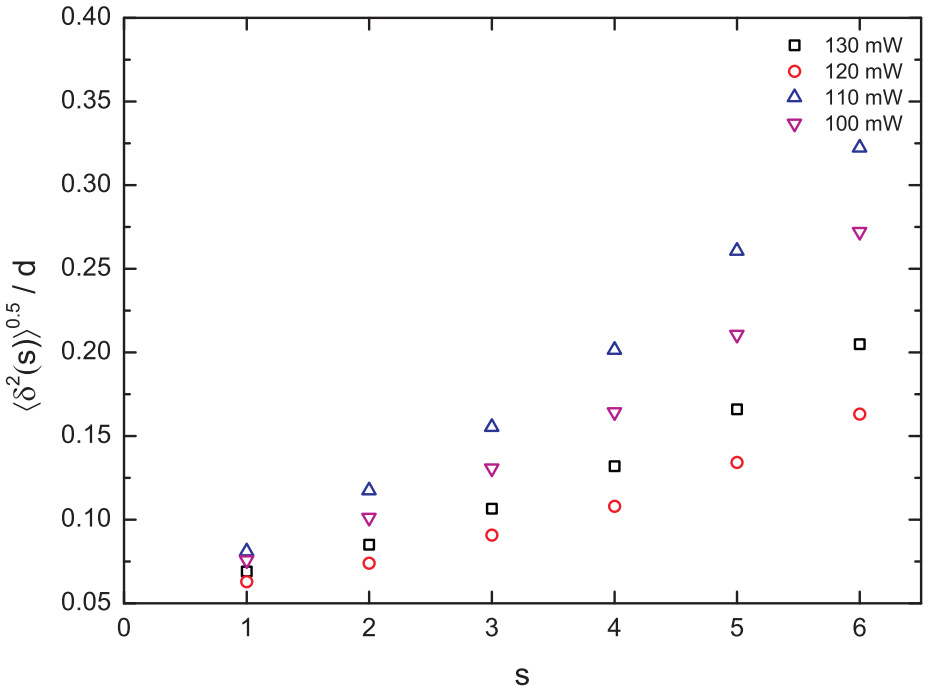


Figure 7.13: Variation of the RMS transverse displacement for a chain of seven 3.5 µm diameter silica particles as a function of optical power.

longest eight particle chain and quantified by the calculated gradient of 0.127 particle diameters per particle, significantly larger than those observed for the shorter chains.

In Figure 7.13 the RMS transverse displacement has been calculated for a chain of seven 3.5 µm diameter silica particles as a function of optical power. As the power is increased larger optical binding forces are expected to result in an decrease in the RMS transverse displacement of the particles, as they are more tightly confined to the inter-beam axis. An opposing effect is also anticipated however, as the increasing power will result in enhanced waveguiding along the chain, so that transverse displacement of a particle results in adjacent particles also being pulled off-axis. Although some evidence of the RMS transverse displacement decreasing with increasing power is seen in Figure 7.13, with the two lowest powers exhibiting RMS transverse displacement values a factor of two larger than the highest powers, the trend with power is clearly a complex one. While it should be noted that an understanding of this trend is not essential for the results presented previously as they were all obtained for chains at a fixed power, modification of the experimental setup in order to allow an investigation of this trend over a larger range of powers would help further understand these on-axis binding effects.

7.2 Chain Dynamics for Smaller Silica Particles

The dynamic behaviour of the chains formed from 1.5 µm diameter silica particles introduced in Chapter 6 shows a number of similarities to that of the larger 3.5 µm diameter spheres. It is clear, however, that the decreasing importance of the forward-scattered radiation as a binding mechanism, and the greater influence of the underlying optical fringes, means that these particles are less tightly constrained to a one-dimensional chain.

Initially the MSD is calculated for a single 1.5 µm diameter particle, and for the centre of mass of chains of two–eight spheres. By fitting the short timescale MSD ($\tau \leq 1\,\mathrm{s}$) to Equation 7.3 as before, α and D_{eff} for both parallel and perpendicular motion are calculated. These are shown as a function of particle number in Figure 7.14. The values of α are again all greater than 1, indicating that the chains still exhibit super-diffusive behaviour, with this value being largest in the perpendicular dimension in each case. This is in contrast to the 3.5 µm diameter silica particles where the parallel and perpendicular diffusion coefficients were generally similar, and can be understood in terms of reduced diffusion across the interference fringes in this case. Effective diffusion coefficients are shown in Figure 7.14 (right). For comparison, the expected diffusion coefficient for a particle in the absence of the evanescent field is $0.372\,\mu\mathrm{m}^2\ \mathrm{s}^{-1}$. The presence of the evanescent field again results in a reduction in D_{eff} when compared to this value, decreasing further with additional particles as expected. All of the optically bound structures display a much larger D_{eff} for perpendicular motion compared to parallel, illustrating the increasing effect of the interference fringes; for each chain there is a higher diffusion coefficient for motion perpendicular to the beam axis, or along the fringes, whereas diffusion is suppressed to a greater extent for particles in the parallel direction due to this potential barrier.

For each of the 1.5 µm diameter silica chains studied, a straight line is fitted through the particle coordinates, allowing the angle that the chain makes with the beam axis, θ, to be measured as a function of time. For all chains $\langle\theta(t)\rangle \approx -2°$, again due to imperfect alignment of the two input beams. θ_{RMS} values are presented in Figure 7.15 for chains of two–eight particles. As observed previously, the optically bound dimer shows a large θ_{RMS} value, with a correspondingly large standard deviation, shown by the error bars in each case. The addition of further particles restricts the range of tilt angles, as the forward-scattered light acts to constrain particles to a one-dimensional chain along the beam axis. As was observed for the 3.5 µm silica case, this value then begins to rise again for the longer

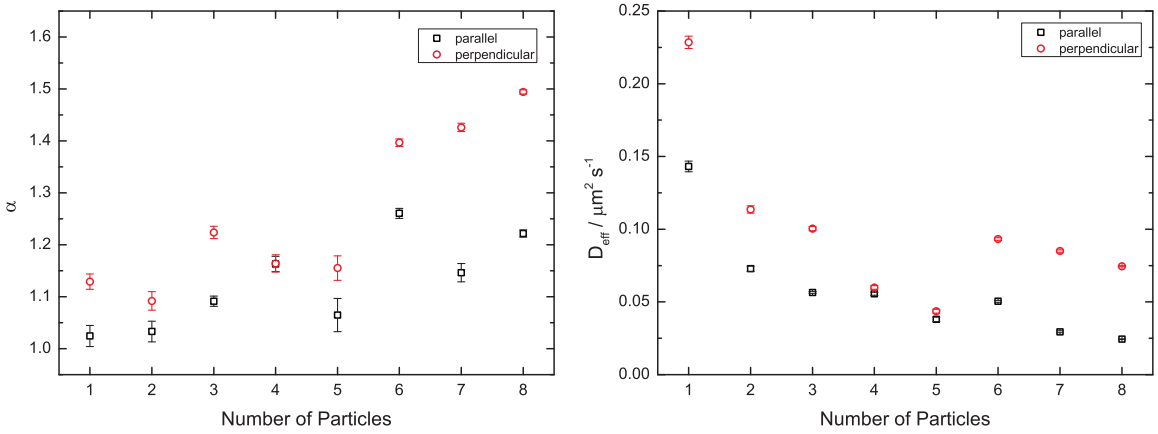


Figure 7.14: Diffusion coefficients determined by fitting the short timescale MSD data to Equation 7.3 for chains formed from 1.5 µm diameter silica particles.
Left: α values, determined for perpendicular and parallel diffusion from the gradient of a $\log(MSD)$-$\log(t)$ plot, show that super-diffusive behaviour is again observed for all chain lengths.
Right: D_{eff} values obtained from the intercept of the same plot. The values are all below that calculated for a freely diffusing particle, illustrating the confining effect of the evanescent field. Unlike the larger 3.5 µm particles, the effective diffusion coefficient is larger for perpendicular motion for all chain lengths, as a result of the potential barrier the particles need to cross to diffuse in the parallel direction across the interference fringes.

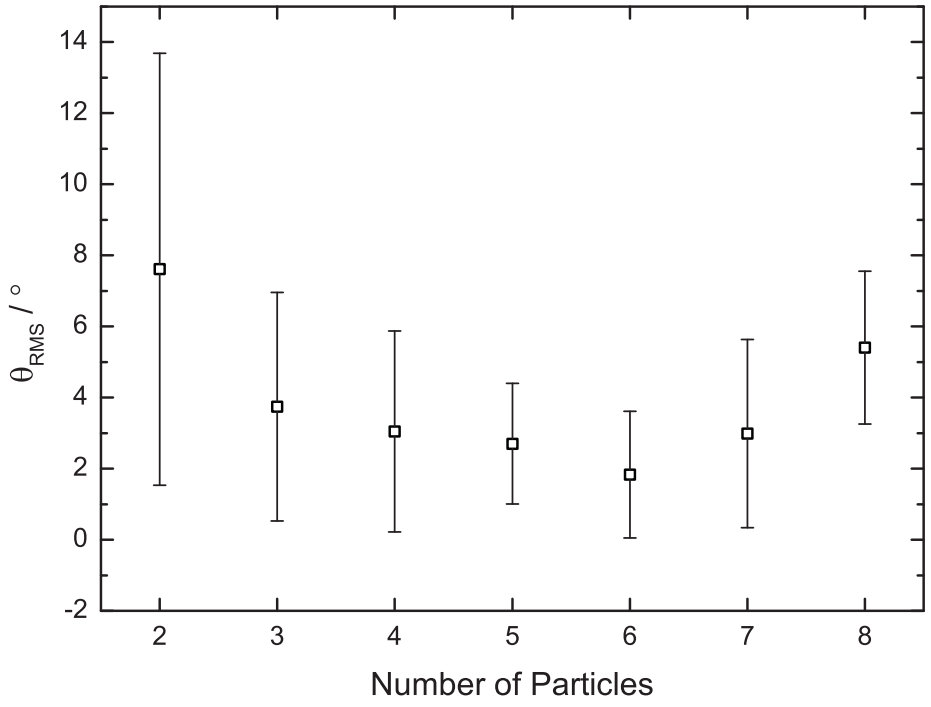


Figure 7.15: A study of θ_{RMS} for 1.5 µm diameter silica particles, where θ is the angle the chain makes with the beam axis, shows that increasing the number of particles in the chain generally decreases the angular variation as expected, as the additional particles act to constrain the others to a one-dimensional chain along the beam axis. This is no longer the case for the longest chains, where the outermost particles start to experience increasing compressive forces due to the counter-propagating evanescent waves.

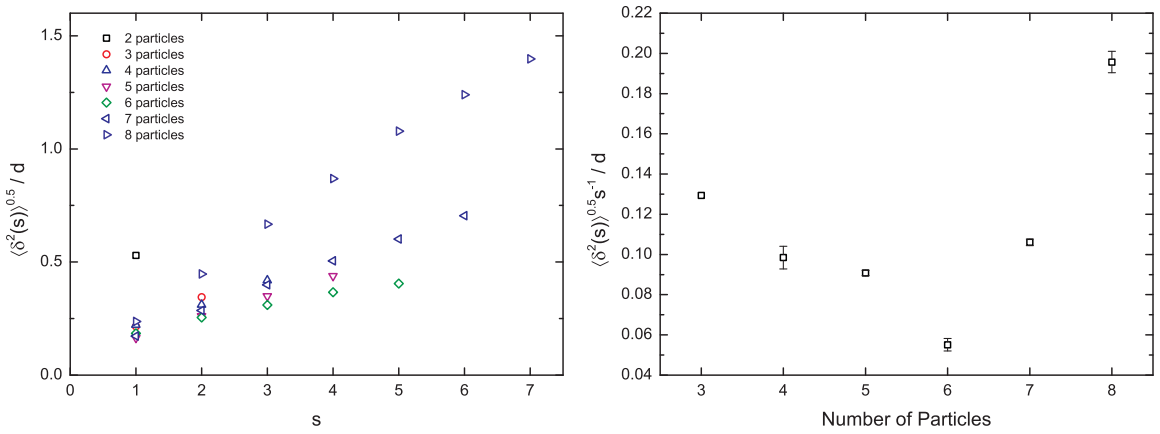


Figure 7.16: Left: RMS transverse displacement for chains of 1.5 µm diameter silica particles. Right: By taking the gradient of the RMS transverse displacement plots as before, and plotting as a function of the number of particles in the chain, the increased stability of the six particle chains can be clearly seen.

optically bound chains. It should be noted that the range of angles accessed for each chain length is generally significantly larger for the 1.5 µm diameter particles when compared to the 3.5 µm diameter silica particles in Figure 7.10, evidenced by the magnitude of the calculated standard deviations and resulting from the increased ease with which these chains can rotate due to the reduced importance of the forward-scattered radiation. For the 1.5 µm diameter particles the length of the eight particle optically bound chain is approaching that of the longest 3.5 µm silica chains which were studied, and the reason for this increased tilt is again believed to be the increasingly large compressive forces acting on the outermost particles.

Finally the root mean square transverse displacement, $\left\langle \delta^2(s) \right\rangle^{1/2}$, was calculated for the different chains as a function of separation along the chain and is shown in Figure 7.16 (left). The same trend demonstrated in Figure 7.11 is observed, with $\left\langle \delta^2(s) \right\rangle^{1/2}$ increasing with position separation, and generally decreasing for the longer chains as the forward-scattered radiation stabilises the one-dimensional chains. These values, normalised to particle diameter, are however slightly larger than those calculated for the 3.5 µm silica case, with typical values approaching 0.4–0.5 particle diameters between the chain ends. As before there is an abrupt increase in these values for the longest chains, indicating their reduced stability. This is quantified in Figure 7.16 (right) where a linear fit through the RMS transverse displacement plot for each chain has enabled the gradient to be calculated as demonstrated earlier for the 3.5 µm diameter particles in Figure 7.11, providing a comparison between chains of different lengths. Again, it can be seen that the RMS transverse displacement

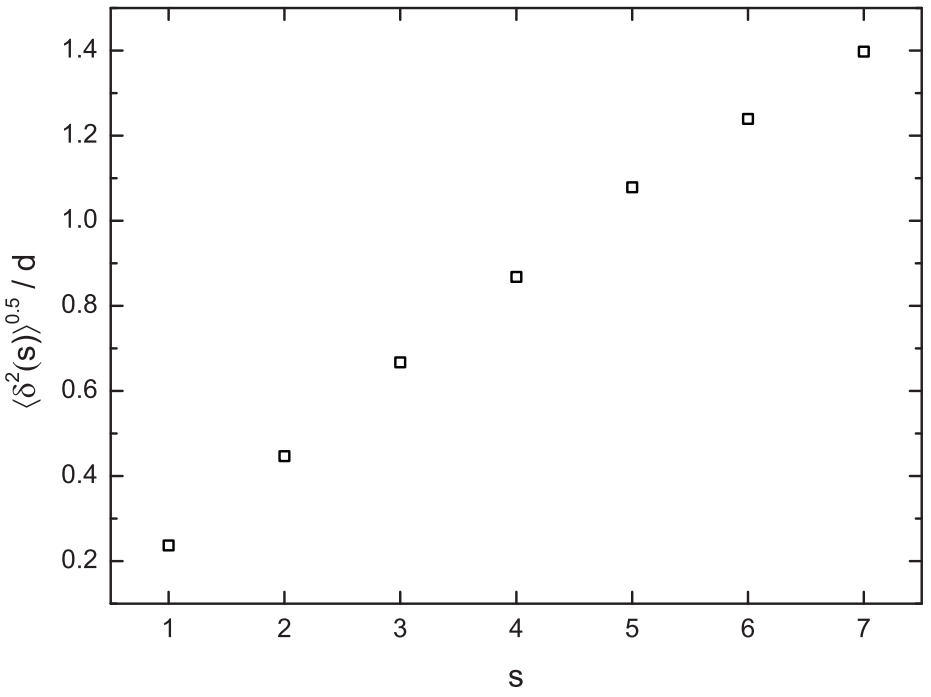


Figure 7.17: RMS transverse displacement as a function of separation for an eight particle optically bound chain of 1.5 µm diameter silica spheres. A smooth increase with separation along the chain is seen, with a maximum value of around 1.4 particle diameters between the particles at the chain ends.

gradient reduces to a minimum for the six particle chain, before sharply rising for the longest chains. The RMS transverse displacement for an eight particle chain is shown in Figure 7.17, showing its smooth increase along the chain with a maximum value of greater than one particle diameter. For the 1.5 µm diameter silica particles the RMS transverse displacement is a linear function of separation, in contrast to the results for the eight particle chain of 3.5 µm diameter silica particles shown in Figure 7.12. This is attributed to the fact that the on-axis inter-particle separation is much more consistent along the entirety of the optically bound chain in this case, highlighting the increased influence of the interference fringe structure within the optical potential.

7.2.1 More Concentrated Silica Samples

The potential for rich, dynamic behaviour is vastly increased when more concentrated samples are used, as the number of scattering particles increases and the multi-particle scattering processes become more important in dictating their resulting behaviour. To investigate this a more concentrated solution of 1.5 µm silica particles was prepared. Initially

long one-dimensional chains are formed but, as the concentration of particles in the evanescent wave region is increased due to gradient forces, multiple parallel chains are observed. As light is scattered predominantly in the forward direction, these chains do not persist side-by-side but instead zip together as can be seen in Figure 7.18. In the first image three parallel chains can be seen, highlighted by dashed lines. The top two of these chains are then seen to merge together in the second image, causing a rapid and immediate ejection of particles from the nascent chain (third image). The particles are ejected out of the sample plane so appear out of focus. In the final images the extended one-dimensional chain of eighteen particles can be seen to split back into shorter sections. This rapid behaviour illustrates the importance of the waveguiding effects on these chains, where the forward-scattered radiation is guided along the chain length, but is hard to controllably study due to the small size of the particles involved. In the final section of this chapter this dynamic behaviour will be explored for 3.5 µm diameter silica particles, allowing modelling using the GLMT simulations.

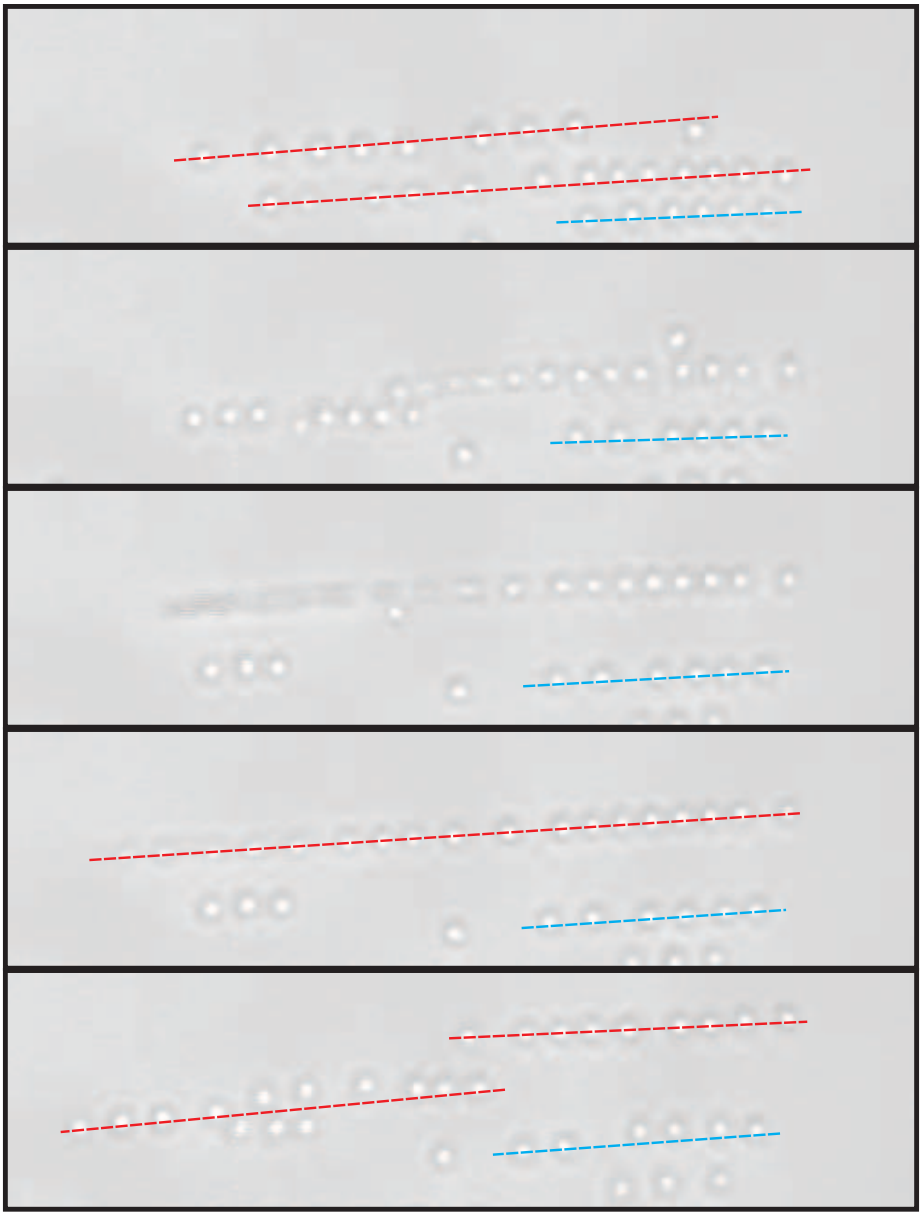


Figure 7.18: More concentrated samples of 1.5 µm diameter silica particles exhibit rich dynamic behaviour. Here two parallel chains are seen to merge, before rapidly ejecting particles along the axis of the nascent chain (third image) and out of the sample plane. The longer chain then splits into two shorter chains before the process is repeated.

7.3 "Newton's Cradle"

As a final example of the dynamic behaviour that can be observed within longer optically bound chains an effect dubbed "Newton's Cradle" is demonstrated. This behaviour was observed for 3.5 µm diameter silica particles using a variation of the evanescent wave setup, as illustrated in Figure 5.1, which allowed higher intensities to be used. Specifically, the Laser Quantum Forte system was still used to form the counter-propagating evanescent waves, except in this case a retro-reflection geometry was employed rather than the dual-fibre output. Despite the difficulties involved with the alignment and balancing of this system, it does allow much higher laser intensities of around 300 mW to be employed.

In this "Newton's Cradle" like motion, particles are ejected from the ends of an optically bound chain, moving both up and out of the rapidly decaying evanescent field. After a certain distance these ejected particles then return to the sample plane, under the influence of both gravitational and optical forces. The evanescent field then acts to propel these particles back towards the chain, before this process is repeated. Screenshots of this dynamic behaviour are given in Figure 7.19. The process is instigated by allowing a particle to drift into the evanescent field from the left hand side, where it is propelled towards the chain. This additional particle increases the scattering forces acting on the other particles within the chain, and causes the final two particles on the right hand side to be ejected. These particles are seen to move out of focus during this process, indicating their movement up and away from the prism surface. In the final images these particles return to the chain and cause two particles from the left of the chain to be ejected, hence the "Newton's Cradle" name.

This complex behaviour is qualitatively predicted by GLMT simulations, shown in Figure 7.20. It should be noted that in this case the simulated particle behaviour is presented from a viewpoint perpendicular to that of the experimental screenshots shown in Figure 7.19, *i.e.* from the side of the chain rather than above. The difficulties associated with simulating the behaviour of longer chains of particles has previously been described in Section 5.4, and is due to the increased number of degrees of freedom which need to be considered. As a result of this, in order to simulate this behaviour the effect of surface reflections has been neglected, although particle Brownian motion has been considered. While the resulting simulations predict a period of oscillation around four times smaller than that which is observed experimentally, perhaps due to the ejection of a single rather

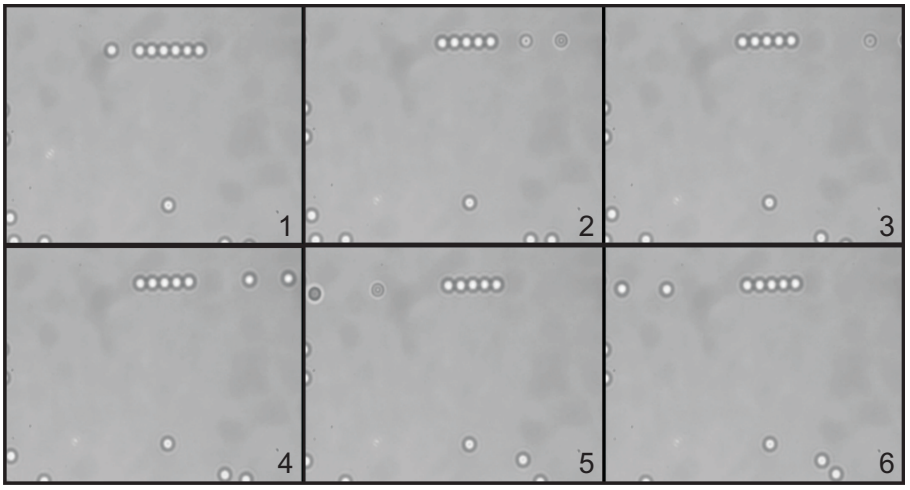


Figure 7.19: Screenshots of the "Newton's Cradle" process, where the addition of a particle to the left of the chain causes two particles to be ejected from the other end, due to the increased scattering forces along the chain caused by the additional particle. These particles are ejected away from the chain and out of the imaging plane, and so appear out of focus. These particles then rejoin the sample plane under the influence of both gravitational and optical forces, and are propelled by the evanescent field to rejoin the chain, where the process is repeated. A video of this process can be found in [151].

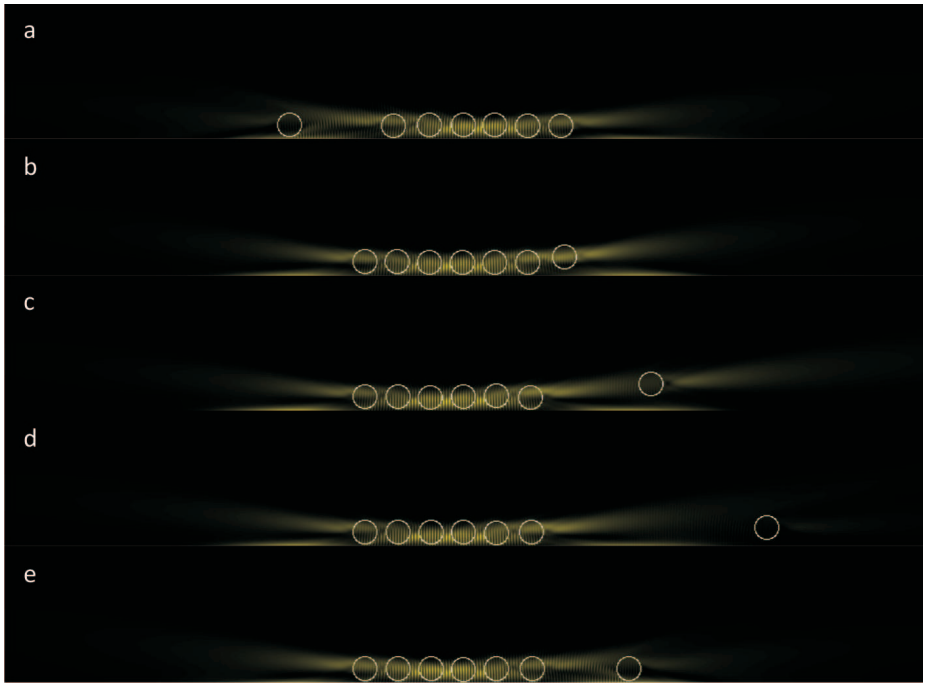


Figure 7.20: Simulation screenshots of the observed "Newton's Cradle" motion (side view). The presence of an additional particle results in particle ejection at the end of the chain. The light intensity, shown in yellow, illustrates the waveguiding effect which is critical in the driving of this process.

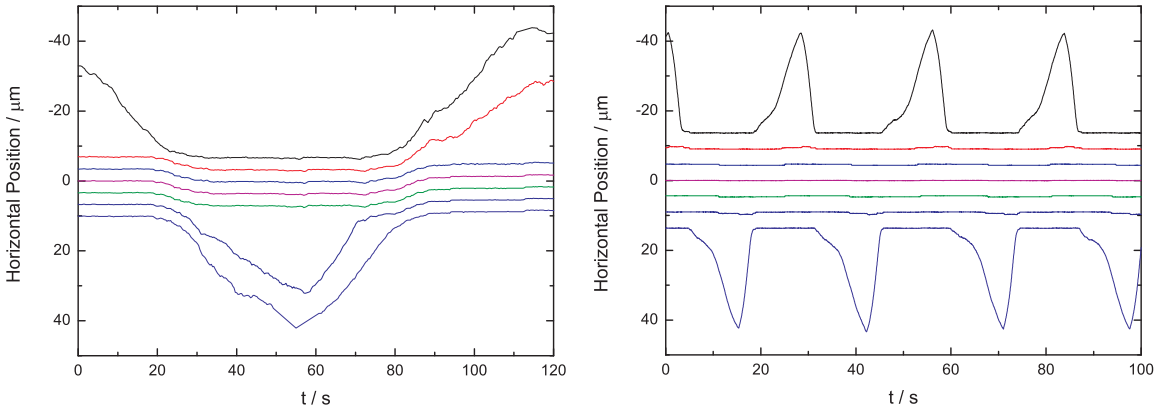


Figure 7.21: Left: Experimentally determined particle trajectories showing the "Newton's Cradle" process. Right: Simulated particle trajectories. A view from above the chain clearly shows one particle joining the chain, resulting in ejection from the opposite end. This process is repeated several times. Although experimentally two particles are ejected instead of one, and the period of oscillation is a factor of four longer, the simulation successfully predicts the general behaviour including the amplitude of oscillation with excellent agreement.

than a pair of particles, it does provide a valuable insight into the physical processes which are responsible for this complex, non-linear behaviour.

One effect which is critical to this dynamic behaviour is that of waveguiding along the optically bound chain. As a particle approaches the chain the forward-scattered field which results is incident upon the first particle in the chain (Figure 7.20 a). This field is waveguided along the optically bound chain, and is sufficiently intense to drive the final particle away from the surface of the prism (b). Due to the rapid decay of the evanescent field with height above the prism surface, this final particle can now be ejected from the chain (c). This particle will then return to the prism surface under the influence of gravity and the gradient force (d), before the evanescent wave propels it back towards the trapping region (e) and the process is repeated. Figure 7.21 (left) shows experimentally determined particle trajectories alongside those taken from the simulation (right). Despite the differences in the period of oscillation, the simulation predicts the general experimental behaviour with great success and in particular the amplitude of the oscillation. A concerted lateral shift of the central particles is also observed experimentally ($t \sim 20\,\mathrm{s}$) but is not apparent in the simulation results, suggesting that in reality the optically bound chain is more flexible than the simulations predict. In Figure 7.22 simulated particle trajectories are shown for the same process, but from a perpendicular view, clearly demonstrating the out-of-plane

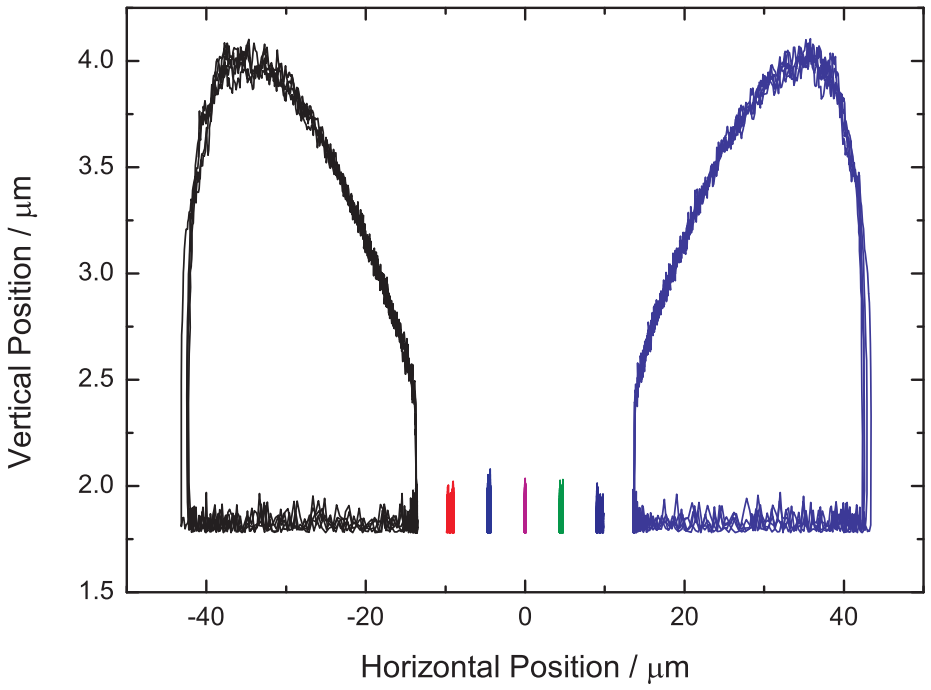


Figure 7.22: Simulated particle trajectories from a perpendicular viewpoint illustrates the out-of-plane nature of the particle ejection process.

ejection already described, and the vertical motion of the central particles in the chain as wave-guiding effects also force them to leave the surface by small distances.

Finally it should be noted that ejection of particles back in the direction from which they have just arrived can also be observed under the same experimental conditions. This has also been observed in simulations, and is very sensitive to the instantaneous configuration of particles within the chain, as well as the exact experimental parameters.

7.4 Conclusions

In this chapter the dynamics of the optically bound matter presented in Chapters 5 and 6 has been studied. By initially looking at the larger 3.5 μm diameter silica particles the mean square displacement (MSD) of these chains was measured and compared to single particle diffusion in each case. The motion of these chains in the evanescent field was shown to be pseudo super-diffusive over short timescales, with diffusion coefficients reduced from that calculated for a single particle as expected due to confinement by the field. Diffusion was shown to be significantly reduced for the collapsed five and six particle chains due to the

strong optical binding effects in this case. Chain tilt was then studied by calculating the angle made with the beam axis for each chain, again showing increased stability for the five and six particle chains. This angular variation rises significantly for the longest eight particle chains as the chain length increases relative to the evanescent wave spot separation and the compressive forces increase. Finally the root mean square transverse displacement was determined for each chain length, again showing the increased stability of five and six particle chains, and the decreasing rigidity of the eight particle chains.

This analysis was then repeated for the smaller 1.5 µm diameter silica particles, showing generally similar effects. Parallel diffusion was seen to be suppressed relative to perpendicular diffusion due to the increased importance of the optical fringes in determining particle positions. More concentrated samples were then used, and complex dynamic behaviour was observed as chains rapidly merged and split due to the multiple particle scattering processes.

Finally an effect dubbed "Newton's Cradle" was presented with the 3.5 µm diameter silica particles. This study was a result of investigating the dynamic behaviour previously observed with the 1.5 µm diameter particles with larger spheres, in order to facilitate the controlled study of this phenomena. These 3.5 µm diameter particles were seen to be ejected from the chain ends due to waveguiding effects, before returning to the chain and repeating the process by ejecting particles from the opposite end. This behaviour was verified using the GLMT simulations first presented in Chapter 5 allowing the physical processes behind this dramatic effect to be understood.

Chapter 8

General Conclusions and Further Work

In this thesis a study of the interaction of colloidal matter with light has been presented, ranging from single particle dynamics in an optical tweezers trap, to dual particle hydrodynamic coupling, and multiple particle optically bound matter formation. Optical tweezers have been utilised in all areas of this work including an investigation of the optical trapping of aerosol droplets. Recent modelling work by Burnham and McGloin [16] had illustrated that the use of annular rather than Gaussian beams for trapping these droplets would have significant improvements in terms of axial trapping efficiency and increasing the size range of trappable droplets. This could have important implications in extending this technique to the study of atmospherically important accumulation mode aerosol droplets.

In order to test this model, an experimental system was designed and built incorporating a Quadrant-PhotoDiode to facilitate fast droplet tracking. Minimum trapping powers were determined for a range of droplet sizes in both Gaussian and annular beams, showing excellent agreement with simulation results. In addition, a study of droplet sizes confirmed that smaller droplets could be trapped with the annular beam, and that these smaller droplets could also be trapped at higher powers. This was investigated further by trapping droplets in both beam types and investigating their axial displacement with increased trapping power. While the droplet trapped in the Gaussian beam exhibited a vertical displacement of 10–20 µm before it was lost, the droplet in the annular beam showed very little axial displacement, and could be stably trapped at much higher powers. Further modelling work

confirmed this trend, again demonstrating excellent agreement with the observed behaviour. This improved axial localisation has potential applications in aerosol spectroscopy such as cavity enhanced Raman scattering (CERS), as the reduced axial position variation could allow measurements to be taken at higher powers. Finally the axial and lateral trapping was compared in each beam type, confirming that in the annular beam the usually limiting axial trapping has been enhanced, and that the mean axial:lateral trap stiffness ratio is greater than one. In order to take this work further it would be desirable to optimise the obstruction size used to form the annular beam, which could be achieved by incorporating a spatial light modulator into the setup. Modifications to the droplet nebulisation techniques could also allow smaller droplets to be produced, enabling experiments designed to push the limits of this technique even further.

While optical tweezers can be utilised to great effect in order to trap and interrogate droplets and particles, they can also be used to confine tracer particles allowing studies of the trapping medium to be undertaken by monitoring their Brownian dynamics. This technique was demonstrated in the micro-rheological investigations of ionic liquids, including the first known demonstration of trapping within pure ionic liquids. Following a comparison of a Quadrant-PhotoDiode and high-speed camera for particle tracking, this technique was used to determine temperature dependent viscosity changes in ionic liquids. The results obtained were in excellent agreement with those determined using macro-rheological techniques, demonstrating the applicability of these micro-rheological investigations, particularly for those ionic liquids which are challenging to produce in large volumes.

Hydrodynamic effects were also probed within these ionic liquids, including an experimental demonstration of Faxén's correction to viscous drag in proximity to a plane surface, agreeing closely with the expected form. This chapter concluded with an investigation of the hydrodynamic coupling between pairs of optically trapped colloidal particles at varying particle separations and in media of a wide range of viscosities, showing excellent agreement with theoretical expectations in each case. The successful demonstration of the use of optical tweezers as a tool for investigating ionic liquids opens up a wide range of potential applications and further studies. This includes the monitoring of CO_2 uptake by these liquids, incorporating spectroscopic studies, and a determination of the effects of impurities on their physical properties, both of which are areas of great current interest.

Following these dual-particle studies, an investigation into optically bound matter was presented, initially focussed on the formation of optically bound chains of 3.5 µm diameter silica particles. The multiple particle scattering effects which determine the structure of this matter make modelling this system extremely challenging. As a result an inverted optical tweezers arrangement was used to controllably assemble this optically bound matter, facilitating the development of an implementation of Generalized Lorentz-Mie Theory (GLMT) through collaboration work with Dr. Jonathan Taylor of The University of Glasgow. Studies of phenomena such as chain collapse, and of the behaviour of these chains with varying salt concentrations, field strength and the polarisation of the input beams, allowed a thorough understanding of the physical processes involved in the formation of these chains to be obtained.

This work on optically bound chains was extended to explore the effects of changing particle size and refractive index. Specifically, optically bound chains of 1.5 µm diameter silica particles were assembled in the same way as previously shown, exhibiting behaviour understood due to the increasing importance of the interference fringes in determining their structure. When 1.0 µm diameter silica particles were studied these effects were further enhanced, resulting in the formation of arrays rather than optically bound chains, in good agreement with previous studies. The structure of these arrays were successfully explained in terms of a preference for these particles to sit between the interference fringes, and the reduced importance of forward-scattered radiation from adjacent particles. The optical binding of 2.31 µm diameter melamine particles was also explored. These particles were large enough that the effects of the interference fringes were deemed to be insignificant, allowing the resulting structures to be understood in terms of the increased forward-scattered radiation from each particle. GLMT simulations were again used to understand these structures, showing good agreement with experimental results.

In the final experimental chapter, the work on optical binding was concluded with a study of the collective dynamics of these particles. Initially 3.5 µm diameter silica particles were used, and the mean square displacement of individual particles was studied in order to quantify the confining effect of the evanescent field. The addition of further particles increased this confinement as a result of the forward-scattered radiation acting to restrict the particles to a linear chain geometry. With the longest chains this effect was reversed, and the decreasing confinement and stability attributed to the increasing length of the chains relative to the range of the underlying optical potential.

After a study of chain diffusion, analysis of the angular distribution of these chains was presented, further quantifying the effects of adding additional particles to the field. A quantitative analysis of chain rigidity in terms of particle number further enforced this trend, confirming the enhanced stability of the five and six particle chains. This analysis was then repeated for chains of the smaller 1.5 µm diameter silica particles, showing similar behaviour. In this case restricted diffusion was seen across the interference fringes as a result of this additional potential barrier.

Finally more complex driven motion was presented for both particle types, where particles were observed to be repeatedly ejected from the chain ends. The GLMT simulation was again utilised in order to explore this behaviour for the 3.5 µm diameter spheres, allowing the effect termed "Newton's Cradle" to be understood. This oscillatory process, reminiscent of the children's toy, is driven by waveguiding along the chain, as demonstrated experimentally and in the GLMT simulations. The excellent agreement observed demonstrates the robust nature of the GLMT simulation and the enhanced understanding of these complex systems that has resulted from a combination of experimental observations and theoretical modelling. There are a range of new directions in which this initial work could be taken, including a study of the behaviour of alternative particle types within the evanescent field such as ellipsoidal or magnetic colloids.

References

[1] K. Svoboda, C. F. Schmidt, D. Branton and S. M. Block. "Conformation and elasticity of the isolated red blood cell membrane skeleton." *Biophysical journal*, **63**, 784–93 (1992).
http://dx.doi.org/10.1016/S0006-3495(92)81644-2

[2] W. Ketterle. "When Atoms Behave as Waves: BoseEinstein Condensation and the Atom Laser (Nobel Lecture)". *ChemPhysChem*, **3**, 736–753 (2002).
http://dx.doi.org/10.1002/1439-7641(20020916)3:9<736::AID-CPHC736>3.0.CO;2-U

[3] C. Gutsche, M. M. Elmahdy, K. Kegler, I. Semenov, T. Stangner, O. Otto, O. Ueberschär, U. F. Keyser, M. Krueger, M. Rauscher, R. Weeber, J. Harting, Y. W. Kim, V. Lobaskin, R. R. Netz and F. Kremer. "Micro-rheology on (polymer-grafted) colloids using optical tweezers." *Journal of physics. Condensed matter : an Institute of Physics journal*, **23**, 184114 (2011).
http://dx.doi.org/10.1088/0953-8984/23/18/184114

[4] S. M. Block, L. S. Goldstein and B. J. Schnapp. "Bead movement by single kinesin molecules studied with optical tweezers." *Nature*, **348**, 348–52 (1990).
http://dx.doi.org/10.1038/348348a0

[5] R. J. Hopkins, L. Mitchem, A. D. Ward and J. P. Reid. "Control and characterisation of a single aerosol droplet in a single-beam gradient-force optical trap". *Physical Chemistry Chemical Physics*, **6**, 4924 (2004).
http://dx.doi.org/10.1039/b414459g

[6] L. J. Moore, R. D. Dear, M. D. Summers, R. P. A. Dullens and G. A. D. Ritchie. "Direct observation of grain rotation-induced grain coalescence in two-dimensional

colloidal crystals." *Nano letters*, **10**, 4266–72 (2010).
http://dx.doi.org/10.1021/nl102786k

[7] J.-C. Meiners and S. R. Quake. "Direct Measurement of Hydrodynamic Cross Correlations between Two Particles in an External Potential". *Physical Review Letters*, **82**, 2211–2214 (1999).
http://dx.doi.org/10.1103/PhysRevLett.82.2211

[8] N. Chattrapiban, E. A. Rogers, D. Cofield, W. T. Hill, III and R. Roy. "Generation of nondiffracting Bessel beams by use of a spatial light modulator". *Optics Letters*, **28**, 2183 (2003).
http://dx.doi.org/10.1364/OL.28.002183

[9] H. Meresman, J. B. Wills, M. Summers, D. McGloin and J. P. Reid. "Manipulation and characterisation of accumulation and coarse mode aerosol particles using a Bessel beam trap." *Physical chemistry chemical physics : PCCP*, **11**, 11333–9 (2009).
http://dx.doi.org/10.1039/b914165k

[10] P. A. Prentice, M. P. MacDonald, T. G. Frank, A. Cuschieri, G. C. Spalding, W. Sibbett, P. A. Campbell and K. Dholakia. "Manipulation and filtration of low index particles with holographic Laguerre-Gaussian optical trap arrays". *Optics Express*, **12**, 593 (2004).
http://dx.doi.org/10.1364/OPEX.12.000593

[11] N. B. Simpson, K. Dholakia, L. Allen and M. J. Padgett. "Mechanical equivalence of spin and orbital angular momentum of light: an optical spanner". *Optics Letters*, **22**, 52 (1997).
http://dx.doi.org/10.1364/OL.22.000052

[12] K. Ladavac and D. G. Grier. "Microoptomechanical pumps assembled and driven by holographic optical vortex arrays". *Optics Express*, **12**, 1144 (2004).
http://dx.doi.org/10.1364/OPEX.12.001144

[13] M. M. Burns, J.-M. Fournier and J. A. Golovchenko. "Optical binding". *Physical Review Letters*, **63**, 1233–1236 (1989).
http://dx.doi.org/10.1103/PhysRevLett.63.1233

[14] C. D. Mellor and C. D. Bain. "Array formation in evanescent waves." *Chemphyschem : a European journal of chemical physics and physical chemistry*, **7**, 329–32 (2006).
http://dx.doi.org/10.1002/cphc.200500348

[15] J. Taylor and G. Love. "Spontaneous symmetry breaking and circulation by optically bound microparticle chains in Gaussian beam traps". *Physical Review A*, **80**, 053808 (2009).
http://dx.doi.org/10.1103/PhysRevA.80.053808

[16] D. R. Burnham and D. McGloin. "Modeling of optical traps for aerosols". *Journal of the Optical Society of America B*, **28**, 2856 (2011).
http://dx.doi.org/10.1364/JOSAB.28.002856

[17] A. Ashkin. "Acceleration and Trapping of Particles by Radiation Pressure". *Physical Review Letters*, **24**, 156–159 (1970).
http://dx.doi.org/10.1103/PhysRevLett.24.156

[18] P. Lebedev. "Experimental examination of light pressure". *Nuovo Cimento*, **834**, 1–26 (1883).

[19] A. Ashkin. "Optical Levitation by Radiation Pressure". *Applied Physics Letters*, **19**, 283 (1971).
http://dx.doi.org/10.1063/1.1653919

[20] A. Ashkin and J. M. Dziedzic. "Optical levitation in high vacuum". *Applied Physics Letters*, **28**, 333 (1976).
http://dx.doi.org/10.1063/1.88748

[21] A. Ashkin and J. M. Dziedzic. "Feedback stabilization of optically levitated particles". *Applied Physics Letters*, **30**, 202 (1977).
http://dx.doi.org/10.1063/1.89335

[22] A. Ashkin, J. M. Dziedzic, J. E. Bjorkholm and S. Chu. "Observation of a single-beam gradient force optical trap for dielectric particles". *Optics Letters*, **11**, 288 (1986).
http://dx.doi.org/10.1364/OL.11.000288

[23] A. Ashkin and J. Dziedzic. "Optical trapping and manipulation of viruses and bacteria". *Science*, **235**, 1517–1520 (1987).
http://dx.doi.org/10.1126/science.3547653

[24] A. Ashkin, J. M. Dziedzic and T. Yamane. "Optical trapping and manipulation of single cells using infrared laser beams." *Nature*, **330**, 769–71 (1987).
http://dx.doi.org/10.1038/330769a0

[25] H. Zhang and K.-K. Liu. "Optical tweezers for single cells." *Journal of the Royal Society, Interface / the Royal Society*, **5**, 671–90 (2008).
http://dx.doi.org/10.1098/rsif.2008.0052

[26] W. Greenleaf, M. Woodside, E. Abbondanzieri and S. Block. "Passive All-Optical Force Clamp for High-Resolution Laser Trapping". *Physical Review Letters*, **95**, 208102 (2005).
http://dx.doi.org/10.1103/PhysRevLett.95.208102

[27] E. A. Abbondanzieri, W. J. Greenleaf, J. W. Shaevitz, R. Landick and S. M. Block. "Direct observation of base-pair stepping by RNA polymerase." *Nature*, **438**, 460–5 (2005).
http://dx.doi.org/10.1038/nature04268

[28] A. Rohrbach. "Stiffness of Optical Traps: Quantitative Agreement between Experiment and Electromagnetic Theory". *Physical Review Letters*, **95**, 168102 (2005).
http://dx.doi.org/10.1103/PhysRevLett.95.168102

[29] K. Svoboda and S. M. Block. "Biological applications of optical forces." *Annual review of biophysics and biomolecular structure*, **23**, 247–85 (1994).
http://dx.doi.org/10.1146/annurev.bb.23.060194.001335

[30] A. D. Mehta. "Single-Molecule Biomechanics with Optical Methods". *Science*, **283**, 1689–1695 (1999).
http://dx.doi.org/10.1126/science.283.5408.1689

[31] S. C. Kuo. "Using Optics to Measure Biological Forces and Mechanics". *Traffic*, **2**, 757–763 (2001).
http://dx.doi.org/10.1034/j.1600-0854.2001.21103.x

[32] A. Ishijima and T. Yanagida. "Single molecule nanobioscience". *Trends in Biochemical Sciences*, **26**, 438–444 (2001).
http://dx.doi.org/10.1016/S0968-0004(01)01860-6

[33] C. Bustamante, J. C. Macosko and G. J. Wuite. "Grabbing the cat by the tail: manipulating molecules one by one." *Nature reviews. Molecular cell biology*, **1**, 130–6 (2000).
http://dx.doi.org/10.1038/35040072

[34] R. Simmons. "Molecular motors: Single-molecule mechanics". *Current Biology*, **6**, 392–394 (1996).
http://dx.doi.org/10.1016/S0960-9822(02)00504-3

[35] M. D. Wang. "Manipulation of single molecules in biology". *Current Opinion in Biotechnology*, **10**, 81–86 (1999).
http://dx.doi.org/10.1016/S0958-1669(99)80015-9

[36] M. Ozkan, M. Wang, C. Ozkan, R. Flynn and S. Esener. "Optical Manipulation of Objects and Biological Cells in Microfluidic Devices". *Biomedical Microdevices*, **5**, 61–67 (2003).
http://dx.doi.org/10.1023/A:1024467417471

[37] D. G. Grier. "Optical tweezers in colloid and interface science". *Current Opinion in Colloid & Interface Science*, **2**, 264–270 (1997).
http://dx.doi.org/10.1016/S1359-0294(97)80034-9

[38] M. D. King, K. C. Thompson and A. D. Ward. "Laser tweezers Raman study of optically trapped aerosol droplets of seawater and oleic acid reacting with ozone: implications for cloud-droplet properties." *Journal of the American Chemical Society*, **126**, 16710–1 (2004).
http://dx.doi.org/10.1021/ja044717o

[39] C. Hertlein, L. Helden, A. Gambassi, S. Dietrich and C. Bechinger. "Direct measurement of critical Casimir forces." *Nature*, **451**, 172–5 (2008).
http://dx.doi.org/10.1038/nature06443

[40] W. Poon. "Physics. Colloids as big atoms." *Science (New York, N.Y.)*, **304**, 830–1 (2004).
http://dx.doi.org/10.1126/science.1097964

[41] A. Mazolli, P. A. Maia Neto and H. M. Nussenzveig. "Theory of trapping forces in optical tweezers". *Proceedings of the Royal Society A: Mathematical, Physical and*

Engineering Sciences, **459**, 3021–3041 (2003).
http://dx.doi.org/10.1098/rspa.2003.1164

[42] N. B. Viana, M. S. Rocha, O. N. Mesquita, A. Mazolli, P. A. Maia Neto and H. M. Nussenzveig. "Towards absolute calibration of optical tweezers". *Physical Review E*, **75**, 021914 (2007).
http://dx.doi.org/10.1103/PhysRevE.75.021914

[43] S. Chandrasekhar. "Stochastic Problems in Physics and Astronomy". *Reviews of Modern Physics*, **15**, 1–89 (1943).
http://dx.doi.org/10.1103/RevModPhys.15.1

[44] R. Di Leonardo, G. Ruocco, J. Leach, M. Padgett, A. Wright, J. Girkin, D. Burnham and D. McGloin. "Parametric Resonance of Optically Trapped Aerosols". *Physical Review Letters*, **99**, 010601 (2007).
http://dx.doi.org/10.1103/PhysRevLett.99.010601

[45] D. R. Burnham, P. J. Reece and D. McGloin. "Parameter exploration of optically trapped liquid aerosols". *Physical Review E*, **82**, 051123 (2010).
http://dx.doi.org/10.1103/PhysRevE.82.051123

[46] K. Berg-Sørensen and H. Flyvbjerg. "Power spectrum analysis for optical tweezers". *Review of Scientific Instruments*, **75**, 594 (2004).
http://dx.doi.org/10.1063/1.1645654

[47] M. D. Summers, D. R. Burnham and D. McGloin. "Trapping solid aerosols with optical tweezers: A comparison between gas and liquid phase optical traps". *Optics Express*, **16**, 7739 (2008).
http://dx.doi.org/10.1364/OE.16.007739

[48] K. C. Neuman and S. M. Block. "Optical trapping." *The Review of scientific instruments*, **75**, 2787–809 (2004).
http://dx.doi.org/10.1063/1.1785844

[49] W. M. Lee, P. J. Reece, R. F. Marchington, N. K. Metzger and K. Dholakia. "Construction and calibration of an optical trap on a fluorescence optical microscope." *Nature protocols*, **2**, 3226–38 (2007).
http://dx.doi.org/10.1038/nprot.2007.446

[50] K. C. Vermeulen, G. J. L. Wuite, G. J. M. Stienen and C. F. Schmidt. "Optical trap stiffness in the presence and absence of spherical aberrations". *Applied Optics*, **45**, 1812 (2006).
http://dx.doi.org/10.1364/AO.45.001812

[51] E. Fällman and O. Axner. "Design for fully steerable dual-trap optical tweezers". *Applied Optics*, **36**, 2107 (1997).
http://dx.doi.org/10.1364/AO.36.002107

[52] K. Visscher, S. Gross and S. Block. "Construction of multiple-beam optical traps with nanometer-resolution position sensing". *IEEE Journal of Selected Topics in Quantum Electronics*, **2**, 1066–1076 (1996).
http://dx.doi.org/10.1109/2944.577338

[53] D. L. J. Vossen, A. van der Horst, M. Dogterom and A. van Blaaderen. "Optical tweezers and confocal microscopy for simultaneous three-dimensional manipulation and imaging in concentrated colloidal dispersions". *Review of Scientific Instruments*, **75**, 2960 (2004).
http://dx.doi.org/10.1063/1.1784559

[54] M. P. N. Juniper, R. Besseling, D. G. A. L. Aarts and R. P. A. Dullens. "Acousto-optically generated potential energy landscapes: potential mapping using colloids under flow". *Optics Express*, **20**, 28707–16 (2012).
http://dx.doi.org/10.1364/OE.20.028707

[55] J.-M. R. Fournier, M. M. Burns and J. A. Golovchenko. "Writing diffractive structures by optical trapping". pp. 101–111 (1995).
http://dx.doi.org/10.1117/12.206208

[56] M. Reicherter, T. Haist, E. U. Wagemann and H. J. Tiziani. "Optical particle trapping with computer-generated holograms written on a liquid-crystal display". *Optics Letters*, **24**, 608 (1999).
http://dx.doi.org/10.1364/OL.24.000608

[57] J. Liesener, M. Reicherter, T. Haist and H. Tiziani. "Multi-functional optical tweezers using computer-generated holograms". *Optics Communications*, **185**, 77–82 (2000).
http://dx.doi.org/10.1016/S0030-4018(00)00990-1

[58] J. E. Curtis, B. A. Koss and D. G. Grier. "Dynamic holographic optical tweezers". *Optics Communications*, **207**, 169–175 (2002).
http://dx.doi.org/10.1016/S0030-4018(02)01524-9

[59] M. K. Cheezum, W. F. Walker and W. H. Guilford. "Quantitative comparison of algorithms for tracking single fluorescent particles." *Biophysical journal*, **81**, 2378–88 (2001).
http://dx.doi.org/10.1016/S0006-3495(01)75884-5

[60] R. E. Thompson, D. R. Larson and W. W. Webb. "Precise nanometer localization analysis for individual fluorescent probes." *Biophysical journal*, **82**, 2775–83 (2002).
http://dx.doi.org/10.1016/S0006-3495(02)75618-X

[61] J. Crocker. "Methods of Digital Video Microscopy for Colloidal Studies". *Journal of Colloid and Interface Science*, **179**, 298–310 (1996).
http://dx.doi.org/10.1006/jcis.1996.0217

[62] G. M. Gibson, J. Leach, S. Keen, A. J. Wright and M. J. Padgett. "Measuring the accuracy of particle position and force in optical tweezers using high-speed video microscopy". *Optics Express*, **16**, 14561 (2008).
http://dx.doi.org/10.1364/OE.16.014561

[63] R. Huang, I. Chavez, K. M. Taute, B. Lukić, S. Jeney, M. G. Raizen and E.-L. Florin. "Direct observation of the full transition from ballistic to diffusive Brownian motion in a liquid". *Nature Physics*, **7**, 576–580 (2011).
http://dx.doi.org/10.1038/nphys1953

[64] D. R. Burnham. *Microscopic Applications of Holographic Beam Shaping and Studies of Optically Trapped Aerosols*. Ph.D thesis, University of St Andrews (2009).
http://hdl.handle.net/10023/699

[65] A. Curran, M. P. Lee, M. J. Padgett, J. M. Cooper and R. Di Leonardo. "Partial Synchronization of Stochastic Oscillators through Hydrodynamic Coupling". *Physical Review Letters*, **108**, 240601 (2012).
http://dx.doi.org/10.1103/PhysRevLett.108.240601

[66] H. Faxén. "Die Bewegung einer starren Kugel längs der Achse eines mit zäher Flüssigkeit gefüllten Rohres". *Arkiv foer Matematik, Astronomi och Fysik*, **17**, 1–28 (1923).

[67] J. Leach, H. Mushfique, S. Keen, R. Di Leonardo, G. Ruocco, J. Cooper and M. Padgett. "Comparison of Faxéns correction for a microsphere translating or rotating near a surface". *Physical Review E*, **79**, 026301 (2009).
http://dx.doi.org/10.1103/PhysRevE.79.026301

[68] E. Fällman and O. Axner. "Influence of a Glass-Water Interface on the On-Axis Trapping of Micrometer-Sized Spherical Objects by Optical Tweezers". *Applied Optics*, **42**, 3915 (2003).
http://dx.doi.org/10.1364/AO.42.003915

[69] R. Omori, T. Kobayashi and A. Suzuki. "Observation of a single-beam gradient-force optical trap for dielectric particles in air". *Optics Letters*, **22**, 816 (1997).
http://dx.doi.org/10.1364/OL.22.000816

[70] N. Magome, M. I. Kohira, E. Hayata, S. Mukai and K. Yoshikawa. "Optical Trapping of a Growing Water Droplet in Air". *The Journal of Physical Chemistry B*, **107**, 3988–3990 (2003).
http://dx.doi.org/10.1021/jp034336h

[71] J. H. Seinfeld and S. M. Pandis. *Atmospheric Chemistry and Physics: From Air Pollution to Climate Change*. Wiley-Blackwell (1998).

[72] J. B. Wills, K. J. Knox and J. P. Reid. "Optical control and characterisation of aerosol". *Chemical Physics Letters*, **481**, 153–165 (2009).
http://dx.doi.org/10.1016/j.cplett.2009.09.020

[73] L. Mitchem and J. P. Reid. "Optical manipulation and characterisation of aerosol particles using a single-beam gradient force optical trap." *Chemical Society reviews*, **37**, 756–69 (2008).
http://dx.doi.org/10.1039/b609713h

[74] M. Z. Jacobson. *Atmospheric Pollution: History, Science, and Regulation*. Cambridge University Press (2002).
http://books.google.co.uk/books?id=NN5S0_3dEvkC

[75] A. E. Carruthers, J. S. Walker, A. Casey, A. J. Orr-Ewing and J. P. Reid. "Selection and characterization of aerosol particle size using a bessel beam optical trap for single particle analysis." *Physical chemistry chemical physics : PCCP*, **14**, 6741–8 (2012).
http://dx.doi.org/10.1039/c2cp40371d

[76] R. Gussgard, T. Lindmo and I. Brevik. "Calculation of the trapping force in a strongly focused laser beam". *Journal of the Optical Society of America B*, **9**, 1922 (1992). http://dx.doi.org/10.1364/JOSAB.9.001922

[77] A. Ashkin. "Forces of a single-beam gradient laser trap on a dielectric sphere in the ray optics regime". *Biophysical Journal*, **61**, 569–582 (1992). http://dx.doi.org/10.1016/S0006-3495(92)81860-X

[78] D. Ganic, X. Gan and M. Gu. "Optical trapping force with annular and doughnut laser beams based on vectorial diffraction". *Optics Express*, **13**, 1260 (2005). http://dx.doi.org/10.1364/OPEX.13.001260

[79] R. Taylor and C. Hnatovsky. "Particle trapping in 3-D using a single fiber probe with an annular light distribution". *Optics Express*, **11**, 2775 (2003). http://dx.doi.org/10.1364/OE.11.002775

[80] M. E. Friese, H. Rubinsztein-Dunlop, N. R. Heckenberg and E. W. Dearden. "Determination of the force constant of a single-beam gradient trap by measurement of backscattered light." *Applied optics*, **35**, 7112–6 (1996). http://www.ncbi.nlm.nih.gov/pubmed/21151316

[81] S. Sato, M. Ishigure and H. Inaba. "Optical trapping and rotational manipulation of microscopic particles and biological cells using higher-order mode Nd:YAG laser beams". *Electronics Letters*, **27**, 1831 (1991). http://dx.doi.org/10.1049/el:19911138

[82] N. B. Simpson, D. McGloin, K. Dholakia, L. Allen and M. J. Padgett. "Optical tweezers with increased axial trapping efficiency". *Journal of Modern Optics*, **45**, 1943–1949 (1998). http://dx.doi.org/10.1080/09500349808231712

[83] A. B. Stilgoe, T. A. Nieminen, G. Knöener, N. R. Heckenberg and H. Rubinsztein-Dunlop. "The effect of Mie resonances on trapping in optical tweezers". *Optics Express*, **16**, 15039 (2008). http://dx.doi.org/10.1364/OE.16.015039

[84] D. R. Burnham and D. McGloin. "Radius measurements of optically trapped aerosols through Brownian motion". *New Journal of Physics*, **11**, 063022 (2009). http://dx.doi.org/10.1088/1367-2630/11/6/063022

[85] P. Walden. "Ueber die Molekulargrösse und elektrische Leitfähigkeit einiger geschmolzenen Salze". *Bulletin de l'Academie Imperiale des Sciences de St. Petersbourg*, **469**, 405–22 (1914).
http://www.mathnet.ru/rus/im6491

[86] F. H. Hurley and T. P. WIer. "The Electrodeposition of Aluminum from Nonaqueous Solutions at Room Temperature". *Journal of The Electrochemical Society*, **98**, 207 (1951).
http://dx.doi.org/10.1149/1.2778133

[87] S. E. Fry and N. J. Pienta. "Effects of molten salts on reactions. Nucleophilic aromatic substitution by halide ions in molten dodecyltributylphosphonium salts". *Journal of the American Chemical Society*, **107**, 6399–6400 (1985).
http://dx.doi.org/10.1021/ja00308a045

[88] J. A. Boon, J. A. Levisky, J. L. Pflug and J. S. Wilkes. "Friedel-Crafts reactions in ambient-temperature molten salts". *The Journal of Organic Chemistry*, **51**, 480–483 (1986).
http://dx.doi.org/10.1021/jo00354a013

[89] H. Zhao, S. Xia and P. Ma. "Use of ionic liquids as green solvents for extractions". *Journal of Chemical Technology & Biotechnology*, **80**, 1089–1096 (2005).
http://dx.doi.org/10.1002/jctb.1333

[90] M. J. Earle and K. R. Seddon. "Ionic liquids. Green solvents for the future". *Pure and Applied Chemistry*, **72**, 1391–1398 (2000).
http://dx.doi.org/10.1351/pac200072071391

[91] J. F. Brennecke and E. J. Maginn. "Ionic liquids: Innovative fluids for chemical processing". *AIChE Journal*, **47**, 2384–2389 (2001).
http://dx.doi.org/10.1002/aic.690471102

[92] N. V. Plechkova and K. R. Seddon. *Methods and Reagents for Green Chemistry*. John Wiley & Sons, Inc., Hoboken, NJ, USA (2007).
http://dx.doi.org/10.1002/9780470124086

[93] J. D. Holbrey and K. R. Seddon. "The phase behaviour of 1-alkyl-3-methylimidazolium tetrafluoroborates; ionic liquids and ionic liquid crystals". *Journal*

of the Chemical Society, Dalton Transactions, pp. 2133–2140 (1999).
http://dx.doi.org/10.1039/a902818h

[94] M. Freemantle. "Designer solvents - Ionic liquids may boost clean technology development". *Chemical & Engineering News*, **76**, 32–37 (1998).
http://dx.doi.org/10.1021/cen-v076n013.p032

[95] M.-D. Bermúdez, A.-E. Jiménez, J. Sanes and F.-J. Carrión. "Ionic liquids as advanced lubricant fluids." *Molecules (Basel, Switzerland)*, **14**, 2888–908 (2009).
http://dx.doi.org/10.3390/molecules14082888

[96] M. Estruga, C. Domingo, X. Domènech and J. A. Ayllón. "Zirconium-doped and silicon-doped TiO_2 photocatalysts synthesis from ionic-liquid-like precursors." *Journal of colloid and interface science*, **344**, 327–33 (2010).
http://dx.doi.org/10.1016/j.jcis.2009.12.063

[97] J. F. Brennecke and B. E. Gurkan. "Ionic Liquids for CO_2 Capture and Emission Reduction". *The Journal of Physical Chemistry Letters*, **1**, 3459–3464 (2010).
http://dx.doi.org/10.1021/jz1014828

[98] A. Ahosseini, E. Ortega, B. Sensenich and A. M. Scurto. "Viscosity of n-alkyl-3-methyl-imidazolium bis(trifluoromethylsulfonyl)amide ionic liquids saturated with compressed CO_2". *Fluid Phase Equilibria*, **286**, 72–78 (2009).
http://dx.doi.org/10.1016/j.fluid.2009.07.013

[99] A. Yao, M. Tassieri, M. Padgett and J. Cooper. "Microrheology with optical tweezers." *Lab on a chip*, **9**, 2568–75 (2009).
http://dx.doi.org/10.1039/b907992k

[100] P. J. Scammells, J. L. Scott and R. D. Singer. "Ionic Liquids: The Neglected Issues". *Australian Journal of Chemistry*, **58**, 155 (2005).
http://dx.doi.org/10.1071/CH04272

[101] L. J. Moore, M. D. Summers and G. A. D. Ritchie. "Optical trapping and spectroscopic characterisation of ionic liquid solutions." *Physical Chemistry Chemical Physics : PCCP*, **15**, 13489–98 (2013).
http://dx.doi.org/10.1039/c3cp50895a

[102] M. M. Elmahdy, C. Gutsche and F. Kremer. "Forces within Single Pairs of Charged Colloids in Aqueous Solutions of Ionic Liquids as Studied by Optical Tweezers". *The Journal of Physical Chemistry C*, **114**, 19452–19458 (2010).
http://dx.doi.org/10.1021/jp107673f

[103] J. Huang and T. Rüther. "Why are Ionic Liquids Attractive for CO_2 Absorption? An Overview". *Australian Journal of Chemistry*, **62**, 298 (2009).
http://dx.doi.org/10.1071/CH08559

[104] C. Cadena, J. L. Anthony, J. K. Shah, T. I. Morrow, J. F. Brennecke and E. J. Maginn. "Why is CO_2 so soluble in imidazolium-based ionic liquids?" *Journal of the American Chemical Society*, **126**, 5300–8 (2004).
http://dx.doi.org/10.1021/ja039615x

[105] D. Evans, A. Yamauchi, R. Roman and E. Z. Casassa. "Micelle formation in ethylammonium nitrate, a low-melting fused salt". *Journal of Colloid and Interface Science*, **88**, 89–96 (1982).
http://dx.doi.org/10.1016/0021-9797(82)90157-6

[106] M. Allen, D. F. Evans and R. Lumry. "Thermodynamic properties of the ethylammonium nitrate + water system: Partial molar volumes, heat capacities, and expansivities". *Journal of Solution Chemistry*, **14**, 549–560 (1985).
http://dx.doi.org/10.1007/BF00649520

[107] C. F. Poole, B. R. Kersten, S. S. Ho, M. E. Coddens and K. G. Furton. "Organic salts, liquid at room temperature, as mobile phases in liquid chromatography". *Journal of Chromatography A*, **352**, 407–425 (1986).
http://dx.doi.org/10.1016/S0021-9673(01)83397-5

[108] A. Ahosseini and A. M. Scurto. "Viscosity of Imidazolium-Based Ionic Liquids at Elevated Pressures: Cation and Anion Effects". *International Journal of Thermophysics*, **29**, 1222–1243 (2008).
http://dx.doi.org/10.1007/s10765-008-0497-7

[109] J. Jacquemin, P. Husson, A. A. H. Padua and V. Majer. "Density and viscosity of several pure and water-saturated ionic liquids". *Green Chemistry*, **8**, 172 (2006).
http://dx.doi.org/10.1039/b513231b

[110] S. Keen, J. Leach, G. Gibson and M. J. Padgett. "Comparison of a high-speed camera and a quadrant detector for measuring displacements in optical tweezers". *Journal of Optics A: Pure and Applied Optics*, **9**, S264–S266 (2007).
http://dx.doi.org/10.1088/1464-4258/9/8/S21

[111] O. Okoturo and T. VanderNoot. "Temperature dependence of viscosity for room temperature ionic liquids". *Journal of Electroanalytical Chemistry*, **568**, 167–181 (2004).
http://dx.doi.org/10.1016/j.jelechem.2003.12.050

[112] S. B. Capelo, T. Méndez-Morales, J. Carrete, E. López Lago, J. Vila, O. Cabeza, J. R. Rodríguez, M. Turmine and L. M. Varela. "Effect of temperature and cationic chain length on the physical properties of ammonium nitrate-based protic ionic liquids." *The journal of physical chemistry. B*, **116**, 11302–12 (2012).
http://dx.doi.org/10.1021/jp3066822

[113] M. Doi and S. F. Edwards. *The Theory of Polymer Dynamics*. Oxford University Press (1986).
http://books.google.co.uk/books/about/The_Theory_of_Polymer_Dynamics.html?id=dMzGyWs3GKcC&redir_esc=y

[114] J. G. de la Torre and V. A. Bloomfield. "Hydrodynamic properties of complex, rigid, biological macromolecules: theory and applications". *Quarterly Reviews of Biophysics*, **14**, 81 (2009).
http://dx.doi.org/10.1017/S0033583500002080

[115] S. Hayward and N. Go. "Collective Variable Description of Native Protein Dynamics". *Annual Review of Physical Chemistry*, **46**, 223–250 (1995).
http://dx.doi.org/10.1146/annurev.pc.46.100195.001255

[116] E. M. Purcell. "Life at low Reynolds number". In "AIP Conference Proceedings", volume 28, pp. 49–64. AIP (1976).
http://dx.doi.org/10.1063/1.30370

[117] H. Fu, V. Shenoy and T. Powers. "Role of slip between a probe particle and a gel in microrheology". *Physical Review E*, **78**, 061503 (2008).
http://dx.doi.org/10.1103/PhysRevE.78.061503

[118] K. R. Seddon, A. Stark and M.-J. Torres. "Influence of chloride, water, and organic solvents on the physical properties of ionic liquids". *Pure and Applied Chemistry*, **72**, 2275–2287 (2000).
http://dx.doi.org/10.1351/pac200072122275

[119] M. M. Burns, J. M. Fournier and J. A. Golovchenko. "Optical matter: crystallization and binding in intense optical fields." *Science (New York, N.Y.)*, **249**, 749–54 (1990).
http://dx.doi.org/10.1126/science.249.4970.749

[120] S. A. Tatarkova, A. E. Carruthers and K. Dholakia. "One-Dimensional Optically Bound Arrays of Microscopic Particles". *Physical Review Letters*, **89**, 283901 (2002).
http://dx.doi.org/10.1103/PhysRevLett.89.283901

[121] W. Singer, M. Frick, S. Bernet and M. Ritsch-Marte. "Self-organized array of regularly spaced microbeads in a fiber-optical trap". *Journal of the Optical Society of America B*, **20**, 1568 (2003).
http://dx.doi.org/10.1364/JOSAB.20.001568

[122] N. K. Metzger, K. Dholakia and E. M. Wright. "Observation of Bistability and Hysteresis in Optical Binding of Two Dielectric Spheres". *Physical Review Letters*, **96**, 068102 (2006).
http://dx.doi.org/10.1103/PhysRevLett.96.068102

[123] M. Guillon, O. Moine and B. Stout. "Longitudinal Optical Binding of High Optical Contrast Microdroplets in Air". *Physical Review Letters*, **96**, 143902 (2006).
http://dx.doi.org/10.1103/PhysRevLett.96.143902

[124] V. Garces-Chavez, D. Roskey, M. D. Summers, H. Melville, D. McGloin, E. M. Wright and K. Dholakia. "Optical levitation in a Bessel light beam". *Applied Physics Letters*, **85**, 4001 (2004).
http://dx.doi.org/10.1063/1.1814820

[125] S. Kawata and T. Sugiura. "Movement of micrometer-sized particles in the evanescent field of a laser beam". *Optics Letters*, **17**, 772 (1992).
http://dx.doi.org/10.1364/OL.17.000772

[126] M. Gu, J.-B. Haumonte, Y. Micheau, J. W. M. Chon and X. Gan. "Laser trapping and manipulation under focused evanescent wave illumination". *Applied Physics Letters*,

84, 4236 (2004).
http://dx.doi.org/10.1063/1.1756200

[127] V. Garces-Chavez, K. Dholakia and G. C. Spalding. "Extended-area optically induced organization of microparticles on a surface". *Applied Physics Letters*, **86**, 031106 (2005).
http://dx.doi.org/10.1063/1.1843283

[128] C. D. Mellor, C. D. Bain and J. Lekner. "Pattern formation in evanescent wave optical traps". In K. Dholakia and G. C. Spalding, editors, "Proc SPIE", volume 5930, pp. 59301C–59301C–10 (2005).
http://dx.doi.org/10.1117/12.616474

[129] M. Siler, M. Sery, T. Cizmar and P. Zemanek. "Submicron particle localization using evanescent field". In K. Dholakia and G. C. Spalding, editors, "Proc SPIE", volume 5930, pp. 59300R–59300R–9 (2005).
http://dx.doi.org/10.1117/12.615741

[130] M. Šiler, T. Čižmár, M. Šerý and P. Zemánek. "Optical forces generated by evanescent standing waves and their usage for sub-micron particle delivery". *Applied Physics B*, **84**, 157–165 (2006).
http://dx.doi.org/10.1007/s00340-006-2235-9

[131] P. J. Reece, V. Garces-Chavez and K. Dholakia. "Near-field optical micromanipulation with cavity enhanced evanescent waves". *Applied Physics Letters*, **88**, 221116 (2006).
http://dx.doi.org/10.1063/1.2208272

[132] V. Garcés-Chávez, R. Quidant, P. J. Reece, G. Badenes, L. Torner and K. Dholakia. "Extended organization of colloidal microparticles by surface plasmon polariton excitation". *Physical Review B*, **73**, 085417 (2006).
http://dx.doi.org/10.1103/PhysRevB.73.085417

[133] N. J. van Leeuwen, L. J. Moore, W. D. Partridge, R. Peverall, G. A. D. Ritchie and M. D. Summers. "Near-field optical trapping with an actively locked cavity". *Journal of Optics*, **13**, 044007 (2011).
http://dx.doi.org/10.1088/2040-8978/13/4/044007

[134] C. D. Mellor, T. A. Fennerty and C. D. Bain. "Polarization effects in optically bound particle arrays". *Optics Express*, **14**, 10079 (2006).
http://dx.doi.org/10.1364/OE.14.010079

[135] J. Lekner. "Force on a scatterer in counter-propagating coherent beams". *Journal of Optics A: Pure and Applied Optics*, **7**, 238–248 (2005).
http://dx.doi.org/10.1088/1464-4258/7/5/005

[136] V. Karásek, O. Brzobohatý and P. Zemánek. "Longitudinal optical binding of several spherical particles studied by the coupled dipole method". *Journal of Optics A: Pure and Applied Optics*, **11**, 034009 (2009).
http://dx.doi.org/10.1088/1464-4258/11/3/034009

[137] J. M. Taylor and G. D. Love. "Optical binding mechanisms: a conceptual model for Gaussian beam traps". *Optics Express*, **17**, 15381 (2009).
http://dx.doi.org/10.1364/OE.17.015381

[138] J. M. Taylor, L. Y. Wong, C. D. Bain and G. D. Love. "Emergent properties in optically bound matter". *Optics Express*, **16**, 6921 (2008).
http://dx.doi.org/10.1364/OE.16.006921

[139] J. Guerra. "Photon tunneling microscopy". *Applied optics*, **29**, 3741–3752 (1990).
http://dx.doi.org/10.1364/AO.29.003741

[140] E. Almaas and I. Brevik. "Radiation forces on a micrometer-sized sphere in an evanescent field". *Journal of the Optical Society of America B*, **12**, 2429 (1995).
http://dx.doi.org/10.1364/JOSAB.12.002429

[141] M. Nieto-Vesperinas, P. C. Chaumet and A. Rahmani. "Near-field photonic forces." *Philosophical transactions. Series A, Mathematical, physical, and engineering sciences*, **362**, 719–37 (2004).
http://dx.doi.org/10.1098/rsta.2003.1343

[142] E. Khaled, S. Hill and P. Barber. "Scattered and internal intensity of a sphere illuminated with a Gaussian beam". *IEEE Transactions on Antennas and Propagation*, **41**, 295–303 (1993).
http://dx.doi.org/10.1109/8.233134

[143] J. A. Stratton. *Electromagnetic theory*. International series in pure and applied physics. McGraw-Hill book company, inc. (1941).
http://books.google.co.uk/books?id=LiZRAAAAMAAJ

[144] S. Chang, J. H. Jo and S. S. Lee. "Theoretical calculations of optical force exerted on a dielectric sphere in the evanescent field generated with a totally-reflected focused gaussian beam". *Optics Communications*, **108**, 133–143 (1994).
http://dx.doi.org/10.1016/0030-4018(94)90228-3

[145] D. Ben-Avraham and S. Havlin. *Diffusion and Reactions in Fractals and Disordered Systems*. Cambridge University Press (2005).
http://www.worldcat.org/isbn/0521617200

[146] E. Furst and A. Gast. "Particle dynamics in magnetorheological suspensions using diffusing-wave spectroscopy". *Physical Review E*, **58**, 3372–3376 (1998).
http://dx.doi.org/10.1103/PhysRevE.58.3372

[147] S. Broersma. "Viscous Force Constant for a Closed Cylinder". *The Journal of Chemical Physics*, **32**, 1632 (1960).
http://dx.doi.org/10.1063/1.1730995

[148] J. Newman, H. L. Swinney and L. A. Day. "Hydrodynamic properties and structure of fd virus". *Journal of Molecular Biology*, **116**, 593–603 (1977).
http://dx.doi.org/10.1016/0022-2836(77)90086-9

[149] K. M. Zero and R. Pecora. "Rotational and translational diffusion in semidilute solutions of rigid-rod macromolecules". *Macromolecules*, **15**, 87–93 (1982).
http://dx.doi.org/10.1021/ma00229a017

[150] E. Furst and A. Gast. "Dynamics and lateral interactions of dipolar chains". *Physical Review E*, **62**, 6916–6925 (2000).
http://dx.doi.org/10.1103/PhysRevE.62.6916

[151] M. D. Summers, R. D. Dear, J. M. Taylor and G. A. D. Ritchie. "Directed assembly of optically bound matter". *Optics Express*, **20**, 1001–12 (2012).
http://dx.doi.org/10.1364/OE.20.001001